Modeling and Simulation of the Dynamic Behavior of Multilayered Piezoelectric Fibers in Smart Structures

by

Shadi Abdel-Gawad

A thesis submitted in partial fulfillment of the requirements for the degree of

Doctor of Philosophy

Department of Mechanical Engineering
University of Alberta

Abstract

The concept of using piezoelectric actuators and sensors to identify damages in advanced structural systems has drawn considerable interest among the research community due to its importance in preventing catastrophic failures. Recent progress in piezoelectric technologies and manufacturing has made it possible to manufacture smart multilayered multifunctional piezoelectric fibers. When these fibers are used in the health monitoring of smart structures, they are generally under dynamic loads. However, the modeling and simulation of these fibers is even more complicated by the fact that they are generally characterized by electromechanical coupling, anisotropy in the transverse plane, and the possible bonding imperfection between their layers. With this in mind, the current research program was undertaken to investigate the dynamic behavior of multiple multilayered piezoelectric fibers in smart structure applications.

Four aspects of the work were accordingly examined. The first is the development of an analytical model of the anisotropic layer in the multilayered piezoelectric fiber, which is capable of predicting stress variations in the anisotropic layer, under dynamic loads. The model is necessary for determining the overall behavior of a layered anisotropic piezoelectric fiber. The analytical formulation is based on the use of Fourier expansion and the separation of variables to reduce the original problem to a set of linear equations in terms of Bessel functions. The resulting set of linear equations are normalized to reduce the numerical ill-conditioning then solved for different boundary conditions. The significance of this newly developed model is manifested by its versatility and application with different material combination, loading frequencies and geometry.

The second is extending and applying the developed anisotropic layer model to analyze the performance of the electromechanical behavior of a multilayered piezoelectric fiber as an actuator or a sensor. The analytical formulation is based on the use of a

newly developed piezoelectric layer model with a transfer matrix representation, which can represent multiple layers including imperfectly bonded layers.

The third is concerned with the development of a general method for the interaction between multilayered piezoelectric fibers and other scatterers. The theoretical formulations are based upon the consistent use of the superposition procedure and cylindrical function coordinate transformations using Graf's theorem. This reduces the original interaction problem to the solution of a set of a single multilayered piezoelectric fiber and embedded scatterer problems. By using this single multilayered piezoelectric fiber solution as the building block, this method provides a general approach to deal with interactions involving complex boundary/interfacial conditions.

The fourth is concerned with the numerical simulation of applying the developed models for the identification of multiple damages using both global and local optimization algorithms. This problem is formulated as an inverse problem which uses optimization techniques to minimize the error between the observed voltage readings induced by damages from a numerical experiment and the calculated voltage predictions induced by trial damages from theoretical simulations on an array of sensors. The models and techniques developed previously are applied to determine the size and location of damages using a newly developed optimization algorithm. The algorithm converges faster than conventional algorithms for single and multiple damages with two types of damages investigated: a circular void and a curved crack.

The methods proposed in this thesis can be used to understand the dynamic behavior of multiple multilayered piezoelectric fibers interacting with damages for the general design of smart structures and the applications of smart structural health monitoring.

Dedication

I would like to dedicate my work to the benefit of science, scientists in specific, and the whole mankind in general. I do hope that this dissertation/thesis will find great industrial applications since I tried my best to make it applicable and at least stimulates the brain with innovative thinking.

After many sleepless nights, early morning studies, missing a lot of fun, and many sacrifices from me and my family, I can finally conclude that the PhD is successfully finished. I would like to dedicate it to my immediate family that is my wife (Nesmahar), children, and mother (Doria Nassef Abdel-Salam).

The dedication goes to my extended family, the members of Advanced Materials and Structures Laboratory (AMSL lab.), Micro/Nano Electro Mechanical Systems (MEMS/NEMS) lab, Maintenance & reliability lab, the graduate coordinators, the department of mechanical engineering, and everyone who intentionally or unintentionally helped me.

Acknowledgments

With heartfelt thanks and deep appreciation, I offer my sincere gratitude to my dear supervisor Dr. Xiaodong Wang. I have been fortunate to have a supervisor who gave me the freedom to explore on my own while guiding, advising, and encouraging me when I went astray, faltered, and stumbled to recover back. His patience, support, motivation, and discussions throughout the study helped me overcome many difficulties and finish this PhD. This work would not have been possible without all the help I received from him.

I would like to thank Dr. Chongqing Ru, Dr. Zhigang Tian, Dr. Weixing Chen, Dr. Tian Tang and Dr. Aleksander Czekanski for their suggestions.

Contents

List of Figures

List of Tables

Chapter 1

General Introduction

This chapter is an introduction to the dynamic behavior of multilayered piezoelectric fiber in smart structural health monitoring. It contains a brief background, motivations for undertaking this study, problem statement, an outline of the research objectives and a preview of the general layout of the study.

1.1   Background

Smart structures are a class of structures which can intelligently self-monitor their health state, act, and execute multiple functionalities in response to detected damages and sensed changes in their surroundings either externally or internally. Typically, a smart structure is composed of a host substructure medium, a network of sensors, actuators, and intelligent controllers. Smart structural health monitoring mimics the human body: the host substructure provides the body, the network of sensors provides the sensory system receiving the external or internal stimuli, the network of actuators provides the muscles or the diagnostic signal, and the intelligent controllers provide the brains to process and analyze the data from the sensory system. In such an integrated structure, in order to monitor the structure's health, possible damages should be detected, evaluated, and quantified.

A *multilayered piezoelectric fiber* is a layered fiber with one or more layers being piezoelectric. Compared with other materials used as sensors and/or actuators such as shape memory alloys, magnetostrictive materials, electrorheological fluids, piezoelectric actuators/sensors (whether polymer or piezoceramics) are the most popular and promising choice in smart structures since they offer a number of advantages over other materials, such as high degree of linearity, high power density, wide range of actuation/sensing frequency, greater efficiency, and low manufacturing costs (Chopra, 2002). Moreover, the same piezoelectric can be used as both a sensor and/or actuator i.e. offering dual transduction functionalities. These advantages make them a good and reliable candidate not only in traditional smart structures but also in the damage identification processes, and therefore, are usually used in structural health monitoring.
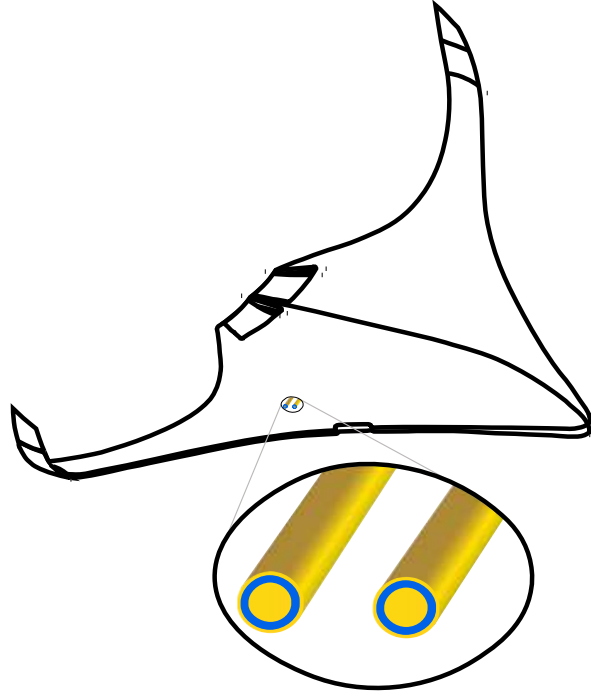
Figure 1.1: A space vehicle using a network of multilayered piezoelectric fibers

Piezoelectric actuators/sensors have been applied or considered to be applied in different industries with typical examples such as, active vibration suppression of aircraft wings, the control of satellites and space structures, the position control of flexible robot arms, and active noise and vibration suppression of helicopter rotor blades (Li et al., 2011; Lin et al., 2013; Williams et al., 2002b). Piezoelectric fibers have also been considered for use in structural health monitoring (Konka, Wahab, and Lian, 2011; Schulz et al., 2000). There have been mainly two types of piezoelectric fiber composites, Active Fiber Composite (AFC) (Bent and Hagood, 1997; Bent, Hagood, and Rodgers, 1995; Bent and Pizzochero, 2000), and Macro Fiber Composite (MFC) (Wilkie et al., 2000; Williams et al., 2002a; Williams et al., 2002b). However, recent progress in fabricating multimaterials (Egusa et al., 2010) and mass manufacturing of multilayered piezoelectric fibers makes it possible to develop new low-cost multifunctional fibers, which can be used in different high-frequency applications (Hadimani et al., 2013; Lu, Qu, and Skorobogatiy, 2017). The recently developed multilayered piezoelectric fiber (Hadimani et al., 2013; Lu, Qu, and Skorobogatiy, 2017) can be applied efficiently in the health monitoring of smart structures.

1.2 Motivation and problem statement

Structural health monitoring techniques are required for many critical structures such as aerospace structures, nuclear reactors, marine structures, submarine structures, large defense/civil structures to ensure functionality, structural integrity, safe operation and prevent catastrophic failures. The lack of or poor structural health monitoring resulted in many major disasters, for example Chernobyl on April of 1986, Aloha airlines Boeing 737 on April of 1988 and Space Shuttle Columbia on February of 2003. Traditional nondestructive testing/evaluation (NDT/NDE) techniques, such as X-radio-graphic detection (X-ray) and ultrasonic evaluation, have been successfully used for the inspection of large structures; however, these techniques usually require bulky instruments, and are often conducted off-site during repairs or scheduled inspection cycles. In the aerospace industry alone, it is estimated that at least 25% of the average aerospace vehicle's life cycle costs are spent on inspection and repair (Chang, 2013; Diamanti and Soutis, 2010). This includes civil, commercial, and military vehicles amounting to a large figure which excludes the downtime costs associated when vehicles are grounded for scheduled maintenance (Giurgiutiu, 2007; Giurgiutiu and Santoni-Bottai, 2011).

Realizing the social and economic impact caused by the catastrophic failures, different organizations and agencies sponsored programs to counteract or mitigate them. Major industrial programs were funded in the aerospace industry with the goal of managing the health of aerospace vehicles. For example, NASA has sponsored the Integrated Vehicle Health Management IVHM program (Ross, 2016), similarly Boeing sponsored the Airplane Health Management AHM program (Boller, 2001). As a result of those programs, research studies have proposed the use of networks of actuators/sensors for structural health monitoring (Giurgiutiu and Santoni-Bottai, 2011). Similar technologies have been tested, used, or considered for use in F-22, F-35, and other aerospace vehicles.

Considering all the aforementioned issues, this study is motivated by applying the newly developed radially polarized multilayered piezoelectric fibers in the health monitoring of smart structures. Since the same piezoelectric can sense and actuate, a network of multilayered piezoelectric fibers could be embedded in those structures with many applications in different industries, such as in aerospace vehicles as shown in the schematic figure 1.1. The network of piezoelectric actuator(s) sends diagnostic signals through the structure medium, the same network of sensors receives the distorted signals then the controller analyzes the received signals to determine the state of the structure. A fundamental issue in using newly developed multilayered piezoelectric fibers (Hadimani et al.,
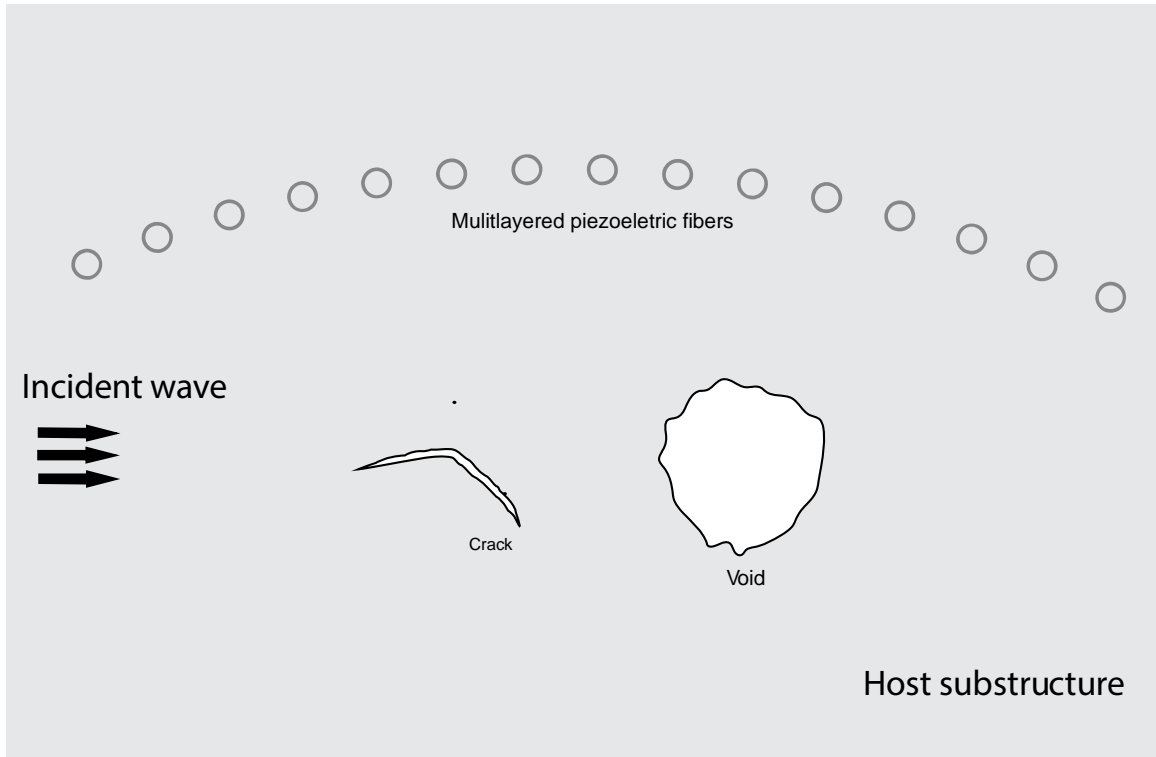
Figure 1.2: Schematic of an array of multilayered piezoelectric fiber sensors for the identification of irregular damages

2013) for damage identification is to determine the dynamic behavior of the radially polarized piezoelectric fibers, the effect of imperfect interfaces on their performance, their interactions and their use to identify developed damages. Another important aspect related to the design of smart structural system is the determination of interfacial debonding that may affect the structural integrity. An accurate assessment of the coupled electromechanical behavior of an integrated structure would, therefore, require the determination of the stress distribution in the composite structure. The piezoelectric layers in these fibers are generally anisotropic in the transverse direction and therefore difficult to analyze when dynamic loads are involved. The dynamic behavior of recently manufactured multilayered piezoelectric fiber (Chocat et al., 2011; Tao et al., 2015) has not been fully understood. The current study develops analytical models for studying the dynamic behavior of multilayered piezoelectric fibers with or without interfacial imperfections and their application in smart structural health monitoring. The developed models can also simulate the interaction of multilayered piezoelectric fibers with irregular damages under harmonic incident waves and identifies damages, such as voids and/or cracks as shown in figure 1.2.

1.3 Research objectives

It is therefore, the objective of this study to conduct a systematic investigation of the electromechanical behavior of multilayered piezoelectric fibers in smart structures and their application in damage identification. Specifically, it is desired to:

1. develop a new anisotropic layer model for a layered cylindrical piezoelectric fibers to investigate the dynamic mechanical behavior of piezoelectric fiber in an elastic medium,

2. extend the developed anisotropic layer model to multilayered piezoelectric fiber to investigate the electromechanical performance of the piezoelectric layer as a sensor and/or actuator with and without interface imperfections,

3. implement the multilayered piezoelectric fiber model into a multiple wave interaction method for cylindrical piezoelectric layer to account for interaction effects between different multilayered fibers with damages,

4. simulate for identifying embedded damages using an array of piezoelectric sensors subject to harmonic elastic waves.

1.4 Approach and research scope

The following section describes the approach road map as used to achieve the aforementioned research objectives:

Modeling and analysis of the dynamic mechanical behavior of a single piezoelectric fiber

Using analytical methods, a new model for examining the dynamic elastic field resulting from a single layered piezoelectric fiber embedded in an elastic solid was developed. The analytical methods are based on the use of a simplified model for the anisotropic piezoelectric layer and Fourier expansion which reduces the original problem to a set of linear equations in terms of Bessel functions. The resulting linear equations are normalized to achieve numerical stability and then solved.

Modeling and analysis of partially bonded multilayered piezoelectric fiber

The newly developed anisotropic layer model is extended to study the dynamic electromechanical behavior of multilayered piezoelectric fibers. The extended model in-

cludes the electric and piezoelectric coupling effects and is represented by transfer matrices. The significance of this representation is manifested by its versatility and ability to represent multiple layers including imperfectly bonded layers. The analytical solution for a partially bonded interface, an arc interface crack, is derived explicitly using Fourier expansion along circumferential direction. The effects of the geometry of the partially bonded interface, elastic material properties and the frequency of the applied loads upon the resulting dynamic stresses are examined.

Multiple wave interactions between multiple multilayered piezoelectric fibers and damages

The electromechanical field in the presence of multiple multilayered fibers and damages is studied based upon the consistent use of superposition principle and cylindrical function coordinate transformations using Graf's theorem, reducing the original interaction problem into the solution of a set of single multilayered piezoelectric fiber problems. The multilayered fiber could have a perfectly bonded or an imperfectly bonded layer as the assumed damages. The dynamic interaction between multiple multilayered fibers and damages such as a crack and/or a void under plane deformations is investigated in details. The solution of the interacting problem provides a numerically stable and reliable prediction of the dynamic stress variations between the fibers, damages and the host structure.

Simulation for multiple damage identification

Numerical simulation is performed based on the previously developed models and techniques for the identification of multiple damages using an improved two-stage optimization method. The first stage is a global optimization based on an intelligently predesigned genetic algorithm while the second is a local optimization using gradient based optimization algorithm. The voltage signals recorded on an array of piezoelectric fiber sensors are used to identify the embedded damages in the structure through minimizing the differences between the numerical experiment voltage recordings and the theoretical voltage predictions.

    The individual models, methods, and techniques developed are verified each independently by comparing the results with that from limiting cases, other published studies, and numerical solutions using a finite element model. The overall theoretical approach encompassing all models, methods, and techniques is further verified using a different finite element model that is considered as the numerical approach for con-

ducting experiments. These numerical experiments generate the observable recorded voltages induced by damages on the array of multilayered piezoelectric fibers. The theoretical approach is then used to simulate the predicted voltages calculated by the guessed damages. The discrepancy between the two voltages is minimized by searching different guessed damages. In addition to identifying multiple damages, the identification process provides a further overall verification to the newly developed models, methods, and techniques since the two different approaches are used independently in this process.

1.5 Thesis Layout

In addition to this introductory chapter, this thesis contains six self-contained chapters, each of which is either a published or to be published article. The current introductory chapter introduces the problem, justifies the undertaking of the study, sets the objectives and outlines the methods of approach adopted. A critical literature review of the relevant work is conducted in the second chapter. An elastic anisotropic layer model is developed and verified in chapter three. The anisotropic layer is modeled as an interphase layer element to overcome the difficulties associated with the dynamic response of the anisotropic layer. The layer model is extended to include the piezoelectric effect in chapter four. With the newly adopted transfer matrices representation consolidating the multilayered piezoelectric fiber an imperfect layer is also considered. Bessel's addition theorem combined with a numerically stable multiple wave interaction between fibers and multiple damages are studied in chapter five. Finally, identifying embedded damages subject to harmonic waves is presented in chapter six. The overall conclusions and future work are discussed in chapter seven. In summary, the thesis contains new models and methods to investigate the dynamic electromechanical behavior of multilayered piezoelectric fibers embedded as actuators or sensors and identify damages in smart structures.

Chapter 2

Fundamentals and literature review

In addition to the existing mono-functionality of traditional smart structures, such as the ability to respond intelligently with a specific functionality to an external stimulus, multifunctional smart structures could also offer multifunctionalities (Bystricky, 2012; Gibson, 2010; Ray, Koh, and Tian, 2000) and, therefore, are receiving significant attention from the research community (Li et al., 2011; Lin et al., 2013). Multifunctional components such as multilayered piezoelectric fibers and some types of piezoelectric composites are essential for these novel multifunctional smart structures (Ferreira, Nóvoa, and Marques, 2016; Mitra and Gopalakrishnan, 2016). Recent advances in multimaterial composites technology enable the fabrication (Egusa et al., 2010) and the mass manufacturing of multilayered piezoelectric fibers (Crawley, 1994; Diamanti and Soutis, 2010). Those recent advances and their rapid expansion in applications have been extensively reported, including their manufacturing (Matt, Bartoli, and Scalea, 2005; Staszewski, Boller, and Tomlinson, 2004), optical properties, and prospects in biomedical field (Chocat et al., 2012; Manbachi and Cobbold, 2011; Wang et al., 2017).

A multilayered piezoelectric fiber is a special kind of multimaterial composites where the materials are shaped into layers of a fiber with one or more layers being piezoelectric. Multimaterial composites, in general, and multilayered piezoelectric fibers, in particular, have undergone a rapid development during the past decade and have been used or considered for use in multifunctional smart structures. A lot of research has been done on multilayered piezoelectric fiber since its theoretical inception (Abouraddy et al., 2007) with an initial focus on the development, fabrication and manufacturing (Chocat et al., 2011; Egusa et al., 2010; Hadimani et al., 2013). After its realization, research has focused on its basic elementary functions since multilayered piezoelectric fibers are multifunctional elements; however, very few published studies have reviewed the modeling of the recently developed multilayered piezoelectric fibers for structural health monitoring applications.

The objective of this chapter is to present a critical literature review on the dynamic behavior of multilayered piezoelectric fiber as actuators, sensors, and/or as a network of integrated systems embedded inside structures for use in different applications with

a focus on structural health monitoring applications. The general layout of the various subsections attempts to organize the presented material in the following order: terminology, earlier historic work, basic concepts, recent publications, related discussions with critic, and potential considerations/applications. The research needs as well as research gabs are discussed under related subsections and then summarized in the conclusions.

2.1 Piezoelectric fibers and composites in smart structures

The word piezo is derived from a Greek word which means pressure. When mechanical stresses are applied certain materials generate electricity that is called the direct piezoelectric effect. The direct piezoelectric effect was first demonstrated in 1880 by the Curie brothers using crystals of quartz (Curie and Curie, 1880a) and Rochelle salt (Curie and Curie, 1880b). They interpreted the piezoelectric effect using their knowledge of the underlying crystal structures.

The Curie brothers, however, did not predict that the application of electricity would generate strain which is termed the converse (indirect/reverse) piezoelectric effect. The converse effect was mathematically derived from the principles of thermodynamics (Lippmann, 1881). In the same year, the Curies published a confirmation of the existence of the converse effect and derived a quantitative proof of the complete reversibility of electric charges to mechanical elastic deformations in piezoelectric crystals (Curie and Curie, 1881).

Piezoelectricity was not applied and remained in research laboratories till World War I (1914-1918). The first direct practical application system was the sonar for submarine detection. The system consisted of two transducers one emitted a high frequency (ultrasonic) pulse using quartz crystals' direct piezoelectric effect and the other transducer picked up the sound bouncing off an object. The object distance was calculated by measuring the travel time and knowledge of the sound speed in a medium. During World War II (1939-1945), independent researchers were able to synthesize and create the first man-made piezoelectric materials leading to PZT (Lead Zirconate Titanate) (Yang, 2006).

The piezoelectric effect is related to the occurrence of electric dipole moments in solids. The piezoelectric material is composed of microscopic electric dipoles which usually have random orientation rendering a small overall dipole density (Doddsa, Meyersb,

and Loh, 2012; Lee and Tarbutton, 2014). The dipole density or electric polarization is responsible for producing the piezoelectric effect. In order to produce an efficient piezoelectric material, it has to be initially oriented such that the electric dipoles align together. This process of forcing the dipoles to orient themselves is called poling or electric polarization. The process usually involves subjecting the material to some type of loading such as stretching, compressing, heating and applying high voltages.

Piezoelectric fiber composites are composed of more than one material with different properties where either the fiber or its layers are piezoelectric and usually the later is called a multimaterial piezoelectric composite or a multilayered piezoelectric fiber if the materials are shaped into layers. In addition to the advantages of engineering the composition of composite materials to desired needs, the usage of composites is necessary to overcome the limitations of piezoceramics mainly its brittleness therefore, allowing for easier surface conformability specially in curved surfaces. Polymer piezoelectric are flexible but have weaker inverse piezoelectric properties, lower elastic stiffness, and weaker actuation performance compared to the same dimension piezoceramic. In addition to these limitations, typical manufacturing conditions did not permit the embedding of polymer piezoelectrics into many materials because they lose their piezoelectric properties under those conditions thus limiting their usage in many smart structures. However, recent advances in multimaterial technologies were able to overcome these limitations.

2.1.1 Theories of piezoelectric

The multi-physics of elastodynamics/electrostatic of a piezoelectric solid continuum is a cross-disciplinary science combining two (seemingly different) branches of continuum physics research (Eringen and Maugin, 2012; Maugin, 2013; Pao, 1978; Tzou, 2012). The foundations of these research sciences were developed in the same period and are associated with the same research scientists such as Cauchy, Faraday, Fresnel, Gauss, Green, Maxwell, Navier and Voigt. In 1821, Navier established the theory of elastic bodies motion which was later adopted by Cauchy and Poisson to model light waves in aether (a hypothesized elastic medium that was thought to carry light-by the early 20's century the aether was abolished) (Pao, 1978). Cauchy's theory of elastodynamics, published in 1827-1828, was developed to investigate the propagation of light waves (Eringen and Maugin, 2012; Pao, 1978). While the theory of elastodynamics is concerned with the deformation of elastic bodies under the influence of loads (forces and couples) within the elastic loading zone, the theory of electrostatic is concerned with studying the electric charges in the absence of magnetic field (no time variation in

magnetic fields). All varying quantities of elastodynamic and electrostatic are being considered as fields, i.e. functions of space and time. The two fields are combined and coupled together through the constitutive piezoelectric material which constitutes the space (See the mathematical theories of a piezoelectric continuum solid in appendix A).

2.1.2 Piezoelectric fibers

Most of the existing piezoelectric materials are transversely anisotropic, with the anisotropy occurring in the electric polarization direction. If the poling direction is chosen (per IEEE standards recommendations (Standard, 1987)) to be direction 3, the constitutive elastic material constants tensor $\mathbf{C}$ can be expressed in a matrix form as (Nayfeh, 1995)

$$\mathbf{C} = \begin{bmatrix} c_{22} & c_{12} & c_{23} & 0 & 0 & 0 \\ c_{12} & c_{22} & c_{23} & 0 & 0 & 0 \\ c_{23} & c_{12} & c_{33} & 0 & 0 & 0 \\ 0 & 0 & 0 & c_{44} & 0 & 0 \\ 0 & 0 & 0 & 0 & c_{44} & 0 \\ 0 & 0 & 0 & 0 & 0 & \frac{1}{2}\left(c_{22} - c_{12}\right) \end{bmatrix}. \tag{2.1}$$

The coupling coefficients $\mathbf{e}$ tensor for most piezoelectric materials, is in the form of

$$\mathbf{e} = \begin{bmatrix} e_{13} & e_{23} & e_{33} & 0 & 0 & 0 \\ 0 & 0 & 0 & e_{24} & 0 & 0 \\ 0 & 0 & 0 & 0 & e_{35} & 0 \end{bmatrix}^{T} \tag{2.2}$$

where the superscript T represents the transpose, (see table 2.1) for commonly used piezoelectric material). The two independent constant coefficients in most piezoelectric materials are e_{32} and e_{33}. The e_{33} coefficient is called the longitudinal coefficient, which describes the electric polarization generated in the same direction as the applied stress. The e_{32} coefficient is called the transverse coefficient, which describes the electric polarization generated in a direction perpendicular to the direction of the applied stress. It is common to use the terminology mode 3-1 and mode 3-3 to distinguish the two transduction mechanisms (Ramadan, Sameoto, and Evoy, 2014).

Researchers realized the importance of utilizing the transduction mode 3-3 by aligning the direction of the piezoelectric effect with the direction of the applied loads to increase transduction efficiency (Bent and Pizzochero, 2000; Sodano, Inman, and Park, 2004). Three leading industrial types of piezoelectric fibers were developed using mode 3-3. These three types are Active Fiber Composites (AFC), Macro Fiber Composites (MFC), and multilayered piezoelectric fibers. Figure 2.1 shows the three industrial

Material	Elastic Constants $\times 10^{10}$(N/m²)					Density 10^3 (kg/m³)	Piezoelectric $\times 10^0$(C/m²)			Relative Permittivity	
	c_{22}	c_{33}	c_{12}	c_{23}	c_{44}	ρ	e_{32}	e_{33}	e_{24}	$\frac{\epsilon_{33}}{\epsilon_0}$	$\frac{\epsilon_{11}}{\epsilon_0}$
isotropic	$\lambda+2\mu$	λ	λ	μ							
PVDF	.25	.9	.075	.072	.025	1.78	.046	-.3	-.01	12	14
P(VDF-TrFE)	.47	.45	.257	.213	.12	1.3	.045	-.18	-.1	12.7	14
PZT-4	13.9	11.5	6.78	7.43	2.5	7.5	-5.2	15.1	12.7	631	728
PZT-5A	16.9	13.2	8.20	9.00	3.3	7.4	-1.7	10.9	12.7	830	916

Table 2.1: Commonly used piezoelectric material properties.

types of piezoelectric fibers, with their time progress, applications, future prospects and cross sections showing their basic components (Konka, Wahab, and Lian, 2011; Schulz et al., 2000; Williams et al., 2002b).

Active Fiber Composites are fabricated by extruding piezoceramic fibers then embedding them in an epoxy matrix with interdigitated electrodes (Lin et al., 2013; Lin and Sodano, 2013). Then, laminated composites can be easily laid up from Active Fiber Composites as initially developed at the Active Materials and Structures Laboratory (AMSL) of Massachusetts Institute of Technology (MIT) (Bent, Hagood, and Rodgers, 1995). Typical research applications of AFC are active vibration control and noise levels reduction of helicopter rotor blades as shown in figure 2.1. In addition to vibration suppression, and noise reduction, Active Fiber Composites are able to adjust the twist of the blades which controls helicopter maneuverability thereby improving the overall performance of these blades reduces noises, enhances the experience for riders, and increases stealth. Research studies on Active Fiber Composites have focused on using them as actuators (Bent, Hagood, and Rodgers, 1995) and enhancing their performance (Bent and Hagood, 1997); however, very few have investigated their application in structural health monitoring (Schulz et al., 2000).

Macro Fiber Composites are manufactured from rectangular piezoceramic fibers, which are cut from piezoceramic wafers using a computer-controlled dicing saw, and hence, saving the overall costs compared to AFC (Wilkie et al., 2000). Macro Fiber Composites (Williams et al., 2002a) are considered in the vertical tail fins of fighter aircraft. The two sides of tail fins have few Macro Fiber Composites actuators embedded under the fiberglass plates as seen in figure 2.1. The fins undergo bending and torsional stresses during flying and the actuators counteract these stresses. This reduction in stress has increased performance and led to longer fin life. Few research studies on applying surface bonded Macro Fiber Composites to generate and sense elastic waves have been conducted (Raghavan, Cesnik, et al., 2007).

Active Fiber Composites (Bent and Hagood, 1997; Bent, Hagood, and Rodgers, 1995; Bent and Pizzochero, 2000) and Macro Fiber Composites (Wilkie et al., 2000; Williams et al., 2002a; Williams et al., 2002b) use interdigitated electrodes where the electric field has to pass through the composite matrix dissipating energy (Raghavan and Cesnik, 2005; Raghavan, Cesnik, et al., 2007). Typically, piezoelectric fiber composites are bonded to the surface of a structure in the form of a patch or laid up as active layers along with fiber-reinforced lamina and were designed for mono functional structures as structural sensing and actuation. Although piezoelectric fiber composite provides advantages over monolithic piezoceramics, they were not integrated in structures and were not intended to provide any additional functionality not even a load- carrying functionality.

Researchers realized the limitations of the piezoelectric fiber composites (AFC and MFC) and developed other alternatives such as the hollow Active Fiber Composites (Brei and Cannon, 2004) and the Active Structural Fiber composites. The Active Structural Fiber Composites were conceptualized (Lin and Sodano, 2008), fabricated, and characterized (Lin and Sodano, 2013) to perform sensing and actuation, in addition to providing critical load-carrying functionality; however, they did not use mode 3-3. The recently developed multilayered piezoelectric fiber (Egusa et al., 2010; Hadimani et al., 2013) uses mode 3-3 efficiently with the electrodes directly connected to the piezoelectric material allowing for individual fiber transduction and control.

The multilayered piezoelectric fibers are fabricated by assembling a large scale preform and repeated drawing from the initial preform to the desired final fiber (Abouraddy et al., 2007; Chocat et al., 2011; Egusa et al., 2010; Stolyarov et al., 2013; Tao, Stolyarov, and Abouraddy, 2012). Researchers proposed large scale continuous production using standard extrusion machines as well as changing the constitutive piezoelectric material meanwhile others considered combining piezoceramics to PVDF (Bian, Liu, and Hui, 2016; Hadimani et al., 2013; Lu, Qu, and Skorobogatiy, 2017). Recent progress in fabricating and mass manufacturing (Hadimani et al., 2013) of multilayered piezoelectric fibers with a transverse poling direction in the cross section makes it possible to develop new multifunctional smart composites, which can be used in different high frequency applications. The multiple functionality fiber can sense pressure, temperature and light as well as it can generate pressure, and light can pass through it. In other words the piezoelectric fibers can see, hear, sense and communicate (Abouraddy et al., 2007). Studies suggest that polymer piezoelectric such as PVDF exhibits better sensing performance than piezoceramic (Rathod et al., 2010).
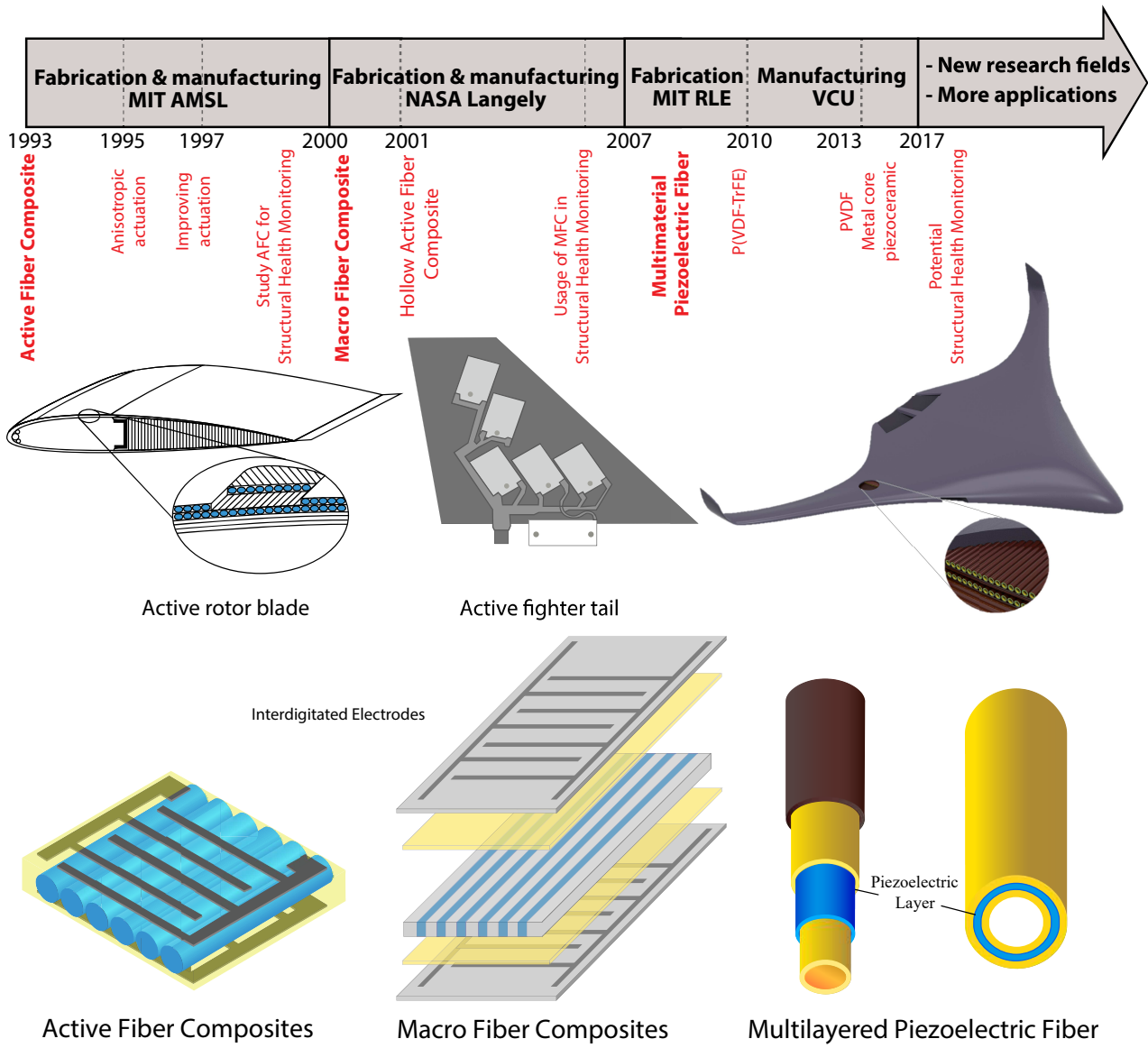
Figure 2.1: Piezoelectric fibers progress landmarks, applications, future prospectives and cross section.

2.2 Modeling techniques of multilayered piezoelectric fibers in structures

Mathematical modeling forms the basis of several studies of theoretical and experimental structural dynamics, such as the dynamic response of structures under elastic waves, and the research concerning the excitation and focusing of waves, among others. The working range of piezoelectric application is in the high-frequency spectrum. Many investigations have been conducted in the field of piezoelectric, smart structures and elastic wave modeling. This section discusses the mathematical modeling of structural dynamics with a focus on the elastodynamics of multilayered piezoelectric fibers.

Mathematical modeling could be divided into modeling the dynamics of anisotropic fibers, multilayered models, interaction models and variational analysis based models. The piezoelectric layer and multilayered models deal with the research work concerning a single layered fiber or cylinder under electromechanical loading while interaction models examine the multiple interactions between multiple fibers and damages.

2.2.1 Dynamics of anisotropic fibers

An important issue in modeling piezoelectric materials in general is that they are anisotropic. Since newly manufactured multilayered piezoelectric fibers are poled transversely in the cross section, existing models for isotropic or transversely-isotropic layers are not sufficient for describing the behavior of the layer.

The analytical solution is quite complicated (for mathematical details see appendix B), involving the solution of eigenvalue problems with three types of elastic waves propagating in an anisotropic media, one quasi-longitudinal and two quasi-transverse (Nayfeh, 1995). The roots of Christoffel equation are the eigen values representing phase velocities c_L, c_{SV}, c_{SH} which correspond to the displacement polarization directions. For a given material, there are three normalized eigen vectors which are dependent on their corresponding eigen values. The normalized eigen vectors are the unit displacement polarization direction vector $\hat{\mathbf{u}}$. For an arbitrarily selected direction in an anisotropic material, three elastic waves can propagate one quasi-longitudinal and two quasi-transverse. In the general case, none are pure longitudinal nor pure transverse. Pure mode is a situation in which the displacement polarization direction coincides with the propagation direction.

In general cases, the dynamic displacement field in an anisotropic elastic medium can no longer be decomposed into independent displacement potentials (Towfighi and

15

Ehsani, 2002). Therefore, well-known solution techniques applicable to isotropic media, based on displacement potentials, cannot be applied directly to anisotropic media. The interaction between elastic waves and anisotropic layers in planar layered media has been studied analytically and numerically (Rokhlin and Huang, 1992; Rokhlin and Huang, 1993). The corresponding problems for cylindrical layers have also been studied under simplified geometric or loading conditions, such as assuming isotropy in the cylinder cross section (Honarvar and Sinclair, 1996; Nayfeh, 1995; Nayfeh, Abdelrahman, and Nagy, 2000; Nayfeh and Nagy, 1996; Sodagar and Honarvar, 2010).

Plate and shell models have also been used in modeling the electromechanical behavior of piezoelectric layers (Dimitriadis, Fuller, and Rogers, 1991; Tzou, 2012). These models were developed based on the assumptions of Kirchhoff-Love for vibration analysis of plates and shells. The formulation of the governing equations is based on angular momentum.

For the current case of anisotropic elastic media coupled with dielectric properties through the piezoelectric coefficients, there are no analytic solutions available. However, there have been various attempts to solve the problem numerically (De Basabe and Sen, 2007; Wang and Rokhlin, 2004).

2.2.2 Multilayered piezoelectric fibers

A multilayered piezoelectric fiber is usually formed by many concentric cylindrical layers with at least one piezoelectric layer. Elastic waves in a medium with layers are often classified according to their displacement polarization directions. Displacement polarization directions that are out of the fiber cross section plane and in the plane of the layers are called SH waves (horizontal shear) or Love waves (1911). Displacement polarization directions that are in the fiber cross section plane and perpendicular to the layers are called P-SV waves (pressure and vertical shear) or Rayleigh waves (1912). Both SH and P-SV waves are dispersive (Love, 2013). On the interface between different media, there is another type of wave traveling along the elastic solid medium, found by Rayleigh in an isotropic halfspace and by Stoneley at the interfaces of solids. Interface waves decay exponentially away from the interface. Half-space surface waves propagating at the interface of fluid-solid are widely known as surface acoustic waves (SAW). When interface waves are guided between layers they are referred to as guided waves. A waveguide is formed by guiding the wave by a plane or by a cylindrical surface.

Host structures can be considered as an embedding layer and an infinite or unbounded layer in cases where this embedding layer's dimensions are relatively larger than the fiber radius. In host structures and for an arbitrarily selected direction in an

Wave type	Particle motion, main assumptions
P-waves	Parallel to the direction of wave propagation
S-waves	Perpendicular to the direction of wave propagation
Flexural waves	Elliptical, plane sections remain plane
Love (SH) waves	Out of plane horizontal shear in layers
P-SV waves	In plane pressure and vertical shear in layers
Interface waves	Elliptical, amplitude decays quickly from interface
Guided waves	Elliptical, guided by plane or cylindrical surfaces

Table 2.2: Wave types in elastic solids.

anisotropic material three elastic waves can propagate one quasi-longitudinal and two quasi-transverse. In the general case, none are pure longitudinal nor pure transverse. All displacement polarizations are pure mode and the transverse wave is arbitrarily polarized in isotropic elastic media. The propagation of two types of elastic waves, P-wave and S-wave in isotropic media, and three types of elastic waves in anisotropic media, one quasi-longitudinal and two quasi-transverse, were found by Cauchy and Poisson (1828). P-waves are primary (or alternatively called pressure, dilatational, irrotational, longitudinal) waves and S-waves are secondary (or alternatively called shear, rotational, distortional, transverse) waves. The different types of elastic waves are shown in table (2.2).

Considering the fact that the piezoelectric layer is relatively thin in comparison to the radius of the fiber, simplified layer models could be used to overcome the difficulties associated in dealing with the anisotropy. Modeling of thin layers in composite materials has been extensively investigated (Kushch et al., 2011; Rajabi and Hasheminejad, 2009; Zhong and Meguid, 1997). In these cases; the interphase, which may represent a third phase between the fiber and host medium (Wang et al., 2005), a bonding layer (Wang and Meguid, 1999) or an imperfect interface caused by deterioration (Chu and Rokhlin, 1995), is usually modeled by distributed interface springs. The spring model (Aboudi, 1987; Bian, Chen, and Lu, 2008; Librescu and Schmidt, 2001; Zhong and Meguid, 1997) however, ignores the hoop stresses and the inertial effect, assuming that the stresses are uniform across the thickness of the layer. As a result, the equations of motion of the layer are not satisfied. When high frequency dynamic loading is applied, the inertial effect of the anisotropic layer needs to be considered.

Numerical solutions for more general anisotropic cylindrically layered media under elastic waves have also been reported in the recent literature (Gsell and Dual, 2004; Norris and Shuvalov, 2010; Norris and Shuvalov, 2012). A possible method in modeling the layer is to simplify it as distributed interface springs to simulate the traction-

displacement relation across the layer. But simplified analytical models for transversely anisotropic cylindrical layers under general dynamic loading are limited to interface-spring models. For the case of radially poled piezoelectric fibers, the piezoelectric layer poses problems in modeling the mechanical behavior because of both its anisotropy and curvature. Abdel-Gawad and Wang (2013) proposed a simple yet an accurate anisotropic layer model.

For relatively few layers the direct approach can be used (Abdel-Gawad and Wang, 2013). However, as the number of layers increases, the direct approach becomes cumbersome, and the transfer matrix technique becomes viable. According to Nayfeh, Abdelrahman, and Nagy (2000), the transfer matrix was originally introduced for flat interfaces by Thomson (1950) and later developed by Haskell (1953). The transfer matrix was later used by many other researchers (Hasheminejad and Alaei-Varnosfaderani, 2012; Huang, Wang, and Rokhlin, 1996; Huang, Rokhlin, and Wang, 1995; Lan and Wei, 2013; Nayfeh and Nagy, 1996; Rajabi and Hasheminejad, 2009) and was categorized as a propagator matrix (Pao, 1983). In this technique, a local layer's transfer matrix relates field variables (i.e. stresses and displacements) between the layer interfaces. Then by extending the solution from one layer to the next while satisfying the continuity condition, a global matrix can be obtained (Wu, Chiu, Wang, et al., 2008).

The weakness of the transfer matrix method is its instabilities when the relative frequency is large (Dunkin, 1965; Lowe, 1995). The cause of the problem is the numeric instability of the transfer matrices due to a combination of both decaying and growing coefficients when inhomogeneous waves are present. Few investigations to develop a numerically robust transfer matrix were conducted (Bouchon, 2003; Kennett and Kerry, 1979).

An alternative to the transfer matrix, and a quite different, method is the direct global matrix method (Knopoff, 1964) and later developed for numerical stability of cylindrical layers by Ricks and Schmidt (1994). In direct global matrix method, the wave fields at all the interfaces and boundaries are assembled together in a single matrix consisting of rows for each equation of each layer, therefore, producing a very large matrix for multilayered media. This method is numerically stable but relatively slow.

Elastic wave functions or Bessel-Fourier functions are the solution tools of analysis for elastic waves in homogeneous isotropic media in curvilinear coordinates. For waves in a cylinder or a sphere, they are derived by separation of variables each depending only on one spatial coordinate (for mathematical details see appendix B). Solutions of the wave equation are called the wave functions in circular cylindrical coordinate (r, θ, z), they are linear combinations of Bessel-Fourier,

$$H_n^{(1),(2)}(kr)e^{in\theta}e^{i\gamma z}e^{-i\omega t} \qquad (2.3)$$

where $H_n^{(1),(2)}(.)$ is a linear combination of Bessel functions of the third kind also known as $H_n^{(1)}(.)$ Hankel function of the first kind and $H_n^{(2)}(.)$ Hankel function of the second kind. The difficulties of solving elastic wave equations for anisotropic and inhomogeneous media is caused by the inability to separate variables. Wave function expansion are not the only tools of analysis available but there are other tools of analysis for example, the integral representation, state space, method of optimal truncation, eigenfunction expansion and mix of methods (Auld, 1990; Honein et al., 1991; Mow and Pao, 1971; Opsal and Visscher, 1985).

The transition or T-matrix is a computational technique introduced by (Waterman, 1969) initially for light wave scattering then for acoustic and elastic waves (Waterman, 1969; Waterman, 1976; Waterman, 2009). In this method which is different from the transfer matrices, the T-matrix relates the unknown scattering coefficients to the incident wave coefficients. The formulation is usually based on the integral representation (Morse and Feshbach, 1953). The method has been extensively researched (Varadan, 1978; Varadan and Varadan, 1979; Varatharajulu and Pao, 1976).

Elastic waves in an inhomogeneous medium are treated by various approximation methods such as perturbation over the averaged material properties of a random medium (Karal Jr and Keller, 1959) and the geometric ray theory (Cerveny, 2005). Most of these approximations are not accurate to identify damages but are suitable for treating the whole inhomogeneous medium as an equivalent substitute composite.

2.2.3 Multiple wave interactions

Multiple interactions refers to "how" multiple piezoelectric fibers interact with each other and "how" they interact with damages. The main reason for studying elastic wave interaction involving piezoelectric fibers and damages is mostly for its potential application to structural health monitoring and damage diagnostics. This and other applications such as the general design of aerospace, nuclear, and submarine structures have generated a great deal of interest in the high-frequency scattering of elastic waves and diffraction by a body with imperfect interfaces. The scatterers, the bodies causing the scatter of waves, are either the piezoelectric or the embedded damages which involve all sorts of damages: voids, inclusions, and cracks, mostly irregularly shaped in finite geometries with complicated free surfaces nearby.

Since the main focus is on the dynamic behavior of piezoelectric fiber, multiple wave interactions are refraction, reflection, diffraction and transmissions as shown in
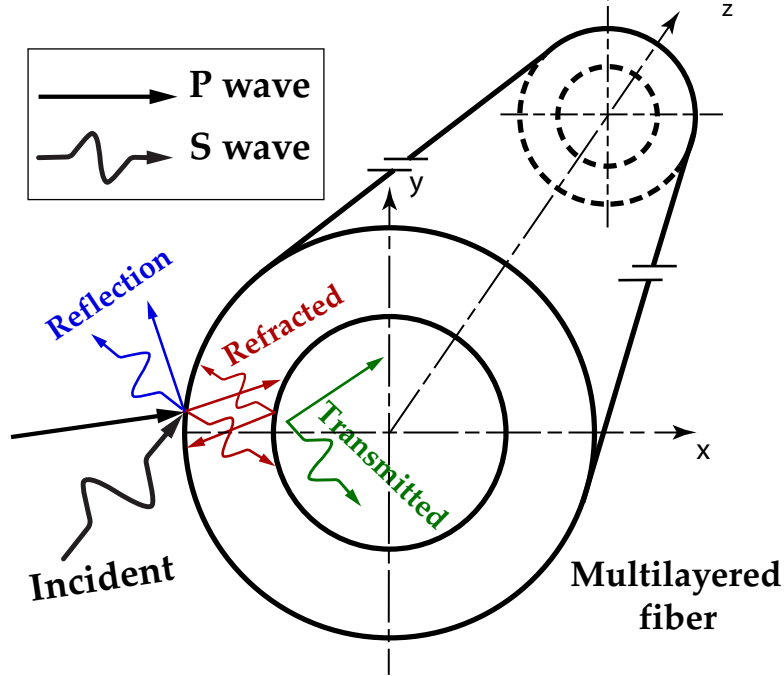
Figure 2.2: Reflection, refraction, transmission of an incident wave on a multilayered fiber.

figure 2.2. Refraction is the change in the direction of propagation of a wave due to a change in its transmission medium. Reflection is the change in the propagation direction of a wavefront at an interface between two different media so that the wavefront returns into the medium from which it originated. Diffraction is the deviation of the wave from its original path and it refers to various phenomena which occur when a wave encounters an obstacle or a slit. Diffraction involves the transmission and bending of waves around an obstacle (Bogan and Hinders, 1994; Kraut, 1975).

There is no general wide consensus on the term scattering and it is often confused with diffraction since researchers use them interchangeably to express different wave phenomena. Rayleigh expressed the scattered wave as the difference of the total wave field observed in the presence of an obstacle and the incident wave, the scattered wave then consisted of the reflected part by the obstacle into the illuminated zone, and both the refracted and diffracted by the obstacle into the shadow zone. In that sense, the definition of wave scattering has a broader implication than the original meaning of "wave diffraction" referring to the general phenomenon of wave changes in propagation direction or splitting into several waves upon encountering a physical boundary (Cai, 1998). However, in the course of studying diffraction of waves, reflections and refractions are integral parts and they both generally describe the wave behavior. Thus "scattering" and "diffraction" are often used to describe the same wave phenomenon. When the

diffracted portion of the scattered waves are of importance, especially in connection with the passage of waves through an object with sharp edges, the usage of "diffraction of waves" usually prevails. When the diffracted part has a lesser role, especially in the case of an obstacle without sharp edges, the title of "scattering of waves" is usually preferred. Since the scattering of elastic waves is not different from the scattering of sound or electromagnetic waves, diffraction can be defined as the deviation of the wave from its original path while scattering is the radiation of secondary waves from the obstacle. In an elastic medium, the obstacle is usually a damage in the form of a cavity, a crack or an inhomogeneity (a substance with a different elastic property from the medium).

There are many different definitions to the term "damage" according to the area of study. In the area of structural health monitoring, damage(s) can be understood as a defect, an imperfection or failing which hinders engineering structures functional and working conditions. In the most general terms, damages can be defined as changes introduced into a structure that negatively affect its current or future performance. Traditionally, the concept that damages are not meaningful without a comparison between two different states of the system, one of which is assumed to represent the initial reference, and often undamaged, reference baseline state can be part of the definition, however, this concept has been modified since the undamaged state is usually unavailable (Anton, Inman, and Park, 2009). The definition of damages in this article will be limited to changes either in the material and/or geometric properties of these structures since the main focus is on the study of structural health monitoring using multilayered piezoelectric fibers. These changes include boundary conditions, interface imperfections, voids, inhomogeneities and embedded cracks, which adversely affect the current or future performance of these structures.

Defects, flaws and/or faults are terms used to represent damages although are not universally accepted. The terms defects or flaws are more often used in the industrial and manufacturing industry to indicate manufacturing defects or flaws in products (Sun, Waisman, and Betti, 2016; Zhao et al., 2007). Fault(s) is a closely related term used more frequently in electrical and reliability engineering (Ruffino and Delsanto, 1999). Defects, flaws or faults could grow and coalesce at various rates depending on loading conditions to cause component and then structural operation deficiencies to failures. The term damage does not necessarily imply a total loss of the system functionality, but rather that the system is no longer operating in its optimal conditions.

Drastic idealization is necessary in order to compute scattering interactions, and all theories, past, and present, make many simplifications. Some simplifications are

done on the differential solution by using eigen functions (Bessel-Fourier) although the singular behavior of the crack opening displacement (COD) cannot be described using eigen functions. It was shown that although the edge singularity in the COD is crucial to the computation of near field local stresses, it has a minor direct effect on the overall field and the overall scattering (Opsal and Visscher, 1985; Visscher, 1981). The total wave outside the scatterer is

$$\mathbf{u} = \mathbf{u}^{in} + \mathbf{u}^{sc} \tag{2.4}$$

where $\mathbf{u}^{in}$ is the incident wave and $\mathbf{u}^{sc}$ is the scattered wave.

The near field stress of the inclusion or inhomogeneity recursively interacts with the incident wave developing stress concentration (Mow and Pao, 1971; Thompson and Wadley, 1989). Stress concentration is the sharp increase of stress over a nominal value in a localized region of a structural member due to diffraction and scattering from geometric discontinuities such as holes, corners, notches and cracks. Therefore, one of the most fundamental issues regarding the use of piezoelectric fibers in smart structures is to accurately evaluate the resulting elastic waves. Elastic waves scattering of circular and cylindrical cavities were studied by Lee and Cao (1989) and Lee and Karl (1992). The interaction of waves with arrays of vertical circular cylinders in water was studied by Linton and Evans (1990). Existing solutions which account for the dynamic interaction and scattering deal mainly with defects using boundary element method (Manolis and Beskos, 1988; Mykhaskiv, 2005; Rizzo, Shippy, and Rezayat, 1985), Bessel's addition theorem (Lee and Cao, 1989; Lee and Karl, 1992; Martin, 2006), surface integral methods (Varadan, 1978; Varadan and Varadan, 1979; Varatharajulu and Pao, 1976), statistical approximations of effective field methods (Varadan, Varadan, and Pao, 1978), the superposition technique (Meguid and Wang, 1995), and the pseudo incident wave method were used to deal with cracks (Meguid and Wang, 2000; Meguid and Wang, 2013; Wang and Meguid, 1997; Wang and Meguid, 1999). Semi-analytical integral equation methods have been used for solving elastic waves in a plate with multiple circular holes (Lee and Chen, 2010) and studying the composite fibers (Bose and Mal, 1974), (Yang and Mal, 1994), layered circular elastic cylinders (Cai, 2004) and (Sumiya, Biwa, and Haïat, 2013). Simplified models have been used to simulate radially polarized piezoelectric embedded actuator dynamics either by considering axisymmetric loading (Kim and Lee, 2007; Lü et al., 2009) or by assuming an isotropic piezoelectric material (Sedighi and Shakeri, 2009).

In spite of the fact that the multiple interaction of fiber reinforced composite has received considerable attention, only a very limited number of published studies treat the electromechanical interaction of wave fields around multilayered piezoelectric fiber

subject to plane elastic waves i.e. longitudinal (P-waves) and in-plane shear (Shear Vertical SV-waves). This is mainly due to the difficulties associated with the mode conversions that occur at the boundaries resulting from the coupling of P/SV wave modes in the dynamic equations and the lack of explicit solutions for anisotropic layers under dynamic loads. In addition, many available techniques, result in a system of equations which are highly singular and cannot be solved directly by numerical methods. Analytical methods are highly accurate, but they are developed for simple specific geometries i.e. for a plate or a cylinder and they are unable to model complex arbitrarily geometries.

The scattering of elastic waves by damages and specially cracks can be investigated by the use of integral equation representation (Erdogan and Gupta, 1972). The boundary conditions around the damage are established which is mixed boundary conditions for cracked surfaces. The integral equations can be analytically solved, for simple cases, by expanding the unknown crack opening displacement in the integral equation in a set of orthogonal polynomial functions and the integral equation is projected onto the same set of functions (Estrada and Kanwal, 2012; Krenk, 1975). The procedure can be used automatically for hypersingularity in the integral equation or by reducing singularity order (Bostrom, 2003; Chan, Fannjiang, and Paulino, 2003). The number of terms needed to numerically solve the expanded polynomial is related to the relative frequency by $kR + 6$ with truncation after 50 terms for $kR < 50$ (Bostrom, 2003).

2.2.4 Variational modeling and numerical analysis

Although analytical solutions have been proposed for a wide variety of cases, sometimes the geometry and/or the boundary conditions increase the mathematical complexity of the solution to such a degree that numerical methods are required to obtain a solution. The variational principles of elastodynamics/electrostatic can be used to reformulate the governing equations so they are amenable for approximate solutions and numerical calculations (Altay and Dokmeci, 2007; Oden and Reddy, 2012).

Finite Element (FE) method is a widely used method to numerically analyze complicated structures. In the analysis of elastic waves, FE method can be divided into time-domain and frequency domain analysis. Time-domain FE methods are obtained by integration over time of the discretized equations. The solution for an elastodynamic problem is based on an assumed polynomial approximation for displacements. These assumed displacement polynomials are required to satisfy the weak form of the governing differential equation, which yields the stiffness and the mass matrices. Time-domain analysis has been used to predict the performance of ultrasound transducers (Hossack

and Hayward, 1991; Lerch, 1990; McKeighen, 2001; Mills and Smith, 2002; Zhou, Wu, and Ma, 2006). The effect of multiple layers, bonding layer and electrodes on the performance of the transducer can be addressed using this technique (McKeighen, 2001; Zhou, Wu, and Ma, 2006).

The frequency domain FE is based on discretizing the Fourier transform of the governing equation (Gopalakrishnan and Mitra, 2010) and the solutions are obtained in terms of the frequency. The Fast Fourier Transform-Spectral Element (FFT-SE) method is essentially a finite element method formulated in the frequency domain (Beskos and Narayanan, 1983; Gopalakrishnan, Chakraborty, and Mahapatra, 2007; Rizzi and Doyle, 1992; Zagrai et al., 2010). Frequency-domain FEM has been broadly used to analyze piezoelectric structures and ultrasound transducers (Bai et al., 2004; Mukdadi and Datta, 2003; Mukdadi et al., 2002; Pauley and Dong, 1976; Siao, Dong, and Song, 1994; Taciroglu et al., 2004) since it can easily identify resonant frequencies. However, some boundary conditions and complicated geometries are difficult to analyze in this domain (Ballandras et al., 2005; Ballandras et al., 2003; Predoi et al., 2007; Wilm, Ballandras, and Laude, 2004; Wilm et al., 2005).

The Spectral Element (SE) method is also reported in the literature to refer to the time domain spectral spatial analysis in which the interpolation nodes of the elements are located at points corresponding to zeros of an appropriate family of Jacobi polynomials (usually Legendre or Chebyshev). A set of local shape functions consisting of Lagrange polynomials, which are defined at these points, are built and used. In his first work on this subject, Patera (1984) proposed a sub-parametric approach for standard FEM. This means that the high-order polynomials are used for field variable approximation while the geometry is described by a low order polynomial. He introduced high-order Lagrange interpolants along with the Chebyshev-Gauss-Lobatto integration rule leading to a diagonal mass matrix allowing for efficient computation. The spectral element method in time domain could be considered a special case of the p-version FEM with the exception for the specific approximation functions it uses.

The Semi Analytical Finite Element (SAFE) combines both the finite element and analytical model to overcome some of their modeling deficiencies. Early research on the (SAFE) method was conducted to solve the problems of guided wave propagation in a laminated orthotropic cylinder (Nelson, Dong, and Kalra, 1971) and a waveguide with an arbitrary shape but uniform cross-section (Lagasse, 1973). The SAFE method was used to study guided wave propagation in rods, rails, and pipes (Hayashi, Song, and Rose, 2003; Lee, 2006). The SAFE method was used to detect the condition of bonded joints with viscoelastic damping (Matt, Bartoli, and Scalea, 2005) and was recently

used to analyze guided wave propagation in hollow cylinders with viscoelastic coatings (Mu and Rose, 2008).

The Finite Difference (FD) method solves the elastodynamic wave equations by replacing the derivatives in space and time with their finite-difference approximations. This numerical approach needs a grid of points to be set up in a structured way. According to this method, the Taylor expansion of a continuous function around some point is truncated after an arbitrary number of terms that determines the order of accuracy of the finite difference formula. FD method was used in modeling the scattering of elastic waves by cracks (Harker, 1984; Scandrett and Achenbach, 1987; Wu and Gong, 1993). The FD method was used to simulate the ultrasonic waves for the inspection of the inner-surface breaking cracks with time-domain signal analysis and processing of displacement propagation (Scandrett and Achenbach, 1987). The FDM with staggered grid was used to study impact induced transient elastic waves in heterogeneous plates with cavities or inclusions (Wu and Gong, 1993). The FD method was applied to study the scattering of Lamb waves in cracked plates (Harker, 1984) and the potential of using the FD method in modeling non destructive testing system was demonstrated by many researchers (Harker, 1984; Scandrett and Achenbach, 1987; Wu and Gong, 1993). A combination of FD method with the Perfectly Matched Layer (PML), an absorbing layer to model unbounded media, has been done to study bulk elastic wave propagation and scattering in an infinite media (Satyanarayan et al., 2008; Satyanarayan et al., 2007; Sridharan et al., 2006; Yin, Morris, and O'Brien Jr, 2003). Also, the use of commercially available FD method software packages is not uncommon (Yang, Cascante, and Anna Polak, 2009).

Another related approach to the finite difference is the Local Interaction Simulation Approach (LISA) (Delsanto et al., 1997) which discretizes the system into a grid or lattice like finite difference method. The formulation is based on replacing the spatial and temporal derivatives in the elastodynamic equilibrium equations by recursive relations based on FD transformations. It was initially developed to study wave propagation in isotropic heterogeneous media in parallel computation computers (Delsanto, Schechter, and Mignogna, 1997; Delsanto et al., 1992; Delsanto et al., 1994). Experimental validations of LISA for both isotropic and anisotropic media were later conducted and reported (Ruffino and Delsanto, 1999). Another LISA was compared with experimental results using laser vibrometer for elastic plates. LISA was used for studying the non-linear interaction of waves and cracks (Shen and Cesnik, 2017).

The development of the generalized finite difference (GFD) method is considered as an evolution of the FD method by combining the variational principles and element free

Galerkin methods (meshless methods) (Gavete, Gavete, and Benito, 2003). The GFD can be applied over general or irregular clouds of points thus simulating irregular shapes. The main drawback of the GFD method is the possibility of obtaining ill-conditioned nodes (Benito, Urena, and Gavete, 2007).

The Boundary Element method (BEM) is a numerical computational method for solving linear partial differential equations which have been formulated in integral form and the formulation is derived by applying Green's identity. This identity converts a volume (domain) integral to a surface (boundary) integral, therefore, the name boundary integral equation method (BIEM). This reduction in dimensions is a significant advantage over domain-type approaches like the FEM and the FDM. However, BEM has been widely used in solving various vibration analysis problems when compared to studies of elastic wave scattering (Manolis and Beskos, 1988).

The Pseudo-spectral (PS) method could be considered as an extension to the finite difference method in which the value of the local derivative of a single collocation point is dependent on all the values of the function at all the collocation points. In periodic boundary conditions, the mesh of points is uniform and the approximating function is expanded in terms of Fourier series. In the case of non-periodic boundary conditions, the mesh is non-uniform and the approximating function is as a type of the Jacobi family of polynomials, usually Chebyshev or Legendre is used (Trefethen, 2000). SE method differs from both PS and conventional FE methods in two aspects: 1) spectral methods utilize high degree approximating functions with support over the entire domain, and 2) FE methods use low degree approximating functions with compact support (piecewise polynomials). SE method exploits the advantage of high degree functions, along with the flexibility finite element methods provide in representing geometrically complex domains (Sprague and Geers, 2008).

Trefftz methods are a type of finite element in which the test and trial functions are solutions of the governing differential equation. For elastic wave problems, their trial functional space contain oscillating basis functions and are expected to achieve better approximation properties than classical piecewise-polynomial spaces. The main difficulties encountered in the implementation are the assembly and the ill-conditioning of linear systems, some strategies have been proposed to cope with these problems (Hiptmair, Moiola, and Perugia, 2015).

The eXtended Finite Element Method XFEM extends the traditional finite element (FEM) by exploiting the partition of unity property (Melenk and Babuška, 1996) which allows enriching the solution with discontinuous functions. It retains the advantages of meshfree methods (Gavete, Gavete, and Benito, 2003) and alleviates the limitations

of classical finite element; therefore, it has been used to model various discontinuities: strong (cracks) and weak (material interfaces) (Moes, Dolbow, and Belytschko, 1999). The method has been successfully applied in solving damage identification of isotropic medium mostly in static problems (Sun, Waisman, and Betti, 2013; Sun, Waisman, and Betti, 2014a; Sun, Waisman, and Betti, 2014b) with few publications handling some cases of the dynamic problem (Jung and Taciroglu, 2016; Rabinovich, Givoli, and Vigdergauz, 2007). In one case, the time harmonic of a reduced elastic wave (with only one wave number was considered) which is equivalent to considering SH waves. The other case considered the transient elastodynamic of plates (Jung and Taciroglu, 2016). Special care should be given to the mesh size while handling the dynamic problems using conventional XFEM (Livani, Khaji, and Zakian, 2018).

Although most of FE methods can model complicated geometries and loads, they are not as efficient as analytical methods in modeling high frequencies since their mesh size needs to be 10 to 20 times the wavelength of the highest frequency contents of interest for proper modeling (Lee, Kim, Leung, et al., 2000). High frequency contents are expected in micro and nano fibered structures which is the size range of multilayered piezoelectric fibers with a ~ 500 μm radius and a layer of ~ 40 μm in thickness. The wavelength contents are comparable to the fibers and damages embedded in those structures. The absolute frequency contents for MEMS, NEMS are high although their dimensionless frequency might be small in which FE fails to model it. FE methods suffer from numerical dispersion leading to false waves (Ostachowicz and Kudela, 2011). The use of FE methods in unbounded media is also an issue (Ekevid and Wiberg, 2002; Kawamura et al., 2011; Pettit et al., 2014; Rajagopal et al., 2012; Wolf and Song, 1996). Almost all FE methods need remeshing for each configuration when searching the space of solutions as in damage identification; therefore, the need to rely on analytical models is essential.

2.3 Applications of piezoelectrics

This section discusses current applications, present research and future of piezoelectric prospectives with a focus on piezoelectric fibers. While the research, development and fabrication of piezoelectric fiber systems is important, the ability to realize these composite structures into realistic applications has dramatically evolved.

Figure 2.3: Applications of piezoelectric in smart composites structures.

2.3.1 General and traditional applications

Numerous research studies have been dedicated to implementing piezoelectrics in general into realistic and industrial applications. Traditional applications of piezoelectric in smart-structures are active vibration control, active vibration suppression of aircraft tail, the position control of flexible robot arms, the smart skin systems for submarines, the control of satellites and space structures and the shape control of advanced structures (Li et al., 2011; Lin et al., 2013; Williams et al., 2002b). Piezoelectrics are being used or considered for use in the different applications outlined in figure 2.3[1] with examples in different fields, industries, and prospects in multifunctional smart structures.

In aerospace industry, the piezoelectrics have been used in active morphing un-

---

[1] All graphics in figure 2.3 are redrawn

manned aerial vehicles wings and tails, active vibration suppression of aircraft wings, the control of satellites and space structures (Barbarino et al., 2011; Li et al., 2011; Lin et al., 2013). Bulk piezoelectric composites, which are manufactured by embedding piezoelectric elements mainly fibers into a matrix material usually a polymer, have been successfully used as composite panels typically in applications where high structural rigidity and low weight are required which are typical in the aerospace industry. The composite panels serve as a multi-functional component forming an airplane fuselage body, reducing the internal noise levels and sensing the outside pressure conditions.

In submarine industry, piezoelectrics have been applied as the smart skin systems for submarines, depth finders and ultrasonic sensing (Uchino, 1996). With the advent of meta-materials as an emerging technology realizing what seemed to be impossible to achieve such as cloaking has been achieved (Haberman and Norris, 2016). The piezoelectrics would be an essential component in the active control of meta-materials (Casadei et al., 2012) with potential applications in cloaking of submersibles vehicles (Cummer and Schurig, 2007; Gustavo Mendez et al., 2017; Rajabi and Mojahed, 2018).

In manufacturing industry, piezoelectrics are used in ultrasonic machining, the position control of flexible robot arms (Williams et al., 2002a). In automotive, they have been applied in airbag sensor, air flow sensor, audible alarms, fuel atomiser, key-less door entry, seat belt buzzers, knock sensors, ultrasonic detectors and lane change sensors (Lin et al., 2013). Bulk piezoelectric composite panels can serve as structurally integrated components forming the body of vehicles while storing energy.

In biomedical industry, piezoelectrics have been used in piezoelectric surgery, health monitoring sensor, energy harvesting, ergonomics bio-interfacing structures and bionic shape control (Manbachi and Cobbold, 2011; Sodano, Inman, and Park, 2004). Piezo-electric surgery is an outstanding successful blood free precision surgery using piezo-electric transducers with a range of frequencies which can be adjusted to produce the desired micro-vibrations. These adjusted micro-vibrations have the ability to cut bones, teeth and hard mineralized tissue without cutting neurovascular tissue and other soft tissue.

Piezoelectric can also be found in disc drives, ink-jet printers, cigarette lighters, fish finders, humidifiers, jewelry cleaners, musical instruments, speakers, and telephones. The use and application of multi-functional piezoelectric components and sets or arrays of piezoelectric has been driven by recent advances in the ability to manufacture such sophisticated devices. Recent applications focus on the multiple functional characteristics (Ferreira, Nóvoa, and Marques, 2016) of piezoelectric composite and their unconventional integrated usage for shape morphing of unmanned aerial vehicles wings,

aircraft tails (Barbarino et al., 2011; Li et al., 2011) and as a structurally integrated batteries for energy storage (Gibson, 2010). Since much of the defense industry funds the majority of piezoelectric fiber research, it would be difficult to clearly document all existing recent applications unless the research application has been publicly published.

Piezoelectrics have been traditionally used in biomedical application as stated earlier however, the focus was not on integrating the different components intelligently with their multi-functionality. The majority of ultrasound therapy, such as cancer treatment and physiotherapy, uses piezoelectric ultrasound transducers as their basis. The piezoelectric fiber has been used or has potential application in all of the above mentioned biomedical application while adding the multiple functionality for example, the fibers can be used in cutting using both ultrasound and laser while visualizing using optical capabilities of the fiber. Piezoelectric fibers can be woven or integrated in wearable suits so the suit will harvest power during normal human activities (Gowthaman et al., 2016; Nilsson et al., 2013; Saini, Bajpai, and Bajpai, 2013) enabling it to be integrated with exoskeleton (Asbeck et al., 2014). Among the suit's applications and in addition to harvesting power, the suit could also monitor the soldier condition (Nilsson et al., 2013; Saini, Bajpai, and Bajpai, 2013).

Although the use of networks of piezoelectric for both organic and non-organic health monitoring is traditional, it has been re-investigated in terms of recent technological advances in materials, manufacturing and functionality (Lynch and Loh, 2006). Recent research shows a trend in applying multiple functional piezoelectrics in therapy, power harvesting, surgery and detection (Manbachi and Cobbold, 2011). The detection is usually accomplished using an array of piezoelectric accompanied by imaging algorithms to display results (Hajati et al., 2012).

Multilayered piezoelectric fibers are multifunctional if integrated in structures they lead to multifunctional smart structures. Such structures are composed of multifunctional components: a host substructure medium, a network of sensors, actuators, and intelligent controllers; therefore, they can execute multiple functionalities in response to their surroundings either externally or internally. They ultimately mimic the human body: the host substructure provides the body, the network of sensors provides the sensory system receiving the external or internal stimuli, the network of actuators provides the muscles, and the intelligent controllers provide the brains to process and analyze the data from the sensory system (it also controls the actuation). In addition to the existing functionality of traditional smart structures, smart multi-functional structures could also offer additional functionalities, therefore, encompassing the mono functional smart structures such as self-monitoring smart structures.

2.3.2 Smart structural health monitoring

At the start of the 1970s, Non-Destructive-Testing/Evaluation (NDT/NDE) of structures using ultrasonic techniques was advancing from the stage of detecting a crack or a void to the stage of identifying its dimensions and properties (Thompson, 1983; Thompson and Thompson, 1985). Since piezoelectric fibers can be easily fabricated into different desired sizes and different cross-sectional shapes (Abouraddy et al., 2007; Egusa et al., 2010; Tao, Stolyarov, and Abouraddy, 2012), the concept of using a network or array of actuators/sensors to form a self-monitoring smart system in smart structural design has attracted significant attention from the industrial and research communities (Drinkwater and Wilcox, 2006; Giurgiutiu and Cuc, 2005; Schmidt et al., 2013; Wang and Huang, 2002; Wang and Huang, 2003; Wang and Huang, 2004a). Unlike the traditional ultrasonic nondestructive testing technique, where the wave can be applied only from the surface of the structure, the usage of piezoelectric actuators/sensors makes it possible to generate elastic waves from other desired positions of the structure and provide more reliable detection of embedded damage. However, the elastic waves resulting from damages may become very complicated, because of the fact that the scattered waves will scatter from the boundaries of scatterers or damages to the host structure then sensed by the sensors.

The main difference between NDT and Structural Health Monitoring (SHM) equipments is noticed from their hardware architecture. NDT techniques, such as X-radiographic detection (X-ray) and ultrasonic acoustics require large bulky equipment and this is not practical for some on-line structures (Chang, 2013; Giurgiutiu, 2000; Giurgiutiu, Zagrai, and Bao, 2004; Kessler, Spearing, and Soutis, 2002; Kessler, 2002). In the case of an SHM system, sensors and actuators are embedded within, built into or integrated with the structure, while NDT is an external system with an independent (not integrated with the structure) set of sensors and actuators (Giurgiutiu and Cuc, 2005; Wang and Huang, 2008). Historically speaking SHM is the evolvement of NDT (GRAFF, 2012; Ursu, Enciu, and Toader, 2017).

Self-health monitoring structures use a network of sensors usually integrated, permanently embedded, in their structures to self monitor changes in their health status. They can be broadly classified as active or passive structures depending on their ability to generate a diagnostic signal to actively zoom into the damage characteristics (location and size). Passive structures need a more dense network of sensors over the corresponding active structures to identify the same damage with the same level of accuracy. The integration of actuation, sensing, and an intelligent controller into the

structure leads to modern concepts of smart structures. Therefore, a smart health monitoring structure must consist of the following basic components:

1. a network of sensors for sensing and collecting performance data;

2. a data analysis algorithm/software acting as the brain for interpreting the data, which represent the physical conditions of the structure.

An actuator or a network of actuators for generating the diagnostic signal is desirable since it can be used for generating as well as directing the diagnostic signal; nonetheless, an optional component that can be replaced by other sources of signals. In this case, the intelligent controller may control the diagnostic signal.

In order to evaluate the structure reliability and plan its maintenance, damages should be detected, evaluated, monitored, and quantified. The quantitative identification by locating and sizing damages plays a critical role in structural health monitoring. Smart structural health monitoring is the process of intelligently monitoring the functional, operational, and performance of a structural integrity throughout its entire lifetime. While classical (traditional) structural health monitoring refers to the ability to function, perform and maintain structural integrity throughout the entire lifetime. Also, within this traditional context, structural integrity are the boundaries between safety and failure of engineering components and structures. Smart structural health monitoring procedure, as shown in figure 2.4, usually consists of the following levels (Chang, 2013; Stepinski, Uhl, and Staszewski, 2013; Su and Ye, 2009):

1. Damage detection

2. Damage approximation

3. Damage localization

4. Damage assessment

An intelligent decision must be made based on the information, and the decision might be made before the prognosis (the prediction). The first and second level are qualitative in nature (Cakoni and Colton, 2005) and provide an approximate estimate. The third and fourth level provide damage characterization and quantitative identification measures (Achenbach, 2000; Huang, Song, and Wang, 2010). All of the four levels form the structure's diagnostic and they are the basic levels for any SHM system. Some researchers add structure's prognosis, which predicts the future performance of a structure given its present status, as a fifth level; however, this is in structural health management (Ihn and Chang, 2008).

Damage detection, damage monitoring, non-destructive evaluation and structural health monitoring are often misunderstood and mixed as synonyms of each other. Damage detection is the process of detecting the existence of damage(s) and it is part of structural health monitoring. Non-Destructive-Testing/evaluation techniques are usually carried out off-line using single point measurements, periodically, or after the damage has been located, to improve the structural performance (Achenbach, 2000; Drinkwater and Wilcox, 2006). Structural health monitoring is usually carried out on-line using multiple point measurements in the form of a network of sensors. Therefore, it is considered by many researchers (Chang, 2013; Stepinski, Uhl, and Staszewski, 2013) to be an evolutionary step from its predecessor non-destructive evaluation by using NDE tools and systems. Smart SHM consists of the four main levels shown in figure 2.4 with the additional use of intelligent computer algorithms to integrate the different levels.

A comparison of the various sensing inspection methods (in-service inspection specifications approved by the Federal Aviation Administration-FAA for composite airframes (Baker, Rose, and Jones, 2003)) can be seen in table (2.3)[2]. Damage parameters can be associated with changes in either global or local properties of the structure under inspection (Benavides, Segura, and Ruiz-Cortés, 2010; Das, Saha, and Patro, 2016; De Rosa, Santulli, and Sarasini, 2009; Doebling, Farrar, Prime, et al., 1998; Drinkwater and Wilcox, 2006; Fan and Qiao, 2011; Su, Ye, and Lu, 2006). Inspection methods based on changes in the global dynamic properties including eigen-frequency, mode shape and curvature, strain energy, and damping properties are less sensitive to damage. Damages are local events which would not significantly change the structure global dynamic properties before they reach a noticeable extent to affect the global dynamic properties (e.g., 10% of the characteristic dimension/area of the structure).

Inspection method	Principles	Limitations	Advantages
Acoustic emission	Sensing the signal generated by the rapid release of strain energy due to damage growth	Complex signal; specially for locating damage; Prone to contamination by environmental noise, Very high data rates, Specialized software, Suitable for small structures, Captures after effects	Lightweight, Conformable, No power required, Triangulation capability, and good coverage

---

[2]Table (2.3) is based on multiple sources (Kessler, 2002; Schmerr, 2013; Schmerr, 2016; Schmerr and Song, 2007; Su and Ye, 2009).

Inspection method	Principles	Limitations	Advantages
Eddy current	Uses the electromagnetism as the basis for sensing damage	Conductive material only Expensive equipment Very complex results Specialized software Safety hazard	Inexpensive to implement Portable Surface mountable Sensitive to small damage
Elastic waves	Sensing the unique scattered waves also mode conversions caused by the presence of damages	Complex signal due to complex wave forms, simultaneously multiple wave modes, multiple wave interaction; difficult to simulate wave propagation in complex structures; strong dependence on prior models or benchmark signals, Specialized software	Lightweight Conformable Medium power consumption, Linear scan results Triangulation capability Cost-effective, fast and repeatable; can inspect a large structure in a short time; sensitive to small damage; able to detect both surface and internal damage.
Modal Analysis	Sensing shift in eigen frequencies also changes in frequency response function, and mode shapes due to reduction in structural stiffness caused by damage.	Insensitive to small damage or damage growth; difficult to excite high frequencies; need many measurement points; hypersensitive to boundary and environmental changes.	Simple and low cost, effective for detecting large damage in large infrastructure or rotating machinery, Lightweight, Conformable, Multi-purpose sensors, Low power required
Optical fibers	Sensing electromagnetic light waves	Expensive to implement Data analysis required High data rates Accuracy in question	Inexpensive equipment Embeddable Quick scan of large area
Strain gauge	Sensing strains caused by damage in comparison with benchmark	Relatively insensitive to small damage or the evolution of deterioration Data analysis required	Sensitive to local damages; simple Lightweight Conformable Very low power draw
Ultrasonic acoustics	Sensing high frequency waves propagating in fluids (acoustic) or air (sound) which excite the damaged structure	Very expensive equipment Complex results Specialized software High data rates Couplant required Require access to both sides	Inexpensive to implement Portable Sensitive to small damage Quick scan of large area

Inspection method	Principles	Limitations	Advantages
Visual inspection	Visually observing using human eyes and maybe a magnifier	Only surface damage Only large damage Human interpretation Can be time consuming	Cheapest, No data analysis, No procedure
X-radiography	Imaging damages through X-rays penetration	Expensive equipment Expensive to implement Human interpretation Can be time consuming Require access to both sides Safety hazard	No data analysis Permanent record of results Simple procedure

Table 2.3: Comparison of principles, limitations and potential SHM implementation for various sensing systems.

SHM is a multidisciplinary area of research which integrates many disciplines and fields of sciences such as solid mechanics, fracture mechanics, materials science, signal processing, electronics and computer science. Damage identification approaches can be roughly classified into model based (Fan and Qiao, 2011; Farrar, Doebling, and Nix, 2001) and signal based methods (Hoseini, Zuo, and Wang, 2013). Model based approaches are usually formulated using physical, constitutive and geometric model parameters to obtain the damage identification model. Signal based approaches are usually formulated using signal processing techniques and they rely on analyzing various types of direct measurements such as noise, vibration, ultrasound or temperature.

All damages begin at very small sizes smaller than the nano scale in which continuum physics fail to model it and a need for other modeling techniques arises (Wang, Wang, and Kitamura, 2016), however, at that scale, damages are usually difficult to detect and usually do not affect performance. As the damages grow, they start to affect the performance and the structural operation resulting in system failure. Damages can accumulate incrementally over long periods of time such as that associated with fatigue or corrosion damage accumulation (Ihn and Chang, 2004; Shen and Cesnik, 2017). On relatively short periods of time, damages can also result from repetitive scheduled

Structural diagnosis

Qualitative identification

1) Damage detection

2) Damage approximation

Quantitative identification

3) Damage localization

4) Damage assessment

A typical classical structural health monitoring

Mulitlayered piezoeletric fibers

Incident wave

Crack

Void

Smart piezoelectric

Intelligent algorithms
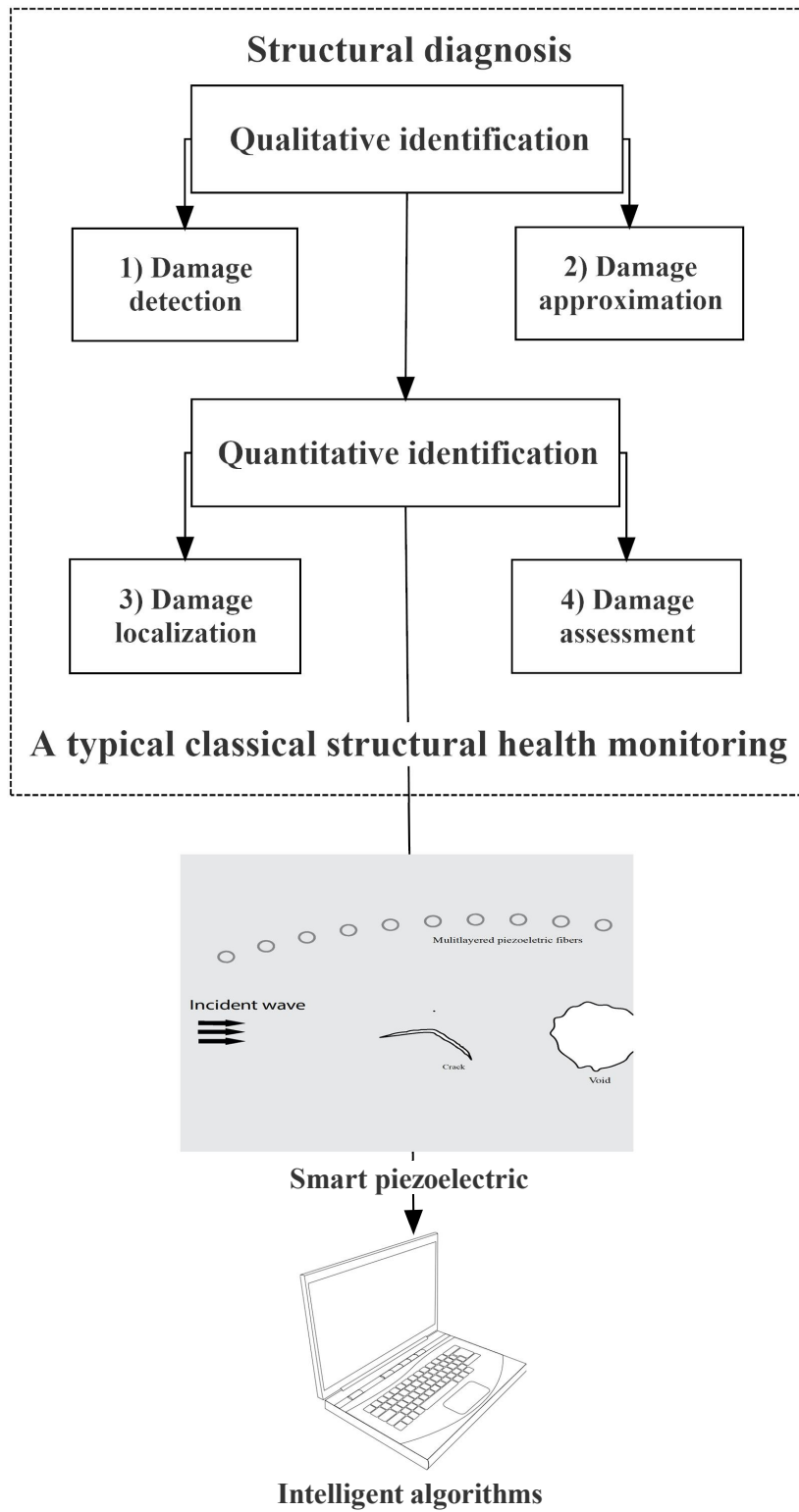
Figure 2.4: Smart structural health monitoring system.

events such as aerospace vehicle landings or from unscheduled events such as an impact (enemy fire) on a military vehicle or natural phenomena hazards such as earthquakes (Ihn and Chang, 2008; Mitra and Gopalakrishnan, 2016).

The mathematical models representing the array/network of piezoelectrics are usually based on either modal analysis (Fan and Qiao, 2011; Hagood and Flotow, 1991) or elastic waves (Willberg et al., 2015). In other words, mechanical model based damage identification can be further classified into modal analysis based (Das, Saha, and Patro, 2016) and elastic wave based methods (Su, Ye, and Lu, 2006). Different mathematical modeling bases have their own advantages and disadvantages. Models based on elastic waves are more sensitive to small damages and changes of material parameters since elastic waves can be excited at a relatively high frequency. Elastic waves are sensitive to various types of damages including voids, porosity, debonding, corrosion, cracking, hole, delamination, resin variation, broken fiber, fiber misalignment, resin crack, cure variation, inclusions, and moisture (Fu et al., 2017; Rose, 2002).

Several solution sets were proposed to solve the inverse problem of damage identification thus diagnosing the structure's health. The majority of available solutions extract the health information of the damaged structure through some known output signals. One solution set is based solely on feature extraction indices or measures to interpret the structure's health either in time or frequency domain. The extracted features can be as simple as the wave velocity, the signal amplitude, the time of flights, the mechanical impedance or as complicated as the combinations of multiple output signals forming indices or complicated measures (Zhou, Su, and Cheng, 2011). Most of these solutions rely on comparing the extracted features of the damaged structure with those of the corresponding undamaged ones (Grisso, 2004; Hoseini, Zuo, and Wang, 2013; Norris and Shuvalov, 2010). The limitation of these solutions is that it requires prior knowledge of the undamaged structure features and mostly require extensive signal processing (Anton, Inman, and Park, 2009).

Solution sets based on phased arrays require the use of a sensor array to scan the target structures. The working mechanism concept creates a beam of waves which can be electronically steered to scan different directions and can image embedded damages (Satyanarayan et al., 2007; Zou and Nehorai, 2009). However, these solutions require scanning every point in the area of interest, so it is not efficient for large structures and does not work for real-time structural health monitoring (Schmerr Jr, 2014; Schmerr, 2016).

Another solution set is the time-reversal method. It is based on the linearity of elastic waves. Through inversion calculation of the measured signals, the back-propagating elastic waves could be determined and then damages can be identified (Sohn et al., 2007; Wang, Rose, and Chang, 2004). This method has been widely used in geological exploration. However, the time-reversal technique requires a dense network of sensors to obtain a comprehensive profile of the major signals and an understandable image. Its images are not usually clear as they suffer from mode conversion of the longitudinal wave and the transverse wave. Other related solution sets are based on the intersection of two or more such as time reversal imaging with multiple signal classification (MUSIC) (Gruber, Marengo, and Devaney, 2004; Marengo, Gruber, and Simonetti, 2007).

A set of solutions are based on formulating the inverse problem into an optimization of an error functional $j(\mathbf{p})$ by finding damage parameters $\mathbf{p} = \{p_1, \ p_2, \ ..., \ p_i, \ ...p_n\}$ such that the simulated measurements $\phi^s(\mathbf{p})$ agree with the actual observed measurements ϕ^o. In practice, the inverse problem can be formulated mathematically as the minimization of an error functional

$$\mathbf{p} = \arg \min j(\mathbf{p}) \tag{2.5}$$

where the error functional $j(\mathbf{p})$ contains dependence on the parameters $\mathbf{p}$. The normalized least squares error function is

$$j(\mathbf{p}) = \frac{(\phi^s(\mathbf{p}) - \phi^o)(\phi^s(\mathbf{p}) - \phi^o)^T}{\phi^s(\mathbf{p})(\phi^o)^T} \tag{2.6}$$

where T is the transpose.

Optimization algorithms make use of intelligent programming algorithms such as artificial neural network (ANN), genetic algorithm, simulated annealing, particle swarms, topology optimization e.g. level-set method, etc. Optimization methods can use traditional algorithms such as gradient based optimization e.g. Broyden-Fletcher-Goldfarb-Shanno (BFGS) algorithm however a good initial guess is needed otherwise the algorithm gets trapped in a local minimum.
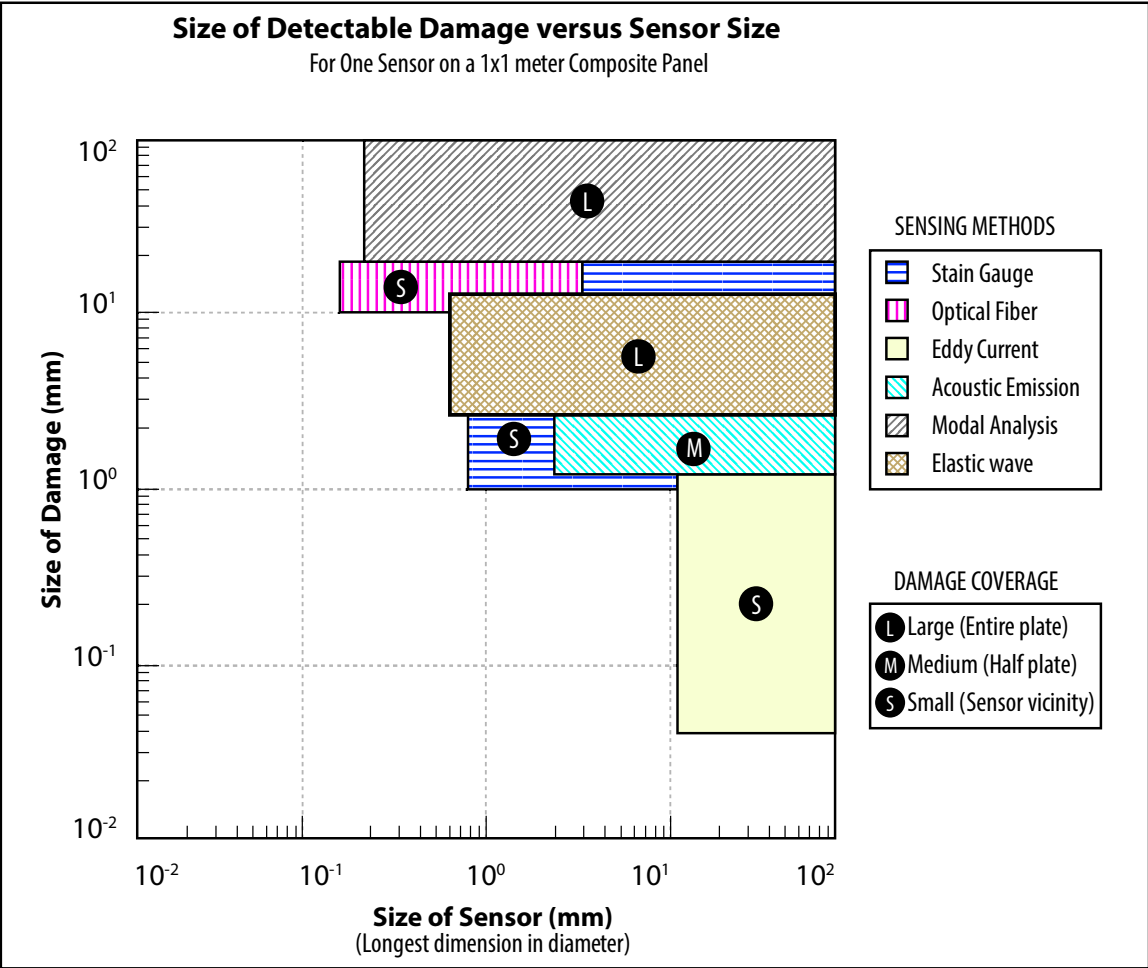
Figure 2.5: Comparison of various sensing methods and damage coverage: minimum size of detectable damage versus size of sensor.

Various sensing methods have been developed, each method has its advantages and disadvantages for damage identification. Figure 2.5 shows a chart[3] of various sensing

---

[3]Chart in figure (2.5) is based on multiple sources (Chocat et al., 2011; Fu et al., 2017; Kessler, 2002; Su and Ye, 2009).

methods and their damage coverage area with a plot of different sensors' sizes against the size of their detectable damage inside a composite plate panel. Smaller instances of damage down to a few millimeters can be accurately detected using elastic waves in the frequency range from 1 to 10 GHz, as shown in figure 2.5, over other well established NDE techniques (Fu et al., 2017). In wave-based sensing methods, the ratio between the smallest detectable damage size l_{damage} and the size of the largest wavelength λ contents is greater than one half for a successful identification

$$\frac{l_{\text{damage}}}{\lambda} > \frac{1}{2}. \tag{2.7}$$

However, damage identification using wave-based sensing methods involves more factors than just the relation between wavelength and damage size since the sensitivity is not a simple linear function in wavelength (Lee and Staszewski, 2003a; Lee and Staszewski, 2003b).

2.4   Conclusions

The newly developed multilayered piezoelectric fiber has attracted the research community; however, most of the research has been devoted to their fabrication, material properties, biomedical development, acoustic, and optical implementations of these devices. Very few published research studies were conducted to investigate using the newly manufactured multilayered piezoelectric fibers in smart structural applications. Accurate modeling of the anisotropic piezoelectric layer as well as characterization of the coupled piezo-elastodynamic behavior between the fiber and the host structure are key issues for their implementation. There is no simple analytical model that takes into account the transversely anisotropic under dynamic loading. Existing methods of modeling multilayered piezoelectric fiber like the transfer matrix are not numerically stable and cannot be used directly to model imperfect interfaces such as partially angular debonding. There is also a need for a method that handles multiple multilayered

piezoelectric fibers wave interactions with damages under plane waves.

In structural health monitoring applications using piezoelectric fibers, a network of piezoelectric fibers is employed for sensing and collecting performance data often generated by using the same fibers as actuators to actuate a high-frequency diagnostic elastic wave. The usage of embedded multilayered piezoelectric fiber as actuators/sensors makes it possible to generate and direct the desired high frequency elastic wave from the appropriate location thus providing more reliable detection of damages. There is a need to study and investigate recently multilayered piezoelectric fibers for damage detection and quantification because in addition to possessing the advantages of piezoelectrics, their electrodes are directly connected to individual fibers allowing for individualized transduction (actuation and/or sensing), therefore, are useful for non-destructive testing and structural health monitoring applications. To effectively use the network of piezoelectric actuators/sensors, the quantitative evaluation of the induced elastic wave and its interaction with damages is strongly needed. This article reviews the state of the art and recent advance in the different modeling techniques for multilayered piezoelectric fibers, including analytical, variational, numerical, and hybrid approaches to model the coupled piezo-elastodynamic behavior.

Chapter 3

A new dynamic model of cylindrical layered anisotropic fibers

3.1 Introduction

In addition to the well known advantages of traditional composites, such as higher strength-to-weight ratio and tailored design, smart composites also offer multifunctionality(Gibson, 2010) and, therefore, are receiving significant attention from the research community (Kreja, 2011; Lin and Sodano, 2008). Recent progress in manufacturing multilayered piezoelectric fibers with a transverse poling direction in the cross section makes it possible to develop new smart composites, which can be used in different high frequency applications (Egusa et al., 2010). The fibers have been used to design single-fiber resonators and piezoelectric transducers. It is a natural step to use these fibers to develop smart multifunctional composite materials.

An important issue in the study of this type of smart composites is how to evaluate the piezoelectric layer in the fiber. Since the piezoelectric layer is poled transversely in the cross section and is in general anisotropic, existing solutions for isotropic or transversely-isotropic layers are not sufficient for describing the behavior of the layer. Considering the fact that the piezoelectric layer is relatively thin compared with the radius of the fibers, simplified layer models could be used to overcome this difficulty. Modeling of thin layers in composite materials has been extensively investigated (Kushch et al., 2011; Rajabi and Hasheminejad, 2009; Zhong and Meguid, 1997) because of its

importance. In these cases, an interphase, which may represent a bonding layer or an imperfect interface caused by deterioration, is usually modelled by distributed interface springs.

When high frequency dynamic loading is applied, the inertial effect of the anisotropic layer needs to be considered. Solutions for the response of anisotropic materials to general dynamic loads or elastic waves are usually complicated and difficult to obtain, although the corresponding problems for isotropic elastic media can be easily dealt with by determining the displacement potentials based on Helmholtz decomposition (Achenbach, 1972). In general cases, the dynamic displacement field in an anisotropic elastic medium can no longer be decomposed into independent displacement potentials. Therefore, well known solution techniques applicable to isotropic media, based on displacement potentials, cannot be applied directly to anisotropic media. The interaction between elastic waves and anisotropic layers in planar layered media has been studied analytically and numerically (Rokhlin and Huang, 1992; Rokhlin and Huang, 1993). The analytical solution is quite complicated, involving the solution of eigenvalue problems. The corresponding problems for cylindrical layers have also been studied under simplified geometric or loading conditions, such as assuming isotropy in the cylinder cross section (Honarvar and Sinclair, 1996; Nayfeh, 1995; Nayfeh, Abdelrahman, and Nagy, 2000; Nayfeh and Nagy, 1996; Sodagar and Honarvar, 2010). Numerical solutions for more general anisotropic cylindrically layered media under elastic waves have also been reported in recent literatures (Gsell and Dual, 2004; Norris and Shuvalov, 2010; Norris and Shuvalov, 2012). But simplified analytical models for transversely anisotropic cylindrical layers under general dynamic loading are limited to interface-spring models.

For the case of radially poled piezoelectric fibers, the piezoelectric layer poses problems in modeling the mechanical behavior because of both its anisotropy and curvature. A possible method in modeling the layer is to simplify it as distributed interface

springs to simulate the traction-displacement relation across the layer. The spring model (Aboudi, 1987; Bian, Chen, and Lu, 2008; Librescu and Schmidt, 2001; Zhong and Meguid, 1997) ignores, however, the hoop stress and the inertial effect, and assumes that the stresses are uniform across the thickness of the layer. As a result, the equations of motion of the layer are not satisfied. It should be mentioned that in a typical radially poled piezoelectric fiber (Egusa et al., 2010), the layer thickness could be as large as 20% of the radius of the fiber and the hoop stress in the curved layer may play a significant role in the deformation. It is therefore desirable to develop an interphase model which can represent the effect of the stress variation cross the layer thickness, the hoop stress in the layer and the anisotropy of the layer.

The objective of this study is to develop a new interphase model for anisotropic layers in multilayered cylindrical fibers. The attention will be limited to the elastodynamic behavior of the interphase layer. Comparison with traditional interface-spring model and finite element analysis indicates that the current model is more accurate than the spring model. Typical simulation results based on the developed model are provided to illustrate the mechanical property of the anisotropic cylindrical layers under dynamic loads.

3.2 Problem formulation

Consider the cross section of a cylindrical multilayered piezoelectric medium consisting of an inner core $0 < r < r_0$, a piezoelectric layer $r_0 < r < r_1$ and an outer layer $r_1 < r < r_2$, as shown in figure 3.1(a). The inner core and the outer layer are linearly elastic, homogeneous and isotropic insulators. These three layers are assumed to be bonded perfectly at the interfaces. Plane strain deformation is considered, which corresponds to the case where the out-of-plane dimension of the medium is significantly greater than its typical radius. The piezoelectric layer is poled along the radial direction and

is, therefore, anisotropic in the cross section. The medium is subjected to general mechanical loading along the outer surface. In the limiting case that r_2 approaches infinity, as shown in figure 3.1(b), the load could be an incident wave.

The dynamic load is assumed to be time harmonic and only the steady state response of the medium is considered. The time dependence of the response can be expressed by an exponential function $e^{-i\omega t}$ where t and ω are time and frequency, respectively. For convenience, the term $e^{-i\omega t}$ will be omitted in the following discussion and only the amplitude of the field variables will be considered.
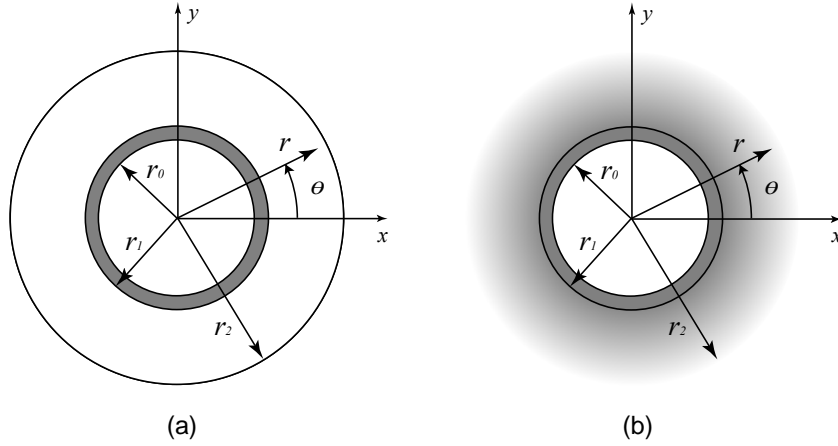
Figure 3.1: The layered composite medium with (a) bounded outer layer and (b) unbounded outer medium.

3.2.1 Governing equations

The dynamic electromechanical property of piezoelectric materials, such as the media shown in figure 3.1, is governed by the equations of motion (Achenbach, 1972; Kessler and Kosloff, 1991). In the polar coordinate system (r, θ) the governing equations are

Equations of Motion

$$\sigma_{r,r} + \frac{1}{r}\sigma_{\theta r,\theta} + \frac{1}{r}(\sigma_r - \sigma_\theta) = -\rho\omega^2 u_r \tag{3.1}$$

$$\sigma_{r\theta,r} + \frac{1}{r}\sigma_{\theta,\theta} + \frac{2}{r}(\sigma_{r\theta}) = -\rho\omega^2 u_\theta \tag{3.2}$$

45

where σ is the stress, u is the displacement, and ρ is the density. The subscripts indicate the corresponding components in the polar coordinate system while the comma indicates differentiation, as commonly used. The constitutive relations of the piezoelectric layer, with the poling direction being alone r, are given by,

$$
\begin{bmatrix} \sigma_r \\ \sigma_\theta \\ \sigma_{\theta r} \end{bmatrix} = \begin{bmatrix} c_{33} & c_{23} & 0 \\ c_{23} & c_{22} & 0 \\ 0 & 0 & c_{44} \end{bmatrix} \begin{bmatrix} \varepsilon_r \\ \varepsilon_\theta \\ \varepsilon_{r\theta} \end{bmatrix} \tag{3.3}
$$

where c's are the elastic coefficients, and ε represents the strain which can be expressed in terms of the displacements u_r and u_θ as

$$
\varepsilon_r = u_{r,r} \tag{3.4}
$$

$$
\varepsilon_\theta = \frac{1}{r} \left(u_{\theta,\theta} + u_r \right) \tag{3.5}
$$

$$
\varepsilon_{r\theta} = \frac{1}{2} \left(\frac{1}{r} u_{r,\theta} + u_{\theta,r} - \frac{u_\theta}{r} \right) . \tag{3.6}
$$

3.2.2 Elastic fields in the inner core and the outer medium

The inner core and the outer medium are linearly elastic, homogeneous and isotropic. In this case, the displacement field can be decomposed into (Achenbach, 1972)

$$
u_r = \varphi_{,r} + \frac{1}{r} \psi_{,\theta} \tag{3.7}
$$

$$
u_\theta = \frac{1}{r} \varphi_{,\theta} - \psi_{,r} \tag{3.8}
$$

where φ and ψ are two displacement potentials satisfying Helmholtz equation, i.e.

$$
\frac{1}{r} \left(r\varphi_{,r} \right)_{,r} + \frac{1}{r^2} \varphi_{,\theta\theta} + k_L^2 \varphi = 0 \tag{3.9}
$$

$$
\frac{1}{r} \left(r\psi_{,r} \right)_{,r} + \frac{1}{r^2} \psi_{,\theta\theta} + k_T^2 \psi = 0. \tag{3.10}
$$

k_L and k_T are two wave numbers given by

$$k_L = \frac{\omega}{c_L}, \quad k_T = \frac{\omega}{c_T} \tag{3.11}$$

where c_L and c_T are the longitudinal and transverse wave speeds of the elastic medium, and

$$c_L = \sqrt{\frac{\lambda + 2\mu}{\rho}}, \quad c_T = \sqrt{\frac{\mu}{\rho}} \tag{3.12}$$

with λ and μ being the Lame constants of the elastic medium.

The general solutions of the displacement potentials in these layers can be determined by solving equations (3.9) and (3.10) using Fourier expansion with respect to θ. The resulting displacement potentials are

$$\varphi(r,\theta) = \sum_{n=0}^{\infty} \left\{ J_n\left(k_L r\right) \begin{pmatrix} A_n^{(1)} \\ A_n^{(2)} \end{pmatrix}^T + H_n^{(1)}\left(k_L r\right) \begin{pmatrix} A_n^{(3)} \\ A_n^{(4)} \end{pmatrix}^T \right\} \begin{pmatrix} \cos\left(n\theta\right) \\ \sin\left(n\theta\right) \end{pmatrix} \tag{3.13}$$

$$\psi(r,\theta) = \sum_{n=0}^{\infty} \left\{ J_n\left(k_T r\right) \begin{pmatrix} A_n^{(5)} \\ A_n^{(6)} \end{pmatrix}^T + H_n^{(1)}\left(k_T r\right) \begin{pmatrix} A_n^{(7)} \\ A_n^{(8)} \end{pmatrix}^T \right\} \begin{pmatrix} \cos\left(n\theta\right) \\ \sin\left(n\theta\right) \end{pmatrix} \tag{3.14}$$

where $J_n\left(.\right)$ and $H_n^{(1)}\left(.\right)$ are Bessel functions and Hankel functions of the first kind, respectively, and A_n are unknown constants to be determined from the boundary and interface conditions. For the inner core $A_n^{(2)}$, $A_n^{(4)}$, $A_n^{(7)}$, $A_n^{(8)}$ are zero to ensure that the field has a limited amplitude at $r = 0$. If the outer layer is infinite, then $A_n^{(1)}$, $A_n^{(2)}$, $A_n^{(5)}$, $A_n^{(6)}$ will be zero to satisfy the radiation condition at infinity for the scattered wave.

3.3   The interphase model for the anisotropic layer

The piezoelectric layer is transversely anisotropic in the cross section since it is poled in the radial direction. For such an anisotropic medium under dynamic loading, the general analytical solution could not be easily found. In the current subsection, a

new interphase model will be presented, which could be used to simulate the dynamic mechanical property of the layer.

The governing equations for the piezoelectric layer, (3.1) and (3.2), can be re-written as

$$\frac{1}{r}\left((r\sigma_r)_{,r} + \sigma_{\theta r,\theta} - \sigma_\theta\right) = -\rho\omega^2 u_r \tag{3.15}$$

$$\frac{1}{r^2}\left((r^2\sigma_{r\theta})_{,r} + r\sigma_{\theta,\theta}\right) = -\rho\omega^2 u_\theta. \tag{3.16}$$

To overcome the difficulties associated with the anisotropy of the layer, for a relatively thin layer, the derivative with respect to r in these equations is simplified such that $(r\sigma_r)_{,r} \approx \dfrac{\Delta(r\sigma_r)}{h}$ and $(r^2\sigma_{r\theta})_{,r} \approx \dfrac{\Delta(r^2\sigma_{r\theta})}{h}$ with $h = r_1 - r_0$ being the thickness of the layer and Δ representing the change from r_0 to r_1. Equations (3.15) and (3.16) can then be approximately expressed as

$$\frac{1}{r}\left(\frac{\Delta(r\sigma_r)}{h} + \sigma_{\theta r,\theta} - \sigma_\theta\right) = -\rho\omega^2 u_r \tag{3.17}$$

$$\frac{1}{r^2}\left(\frac{\Delta(r^2\sigma_{r\theta})}{h} + r\sigma_{\theta,\theta}\right) = -\rho\omega^2 u_\theta. \tag{3.18}$$

The layer can now be modeled as a one dimensional element governed by equations (3.17) and (3.18). A stress component is decomposed into two parts, (i) a uniform stress across the thickness of the layer element, representing the average stress and (ii) a linear stress across the thickness with a zero average, resulting in the 'Δ' terms in equations (3.17) and (3.18), which represent the general 'body forces' acting on the interphase. The other terms in equations (3.17) and (3.18), except for the terms with r derivative, are the average values over the thickness of the layer.

The constitutive equation (3.3) can be rewritten in terms of the displacements in the layer as

$$\sigma_r = c_{33}u_{r,r} + \frac{c_{23}}{r}\left(u_{\theta,\theta} + u_r\right) \tag{3.19}$$

$$\sigma_\theta = c_{23}u_{r,r} + \frac{c_{22}}{r}\left(u_{\theta,\theta} + u_r\right) \tag{3.20}$$

$$\sigma_{r\theta} = c_{44} \left(\frac{1}{r} u_{r,\theta} + u_{\theta,r} - \frac{u_\theta}{r} \right) . \tag{3.21}$$

For the layer element the derivatives with respect to r in these equations can be approximated, such that

$$u_{r,r} = \frac{\triangle u_r}{\triangle r}, \ u_{\theta,r} = \frac{\triangle u_\theta}{\triangle r} \tag{3.22}$$

and the stress should be considered to be the average value across the thickness.

Substituting equation (3.22) into equations (3.19)-(3.21) the constitutive equations for the interphase can be written as

$$\sigma_r = c_{33} \left(\frac{u_r^+ - u_r^-}{h} \right) + \frac{c_{23}}{r} \left(\frac{u_{\theta,\theta}^+ + u_{\theta,\theta}^-}{2} + \frac{u_r^+ + u_r^-}{2} \right) \tag{3.23}$$

$$\sigma_\theta = c_{23} \left(\frac{u_r^+ - u_r^-}{h} \right) + \frac{c_{22}}{r} \left(\frac{u_{\theta,\theta}^+ + u_{\theta,\theta}^-}{2} + \frac{u_r^+ + u_r^-}{2} \right) \tag{3.24}$$

$$\sigma_{r\theta} = c_{44} \left(\frac{1}{r} \frac{u_{r,\theta}^+ + u_{r,\theta}^-}{2} + \frac{u_\theta^+ - u_\theta^-}{h} - \frac{1}{r} \frac{u_\theta^+ + u_\theta^-}{2} \right) \tag{3.25}$$

where the superscripts $(+)$ and $(-)$ refer to the outer and inner surfaces of the layer, and the averaged values in these equations are given by

$$\sigma_r = \frac{\sigma_r^+ + \sigma_r^-}{2} \tag{3.26}$$

$$\sigma_{r\theta} = \frac{\sigma_{r\theta}^+ + \sigma_{r\theta}^-}{2} \tag{3.27}$$

$$r = \frac{r_1 + r_0}{2}. \tag{3.28}$$

Finally, substituting equations (3.23)-(3.25) into the equations of motion (3.17) and (3.18) results in the following equations for the layer,

$$\frac{1}{r^2}\left\{\frac{r_1^2\sigma_{r\theta}^+ - r_0^2\sigma_{r\theta}^-}{h} + r\left[c_{23}\frac{u_{r,\theta}^+ - u_{r,\theta}^-}{h} + \frac{c_{22}}{r}\left(\frac{u_{\theta,\theta\theta}^+ + u_{\theta,\theta\theta}^-}{2} + \frac{u_{r,\theta}^+ + u_{r,\theta}^-}{2}\right)\right]\right\}$$

$$= -\rho\omega^2\left(\frac{u_\theta^+ + u_\theta^-}{2}\right) \quad (3.29)$$

$$\frac{1}{r}\left\{\frac{r_1\sigma_r^+ - r_0\sigma_r^-}{h} + \frac{\sigma_{r\theta,\theta}^+ + \sigma_{r\theta,\theta}^-}{2} - \left[c_{23}\frac{u_r^+ - u_r^-}{h} + \frac{c_{22}}{r}\left(\frac{u_{\theta,\theta}^+ + u_{\theta,\theta}^-}{2} + \frac{u_r^+ + u_r^-}{2}\right)\right]\right\}$$

$$= -\rho\omega^2\left(\frac{u_r^+ + u_r^-}{2}\right) \quad (3.30)$$

and the constitutive relations of the layer become

$$\frac{\sigma_r^+ + \sigma_r^-}{2} = c_{33}\frac{u_r^+ - u_r^-}{h} + \frac{c_{23}}{r}\left(\frac{u_{\theta,\theta}^+ + u_{\theta,\theta}^-}{2} + \frac{u_r^+ + u_r^-}{2}\right) \quad (3.31)$$

$$\frac{\sigma_{r\theta}^+ + \sigma_{r\theta}^-}{2} = c_{44}\left(\frac{1}{r}\frac{u_{r,\theta}^+ + u_{r,\theta}^-}{2} + \frac{u_\theta^+ - u_\theta^-}{h} - \frac{1}{r}\frac{u_\theta^+ + u_\theta^-}{2}\right). \quad (3.32)$$

Equations (3.29)-(3.32) established a new interphase model, which relates the outer (+) and inner (-) surfaces of the layer based on the property of the layer itself. The model satisfies the equations of motion and the constitutive relations of the layer.

The commonly used interface-spring model can be represented as (Bian, Chen, and Lu, 2008; Rajabi and Hasheminejad, 2009),

$$\sigma_r^+ = \sigma_r^- = \frac{c_{33}}{h}\left(u_r^+ - u_r^-\right) \quad (3.33)$$

$$\sigma_{r\theta}^+ = \sigma_{r\theta}^- = \frac{c_{44}}{h}\left(u_\theta^+ - u_\theta^-\right) \quad (3.34)$$

which assumes a simple linear relation between displacements and stresses across the thickness of the layer. In comparison, in the traditional interface-spring model σ_r and $\sigma_{r\theta}$ are assumed to be constants across the thickness of the layer. σ_θ and the inertial force of the layer are ignored. Only when the thickness of the interphase approaches

zero, $h \to 0$, the two models become identical. The spring model is therefore a special case of the currently proposed model.

To determine the solution for a specific boundary condition, the governing equations (3.29)-(3.32) for the layer should be combined with the general solutions for the inner core and the outer medium, as given by equations (3.13) and (3.14). The continuity condition for stresses and displacements between different layers should be satisfied. Therefore, the components with superscript $(+)$ equal to the values of the corresponding components for the outer medium at $r = r_1$, and the components with superscript $(-)$ equal to that for the inner core at $r = r_0$. The general expressions of the stress and displacement fields can be obtained directly from the displacement potentials given by equations (3.13) and (3.14). The results are provided in the appendix.

By substituting these stress and displacement components into equations (3.29)-(3.32), a set of linear equations can be obtained, from which the unknown coefficients $A_n^{(1)}$ to $A_n^{(8)}$ in equations (3.13) and (3.14) can be determined for specific boundary conditions.

It should be noted that the developed interphase model given by equations (3.29)-(3.32) are general in nature, and will replace the four governing equations for the traditional spring model given by (3.33) and (3.34). The new layer model can be used to deal with general boundary and loading conditions when the layer is bonded to different inner and outer media.

3.4   Results and discussion

In this section, the mechanical behavior of cylindrically layered media, shown in figure 3.1, is considered. The attention will be focused on (i) the validation of the developed interphase model and (ii) the usage of this interphase model for evaluating the stress distribution in the layered media under different loading and geometric condi-

tions.

3.4.1 Static axisymmetric problems

To evaluate the accuracy of the developed interphase model, consider first the stress field of an unbounded three-layer medium subjected to static axisymmetric loading $\sigma_r = p$, $\sigma_{r\theta} = 0$ at infinity. The middle layer is assumed to be isotropic so the closed form solution can be obtained. In this case, the general solution of the displacement field is,

Inner core

$$u_r = a_0 r \tag{3.35}$$

Middle layer

$$u_r = a_1 r + \frac{b_1}{r} \tag{3.36}$$

Outer medium

$$u_r = a_2 r + \frac{b_2}{r} \ . \tag{3.37}$$

By applying the boundary conditions, $\sigma_r = p$, $\sigma_{r\theta} = 0$ at infinity, and the continuity conditions at the interfaces, the unknown constants in the general solution, a_0, a_1, a_2 and b_0, b_1, b_2, can be determined and the closed form solution of the problem can be obtained.

For this simple problem the solution based on the current interphase model can be obtained analytically. For the special case where the inner core is rigid and the Poisson's ratio is zero, the interphase model can be rewritten as,

$$\left(\frac{r_1 \sigma_r^+ - r_0 \sigma_r^-}{r_1 - r_0} \right) - E_1 \left(\frac{u_r^+}{r_1 + r_0} \right) = 0 \tag{3.38}$$

$$\frac{1}{2} \left(\sigma_r^+ + \sigma_r^- \right) - E_1 \left(\frac{u_r^+}{r_1 - r_0} \right) = 0 \tag{3.39}$$

where '+' and '−' represent the corresponding values of the outer medium and the inner core at the two interfaces of the layer, with $u_r^- = 0$. $E_1 = c_{33}^{<1>}$ is the Young's modulus of the layer. Using the solution given by (3.35) and (3.37) and the boundary conditions at infinity, the stress field based on the current interphase model can be determined. The solution based on the interface-spring model, (3.33) and (3.34), can be similarly obtained.

The radial stress σ_r at the interface between the inner core and the layer $(r = r_0)$ is

The exact solution:

$$\frac{\sigma_r^-}{p} = \frac{4}{2 + (\lambda_{21} - 1)(1 - \alpha^2)} \tag{3.40}$$

The current model:

$$\frac{\sigma_r^-}{p} = \frac{4 - \left(2(1 - \alpha)^2/(\alpha + 1)\right)}{2 + 2(\alpha - 1) + (1 - \alpha^2)\lambda_{21} + \left((1 - \alpha)^2/(\alpha + 1)\right)} \tag{3.41}$$

The spring model:

$$\frac{\sigma_r^-}{p} = \frac{4}{2 + 2\lambda_{21}(1 - \alpha)} \tag{3.42}$$

where $\alpha = r_0/r_1$, $\lambda_{21} = \dfrac{c_{33}^{<2>}}{c_{33}^{<1>}} = \dfrac{E_2}{E_1}$ with E_1 and E_2 being the Young's moduli of the layer and the outer medium, respectively.

Figure 3.2 shows the comparison between the results of σ_r^-, given by (3.40)-(3.42), from the closed form solution, the current model, and the interface spring model for different E_2/E_1 ratios and layer thicknesses. For all three E_2/E_1 values considered, 0.5, 1.0 and 2.0, the current model shows an excellent agreement with the closed form solution even when the thickness of the layer is quite significant $(r_1/r_0 = 1.5)$. The results are, however, very different from that by the interface spring model.

The extreme case where the core is a void is also considered for the validation of the model. In this case, $\sigma_r = 0$ at $r = r_0$ and the governing equations of the interphase model for the layer, (3.29)-(3.32), are reduced to

$$\frac{1}{2}\left(\sigma_r^+\right) - E_1\left(\frac{u_r^+ - u_r^-}{r_1 - r_0}\right) = 0 \tag{3.43}$$
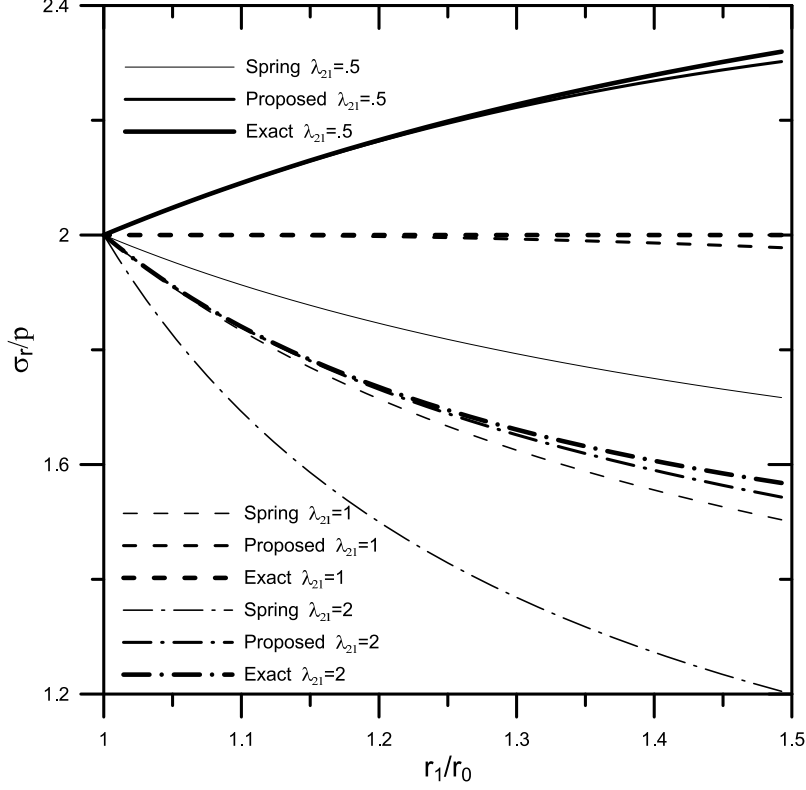
Figure 3.2: Axisymmetric radial stress with a rigid core

$$\left(\frac{r_1\sigma_r^+}{r_1 - r_0}\right) - E_1\left(\frac{u_r^+ + u_r^-}{r_1 + r_0}\right) = 0 \tag{3.44}$$

with the hoop stress in the layer being given by

$$\begin{aligned}
\sigma_\theta &= E_1\left(\frac{u_r}{r}\right) \\
&= E_1\left(\frac{u_r^+ + u_r^-}{r_0 + r_1}\right).
\end{aligned} \tag{3.45}$$

By solving this problem, the hoop stress at $r = r_0^+$ in the layer is determined to be

The exact solution:

$$\frac{\sigma_\theta^-}{p} = \frac{4}{\lambda_{21}(1 + \alpha^2) + (1 - \alpha^2)} \tag{3.46}$$

The current model:

$$\frac{\sigma_\theta^-}{p} = \frac{4}{\lambda_{21}\left(3 + \alpha^2\right)/2 + 2\left(1 - \alpha\right)} \tag{3.47}$$

The spring model:

$$\frac{\sigma_\theta^-}{p} = 0. \tag{3.48}$$

The hoop stress at $r = r_1^+$ in the outer medium is

The exact solution:

$$\frac{\sigma_\theta^+}{p} = \frac{2}{1 + (1 - \alpha^2)/\lambda_{21}/(1 + \alpha^2)} \tag{3.49}$$

The current model:

$$\frac{\sigma_\theta^+}{p} = \frac{2}{1 + 4(1 - \alpha)/\lambda_{21}/(3 + \alpha^2)} \tag{3.50}$$

The spring model:

$$\frac{\sigma_\theta^+}{p} = 2. \tag{3.51}$$

Figures 3.3 and 3.4 show the results of σ_θ^- and σ_θ^+, respectively, obtained from the closed form solution, the current model and the spring model, for different material combinations and geometries. For σ_θ^- shown in figure 3.3, the difference between the exact solution and the current model is within 10% even when the thickness of the layer reaches 30% of the radius of the inner core. The interface spring model, which predicts zero stress, is incapable of reasonably predicting the stress distribution. As shown in figure 3.4, σ_θ^+ from the current model coincides with that from the closed form solution, while the spring model predicts a constant stress $\sigma_\theta^+ = 2p$, which is quite different from the result of the closed form solution.

3.4.2 Bounded layered media subjected to surface loads

The current interphase model is used to simulate the dynamic behavior of a three-layer medium, shown in figure 3.1, under different loading conditions. Both the case shown in figure 3.1(a), which has an outer layer with a limited radius, and the case shown in figure 3.1(b), in which the radius of the outer layer is infinite, are considered to validate the interphase model and to study the dynamic response of the layered medium.
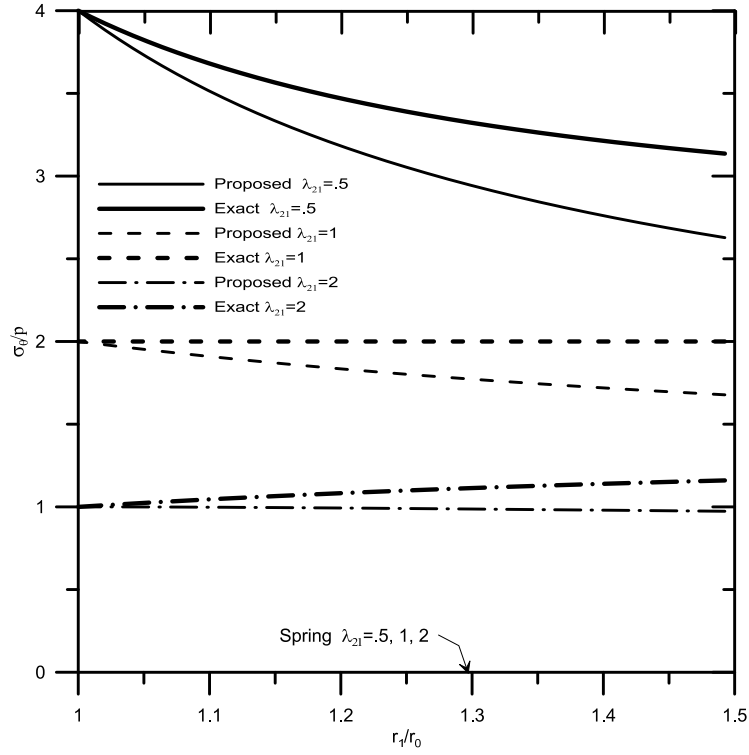
Figure 3.3: Axisymmetric hoop stress with a void core: inner interface
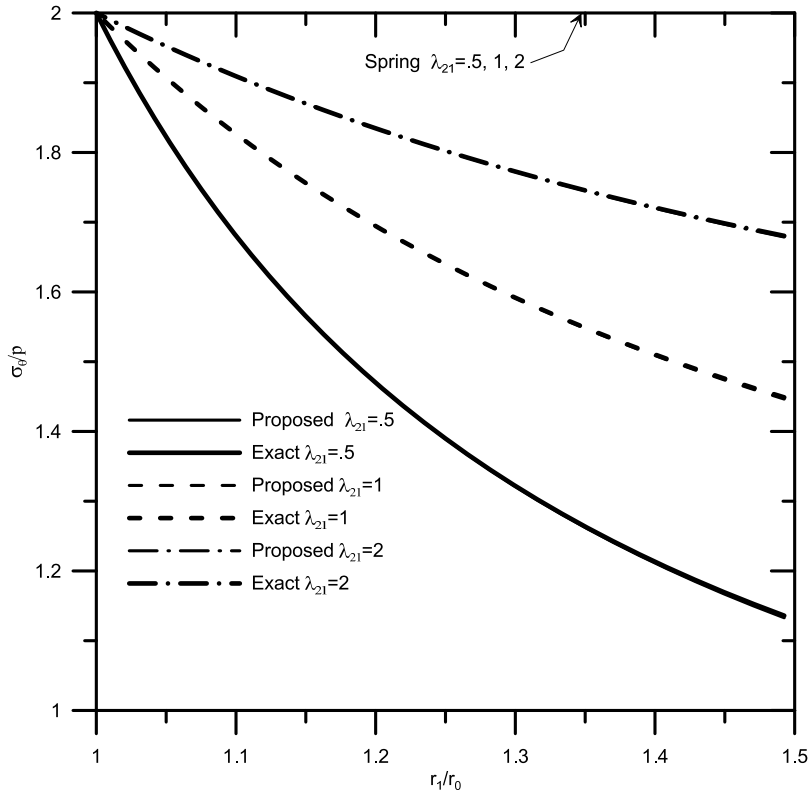
Figure 3.4: Axisymmetric hoop stress with a void core: outer interface

56

The difficulties in the analysis of such transversely anisotropic multilayered media are two folds. Firstly, the piezoelectric layer needs to be properly modeled to provide simple yet accurate description of the stress distribution in the layer. This is considered through the proposed interphase model. Secondly, in the numerical simulation the Bessel functions used need to be properly normalized (Ricks and Schmidt, 1994) to avoid overflow, which results in ill-conditioned (Zhang et al., 2010) equations. In the current simulation a numerical normalization algorithm is used to overcome this problem.

Material properties used in the study are shown in table 6.1 (Nakatani et al., 2007; Qian et al., 2008). Different selections of material properties are considered in the simulation to study the effect of material combinations.

Material	Elastic Constants					Density
	$\times 10^{10}(\mathrm{N/m^2})$					$\times 10^3(\mathrm{kg/m^2})$
	c_{22}	c_{33}	c_{12}	c_{23}	c_{44}	ρ
isotropic	$c_{22}{=}c_{33}{=}\lambda + 2\mu$		λ	λ	μ	
Aluminum	11.27	11.27	6.07	6.07	2.6	2.7
Polythene	.554	.554	.298	.298	.128	1.2
PZT-4	13.9	12.4	6.78	7.43	2.5	7.5
Steel	26.3	26.3	10.2	10.2	8.05	7.8

Table 3.1: Material constants used

To evaluate the developed interphase model, consider the response of a finite three-layer medium shown in figure 3.5, subjected to a distributed surface load along the outer boundary $r = r_2$,

$$
\sigma_r = \begin{cases} p & |\pi - \beta| \leq \theta \leq |\beta| \\ 0 & \text{elsewhere} \end{cases}
\tag{3.52}
$$

$$
\sigma_{r\theta} = 0 \ .
\tag{3.53}
$$

The applied surface stress can be expressed in terms of Fourier expansion as

$$
\sigma_r = p\left(d_0 + \sum_{n=1}^{\infty} d_n cosn\theta\right)
\tag{3.54}
$$

where

$$d_0 = \frac{2\beta}{\pi}, \; d_n = \frac{2sin\,(n\beta)}{\pi n}\,[1 + (-1)^n] \qquad (3.55)$$

with p being the amplitude of the applied load and β being the range of the load.
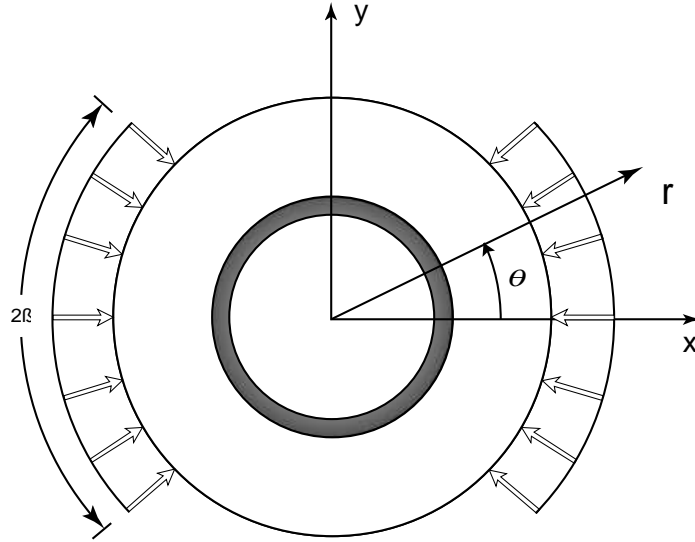
Figure 3.5: Bounded layered medium subjected to surface loads

Figure 3.6 shows the normalized radial stress distribution along the radial direction at $\theta = 0$ for the case where $\beta = \pi/6$ at a very low loading frequency $kR = 0.025$ with k being the shear wave number of the outer medium $k_T = \omega/c_T$, R being the outer radius of the interphase, $R = r_1$, and $r_2 = 1.5r_1$. To evaluate the accuracy of the current interphase model, the core, the interphase and the outer layer are assumed to be of the same material and different interphase thicknesses are considered. The results from the interface-spring model, the current model and the finite element analysis (ANSYS) are compared. For layer thicknesses $h/R = 0.1, 0.2, 0.3$ the current model shows a very good agreement with the finite element results, while the interface-spring model shows much more significant errors for all thicknesses considered. The corresponding distribution of σ_θ along $\theta = 0$ is given in figure 3.7. Again the current model provides excellent prediction of the stress distribution but the result from the interface-spring

58

model is quite different from the finite element prediction around the middle layer. The corresponding dynamic stress σ_r is shown in figures 3.8 and 3.9 for $kR = 0.5$ and $kR = 1.1$ for different layer thicknesses. The simulation results indicate that for very small thickness $h/R = 0.01$ the interface-spring model, the current model and the finite element analysis provide almost identical results. But for larger thicknesses of the layer $(h/R = 0.1, 0.2, 0.3)$, the current model shows much better results in comparison with the interface-spring model.

Figure 3.10 and figure 3.11 show the corresponding radial stress distribution for dissimilar media at $kR = 0.4$ and 0.8, respectively, with the outer layer being aluminum, the core being steel and the middle layer being PZT-4. For very thin layer, $h/R = 0.01$, the results from the FEM, the current model and the interface spring model are almost identical. But for $h/R = 0.1, 0.2, 0.3$, the spring model shows significant different results from the current model and the FEM.

3.4.3   Infinite layered media subjected to incident waves

Consider now the dynamic response of a layered medium with an infinite outer medium $(r_2 = \infty)$ subjected to an incident P-wave, as shown in figure 3.1(b). The incident P-wave with a general incident angle θ_0 can be expressed in terms of the displacement potential as

$$\varphi^{in} = \varphi_0 e^{-ik_L r cos(\theta - \theta_0)} \tag{3.56}$$

where φ_0 is the magnitude of the incident wave, and k_L is the longitudinal wave number of the outer medium. In the following discussion, $\theta_0 = 0$ is considered. The incident displacement and stress fields can be determined from φ^{in} directly.

The total field in the outer medium consists of an incident field and a scattered field. By separating the incident field from the total field, the governing equations of the current interphase model become

$$\frac{1}{r^2}\left\{\frac{r_1^2\sigma_{r\theta}^{sc}-r_0^2\sigma_{r\theta}^-}{h}+r\left[c_{23}\frac{u_{r,\theta}^{sc}-u_{r,\theta}^-}{h}+\frac{c_{22}}{r}\left(-n^2\frac{u_\theta^{sc}+u_\theta^-}{2}+\frac{u_{r,\theta}^{sc}+u_{r,\theta}^-}{2}\right)\right]\right\}$$

$$=\sigma_{r\theta}^*-\rho\omega^2 u_\theta \quad (3.57)$$

$$\frac{1}{r}\left\{\frac{r_1\sigma_r^{sc}-r_0\sigma_r^-}{h}+\frac{\sigma_{r\theta,\theta}^{sc}+\sigma_{r\theta,\theta}^-}{2}-\left[c_{23}\frac{u_r^{sc}-u_r^-}{h}+\frac{c_{22}}{r}\left(\frac{u_{\theta,\theta}^{sc}+u_{\theta,\theta}^-}{2}+\frac{u_r^{sc}+u_r^-}{2}\right)\right]\right\}$$

$$=\sigma_r^*-\rho\omega^2 u_r \quad (3.58)$$

$$\frac{\sigma_r^{sc}+\sigma_r^-}{2}-\left\{c_{33}\frac{u_r^{sc}-u_r^-}{h}+\frac{c_{23}}{r}\left(\frac{u_{\theta,\theta}^{sc}+u_{\theta,\theta}^-}{2}+\frac{u_r^{sc}+u_r^-}{2}\right)\right\}=u_r^* \quad (3.59)$$

$$\frac{\sigma_{r\theta}^{sc}+\sigma_{r\theta}^-}{2}-c_{44}\left(\frac{1}{r}\frac{u_{r,\theta}^{sc}+u_{r,\theta}^-}{2}+\frac{u_\theta^{sc}-u_\theta^-}{h}-\frac{1}{r}\frac{u_\theta^{sc}+u_\theta^-}{2}\right)=u_\theta^* \quad (3.60)$$

where the superscript 'sc' represents the scattered field in the outer medium to be determined from the solution, and the terms with superscript '*' represent the incident wave, which are given by

$$u_r^*=-\frac{\sigma_r^{in}}{2}+c_{33}\frac{u_r^{in}}{h}+\frac{c_{23}}{r}\left[\frac{\partial}{\partial\theta}\left(\frac{u_\theta^{in}}{2}\right)+\frac{u_r^{in}}{2}\right] \quad (3.61)$$

$$\sigma_r^*=-\frac{1}{r}\left\{\frac{r_1\sigma_r^{in}}{h}+\frac{\sigma_{r\theta,\theta}^{in}}{2}-\left[c_{23}\frac{u_r^{in}}{h}+\frac{c_{22}}{r}\left(\frac{u_{\theta,\theta}^{in}}{2}+\frac{u_r^{in}}{2}\right)\right]\right\} \quad (3.62)$$

$$u_\theta^*=-\frac{\sigma_{r\theta}^{in}}{2}+c_{44}\left[\frac{u_{r,\theta}^{in}}{2r}+\frac{u_\theta^{in}}{h}-\frac{u_\theta^{in}}{2r}\right] \quad (3.63)$$

$$\sigma_{r\theta}^*=-\frac{1}{r^2}\left\{\frac{r_1^2\sigma_{r\theta}^{in}}{h}+r\left[c_{23}\frac{u_{r,\theta}^{in}}{h}+\frac{c_{22}}{r}\left(-n^2\frac{u_\theta^{in}}{2}+\frac{u_{r,\theta}^{in}}{2}\right)\right]\right\}. \quad (3.64)$$

Figure 3.12 shows the normalized radial stress distribution along $\theta=0$ caused by an incident wave with a very low loading frequency $kR=0.01$ with p being the magnitude

of the maximum stress of the incident wave. In this case the inner core is void, the middle layer is PZT-4 and the outer medium is aluminum. For different PZT layer thicknesses, the radial stress shows a monotonic increase from the inner surface of the PZT layer. The result from the spring model, however, could not capture the variation of the stress in the layer. Similar results are observed for the corresponding problem with a higher loading frequency, $kR = 0.6$, as shown in figure 3.13.

Figure 3.14 shows the corresponding radial stress distribution for the case where the inner core is steel, the middle layer is PZT-4 and the outer medium is polythene, subjected to an incident wave of low frequency $kR = 0.01$. Both the current model and the spring model could predict the well-known result that the stress in the core is a constant for such a static load. But the spring model is not sensitive to the change of the thickness of the middle layer, which has been reasonably predicted by the current interphase model. Figures 3.15 and 3.16 show the corresponding normalized radial stress distribution along $\theta = 0$ with $kR = 0.02$ and $kR = 0.9$, for the case where the inner core is steel, the middle layer is PZT-4 and the outer medium is aluminum. For different PZT layer thicknesses considered, which are rather large, the result from the spring model shows significant difference from that by the current model.
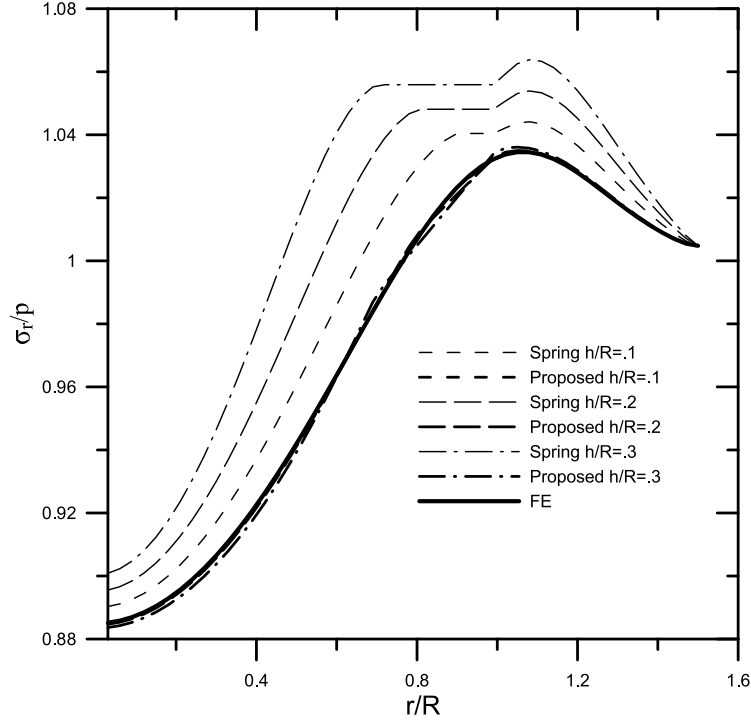
Figure 3.6: Radial stress distribution for a homogenous medium at kR=0.025

3.5 Conclusions

The proposed interphase model for cylindrical anisotropic layers, which contains the effect of the hoop stress and satisfies the equations of motion, shows an excellent accuracy in simulating the stress distribution, and agrees well with the FEM prediction. The proposed model is significantly superior to the traditional interface spring model and, as a result, provides an efficient way to model complicated dynamic deformation caused by anisotropic layers. The current model has been verified at frequencies lower or higher than typical resonance frequencies. It has also been used in situations where the thickness of the layer is significant large, 30% of the typical radius for example. The model can be used to accurately simulate dynamic behavior of cylindrical anisotropic layers, which are otherwise difficult to dealt with.
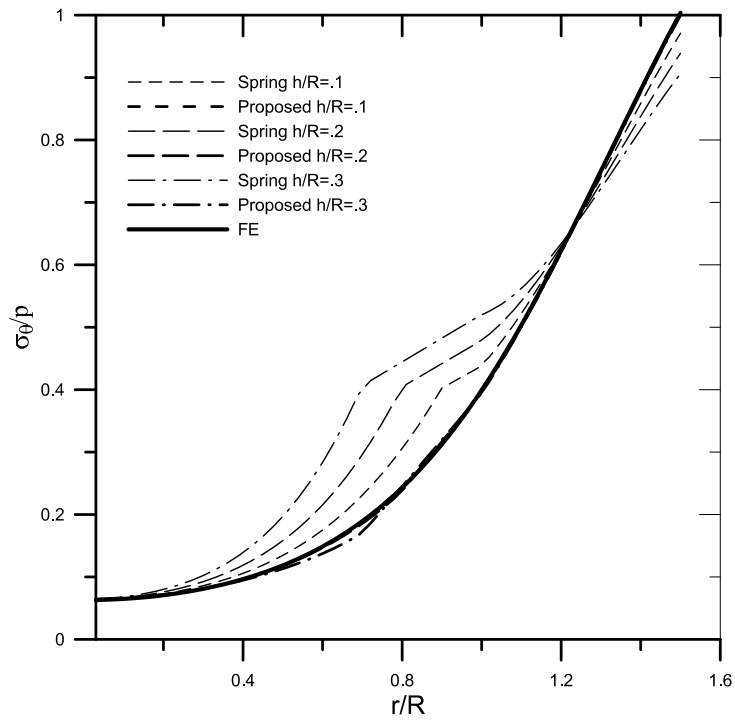
Figure 3.7: Hoop stress distribution for a homogenous medium at kR=0.025
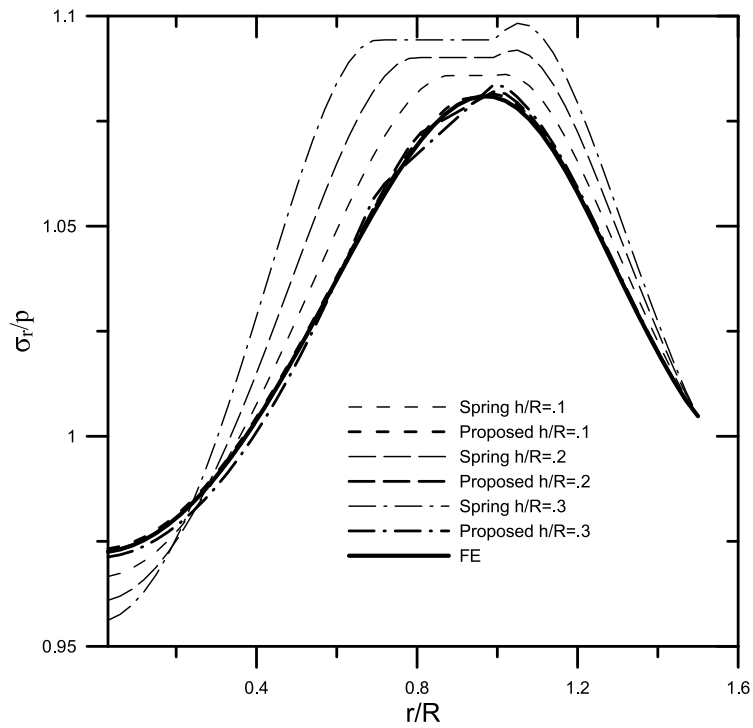
Figure 3.8: Radial stress distribution for a homogenous medium at kR=0.5

63
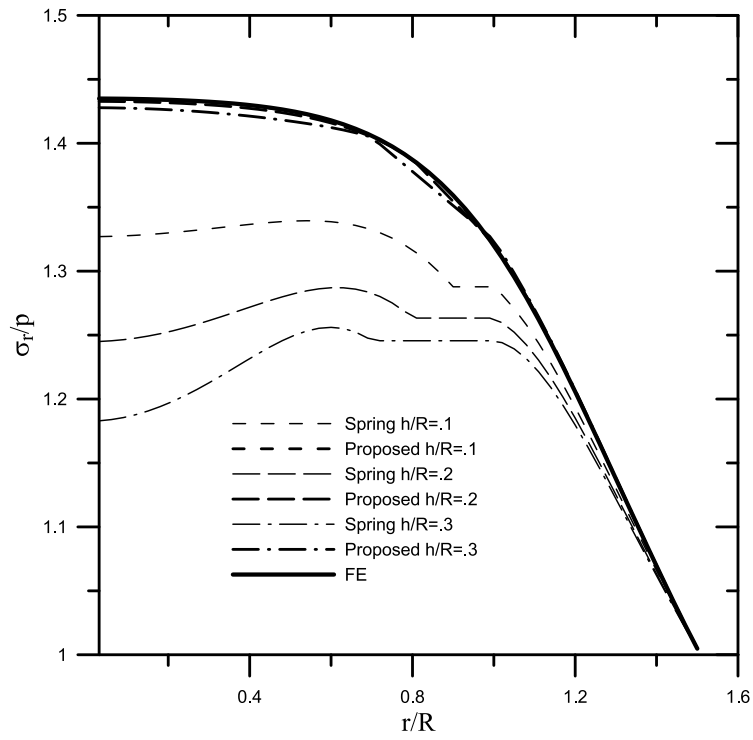
Figure 3.9: Radial stress distribution for a homogenous medium at kR=1.1
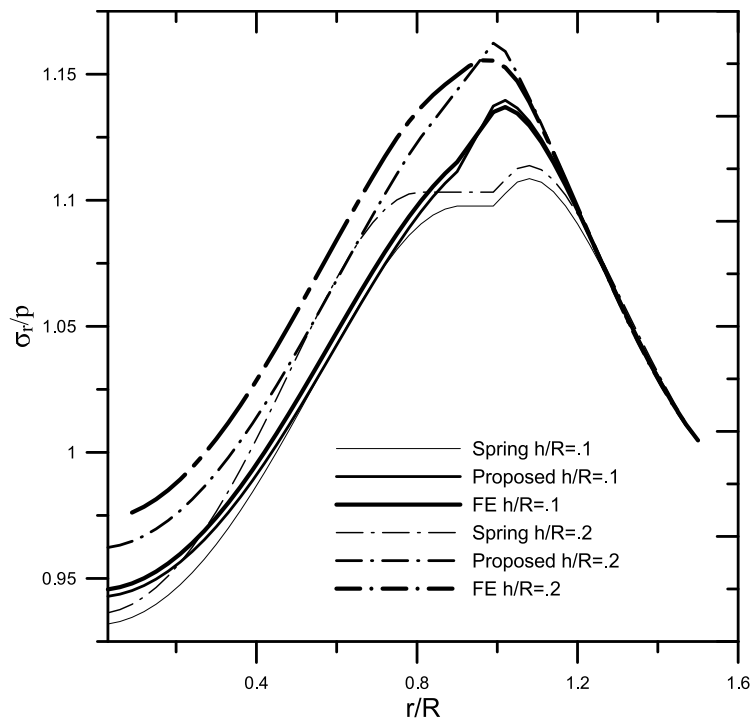
Figure 3.10: Radial stress distribution for a dissimilar medium at kR=0.4
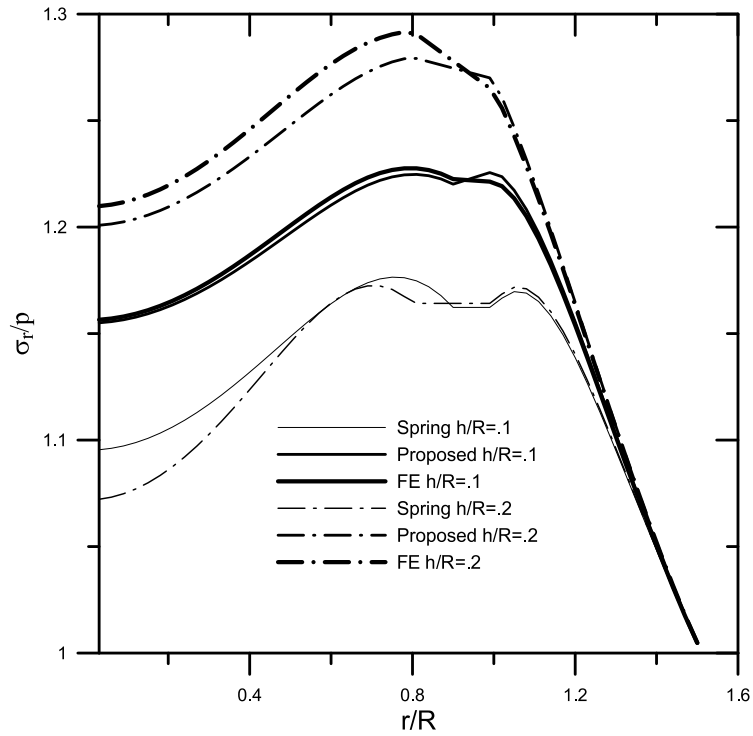
Figure 3.11: Radial stress distribution for a dissimilar medium at kR=0.8
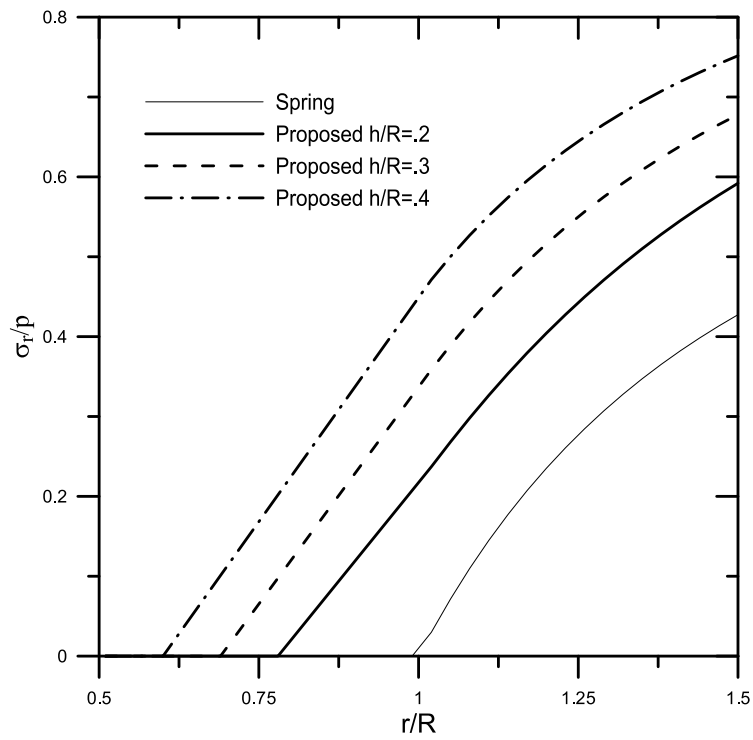
Figure 3.12: Radial stress distribution for a dissimilar medium with a void core at kR=0.01
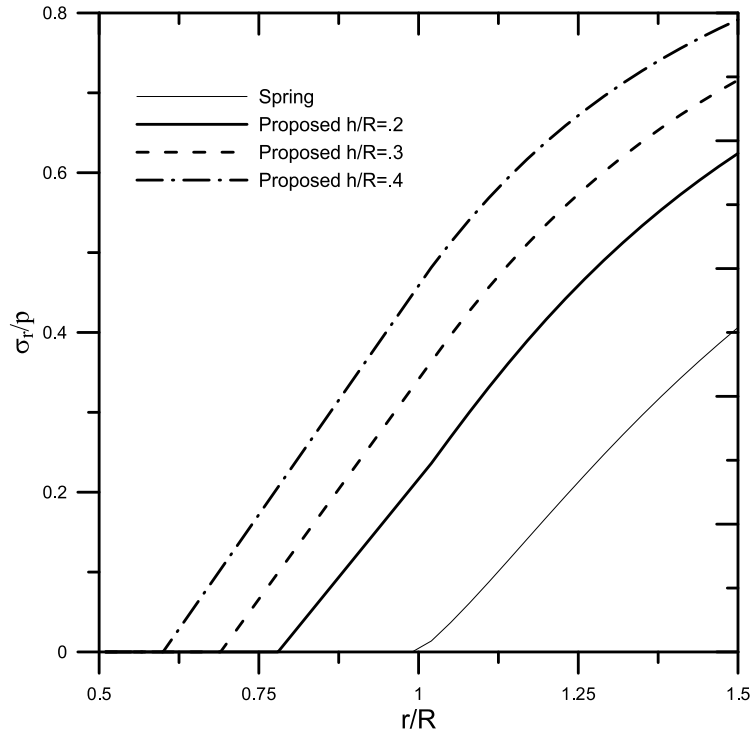
Figure 3.13: Radial stress distribution for a dissimilar medium with a void core at kR=0.6
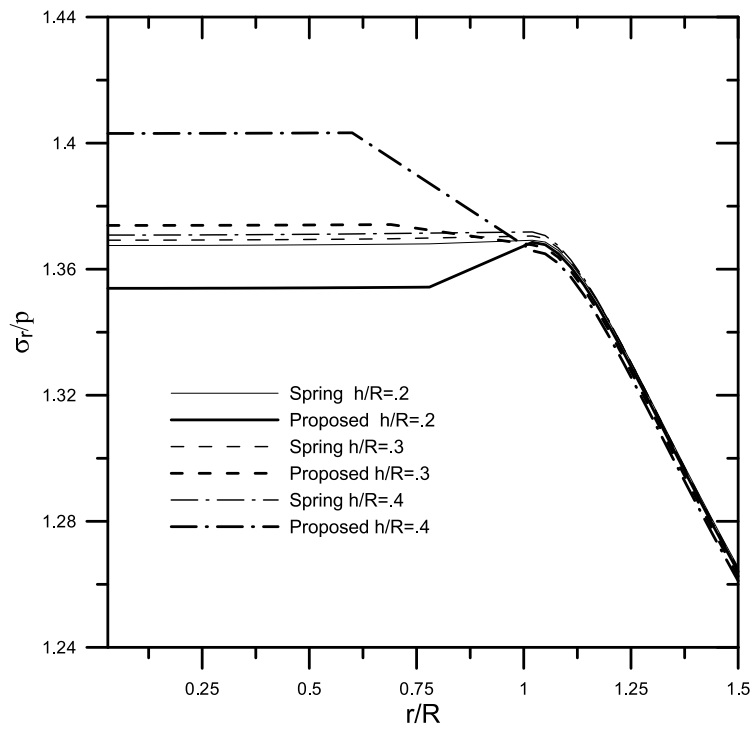
Figure 3.14: Radial stress distribution for a dissimilar medium with a stiff core at kR=0.01

66
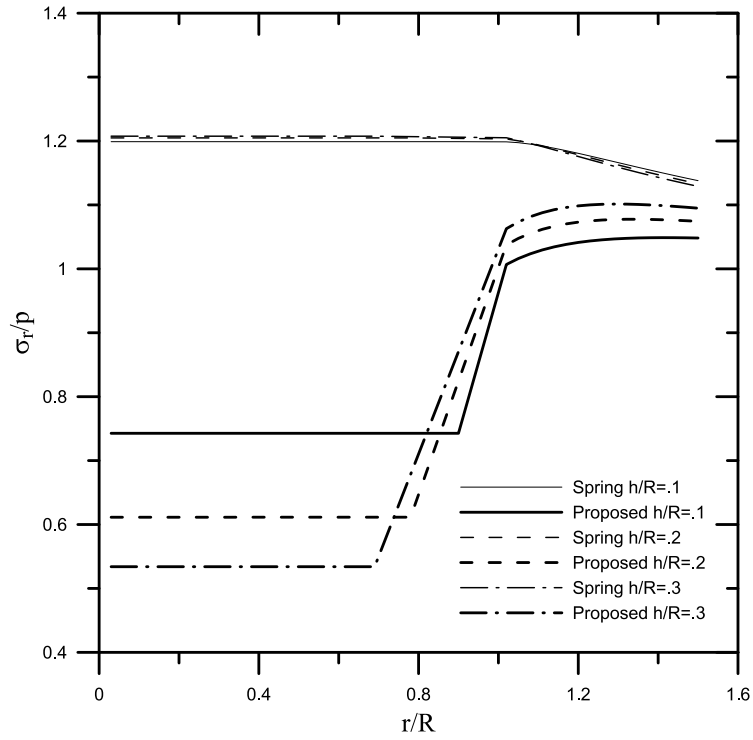
Figure 3.15: Radial stress distribution for a dissimilar medium at kR=0.02
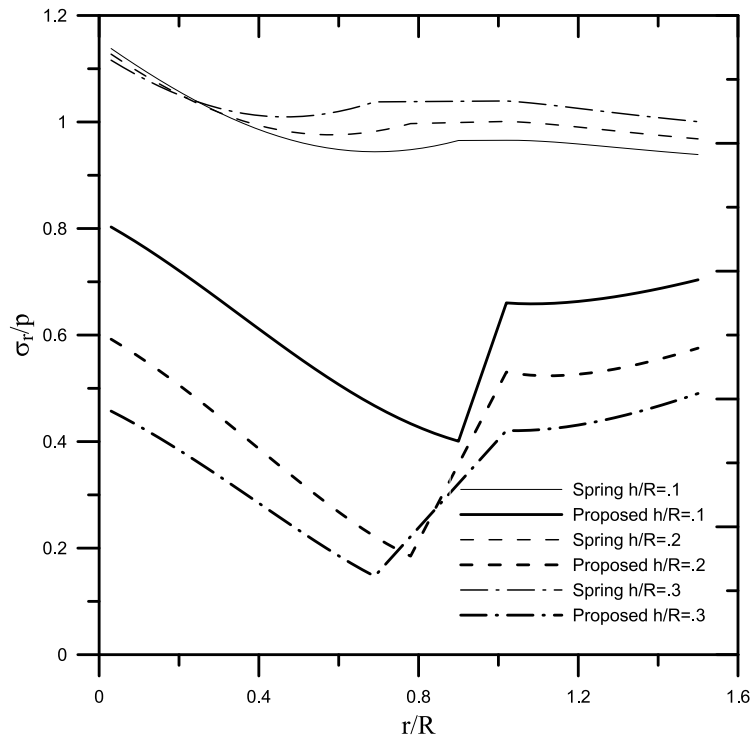
Figure 3.16: Radial stress distribution for a dissimilar medium at kR=0.9

67

Chapter 4

The dynamic electromechanical behavior of a multilayered piezoelectric fiber

4.1 Introduction

An important issue in the study of multilayered piezoelectric fibers in smart structures is how to accurately predict the elastic field around the piezoelectric fiber through the collected electric signal in the piezoelectric layer. Existing solutions for axially polarized piezoelectric layer or rings (Ramesh and Ebenezer, 2005) are not sufficient for describing the dynamic behavior of the piezoelectric fiber. Considering the fact that the piezoelectric layer is relatively thin compared with the radius of the fiber, simplified layer models can overcome this difficulty. In the study of composite structures, modeling of thin layers, interphases, has been extensively investigated and is still attracting significant attention (Kushch et al., 2011; Rajabi and Hasheminejad, 2009; Wang and Zhong, 2003; Wang, Pan, and Roy, 2007; Zhong and Meguid, 1997) because of its importance in evaluating the multi-layered composite materials.

In the case of the multilayered piezoelectric fiber with poling in the transverse direction, the piezoelectric layer poses problems in modeling because of the combined effect between its anisotropy and the elastic wave. For mechanical response, a commonly used method is to simplify the anisotropic interphase with distributed interface springs to avoid dealing with the solution of mechanical field in the anisotropic layer. The spring is used to simulate the traction–displacement relation across the interphase.

The spring model (Bian, Chen, and Lu, 2008; Chen et al., 2004; Librescu and Schmidt, 2001; Wang and Zhong, 2003; Zhong and Meguid, 1997) does not account for, curved interphases, the hoop stress in the equilibrium equations and assumes that the stresses are uniform across the thickness of the interphase. It should be mentioned that for a piezoelectric layer in a typical cylindrical piezoelectric fiber with a transverse poling direction (Chocat et al., 2011), the layer thickness could be significant compared with the radius of the fiber. Also, because of the curved geometry of the layer, even under the simplest loading conditions, the stress will not be constant across the layer thickness. In addition, the hoop stress in the curved layer will also play a significant role in the deformation. The interphase model presented in chapter 3 (Abdel-Gawad and Wang, 2013) which can represent the effect of the stress variation across the layer thickness, the hoop stress in the layer and the anisotropy of the layer will be adopted here but extended to include the piezoelectric effect of a multilayered piezoelectric fiber.

For the analysis of the layered fiber, as the number of layers increases, the transfer matrix technique becomes viable to avoid the cumbersome direct approach. The transfer matrix technique has been introduced originally for flat interfaces by Thomson (1950) and later used by many other researchers (Hasheminejad and Alaei-Varnosfaderani, 2012; Huang, Wang, and Rokhlin, 1996; Lan and Wei, 2013; Lowe, 1995; Nayfeh and Nagy, 1996; Rajabi and Hasheminejad, 2009). According to this technique, a local layer's transfer matrix is constructed to transfer the field variables (i.e. stresses and displacements) between the layers outer and inner interface. Then by extending the solution from one layer to the next while satisfying the continuity condition, a global matrix can be attained which in turn transfers the boundary conditions to the different interface composite layers. The weakness of the transfer matrix method is its instabilities when the relative frequency is large (Lowe, 1995). An alternative technique is the direct global matrix method, provided by (Ricks and Schmidt, 1994). This numerical algorithm is applied to the transfer matrix eliminating its instabilities. In the

direct global matrix method, the wave fields at all the interfaces and boundaries are assembled together in a single matrix. This method is numerically stable but relatively computationally slow because of the large matrix.

The objective of this study is to investigate the electrostatic elastodynamic behavior of a piezoelectric layer in a multilayered fiber embedded in a piezoelectric medium for the potential use as a sensor/actuator in damage detection. A generalized sensor/actuator model coupling the mechanical deformations and electric signals around a radially polarized piezoelectric layer is developed. The developed model is used as an actuator to generate a mechanical signal and as a sensor to retrieve the mechanical deformations from the electric signal. Typical simulation results based on the developed model are provided to illustrate the electromechanical property of embedded radially polarized piezoelectric layer under alternating electric or dynamic loads. Attention will be focused on the response of the piezoelectric layer in accurately sensing the elastic field around the piezoelectric sensor under different loading conditions and material combination.

4.2 Problem formulation

The problem envisaged is the electromechanical behavior of a cylindrical piezoelectric fiber embedded in a dielectric media. The cross section of a long cylindrical multilayered piezoelectric fiber consisting of q layers bonded at their interfaces and lined up with their axes of symmetry coincide with each other. The layers are sequentially numbered 1, 2, ...q from the center of the fiber, and a polar coordinate system (r, θ) is used to describe the geometry of the problem as shown in figure 4.1. The outer radius of layer j is located at $r = r_j$ measured from the center of the fiber, and the total radius of the cylinder will be r_q. The piezoelectric layer could be any layer or more than one layer in the multilayered fiber except for layer 1 without losing generality the inner radius
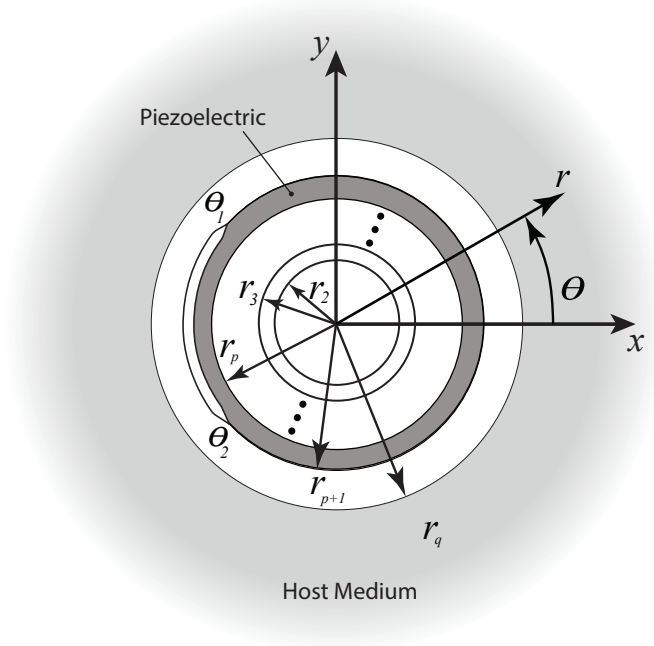
Figure 4.1: The layered composite medium with an unbounded boundary.

will be r_p and the outer radius r_{p+1} and only one layer will be discussed. Other layers are linear elastic, homogeneous and isotropic. Interfacial debonding of the piezoelectric layer is considered and assumed to be between $\theta = \theta_1$ and $\theta = \theta_2$ ($\theta_2 > \theta_1$). Since the main interest of the current study is the local coupled electromechanical behavior between the piezoelectric layer and its surrounding layers, the host structure is assumed to be infinite. This represents the case where the host structure is much thicker than the piezoelectric layer. Plane strain deformation is considered, which corresponds to the assumption that the fiber is very long relative to its radius.

An alternating electric field as well as mechanical dynamic loads are applied to the piezoelectric layer and through the hosting medium respectively. The loads are assumed to be time-harmonic and only the steady state response of the system is considered. For convenience, the term $e^{-i\omega t}$, with $i = \sqrt{-1}$, t and ω are being imaginary number, time and circular frequency, respectively, will be omitted in the following discussion and only the amplitude of the field variables will be considered.

4.2.1 Governing equations

The electromechanical behavior of the different layers shown in figure 4.1 is governed by Gauss's law of electrostatic and the equations of motion (Chadwick, 1999; Chandrasekharaiah and Debnath, 1994; Kessler and Kosloff, 1991; Nayfeh, 1995). In the polar coordinate (r, θ) these equations are

Electrostatic Equation

$$(rD_r)_{,r} + D_{\theta,\theta} = 0 \tag{4.1}$$

Equations of Motion

$$\frac{1}{r}\left((r\sigma_r)_{,r} + \sigma_{\theta r,\theta} - \sigma_\theta\right) = -\rho\omega^2 u_r \tag{4.2}$$

$$\frac{1}{r^2}\left((r^2\sigma_{r\theta})_{,r} + r\sigma_{\theta,\theta}\right) = -\rho\omega^2 u_\theta \tag{4.3}$$

where D is the electric displacement, σ is the stress, ρ is the mass density, and u is the displacement. The subscripts indicate the corresponding components in the polar coordinate while the comma separates the components from the partial differentiation with respect to that coordinate. The constitutive relations for piezoelectric materials, with the poling direction along r, are given by (Larbi and Deü, 2011; Standard, 1987),

$$\begin{bmatrix} D_r \\ D_\theta \end{bmatrix} = \begin{bmatrix} e_{33} & e_{32} & 0 \\ 0 & 0 & e_{24} \end{bmatrix} \begin{bmatrix} \varepsilon_r \\ \varepsilon_\theta \\ \varepsilon_{r\theta} \end{bmatrix} + \begin{bmatrix} \epsilon_{33} & 0 \\ 0 & \epsilon_{22} \end{bmatrix} \begin{bmatrix} E_r \\ E_\theta \end{bmatrix} \tag{4.4}$$

$$\begin{bmatrix} \sigma_r \\ \sigma_\theta \\ \sigma_{\theta r} \end{bmatrix} = \begin{bmatrix} c_{33} & c_{23} & 0 \\ c_{23} & c_{22} & 0 \\ 0 & 0 & c_{44} \end{bmatrix} \begin{bmatrix} \varepsilon_r \\ \varepsilon_\theta \\ \varepsilon_{r\theta} \end{bmatrix} - \begin{bmatrix} e_{33} & 0 \\ e_{32} & 0 \\ 0 & e_{24} \end{bmatrix} \begin{bmatrix} E_r \\ E_\theta \end{bmatrix} \tag{4.5}$$

where e's are the piezoelectric coupling constants, ε's are the strain components, ϵ's are the permittivity constants, and E's are the electric field intensity components which can be expressed in terms of the electric potential ϕ as

$$E_r = -\phi_{,r} \tag{4.6}$$

$$E_\theta = -\frac{1}{r}\phi_{,\theta}. \tag{4.7}$$

The strain ε can be expressed in terms of the displacements u_r and u_θ as

$$\varepsilon_r = u_{r,r} \tag{4.8}$$

$$\varepsilon_\theta = \frac{1}{r}\left(u_{\theta,\theta} + u_r\right) \tag{4.9}$$

$$\varepsilon_{r\theta} = \frac{1}{2}\left(\frac{1}{r}u_{r,\theta} + u_{\theta,r} - \frac{u_\theta}{r}\right). \tag{4.10}$$

4.3 Radially polarized piezoelectric layer

Since the main concern of the current study is how to model the electrical property of a radially polarized piezoelectric layer as a sensor or actuator, the focus will be to develop the electric model then couple it with the mechanical. Substituting equations (4.6), (4.7), (4.8), (4.9), and (4.10) into equations (4.4) and (4.5) then into equations (4.1), (4.2) and (4.3) yields,

$$
\begin{aligned}
e_{33}u_{r,rr} + \left(\frac{e_{32}}{r} + \frac{e_{33}}{r}\right)u_{r,r} + \frac{e_{24}}{2r^2}u_{r,\theta} + \\
\frac{e_{32}}{r}u_{\theta,\theta r} + \frac{e_{24}}{2r}u_{\theta,r} - \frac{e_{24}}{2r^2}u_\theta \\
-\epsilon_{33}\phi_{,rr} - \epsilon_{33}\phi_{,r} - \frac{\epsilon_{22}}{r^2}\phi_{,\theta\theta} = 0
\end{aligned}
\tag{4.11}
$$

$$
\begin{aligned}
c_{33}u_{r,rr} + \frac{c_{33}}{r}u_{r,r} - \frac{c_{22}}{r^2}u_r + \frac{c_{44}}{r^2}u_{r,\theta\theta} + \\
\left(-\frac{c_{44}}{r^2} - \frac{c_{22}}{r^2}\right)u_{\theta,\theta} + \left(\frac{c_{23}}{r} + \frac{c_{44}}{r}\right)u_{\theta,r\theta} + \\
e_{33}\phi_{,rr} + \left(\frac{e_{33}}{r} - \frac{e_{32}}{r}\right)\phi_{,r} + \frac{e_{24}}{r^2}\phi_{,\theta\theta} = -\rho\omega^2 u_r
\end{aligned}
\tag{4.12}
$$

$$
\begin{aligned}
c_{44}\left(\frac{1}{r}u_{r,\theta r} + u_{\theta,rr} - \frac{1}{r}u_{\theta,r}\right) + \frac{1}{r}\left(c_{23}u_{r,r\theta} + \frac{c_{22}}{r}\left(u_{\theta,\theta\theta} + u_{r,\theta}\right)\right) \\
+ \frac{2}{r}c_{44}\left(\frac{1}{r}u_{r,\theta} + u_{\theta,r} - \frac{1}{r}u_\theta\right) + \frac{1}{r^2}\left(\left(r^2 e_{24}\phi_{,\theta}\right)_{,r} + re_{32}\phi_{,r\theta}\right) = -\rho\omega^2 u_\theta
\end{aligned}
\tag{4.13}
$$

The differential equations (4.11), (4.12), and (4.13) are coupled without general analytic solutions. Next sections propose a solution.

4.3.1 The electric field in the piezoelectric layer element

Since the piezoelectric layer is relatively thin with respect to the fiber radius, equations (4.1) and (4.11) is simplified such that $(rD_r)_{,r} \approx \frac{\Delta(rD_r)}{h}$ with $h = r_{p+1} - r_p$ being the thickness of the layer and Δ representing the change from r_p to r_{p+1}. The electrostatic equation (4.1) can then be approximately expressed as

$$\frac{\Delta(rD_r)}{h} + \overline{D}_{\theta,\theta} = 0. \tag{4.14}$$

The piezoelectric layer can now be modeled as a layer element governed by equation (4.14). The electric displacement component is decomposed into two parts a uniform part and a linear part across the layer thickness with a zero average, resulting in the 'Δ' term in the equation. The other term, $\overline{D}_{\theta,\theta}$ in equation (4.14) is the average value over the thickness of the layer. The over bar $\overline{(.)} = \frac{(.)^{p+}+(.)^{p-}}{2}$ represents the average value and the superscripts $(p+)$ and $(p-)$ refer to the variables evaluated at the outer and inner surfaces of the piezoelectric layer, for convenience p will be omitted, for example

$$\overline{D}_r = \frac{D_r^+ + D_r^-}{2}. \tag{4.15}$$

For the layer element, the derivatives with respect to r in these equations can be approximated, such that

$$\phi = \frac{\Delta\phi}{\Delta r}, \; u_{,r} = \frac{\triangle u_r}{\triangle r}, \; u_{\theta,r} = \frac{\triangle u_\theta}{\triangle r}. \tag{4.16}$$

Substituting equations (4.16) into constitutive equation (4.4) results in the layer element constitutive equation as

$$\overline{D}_r = e_{33}\left(\frac{u_r^+ - u_r^-}{h}\right) + \frac{e_{32}}{\overline{r}}(\overline{u}_{\theta,\theta} + \overline{u}_r) - \epsilon_{33}\frac{\phi^+ - \phi^-}{h} \tag{4.17}$$

$$\overline{D}_\theta = \frac{e_{24}}{2}\left(\frac{1}{\overline{r}}\overline{u}_{r,\theta} + \frac{u_\theta^+ - u_\theta^-}{h} - \frac{\overline{u}_\theta}{\overline{r}}\right) + \frac{\epsilon_{22}}{\overline{r}}\overline{\phi}_{,\theta} \tag{4.18}$$

74

Substituting equation (4.18) into equation (4.14), the electrostatic equation becomes,

$$\frac{1}{r}\left(\frac{r^+ D_r^+ - r^- D_r^-}{h} + e_{24}\left(\frac{\overline{u}_{r,\theta}}{r} + \frac{u_\theta^+ - u_\theta^-}{h} - \frac{\overline{u}_\theta}{r}\right)_{,\theta} - \epsilon_{22}\frac{\overline{\phi}_{,\theta\theta}}{r}\right) = 0. \qquad (4.19)$$

4.3.2 The mechanical field in the piezoelectric layer element

The anisotropic layer developed in chapter 3 (Abdel-Gawad and Wang, 2013) can now be coupled into the newly developed electric property of the piezoelectric layer element. The anisotropic layer model overcomes the difficulties associated with the anisotropy of the layer through simplifications such as $(r\sigma_r)_{,r} \approx \frac{\Delta(r\sigma_r)}{h}$ and $(r^2\sigma_{r\theta})_{,r} \approx \frac{\Delta(r^2\sigma_{r\theta})}{h}$. The equations of motion (4.2) and (4.3) can be re-written in a manner similar to equation (4.14) which can then be approximately expressed as

$$\frac{1}{\overline{r}}\left(\frac{\Delta(r\sigma_r)}{h} + \overline{\sigma}_{\theta r,\theta} - \overline{\sigma}_\theta\right) = -\rho\omega^2\overline{u}_r \qquad (4.20)$$

$$\frac{1}{\overline{r}^2}\left(\frac{\Delta(r^2\sigma_{r\theta})}{h} + r\overline{\sigma}_{\theta,\theta}\right) = -\rho\omega^2\overline{u}_\theta. \qquad (4.21)$$

Substituting equation (4.16) into equations (4.4)-(4.5) the constitutive equations for the piezoelectric layer can be written as

$$\overline{\sigma}_r = c_{33}\left(\frac{u_r^+ - u_r^-}{h}\right) + \frac{c_{23}}{\overline{r}}\left(\overline{u}_{\theta,\theta} + \overline{u}_r\right) + e_{33}\frac{\phi^+ - \phi^-}{h} \qquad (4.22)$$

$$\overline{\sigma}_\theta = c_{23}\left(\frac{u_r^+ - u_r^-}{h}\right) + \frac{c_{22}}{\overline{r}}\left(\overline{u}_{\theta,\theta} + \overline{u}_r\right) + e_{32}\frac{\Delta\phi}{h} \qquad (4.23)$$

$$\overline{\sigma}_{r\theta} = c_{44}\left(\frac{\overline{u}_{r,\theta}}{\overline{r}} + \frac{u_\theta^+ - u_\theta^-}{h} - \frac{\overline{u}_\theta}{\overline{r}}\right) + \frac{e_{24}}{\overline{r}}\overline{\phi}_{,\theta}^+. \qquad (4.24)$$

Finally, substituting equations (4.17)-(4.24) into equations (4.1), (4.20) and (4.21), the equations of motion for the layer become

$$\frac{1}{\overline{r}}\left\{\frac{r^+\sigma_r^+ - r^-\sigma_r^-}{h} + \overline{\sigma}_{r\theta} - \left\{c_{23}\frac{(u_r^+ - u_r^-)}{h} + \frac{c_{22}}{\overline{r}}\left(\overline{u}_{\theta,\theta} + \overline{u}_r\right)\right\}\right\} + \rho\omega^2\overline{u}_r = \frac{e_{32}}{\overline{r}}\frac{(\phi^+ - \phi^-)}{h}$$
$$(4.25)$$

$$\frac{1}{\bar{r}^2}\left\{\frac{\left(r^+\right)^2\sigma_{r\theta}^+ - \left(r^-\right)^2\sigma_{r\theta}^-}{h} + \bar{r}\left\{c_{23}\left(\frac{u_{r,\theta}^+ + u_{r,\theta}^-}{h}\right) + \frac{c_{22}}{\bar{r}}\left(\bar{u}_{\theta,\theta\theta} + \bar{u}_{r,\theta}\right)\right\}\right\} + \rho\omega^2\bar{u}_\theta$$

$$= -\frac{e_{32}}{\bar{r}}\frac{\left(\phi_{,\theta}^+ - \phi_{,\theta}^-\right)}{h}. \quad (4.26)$$

4.3.3 The piezoelectric layer element transfer matrix

For any layer, the inner and outer interface field variables (displacements, stresses, electric potential and electric displacement) are all periodic and can be expanded using Fourier expansion with respect to θ. The obtained general solutions can be represented in matrix form for the nth expansion order as

$$\mathbf{W}_n^+ = \mathbf{M}_n^{(p)}\mathbf{W}_n^-, \quad (4.27)$$

$$\mathbf{W}_n = \begin{bmatrix} u_r & u_\theta & \sigma_r & \sigma_{r\theta} & \phi & D_r \end{bmatrix}_n^T \quad (4.28)$$

with superscript T indicating the transpose. The local transfer matrix for the pth layer $\mathbf{M}_n^{(p)}$, relates the field variables $\mathbf{W}_n$ at its outer interface $\mathbf{W}_n^+$ to those at its inner interface $\mathbf{W}_n^-$. Equations (4.22), (4.24), (4.25), (4.26), (4.14) and (4.17) establish the relation between $\mathbf{W}_n^+$ and inner $\mathbf{W}_n^-$ of the piezoelectric layer based on the properties of the layer itself. The local transfer matrix for the piezoelectric layer is defined as

$$\mathbf{M}_n^{(p)} = \mathbf{K}_n^+ \left[\mathbf{K}_n^-\right]^{-1} \quad (4.29)$$

where the elements of $\mathbf{K}^+$ and $\mathbf{K}^-$ matrices for the proposed piezoelectric layer model are

$$\mathbf{K}_n^+ = \begin{bmatrix} -\dfrac{c_{33}}{h} - \dfrac{c_{23}}{2\bar{r}} & -\dfrac{c_{23}in}{2\bar{r}} & \dfrac{1}{2} & 0 & -\dfrac{e_{33}}{h} & 0 \\[2mm] -\dfrac{c_{44}in}{2\bar{r}} & c_{44}\left(\dfrac{1}{2\bar{r}} - \dfrac{1}{h}\right) & 0 & \dfrac{1}{2} & -\dfrac{e_{24}}{h} & 0 \\[2mm] \dfrac{\rho h\omega^2}{2} - \dfrac{hc_{22}}{2\bar{r}^2} - \dfrac{c_{23}}{\bar{r}} & -\dfrac{c_{22}hin}{2\bar{r}^2} & \dfrac{r_1}{\bar{r}} & \dfrac{hni}{2\bar{r}} & 0 & 0 \\[2mm] \dfrac{ni\left(c_{22}h + 2c_{13}\bar{r}\right)}{2\bar{r}^2} & \dfrac{\rho h\omega^2}{2} - \dfrac{c_{22}n^2}{2\bar{r}^2} & 0 & \dfrac{r_1^2}{\bar{r}^2} & 0 & 0 \\[2mm] -e_{33} - \dfrac{e_{32}h}{2\bar{r}} & \dfrac{e_{32}hin}{2\bar{r}} & 0 & 0 & \epsilon_{33} & \dfrac{h}{2} \\[2mm] -\dfrac{e_{24}n^2}{2\bar{r}} & e_{24}in\left(\dfrac{1}{h} - \dfrac{1}{2\bar{r}}\right) & 0 & 0 & -\dfrac{n^2\epsilon_{22}}{2\bar{r}} & \dfrac{r_1}{h} \end{bmatrix}^{-1} \tag{4.30}$$

$$\mathbf{K}_n^- = -\begin{bmatrix} \dfrac{c_{33}}{h} - \dfrac{c_{23}}{2\bar{r}} & -\dfrac{c_{23}in}{2\bar{r}} & \dfrac{1}{2} & 0 & \dfrac{e_{33}}{h} & 0 \\[2mm] -\dfrac{c_{44}in}{2\bar{r}} & c_{44}\left(\dfrac{1}{2\bar{r}} + \dfrac{1}{h}\right) & 0 & \dfrac{1}{2} & \dfrac{e_{24}}{h} & 0 \\[2mm] \dfrac{\rho h\omega^2}{2} - \dfrac{hc_{22}}{2\bar{r}^2} + \dfrac{c_{23}}{\bar{r}} & -\dfrac{c_{22}hin}{2\bar{r}^2} & \dfrac{-r_0}{\bar{r}} & \dfrac{hni}{2\bar{r}} & 0 & 0 \\[2mm] \dfrac{ni\left(c_{22}h - 2c_{23}\bar{r}\right)}{2\bar{r}^2} & \dfrac{\rho h\omega^2}{2} - \dfrac{c_{22}n^2}{2\bar{r}^2} & 0 & \dfrac{-r_0^2}{\bar{r}^2} & 0 & 0 \\[2mm] e_{33} - \dfrac{e_{32}h}{2\bar{r}} & -\dfrac{e_{32}hin}{2\bar{r}} & 0 & 0 & -\epsilon_{33} & \dfrac{h}{2} \\[2mm] -\dfrac{e_{24}n^2}{2\bar{r}} & -e_{24}in\left(\dfrac{1}{h} - \dfrac{1}{2\bar{r}}\right) & 0 & 0 & -\dfrac{n^2\epsilon_{22}}{2\bar{r}} & \dfrac{r_0}{h} \end{bmatrix}^{-1} . \tag{4.31}$$

Under the open-loop mode, no external charge is supplied and the piezoelectric charge collected on the two electrodes will generate an electric field.

4.4   The imperfect layer

The imperfect layer is angularly imperfect with varying properties along the θ direction. The imperfect layer model is developed by simplifying equations (4.25) and (4.26) without ignoring the layer's curvature and inertia as

$$\frac{1}{h\bar{r}}\left(r^{(l+)}\sigma_r^{(l+)} - r^{(l-)}\sigma_r^{(l-)}\right) + \rho\omega^2 u_r^{(l-)} = 0 \tag{4.32}$$

$$\frac{1}{h\bar{r}^2}\left(\left(r^{(l+)}\right)^2 \sigma_{r\theta}^{(l+)} - \left(r^{(l-)}\right)^2 \sigma_{r\theta}^{(l-)}\right) + \rho\omega^2 u_\theta^{(l-)} = 0 \tag{4.33}$$

$$\frac{1}{h}\left(r^{(l+)}D_r^{(l+)} - r^{(l-)}D_r^{(l-)}\right) = 0. \tag{4.34}$$

The discontinuities in displacements at the interfaces are assumed to be proportional, in terms of a compliance interface parameter χ, to their average interface traction components

$$\frac{\sigma_r^{(l+)} + \sigma_r^{(l-)}}{2} = \frac{1}{\chi}\left(u_r^{(l+)} - u_r^{(l-)}\right) \tag{4.35}$$

$$\frac{\sigma_{r\theta}^{(l+)} + \sigma_{r\theta}^{(l-)}}{2} = \frac{1}{\chi}\left(u_\theta^{(l+)} - u_\theta^{(l-)}\right) \tag{4.36}$$

$$\frac{D_r^{(l+)} + D_r^{(l-)}}{2} = \frac{1}{\chi}\left(\phi^{(l+)} - \phi^{(l-)}\right). \tag{4.37}$$

For achieving different bonding interfaces, $^p\chi$ is changed from perfectly bonded $^p\chi \to 0$ to a completely debonded $^p\chi \to \infty$. The compliance is expressed in terms of θ and arbitrarily constants s_1 and s_2 representing two values of the imperfect compliance,

$$\chi = \frac{h}{c}\begin{cases} s_2 & \left|\dfrac{\theta - \theta_0}{\theta_w}\right| \leq 1 \\[2mm] s_1 & \theta \text{ elsewhere} \end{cases}, \tag{4.38}$$

where h, c, $\theta_0 = \dfrac{\theta_1 + \theta_2}{2}$, $\theta_w = \dfrac{\theta_2 - \theta_1}{2}$ are for the imperfect interphase layer thickness, constitutive property, average angles and half width angle respectively.

Equations (4.33) and (4.36) can be represented in matrix form

$$\mathbf{W}^{(l+)} = \mathbf{M}(\theta)^{(l)}\mathbf{W}^{(l-)} \tag{4.39}$$

where $\mathbf{M}(\theta)^{(l)}$ is formed using equations (4.32) to (4.37)

$$\mathbf{M}(\theta)^{(l)} = \begin{bmatrix} 1 - \rho\omega^2 h\dfrac{\chi\bar{r}}{r_{l+1}} & 0 & \dfrac{\chi\bar{r}}{r_{l+1}} & 0 & 0 & 0 \\[3mm] 0 & 1 - \rho\omega^2 h\dfrac{\chi_0\bar{r}^2}{r_{l+1}^2} & 0 & \dfrac{\chi\left(r_{l+1}^2 + r_l^2\right)}{r_{l+1}^2} & 0 & 0 \\[3mm] -\rho\omega^2 h\dfrac{\bar{r}}{r_{l+1}} & 0 & \dfrac{r_l}{r_{l+1}} & 0 & 0 & 0 \\[3mm] 0 & -\rho\omega^2 h\dfrac{\bar{r}^2}{r_{l+1}^2} & 0 & \dfrac{r_l^2}{r_{l+1}^2} & 0 & 0 \\[3mm] 0 & 0 & 0 & 0 & 1 & \dfrac{\chi\bar{r}}{r_{l+1}} \\[3mm] 0 & 0 & 0 & 0 & 0 & \dfrac{r_l}{r_{l+1}} \end{bmatrix} \tag{4.40}$$

with its expansion in θ as

$$\sum_{k=-\infty}^{+\infty} \mathbf{W}_k{}^{(l+)} e^{ik\theta} = \mathbf{M}(\theta)^{(l)} \sum_{m=-\infty}^{+\infty} \mathbf{W}_m{}^{(l-)} e^{im\theta}, \tag{4.41}$$

multiplying both sides by $e^{-in\theta}$ and integrating from $-\pi$ to π

$$\mathbf{W}_n{}^{(l+)} = \int_{-\pi}^{\pi} \mathbf{M}(\theta)^{(l)} \sum_{m=-\infty}^{+\infty} \mathbf{W}_m{}^{(l-)} e^{im\theta} e^{-in\theta} d\theta \tag{4.42}$$

$$\mathbf{W}_n{}^{(l+)} = \sum_{m=-\infty}^{+\infty} \mathbf{M}_{m,n}^{(l)} \mathbf{W}_m{}^{(l-)} \tag{4.43}$$

The elements of $\mathbf{M}_{m,n}^{(l)}$ matrices for the imperfect interphase at $m = n$ are

$$\mathbf{M}_{m,m}^{(l)} = \begin{bmatrix} 1 - \rho\omega^2 h \dfrac{\chi_0 \overline{r}}{r_{l+1}} & 0 & \dfrac{\chi_0 \overline{r}}{r_{l+1}} & 0 & 0 & 0 \\[2ex] 0 & 1 - \rho\omega^2 h \dfrac{\chi_0 \overline{r}^2}{r_{l+1}^2} & 0 & \dfrac{\chi_0 \left(r_{l+1}^2 + r_l^2\right)}{r_{l+1}^2} & 0 & 0 \\[2ex] -\rho\omega^2 h \dfrac{\overline{r}}{r_{l+1}} & 0 & \dfrac{r_l}{r_{l+1}} & 0 & 0 & 0 \\[2ex] 0 & -\rho\omega^2 h \dfrac{\overline{r}^2}{r_{l+1}^2} & 0 & \dfrac{r_l^2}{r_{l+1}^2} & 0 & 0 \\[2ex] 0 & 0 & 0 & 0 & 1 & \dfrac{\chi_0 \overline{r}}{r_{l+1}} \\[2ex] 0 & 0 & 0 & 0 & 0 & \dfrac{r_l}{r_{l+1}} \end{bmatrix},$$

where $\chi_0 = \dfrac{s_2}{c} \left(\dfrac{\dfrac{2\pi s_1}{s_2} + \theta_w \left(1 - \dfrac{s_1}{s_2}\right)}{2\pi} \right)$ at $m \neq n$,

$$\mathbf{M}_{m,n}^{(l)} = \begin{bmatrix} -\rho\omega^2 h \dfrac{\chi_{m,n} \overline{r}}{r_{l+1}} & 0 & \dfrac{\chi_{m,n} \overline{r}}{r_{l+1}} & 0 & 0 & 0 \\[2ex] 0 & -\rho\omega^2 h \dfrac{\chi_{m,n} \overline{r}^2}{r_{l+1}^2} & 0 & \dfrac{\chi_{m,n} \left(r_{l+1}^2 + r_l^2\right)}{r_{l+1}^2} & 0 & 0 \\[2ex] 0 & 0 & 0 & 0 & 0 & 0 \\[2ex] 0 & 0 & 0 & 0 & 0 & 0 \\[2ex] 0 & 0 & 0 & 0 & 0 & \dfrac{\chi_{m,n} \overline{r}}{r_{l+1}} \\[2ex] 0 & 0 & 0 & 0 & 0 & 0 \end{bmatrix},$$

79

where $\chi_{m,n} = \dfrac{s_2}{c} \left(\dfrac{\left(1 - \dfrac{s_1}{s_2}\right) \left(e^{i(m-n)\theta_w} - e^{-i(m-n)\theta_w}\right)}{2\pi i (m-n)} \right) e^{i(m-n)\theta_0}.$

4.5   Wave field in dielectric isotropic layers

Since the thickness of the host medium is much larger than the fiber radius, the host medium is modeled as infinite, the dielectric property of the host and other dielectric isotropic layers are governed by the electric displacement

$$D_r = -\epsilon \phi_{,r}, \; D_\theta = -\frac{\epsilon}{r}\phi_{,\theta}, \tag{4.44}$$

$$\phi_{,rr} + \frac{1}{r}\phi_{,r} - \frac{1}{r^2}\phi_{,\theta\theta} = 0, \tag{4.45}$$

where ϵ is the layer dielectric constant.

For linearly elastic, homogeneous and isotropic dielectric layers the displacement field (u_r, u_θ) can be decomposed into (Achenbach, 1972; Pao, 1983)

$$u_r = \varphi_{,r} + \frac{1}{r}\psi_{,\theta}, \; u_\theta = \frac{1}{r}\varphi_{,\theta} - \psi_{,r} \tag{4.46}$$

where φ and ψ are two displacement potentials satisfying Helmholtz equation

$$\frac{1}{r}\left(r\varphi_{,r}\right)_{,r} + \frac{1}{r^2}\varphi_{,\theta\theta} + k_L^2\varphi = 0 \tag{4.47}$$

$$\frac{1}{r}\left(r\psi_{,r}\right)_{,r} + \frac{1}{r^2}\psi_{,\theta\theta} + k_s^2\psi = 0 \;. \tag{4.48}$$

k_L and k_s are wave-numbers given by

$$k_L = \frac{\omega}{c_L}, \quad k_s = \frac{\omega}{c_s} \tag{4.49}$$

where c_L and c_S are the longitudinal and transverse wave speeds of the elastic medium,

$$c_L = \sqrt{\frac{\lambda + 2\mu}{\rho}}, \quad c_s = \sqrt{\frac{\mu}{\rho}} \tag{4.50}$$

with λ and μ being the Lame constants of the elastic medium.

The general solutions of the electric and displacement potentials can be determined by applying Fourier expansion with respect to θ, as (Mow and Pao, 1971; Oden and Reddy, 2012)

$$\phi = \sum_{n=-\infty}^{\infty} \left\{ A_n^{(1)} \, \tilde{J}_n(r) + A_n^{(2)} \, \tilde{H}_n(r) \right\} e^{in\theta} \tag{4.51}$$

where $\tilde{J}_n(.)$, $\tilde{H}_n(.)$ are the small argument asymptotic forms of Bessel function and Hankel function of the first kind respectively (Abramowitz and Stegun, 1965; Watson, 1995).

$$\varphi = \sum_{n=-\infty}^{\infty} \left\{ J_n(k_L r) \, A_n^{(3)} + H_n(k_L r) \, A_n^{(4)} \right\} e^{in\theta} \tag{4.52}$$

$$\psi = \sum_{n=-\infty}^{\infty} \left\{ J_n(k_s r) \, A_n^{(5)} + H_n(k_s r) \, A_n^{(6)} \right\} e^{in\theta} \tag{4.53}$$

where $J_n(.)$ is Bessel function of the first kind, $H_n(.)$ is Hankel function of the first kind and the subscript n is the circumferential order of expansion. A_n are the unknown parameters with the superscripts identifying the different amplitudes. The stress fields in terms of displacement potentials are provided in appendix (A).

The dielectric elastic layer solutions can be represented in matrix form by substituting equations (4.52) and (4.53) into equations (4.46), (4.A.1) and (4.A.3) resulting in the following equation for the jth layer,

$$\mathbf{W}_n = \mathbf{Q}_n(r) \mathbf{A}_n^{(j)}, \tag{4.54}$$

where $\mathbf{Q}_n(r)$ is the coefficient matrix evaluated at r given in appendix A. The total field variables can then be determined from

$$\mathbf{W} = \sum_{n=-\infty}^{+\infty} \mathbf{Q}_n(r)\mathbf{A}_n^{(j)}e^{in\theta} \tag{4.55}$$

At the jth layer's inner $r = r_j$ and outer radii $r = r_{j+1}$,

$$\mathbf{W}_n^{(j-)} = \mathbf{Q}_n(r_j)\mathbf{A}_n^{(j)}, \tag{4.56}$$

$$\mathbf{W}_n^{(j+)} = \mathbf{Q}_n(r_{j+1})\mathbf{A}_n^{(j)} \tag{4.57}$$

For two perfectly bonded layers eliminating the common amplitude $\mathbf{A}_n$ the field vector $\mathbf{W}_n^{(j-)}$ and $\mathbf{W}_n^{(j+)}$ can be related by

$$\mathbf{W}_n^{(j+)} = \mathbf{M}_n^{(j)} \ \mathbf{W}_n^{(j-)} \tag{4.58}$$

where $\mathbf{M}_n^{(j)} = \mathbf{Q}_n(r_{j+1}) \left[\mathbf{Q}_n(r_j)\right]^{-1}$ is the local transfer matrix for the layer under consideration, which relates the field variables at its outer interface to those at its inner interface.

4.6 Adapted global matrix

The wave field variables are related between the outer radius r_{l+1} of the lth layer to the inner radius r_k of the kth layer via the adapted global transfer matrix, $[\mathbf{T}_n]_k^l$, for all perfectly bonded interfaces except on $l+$

$$\mathbf{W}_n^{(l+)} = [\mathbf{T}_{m,n}]_k^l \ \mathbf{W}_m^{(k-)} \tag{4.59}$$

The elements of the adapted global transfer matrix $[\mathbf{T}_{m,n}]_k^l$ are calculated by using equation (4.43) for the imperfect layer and the multiple application of the continuity conditions between different perfectly bonded layers' interfaces using equation (4.58) which couples all circumferential orders around the imperfect layer

$$[\mathbf{T}_{m,n}]_k^l = \sum_{m=-\infty}^{+\infty} \mathbf{M}_{m,n}^{(l)}\mathbf{M}_m^{(l-1)}\mathbf{M}_m^{(l-2)}.....\mathbf{M}_m^{(k+1)}\mathbf{M}_m^{(k)} \tag{4.60}$$

For simplicity in notation $\mathbf{T}_k^l$ will be used to refer to it.

To avoid singularities at the origin $r = 0$, $A_n^{(2)}$, $A_n^{(4)}$, $A_n^{(6)}$ for the inner central layer (layer 1) are set to zero to ensure that the field has a limited amplitude. Therefore, equation (4.54) is rewritten in its expanded amplitude form for the core layer as

$$\mathbf{W}_n^{(1+)} = \mathbf{Q}_n^{(1+)} \begin{bmatrix} A_n^{(1)} & 0 & A_n^{(3)} & 0 & A_n^{(5)} & 0 \end{bmatrix}^T. \tag{4.61}$$

To model a void core with internal pressure or free surface $\mathbf{W}_n^{(1+)}$ is used directly.

The medium can be either unbounded or bounded, for unbounded outer layer, $A_n^{(1)}$, $A_n^{(3)}$ and $A_n^{(5)}$ will be zero to satisfy the radiation condition at infinity for the scattered wave. Equation (4.54) is rewritten for the medium interface with other layers as

$$\left(\mathbf{W}_n^{(q-)}\right)^{sc} = \mathbf{Q}_n^{(q-)} \begin{bmatrix} 0 & A_n^{(2)} & 0 & A_n^{(4)} & 0 & A_n^{(6)} \end{bmatrix}^T \tag{4.62}$$

the superscript sc indicating scatter. The total wave field in the medium $\mathbf{W}_n = \mathbf{W}_n^{in} + \left(\mathbf{W}_n\right)^{sc}$ where $\mathbf{W}_n^{in}$ is the incident wave field. If the multilayered fiber is bounded, the outer medium layer is replaced with air properties and a direct application of the desired boundary conditions on the inner interface of the air layer. The following relation between the unknowns of the inner central layer and the unbounded media can be written

$$\mathbf{G}_{m,n} \left\{ \begin{bmatrix} A_m^{(1)} \\ A_m^{(3)} \\ A_m^{(5)} \\ \\ A_n^{(2)} \\ A_n^{(4)} \\ A_n^{(6)} \end{bmatrix} \right\} = \left\{ \mathbf{W}_n^{in} \right\}, \tag{4.63}$$

$$
\mathbf{G}_{m,n}
$$

$$
= \begin{bmatrix}
\underbrace{\begin{matrix}
\left(T_{s+}^{q-}\right)_{1,1} & \left(T_s^{q-}\right)_{1,3} & \left(T_s^{q-}\right)_{1,5} \\[4pt]
\left(T_s^{q-}\right)_{2,1} & \left(T_s^{q-}\right)_{2,3} & \left(T_s^{q-}\right)_{2,5} \\[4pt]
\left(T_s^{q-}\right)_{3,1} & \left(T_s^{q-}\right)_{3,3} & \left(T_s^{q-}\right)_{3,5} \\[4pt]
\left(T_s^{q-}\right)_{4,1} & \left(T_s^{q-}\right)_{4,3} & \left(T_s^{q-}\right)_{4,5} \\[4pt]
\left(T_s^{q-}\right)_{5,1} & \left(T_s^{q-}\right)_{5,3} & \left(T_s^{q-}\right)_{5,5} \\[4pt]
\left(T_s^{q-}\right)_{6,1} & \left(T_s^{q-}\right)_{6,3} & \left(T_s^{q-}\right)_{6,5}
\end{matrix}}_{\text{transmission coefficients } T_s^{q-}}
&
\underbrace{\begin{matrix}
-\left(Q_n^{(q-)}\right)_{1,2} & -\left(Q_n^{(q-)}\right)_{1,4} & -\left(Q_n^{(q-)}\right)_{1,6} \\[4pt]
-\left(Q_n^{(q-)}\right)_{2,2} & -\left(Q_n^{(q-)}\right)_{1,4} & -\left(Q_n^{(q-)}\right)_{1,6} \\[4pt]
-\left(Q_n^{(q-)}\right)_{3,2} & -\left(Q_n^{(q-)}\right)_{1,4} & -\left(Q_n^{(q-)}\right)_{1,6} \\[4pt]
-\left(Q_n^{(q-)}\right)_{4,2} & -\left(Q_n^{(q-)}\right)_{1,4} & -\left(Q_n^{(q-)}\right)_{1,6} \\[4pt]
-\left(Q_n^{(q-)}\right)_{5,2} & -\left(Q_n^{(q-)}\right)_{5,4} & -\left(Q_n^{(q-)}\right)_{5,6} \\[4pt]
-\left(Q_n^{(q-)}\right)_{6,2} & -\left(Q_n^{(q-)}\right)_{6,4} & -\left(Q_n^{(q-)}\right)_{6,6}
\end{matrix}}_{\text{scattering coefficients } -Q_n^{(q-)}}
\end{bmatrix}
$$

$$(4.64)$$

where $\mathbf{T}_s^{q-} = \mathbf{T}_2^q \mathbf{Q}_m^{(1+)}$, $\mathbf{T}_2^q$ is the transfer matrix from the inner interface of layer q to the outer of layer 1 given by equation (4.60), $\mathbf{Q}_m^{(1+)}$, and $\mathbf{Q}_n^{(q-)}$ are the coefficient matrices of layer 1 evaluated at its outer, and layer q evaluated at its inner interface, the parentheses represent the matrix element denoted by the subscript. In addition to using a problem-oriented approach to scale rows and columns (Ricks and Schmidt, 1994), a high multi-precision algorithm (Fousse et al., 2007) was used (Advanpix, 2018). The boundary conditions around a piezoelectric layer interface is achieved by controlling its surrounding material permittivity for example for $\phi^- = 0$ the inner material interfacing the piezoelectric should have a large permittivity.

4.7   Results and discussion

In this section, the electromechanical behavior of a multilayered radially polarized piezo-electric fiber, shown in figure 4.1, is considered. Few limiting cases, shown in figure 4.1, are discussed then compared with finite element as well as with the proposed model without the limitations.
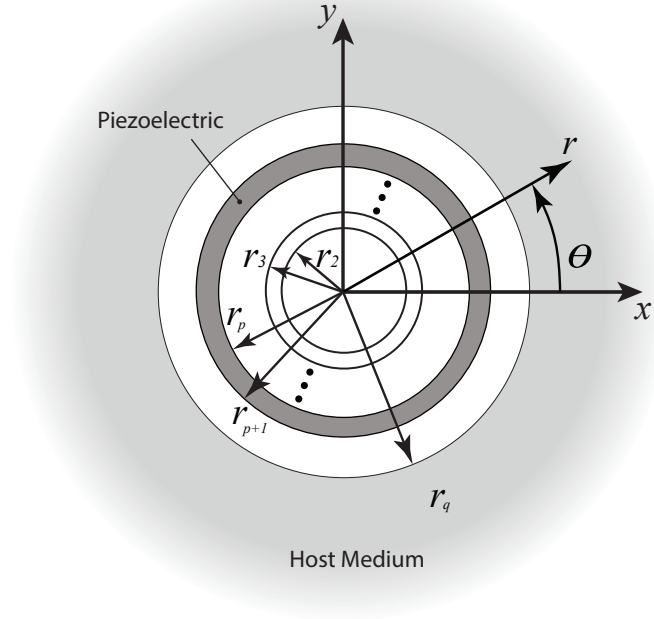
Figure 4.2: Perfectly bonded multilayered piezoelectric fiber

4.7.1 Exact solution for limiting cases

Exact solutions can be obtained when the problem is axisymmetric. Few limiting cases are discussed of a radially polarized piezoelectric sensor. A fluid-filled radially polarized multilayered piezoelectric (hydrophone) is considered to validate and evaluate the accuracy of the developed piezoelectric layer model by comparing with existing results (Ebenezer and Joseph, 2001). Then a multilayered piezoelectric fiber embedded in an elastic insulator is also considered. The piezoelectric interfaces are completely electroded under equi-electric potential and the generated voltage is assumed to be independent of the antisymmetric components. As a consequence, the rates of changes along the circumferential direction, derivatives with respect to θ, are ignored. Equation (4.1) for the piezoelectric sensor under consideration can be written as

$$\left(rD_r\right)_{,r} = 0 \tag{4.65}$$

and equation (4.11) and (4.12) reduce to

$$r^2 e_{33} u_{r,rr} + r\left(e_{32} + e_{33}\right) u_{r,r} + r e_{32} u_r - \epsilon_{33}^s \left(r^2 \phi_{,rr} + r\phi_{,r}\right) = 0 \tag{4.66}$$

$$r^2 c_{33} u_{r,rr} + r c_{33} u_{r,r} + \left(\rho \omega^2 r^2 - c_{22}\right) u_r + r^2 e_{33} \phi_{,rr} + r \left(e_{33} - e_{32}\right) \phi_{,r} = 0. \quad (4.67)$$

The piezoelectric layer is used as a sensor embedded in insulator materials with an open circuit boundary condition, $D_r^+ = D_r^- = 0$ and it must satisfy equation (4.1), the constitutive equation (4.4) reduces to

$$\phi_{,r} = \frac{1}{\epsilon_{33}} \left(e_{33} u_{r,r} + e_{32} \frac{u_r}{r}\right). \quad (4.68)$$

Equation (4.68) can be used to decouple the differential equations (4.66), (4.67) and equation (4.67) can be reduced to the following solvable form

$$r^2 \bar{c}_{33}^{(p)} u_{r,rr} + r \bar{c}_{33}^{(p)} u_{r,r} + \left(\rho \omega^2 r^2 - \bar{c}_{22}^{(p)}\right) u_r = 0 \quad (4.69)$$

where $\bar{c}_{33}^{(p)} = c_{33}^{(p)} + \dfrac{e_{33}^2}{\epsilon_{33}}$, $\bar{c}_{22}^{(p)} = c_{22}^{(p)} + \dfrac{e_{32}^2}{\epsilon_{33}}$.

The following is the exact analytic solutions for a four-layered radially polarized piezoelectric fiber embedded in an infinite host medium for the cases of fluid as well as elastic layers,

Inner central layer 1

The inner central layer has two cases, either a fluid or an elastic solid layer.

Fluid layer case

$$\sigma_r = -p = -A^{(1)} J_0 \left(k_L^{(1)} r\right),$$
$$u_r = \frac{A^{(1)}}{\omega \rho^{(1)} c_L^{(1)}} J_1 \left(k_L^{(1)} r\right) \quad (4.70)$$

Elastic layer case

$$u_r = A^{(1)} J_\gamma \left(\kappa^{(1)} r\right), \quad \sigma_r = A^{(1)} \left(c_{33}^{(1)} J_{\gamma,r} \left(\kappa^{(1)} r\right) + \frac{c_{23}^{(1)}}{r} J_\gamma \left(\kappa^{(1)} r\right)\right) \quad (4.71)$$

Piezoelectric layer 2

$$u_r = A_1^{(p)} J_\gamma \left(\kappa^{(p)} r\right) + A_2^{(p)} H_\gamma \left(\kappa^{(p)} r\right) \quad (4.72)$$

$$\sigma_r = A_1^{(p)} \left(\bar{c}_{33}^{(p)} J_{\gamma,r} \left(\kappa^{(p)} r\right) + \frac{\bar{c}_{23}^{(p)}}{r} J_\gamma \left(\kappa^{(p)} r\right)\right) + A_2^{(p)} \left(\bar{c}_{33}^{(p)} H_{\gamma,r} \left(\kappa^{(p)} r\right) + \frac{\bar{c}_{23}^{(p)}}{r} H_\gamma \left(\kappa^{(p)} r\right)\right)$$
$$(4.73)$$

$$\phi_{,r} = A_1^{(p)} \left(h_{33} J_{\gamma,r} \left(\kappa^{(p)} r \right) + \frac{h_{32}}{r} J_\gamma \left(\kappa^{(p)} r \right) \right) + A_2^{(p)} \left(h_{33} H_{\gamma,r} \left(\kappa^{(p)} r \right) + \frac{h_{32}}{r} H_\gamma \left(\kappa^{(p)} r \right) \right)$$

$$(4.74)$$

Elastic coating layer 3

$$u_r = A_1^{(3)} J_\gamma \left(\kappa^{(3)} r \right) + A_2^{(3)} H_\gamma \left(\kappa^{(3)} r \right) \tag{4.75}$$

$$\sigma_r = A_1^{(3)} \left(c_{33}^{(3)} J_{\gamma,r} \left(\kappa^{(3)} r \right) + \frac{c_{23}^{(3)}}{r} J_\gamma \left(\kappa^{(3)} r \right) \right) + A_2^{(3)} \left(c_{33}^{(3)} H_{\gamma,r} \left(\kappa^{(3)} r \right) + \frac{c_{23}^{(3)}}{r} H_\gamma \left(\kappa^{(3)} r \right) \right)$$

$$(4.76)$$

Infinite host medium 4

The infinite host medium has two cases, either a fluid or an elastic solid layer.

Fluid layer case

$$\sigma_r^{in} = J_0 \left(k_L^{(4)} r \right), \ u_r$$
$$= \frac{A^{(4)}}{\omega \rho^{(4)} c_L^{(4)}} J_1 \left(k_L^{(4)} r \right) \tag{4.77}$$

Elastic layer case

$$u_r^{sc} = A^{(4)} H_\gamma \left(\kappa^{(4)} r \right), \ \sigma_r^{sc} = A^{(4)} \left(c_{33}^{(4)} H_{\gamma,r} \left(\kappa^{(4)} r \right) + \frac{c_{23}^{(4)}}{r} H_\gamma \left(\kappa^{(4)} r \right) \right) \tag{4.78}$$

$$u_r^{in} = \frac{1}{\sigma_0} J_\gamma \left(\kappa^{(4)} r \right), \ \sigma_r^{in} = \frac{1}{\sigma_0} \left(c_{33}^{(4)} J_{\gamma,r} \left(\kappa^{(4)} r \right) + \frac{c_{23}^{(4)}}{r} J_\gamma \left(\kappa^{(4)} r \right) \right) \tag{4.79}$$

where $k_L^{(j)} = \omega/c_L^{(j)}$, $c_L^{(j)} = \sqrt{\frac{c_{33}^{(j)}}{\rho^{(j)}}}$, $\gamma = \sqrt{\frac{\bar{c}_{22}^{(j)}}{\bar{c}_{33}^{(j)}}}$, $\kappa^{(j)} = \omega/\sqrt{\frac{\bar{c}_{33}^{(j)}}{\rho^{(j)}}}$, $h_{33} = \frac{e_{33}}{\epsilon_{33}}$, $h_{32} = \frac{e_{32}}{\epsilon_{33}}$, $\sigma_0 = \rho^{(4)}\omega^2$ and the superscript(j) denote the jth layer property. A general elastic, general fluid, the limiting cases analytic piezoelectric layer and the proposed piezoelectric layer model coefficient matrices are constructed appendix B. The unknown constants in the general solution using equation (4.63), $A^{(1)}$, $A_1^{(p)}$, $A_2^{(p)}$, $A_3^{(p)}$, $A_4^{(p)}$, $A_1^{(3)}$, $A_2^{(3)}$, and $A^{(4)}$ can be determined. The open circuit voltage for the exact analytic limiting cases after grounding the inner interface voltage to zero $\phi^- = 0$ is

$$\phi^+ = A_1^{(p)} h_{33} J_\gamma \left(\kappa^{(p)} r^+ \right) + A_2^{(p)} h_{33} H_\gamma \left(\kappa^{(p)} r^+ \right)$$
$$+ \int_{r_2}^{r_3} \left(A_1^{(p)} \frac{h_{32}}{r} J_\gamma \left(\kappa^{(p)} r^+ \right) + A_2^{(p)} \frac{h_{32}}{r} H_\gamma \left(\kappa^{(p)} r^+ \right) \right) dr \qquad (4.80)$$

and the voltage on the outer interface in the proposed layer model is

$$\phi^+ = \frac{1}{\epsilon_{33}} \left(e_{33} \left(u_r^+ - u_r^- \right) + \frac{e_{32}}{h \overline{r}} \overline{u}_r \right). \qquad (4.81)$$

The receiving sensitivity of a piezoelectric layer as a sensor, S, is defined as the induced voltage ϕ^+ on the piezoelectric layer's outer interface in response to $1 \mu Pa = 10^{-6}$ N/m^2 of a plane incident wave and calculated as (Ebenezer and Joseph, 2001; George, Ebenezer, and Bhattacharyya, 2010)

$$S = 20 \log_{10} \left(\text{abs} \left(\phi^+ \right) \right). \qquad (4.82)$$

The material properties for the used piezoelectric layer and elastic coating in the fluid filled limiting case study were synthesized, table 6.1, to provide the same exact coefficients as used by Ebenezer and Joseph (2001) and George, Ebenezer, and Bhattacharyya (2010). The used fluids are water and air with a density of 1000 kg/m^3, 1.2 kg/m^{3}and a speed of 1500 m/s, 340 m/s respectively. The dimension $r^- = 8$ mm, $r^+ = 10$ mm and $r_4 = 15$ mm. Although the derivation holds for anisotropic layers, all layers are assumed isotropic except for the piezoelectric layer. Figure 4.3 shows a good agreement for the two cases of piezoelectric coating materials (elastic layer 3).

Figures 4.4 and 4.5 show the sensitivity of a radially polarized P(VDF-TrFE) and PZT sensor fiber embedded in different material combinations q $= \dfrac{c_{33}^{(1)}}{c_{33}^{(p)}}, \dfrac{c_{33}^{(3)}}{c_{33}^{(p)}}$ with $h/r_{p+1} = .2$, the proposed model provides excellent agreement with the exact model even at very high relative frequencies (up to kR=8) with the exception around resonance frequencies. Material combinations used in the study are P(VDF-TrFE), ρc rubber and titanium providing q=1.2 and 42.9 respectively also PZT, rubber, synthetic and steel providing q=.05, 1 and 2.2. Figure 4.4 shows that the sensitivity increases

when the fiber inner central layer is stiffer than the piezoelectric and host medium material specially at low frequencies. Figure 4.5 shows that the sensitivity increases when the piezoelectric fiber is embedded in a host medium and/or inner central layer that has more compliant material compared to the piezoelectric layer. From figures 4.4, 4.5, and 4.6 the overall sensitivity of P(VDF-TrFE) is higher than that of PZT also the worst sensitivity is attained when the piezoelectric fiber is embedded in a stiff host material. It can be seen that the proposed model can be used with high accuracy at significantly high frequency, even at kR=8 yet it attains excellent agreements with the exact limiting case model.

4.7.2 Piezoelectric fibers embedded in elastic solid medium

The limiting case assumptions are not always true and do not hold for elastic solids under general loading, $\mathbf{W}^{in}$, the need for the proposed model becomes essential. For further comparisons under general loading a finite element model (ANSYS) is developed, the model represents an embedded piezoelectric fiber in an unbounded media as shown in figure 4.7. The finite element model uses gradually damped layers to simulate the unbounded media. Both the sensor and actuator cases of a multilayered piezoelectric fiber have been studied using different selection of material properties for the different layers as shown in table 6.1.

In the following discussion, the piezoelectric layer is subject to an incident p-wave with a general incident angle θ_0,

$$\varphi^{in} = \varphi_0 e^{ik_L r cos(\theta - \theta_0)} \tag{4.83}$$

where φ_0 is the magnitude of the incident wave, and k_L is the longitudinal wave number of the host outer medium. The corresponding expanded wave field in the host medium can be determined directly from φ^{in} as

$$\mathbf{W}_n^{in} = \mathbf{Q}_n^{(q-)} \begin{bmatrix} \varphi_0 i^n e^{n\theta_0} & 0 & 0 & 0 & 0 & 0 \end{bmatrix}^T. \tag{4.84}$$

Materials	Elastic Constants $\times 10^{10}(\text{N/m}^2)$					Density $\times 10^3$	Piezoelectric $\times 10^0(\text{C/m}^2)$				Permittivity $\times 10^{-9}(\text{C/Vm})$	
	c_{22}	c_{33}	c_{12}	c_{23}	c_{44}	ρ	e_{31}	e_{32}	e_{33}	e_{24}	ϵ_{33}	ϵ_{11}
	$\lambda+2\mu$		λ	λ	μ							
Aluminum	11.27	11.27	6.07	6.07	2.6	2.7	-	-	-	-	-	-
ρc rubber	.225	.225	.1	.1	.063	1	-	-	-	-	-	-
Polycarbonate	.554	.554	.298	.298	.128	1.18	-	-	-	-	.03	.03
P(VDF-TrFE)	.47	.45	.257	.213	.12	1.3	.045	.045	-.18	-.1	.1	.12
PZT-4	14.2	11.8	7.43	6.78	2.5	7.5	-5.2	-5.2	15.1	12.7	5.63	6.45
Steel	26.3	26.3	10.2	10.2	8.05	7.8	-	-	-	-	-	-
Synthetic-P	11.8	11.8	4.72	4.72	3.54	7.5	-	-	-	-	-	-
Titanium	19.3	19.3	10.3	10.3	4.5	5.4	-	-	-	-	-	-

Table 4.1: Material constants used.

First the case of a sensor with the same material for the outer unbounded layer and the central inner layer as polycarbonate with elastic dielectric properties while the piezoelectric layer is P(VDF-TrFE) with $h/r_{p+1} = .2$. Figure 4.8 shows the normalized radial stress around the interface between the piezoelectric layer and outer layer at different relative frequencies kR=.02, 1, 1.5, π and 2π with k being the shear wave number of the outer medium; R=r_{p+1} being the outer radius of the piezoelectric layer. Figure 4.9 and Figure 4.10 show the normalized circumferential stress and normalized voltage around the same interface with σ_0 is a unit incident p-wave pressure or applied load and $\phi_0 = \dfrac{h_{33}}{c_{33}}h\sigma_0$ is a normalization voltage around the interface. The inner interface of the piezoelectric layer is grounded and set to zero. Comparisons with finite element (FE) at kR=1 and 1.5 show an excellent agreement. It can be noted that the voltage error difference between the proposed model and the finite element is very small. The case of a sensor with an interface arc crack starting with angles of $\theta_1 = 170, 160, 150$ and ending with $\theta_1 = 190, 200, 210$ respectively at kR=1 also at kR=1.5 shows an excellent agreement with finite element as shown in figure 4.16 and 4.17. The jump discontinuity is manifested by errors in both the proposed and the finite element model as shown in a zoomed window in figure 4.16 and 4.17. Gibbs phenomenon can be reduced by increasing the number of Fourier terms while errors in

finite element can be reduced by using a very refined mesh. The Gibbs phenomenon as well as errors in finite element can be noticed more for small crack angles. The problem of simulating a small crack is not inclusive to the current model but it can be found in almost all available models including models based on singular integral equations as reported in the literature (Erdogan and Gupta, 1972; Estrada and Kanwal, 2012).

Second the case of an actuator with the outer layer material is aluminum, the inner central material is steel and the middle layer being PZT-4. Aluminum and steel are considered as insulators with the permittivity of air 8.85×10^{-12}C/Vm. In addition to the incident load, the actuator is subject to a unit voltage applied at the outer piezoelectric interface. Figure 4.11 and 4.12 show the normalized radial stress, the normalized circumferential stress respectively around the interface between the piezoelectric layer and outer layer at kR=1 and 1.5 with different piezoelectric layer thickness. For the case of h/R=.2, Figure 4.13, Figure 4.14 and Figure 4.15 show the normalized radial stress, the normalized circumferential stress and normalized voltage respectively around the interface between the piezoelectric layer and the outer layer at different relative frequencies kR=.02, 1, 1.5, π and 2π. Again, comparisons with finite element (FE) at kR=1 and 1.5 show an excellent agreement.

4.8   Conclusions

In cases where an analytical model is not available, the proposed piezoelectric layer model can be used to simulate and calculate the dynamic electromechanical behavior of multilayered piezoelectric fiber with good accuracy. The proposed model agrees with analytically derived limiting cases and shows an excellent agreement with the FEM prediction. The proposed model has been verified at different frequencies lower and higher than typical resonance frequencies yet it still provides accurate results. It has also been verified for a variety of different material combinations. The proposed imperfectly

bonded layer model can describe the overall wave field and the overall scattering around the crack tip. The singular behavior of the crack opening displacement is crucial only to the computation of the near field local stresses.

The sensitivity of multilayered piezoelectric fiber as a sensor increases when the fiber inner central layer is stiffer than the piezoelectric and host medium material. A relatively more compliant elastic host material than the piezoelectric layer increases the sensitivity of the piezoelectric fiber as a sensor. The proposed model as well as the exact analytic showed that the overall sensitivity of P(VDF-TrFE) is higher than that of PZT.
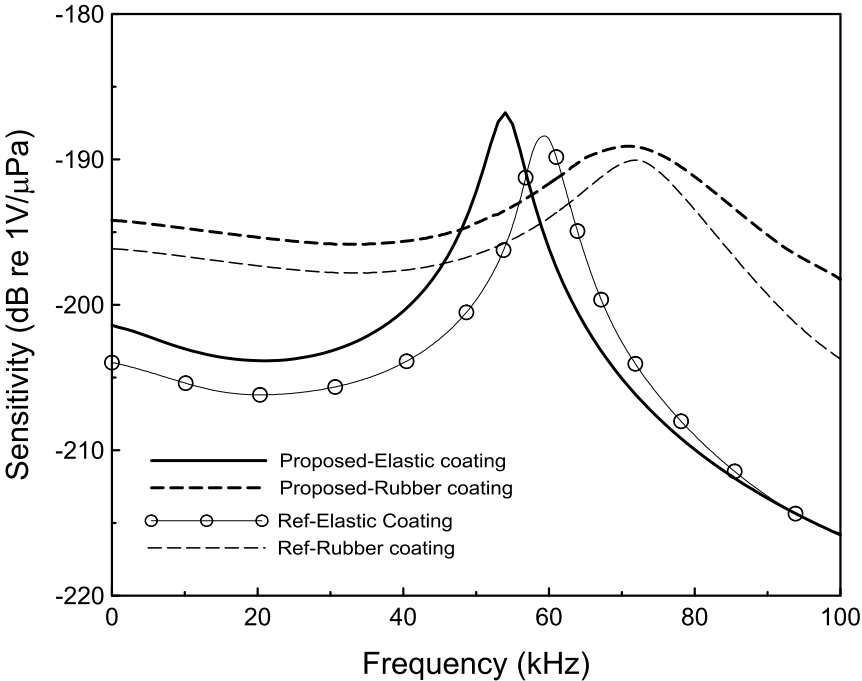
Figure 4.3: Acoustic sensitivity of fluid-filled coated radially polarized piezoelectric.
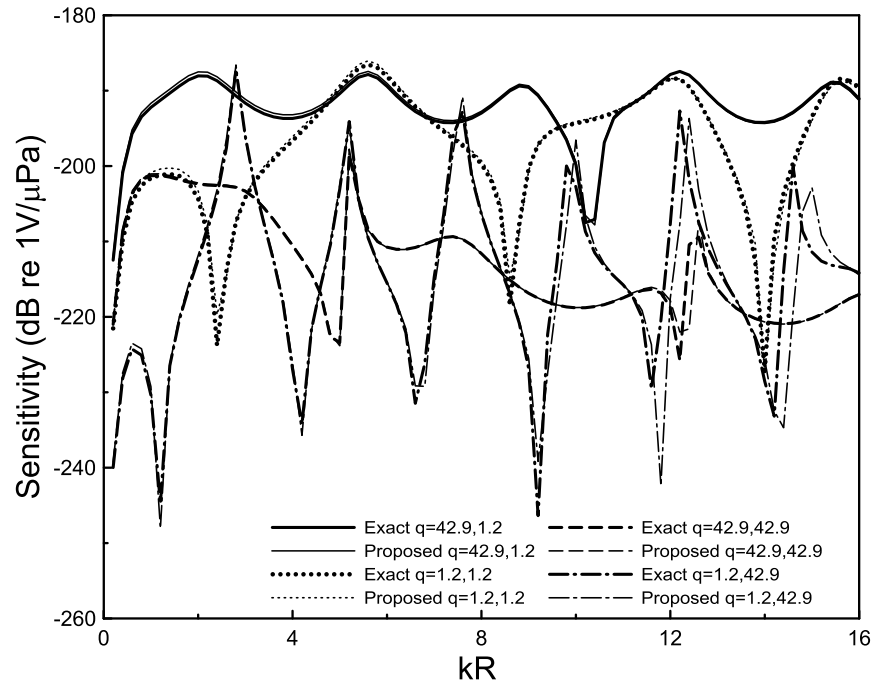
Figure 4.4: P(VDF-TrFE) sensor sensitivity with different material combinations.
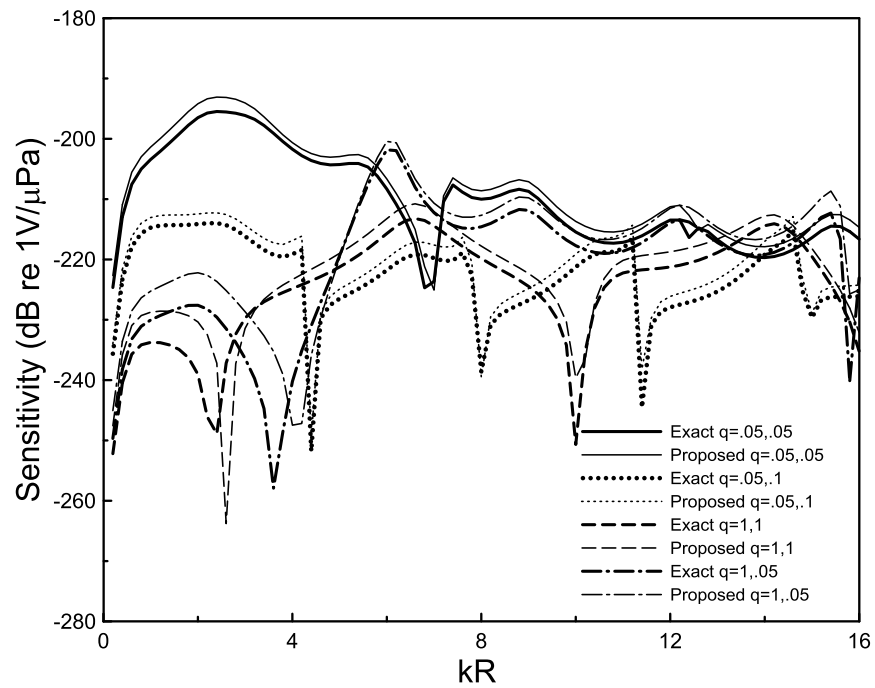
Figure 4.5: PZT sensor sensitivity with different material combinations.
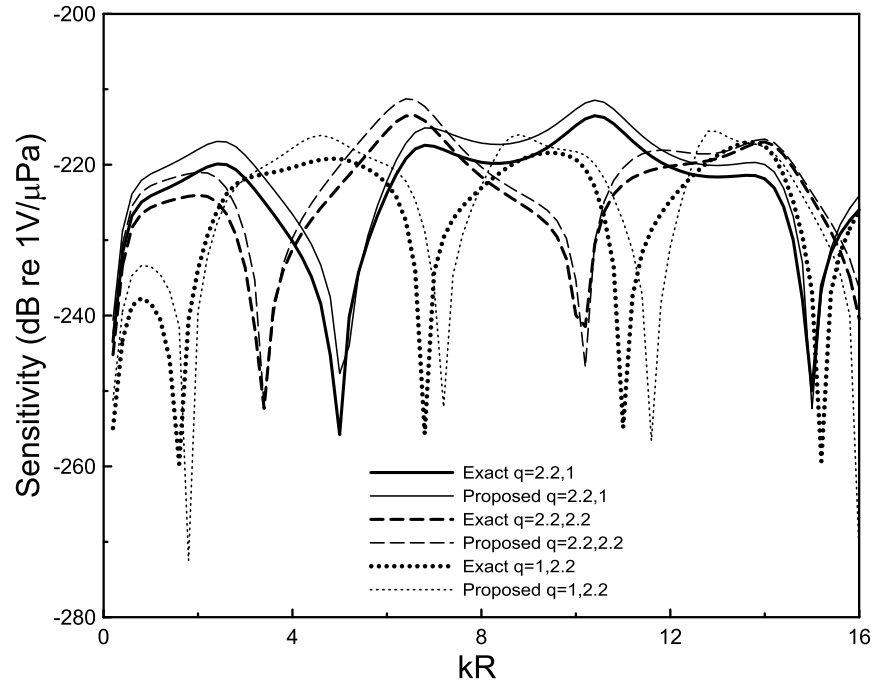
Figure 4.6: PZT sensor sensitivity different material combinations.
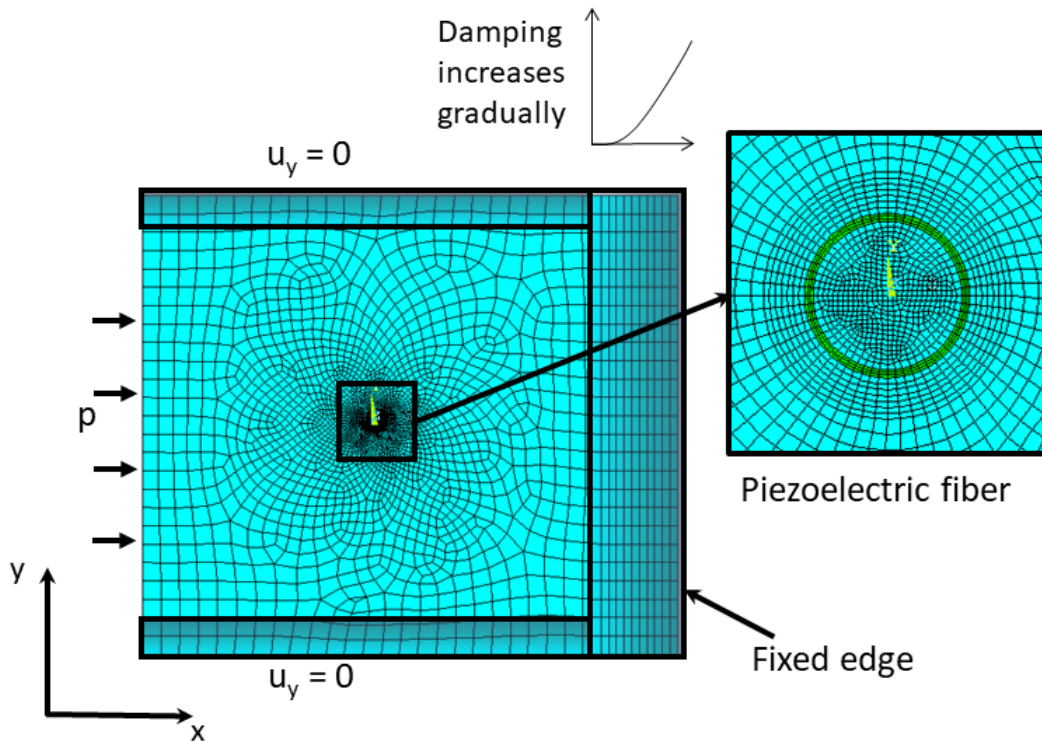
Figure 4.7: Finite Element Model used.
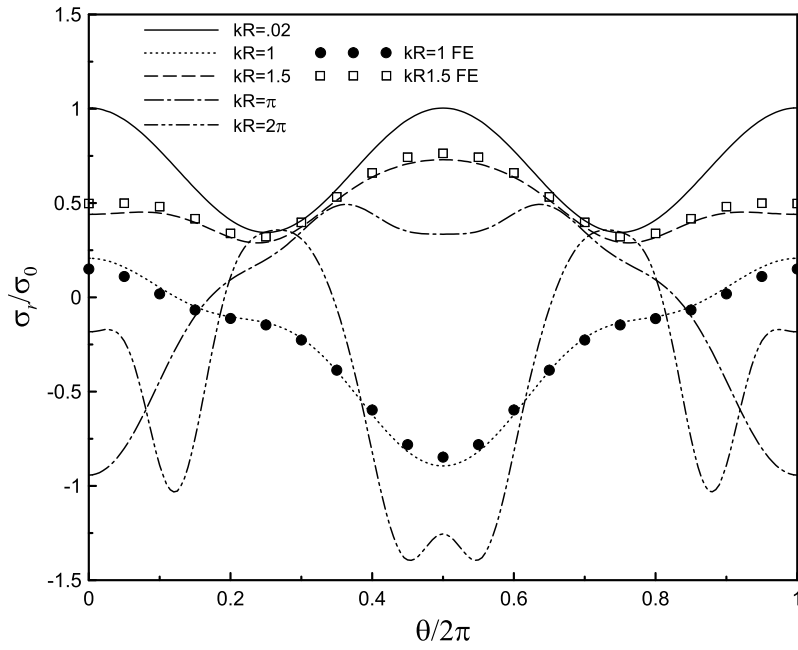
Figure 4.8: Normalized radial stress around the piezoelectric sensor outer interface.
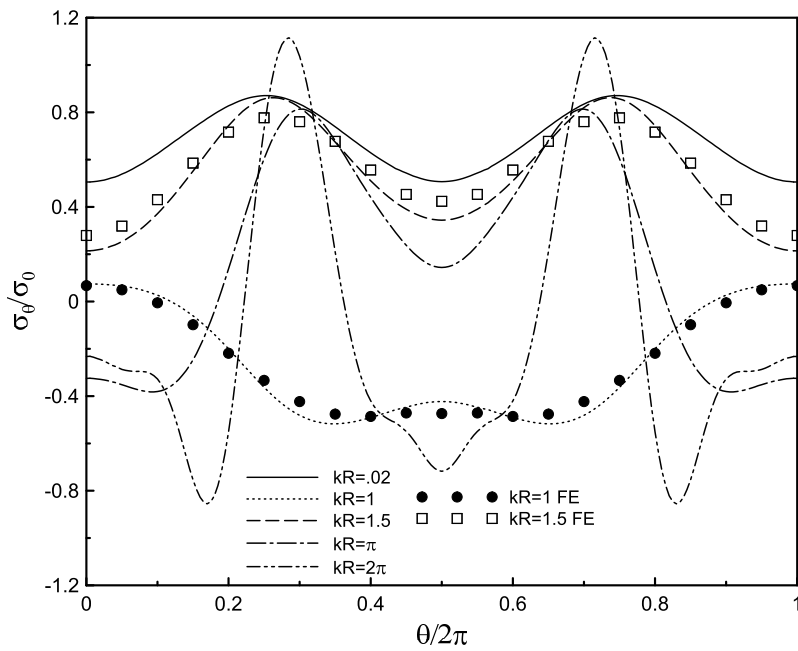
Figure 4.9: Normalized circumferential stress around the piezoelectric sensor outer interface.

95
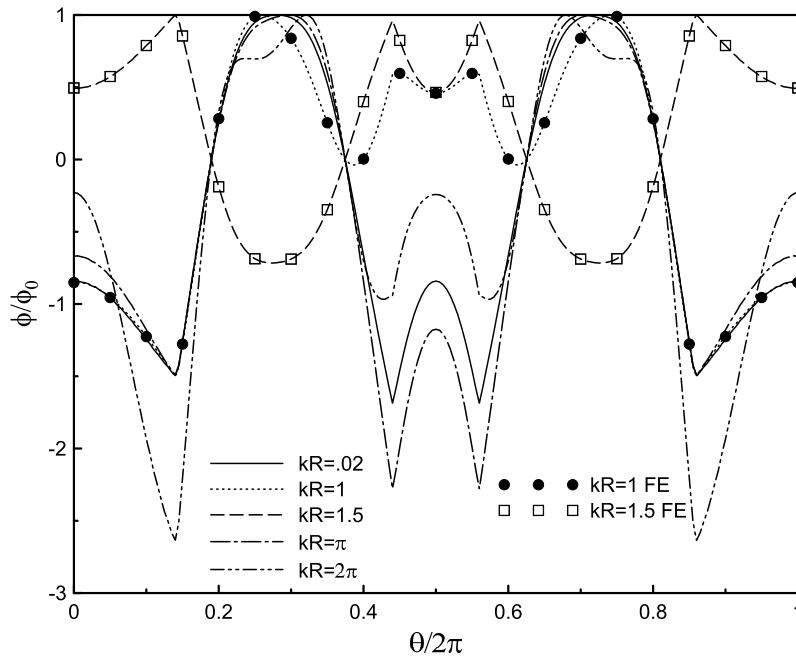
Figure 4.10: Normalized voltage around the piezoelectric sensor outer interface.
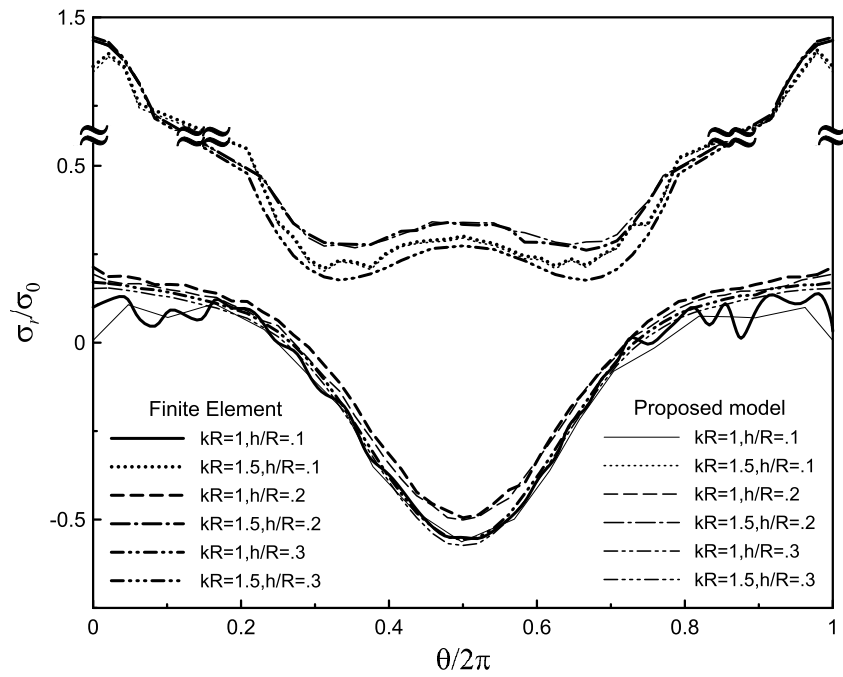
Figure 4.11: Normalized radial stress around the piezoelectric actuator inner interface.
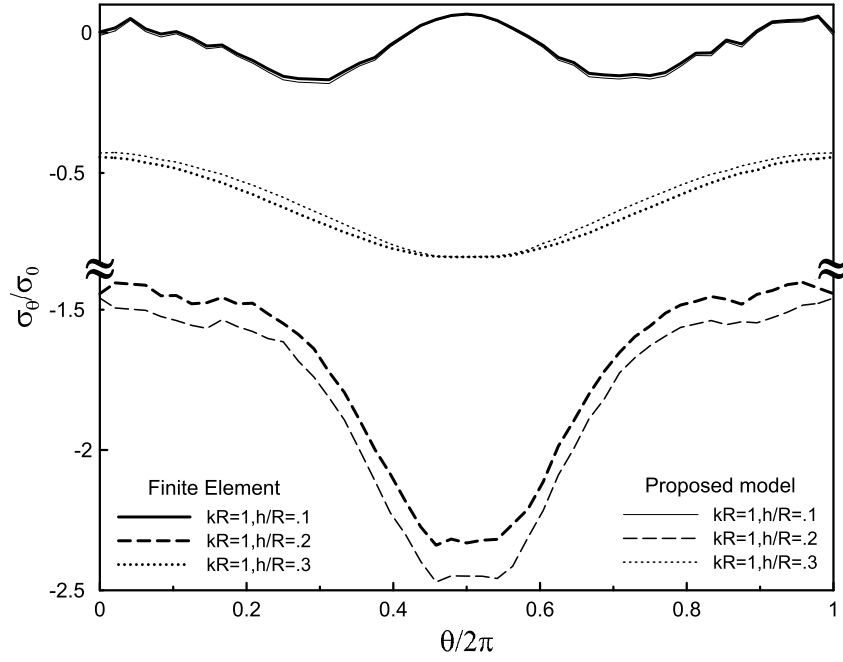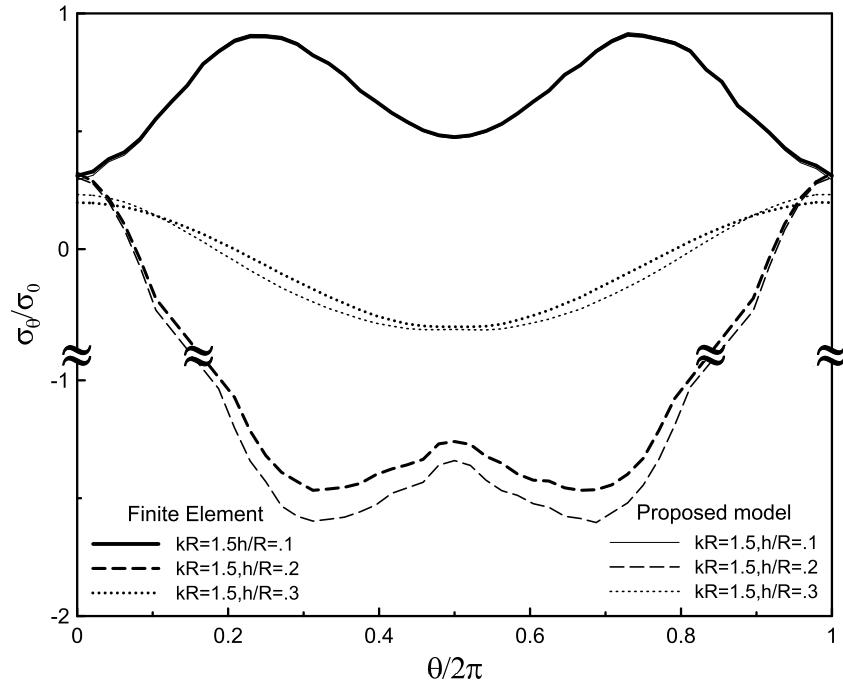
Figure 4.12: Normalized circumferential stress around the piezoelectric actuator inner interface with (a) kR=1 (b) kR=1.5.
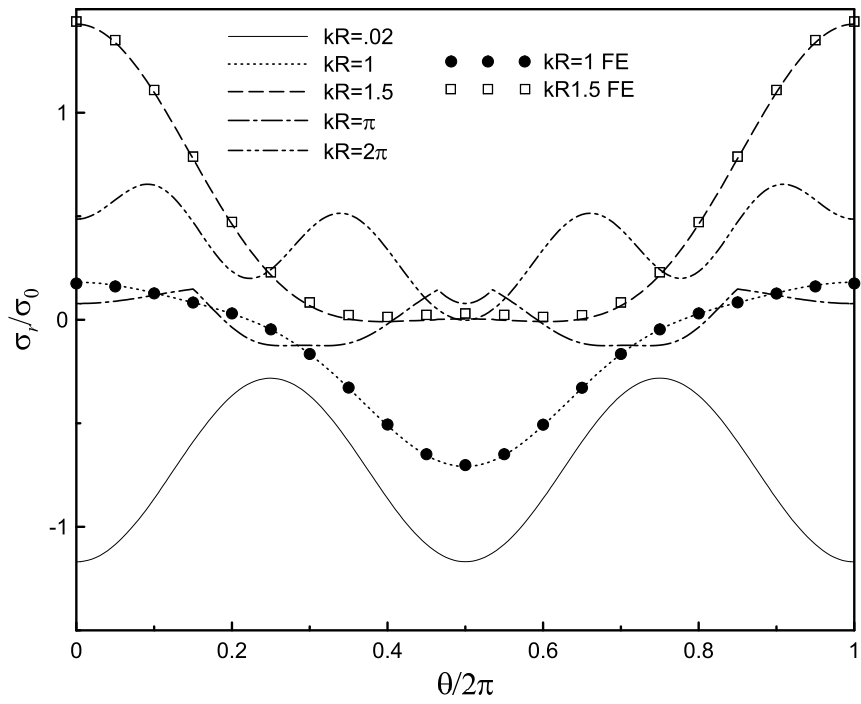
Figure 4.13: Normalized radial stress around the piezoelectric actuator outer interface.
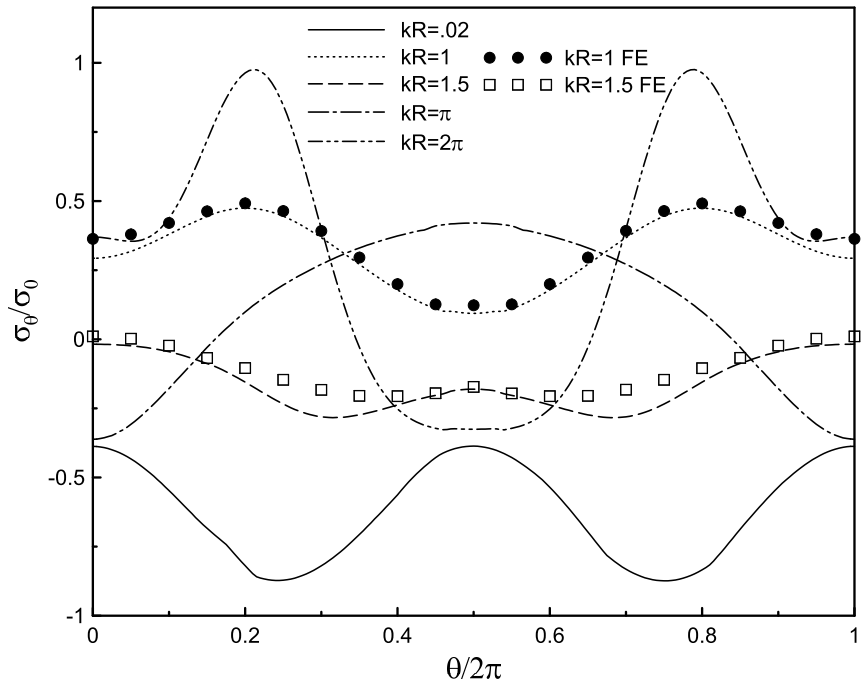
Figure 4.14: Normalized circumferential stress around the piezoelectric actuator outer interface.
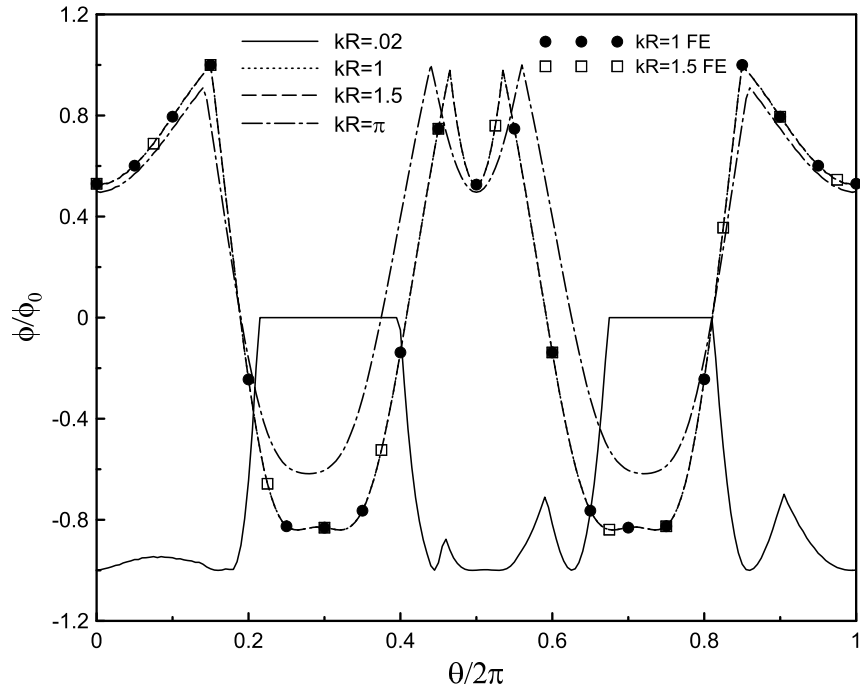
Figure 4.15: Normalized voltage around the piezoelectric actuator outer interface.
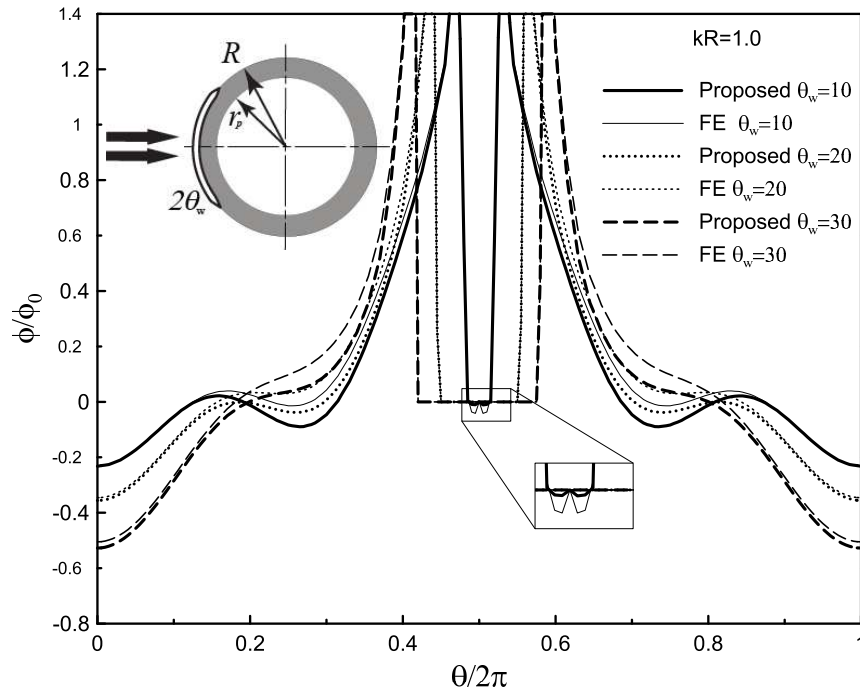
Figure 4.16: Normalized voltage around the piezoelectric sensor outer interface at kR=1.

99
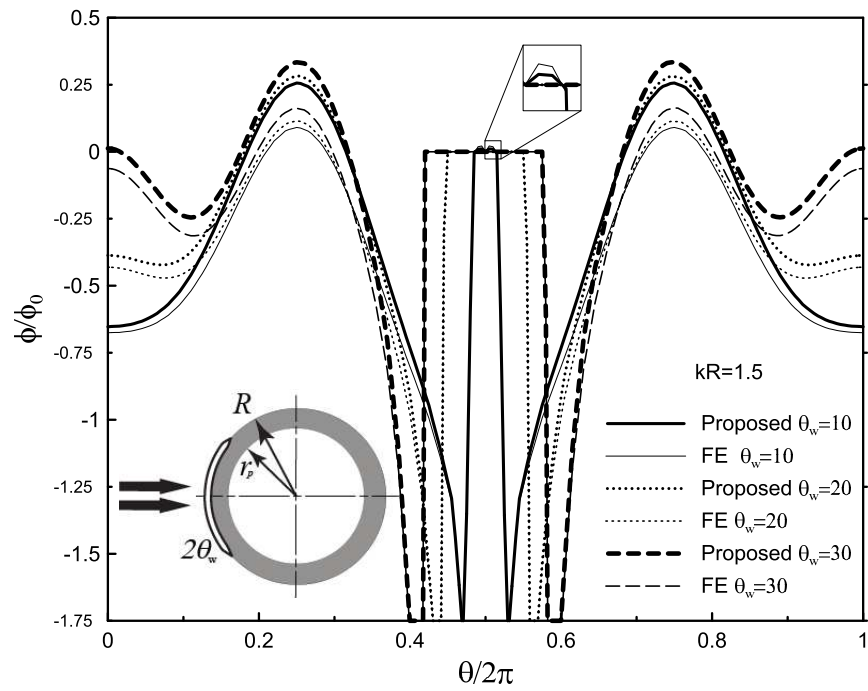
Figure 4.17: Normalized voltage around the piezoelectric sensor outer interface at kR=1.5.

Chapter 5

Multiple wave interactions in multiple multilayered piezoelectric fibers and damages

5.1 Introduction

Multilayered Piezoelectric fibers are considered for use in multifunctional smart structures (Ferreira, Nóvoa, and Marques, 2016; Li et al., 2011; Lin et al., 2013; Saini, Bajpai, and Bajpai, 2013). Unlike the traditional surface bonded piezoelectric fiber composites, where the wave can be applied only from the accessible surface of the structure, the usage of embedded piezoelectric fibers makes it possible to generate and sense elastic waves from other desired positions of the structure providing more reliable detection of the embedded damage. However, the elastic wave field may become very complicated, because of the fact that the wave fields around the multilayered piezoelectric fiber recursively interact redistributing both the mechanical and electric field. The mechanical wave is also generated and sensed by a radially polarized piezoelectric layer and is, therefore, anisotropic in the cross section (Abdel-Gawad and Wang, 2013; Abdel-Gawad and Wang, 2018). It is, therefore, one of the most fundamental issues regarding the use of piezoelectric fibers for the health monitoring of structures is to accurately evaluate the resulting elastic waves.

The interactions of elastic waves in fiber-reinforced composite materials has received considerable attention (Biwa et al., 2004; Bose and Mal, 1973; Bose and Mal, 1974; Sumiya, Biwa, and Haïat, 2013; Varadan, 1978; Varadan and Varadan, 1979; Varadan, Varadan, and Pao, 1978). Two basic approaches were proposed for the multiple scattering of elastic waves using the eigen function expansion method both were proved to be mathematically exact (Liu and Kriz, 1998). One is based on calculating scattering orders in terms of previous scattering orders successively starting with a single scatterer problem (Cai and Williams Jr, 1999; Twersky, 1952). The second approach calculates the scattering wave function for all scatterers boundaries and the boundary conditions are satisfied simultaneously (Bose and Mal, 1973; Bose and Mal, 1974). Various approximation models have been developed to approximate the behavior of elastic wave fields in composites with large number of fibers. The micro-structure in the fiber composite is assumed to be smeared out, resulting in an equivalent homogeneous material with effective elastic properties that are functions of the constitutive properties of the fiber composite. Statistical averaging and different composite constitutive models have been developed to evaluate the effective dynamic properties of fiber reinforced composites (Huang, Rokhlin, and Wang, 1995; Norris and Conoir, 2011; Yang and Mal, 1994). Models based on extending existing fiber composite micro-mechanical static models such as the self-consistent and the generalized self-consistent were also developed to evaluate the equivalent dynamic properties of composites (Nemat-Nasser and Srivastava, 2011; Yang and Mal, 1996). Different models and numerical procedures were proposed for the study of periodic composite structures such as the classical representative volume element (Sun and Vaidya, 1996) or the scatterer polymerization procedure by reducing an assemblage of actual scatterers to a lesser number of scatterers using the T-matrix which can be analyzed using multiple scattering. In the latter procedure, a single actual scatterer is called an element and the scatterer assemblage is called a molecule (Cai and Williams Jr, 1999; Cai and Williams, 1999). The multiple scattering of antiplane

elastic waves (Biwa et al., 2004) and plane waves (Sumiya, Biwa, and Haïat, 2013) in periodic fiber-reinforced composite were analyzed by using Graf's addition theorem with collocation points at the fibers.

The diffraction of acoustic waves by underground circular and cylindrical cavities (Lee and Cao, 1989; Lee and Karl, 1992) and the interaction of waves with arrays of circular cylinders were studied (Linton and Evans, 1990). The diffraction of elastic waves due to multiple scattering around multiple scatterers such rigid inclusions (Cheng, 1969), cavities (Sancar and Pao, 1981; Sancar and Sachse, 1981) and cracks (Meguid and Wang, 2013) was conducted. Existing solutions which account for the dynamic interaction and scattering deal mainly with defects using boundary element method (Manolis and Beskos, 1988; Mykhaskiv, 2005; Rizzo, Shippy, and Rezayat, 1985), Bessel's addition theorem (Lee and Cao, 1989; Lee and Karl, 1992; Martin, 2006), surface integral methods (Varadan, 1978; Varadan and Varadan, 1979; Varatharajulu and Pao, 1976), statistical approximations of effective field methods (Varadan, Varadan, and Pao, 1978), semi-analytical integral equation method (Lee and Chen, 2010), the superposition technique (Meguid and Wang, 1995), and the pseudo incident wave method which used collocation points to obtain the solution of a system of linear equations (Meguid and Wang, 2000; Meguid and Wang, 2013; Wang and Meguid, 1997; Wang and Meguid, 1999; Wang et al., 2015).

In spite of the fact that the multiple interaction of fiber reinforced composite has received considerable attention, only very few published studies treat the electromechanical interaction of wave fields around multilayered piezoelectric fiber subject to plane elastic waves i.e. longitudinal (P-waves) and in-plane shear (Shear Vertical SV-waves). This is due to the difficulties associated with the mode conversions that occur at the boundaries resulting from the coupling of P/SV wave modes in the dynamic equations and to the lack of explicit expression for anisotropic layers. In addition, many available techniques, result in a system of equations which are highly singular

and cannot be solved directly by numerical methods.

It is therefore, the objective of this study is to provide a computationally efficient approach to the time harmonic wave field interaction around multiple multilayered fibers mainly between piezoelectrics and damages or another with interface imperfections under different loading frequency. The analysis is based upon decomposing the wave function using Bessel's addition theorem and an appropriate application of the superposition procedure. By using this procedure, the multiple interaction problem is reduced to single multilayered fiber problems subject to the original wave field. As a result of such reduction, the unknown coefficients of the first order interaction are obtained. The procedure is repeated to obtain the unknown coefficients of higher orders due to the scatter of wave fields producing higher orders of Pseudo incident waves. The present approach not only bridges between different approaches but also increases the numeric stability and provides tools to adjust the desired interaction or circumferential accuracy. Numerical examples are presented to show the effectiveness of the proposed approach in simulating dynamic interaction problems of electromechanical structures under complicated geometries.

5.2   Problem formulation

Consider the interaction between multiple multilayered fibers embedded in a common infinitely large linearly elastic isotropic medium. Each fiber may consist of an arbitrary number of layers perfectly bonded or with an imperfection at their interfaces and lined up with their axes of symmetry coincide with each other such that r is normal to their interfaces. The layers of the fiber are consequently numbered 1, 2, ...N from the central elastic core as illustrated in figure 5.1. The inner radius of a typical layer l is located at $r = r_l$ measured from the center of the fiber. It follows that the thickness of layer l will be $r_{l+1} - r_l$. Each fiber has a local coordinate system with the origin o_j attached
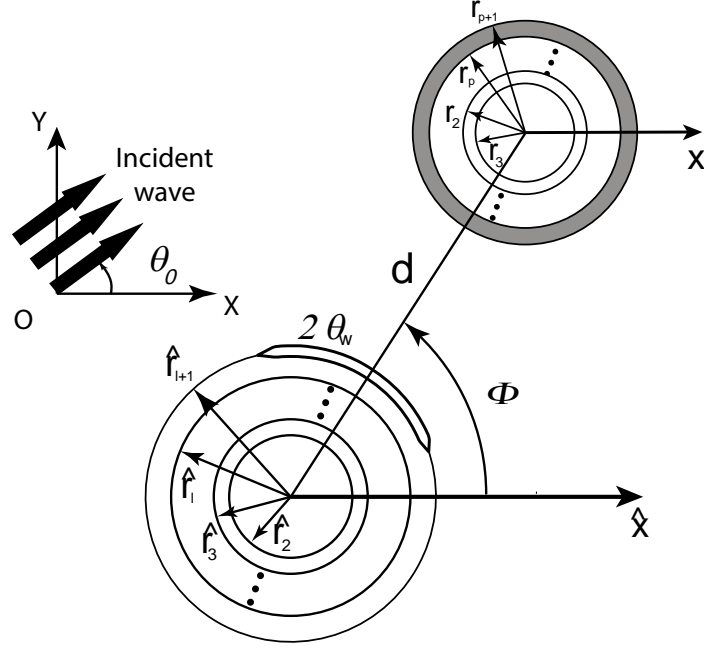
Figure 5.1: Interaction between a multilayered piezoelectric fiber and damages.

to its center. All the layers are linear elastic, homogeneous and isotropic except for the piezoelectric layer is anisotropic. The fibers are long with their axes parallel to each other and cylindrical in cross section. A time harmonic incident wave propagates in a plane that is perpendicular to the axes of the multilayered fibers. The steady-state responses at any location within the host medium are sought.

Since the thickness of the host medium is much larger than the radius fiber, the host medium is modeled as infinite, the host medium is both isotropic elastic and isotropic dielectric in the transverse plane. The elastodynamic and electrostatic fields are not coupled in the transverse plane. The governing equations of the linear elastodynamics behavior of the host medium can be written as

$$(\lambda + 2\mu) \, \boldsymbol{\nabla} \, (\boldsymbol{\nabla} \cdot \mathbf{u}) - \mu \boldsymbol{\nabla} \times (\boldsymbol{\nabla} \times \mathbf{u}) = -\rho \omega^2 \mathbf{u} \, , \qquad (5.1)$$

where $\boldsymbol{\nabla}$ is the gradient operator, λ , μ are the elastic medium Lamé constants, $\mathbf{u}$ is the displacement vector, ρ is the mass density and ω is the angular frequency. The electrostatic equation in terms of electric potential, ϕ,

$$\boldsymbol{\nabla}^2 \phi = 0. \qquad (5.2)$$

105

The displacement field $\mathbf{u}$ can be decomposed into (Achenbach, 1972; Pao, 1983)

$$\mathbf{u} = \boldsymbol{\nabla}\varphi + \boldsymbol{\nabla}\times\boldsymbol{\psi} \qquad (5.3)$$

where φ and ψ are two displacement potentials satisfying Helmholtz equation

$$\left(\boldsymbol{\nabla}^2 + k_L^2\right)\varphi = 0, \ \left(\boldsymbol{\nabla}^2 + k_T^2\right)\psi = 0 \qquad (5.4)$$

k_L and k_T are wave numbers given by

$$k_L = \frac{\omega}{c_L}, \quad k_T = \frac{\omega}{c_T} \qquad (5.5)$$

where c_L and c_T are the longitudinal and transverse wave speeds of the elastic medium,

$$c_L = \sqrt{\frac{\lambda + 2\mu}{\rho}}, \quad c_T = \sqrt{\frac{\mu}{\rho}} \ . \qquad (5.6)$$

The general solutions of the differential equations (5.2) and (5.4) in an isotropic elastic medium with respect to the jth scatterer polar coordinate system $(r,\ \theta)$ using wave-function expansion can be composed of Bessel-Fourier basis,

$$\varphi = \sum_{k=1}^{\infty}\sum_{n=-\infty}^{\infty}\left(H_n^{(1)}(k_L r) \ _j^o A_n^{L,k} + J_n(k_L r) \ _j^i A_n^{L,k}\right)e^{in\theta}e^{-i\omega t}, \qquad (5.7)$$

$$\psi = \sum_{k=1}^{\infty}\sum_{n=-\infty}^{\infty}\left(H_n^{(1)}(k_T r) \ _j^o A_n^{s,k} + J_n(k_T r) \ _j^i A_n^{s,k}\right)e^{in\theta}e^{-i\omega t}, \qquad (5.8)$$

$$\phi = \sum_{k=1}^{\infty}\sum_{n=-\infty}^{\infty}\left(H_n^{(1)}(k_e r) \ _j^o A_n^{e,k} + J_n(k_e r) \ _j^i A_n^{e,k}\right)e^{in\theta}e^{-i\omega t}, \qquad (5.9)$$

where $J_n\left(.\right)$ is Bessel function of the first kind, $H_n^{(1)}\left(.\right)$ is Bessel function the third kind also known as Hankel function of the first kind, $i = \sqrt{-1}$ is the unit complex number, A_n are unknown coefficients, the left hand subscript represent the jth scatterer, the subscript n is the circumferential order and k is the interaction order. When wave functions (Bessel-Fourier) are combined with the time factor, $e^{-i\omega t}$, the direction of the wave functions is established using large argument asymptotic, the outgoing sub-wave amplitudes are $_j^o A_n$ and the incident/transmitted sub-wave amplitudes are $_j^i A_n$

with the left hand superscript representing direction (Bogan and Hinders, 1994). Sub-waves refer to the potential mechanical displacements and the electric potentials in equations (5.7)-(5.9). The temporal factor $e^{-i\omega t}$ has established the direction and will be suppressed from here-after. The following subsections explain, the wave interaction effects inside the host medium exterior to a scatterer and the interaction inside the scatterer interior.

5.3 Multiple wave interactions

The multilayered piezoelectric fibers and/or multilayered fiber with or without imperfection will be collectively referred to as scatterers. The use of fully coupled system would produce a very large system and is numerically ill-conditioned due to coupling with circumferential orders. A single scatterer or piezoelectric fiber contains 6 field variables and if Bessel-Fourier series are truncated after 80 terms then the produced coupled system would be of $80 \times 6 \times N$ and N represents number of scatterers.

In multiple scatterers embedded in a host medium subject to a time harmonic wave field, the multiple scatterer problem can be decomposed into simpler subproblems involving one of the scatterers as shown in figure 6.3. These subproblems will be further decomposed to study further interactions then all will be summed up to provide the superimposed solution of the original problem. Considering one of the scatterers, scatterer j as the nominal scatterer, this scatterer is subject to a Pseudo incident wave field which consists of the original incident wave field inside the host medium and all the unknown scattering from all of the other scatterers,

$$\{_j\mathbf{W}\} = \{_j^{in}\mathbf{W}\} + \sum_{\substack{s=1 \\ s \neq j}}^{N} \{_s^{sc}\mathbf{W}\} \text{ at } S_j \tag{5.10}$$

where the effects of this Pseudo incident inside the jth scatterer

$$\{_j\mathbf{W}\} = \{_j^{tr}\mathbf{W}\} - \{_j^{sc}\mathbf{W}\} \text{ at } S_j, \tag{5.11}$$

$$\{\mathbf{W}\} = \begin{bmatrix} u_r & u_\theta & \sigma_r & \sigma_{r\theta} & \phi & D_r \end{bmatrix}^T, \tag{5.12}$$

$\{_j^{in}\mathbf{W}\}$ represents the original incident wave field originating from infinity, $\{_j^{tr}\mathbf{W}\}$ represents the scatter wave field radiating from the scatterer, $\{_j^{tr}\mathbf{W}\}$ represents the transmitted wave field inside the scatterer, S_j represents the interface of scatterer j with the host and the left hand subscript representing scatterer number starting with 1. For each scatterer the exterior host medium incident wave as well as all the scatter from all the other scatterers form the Pseudo incident waves with respect to the scatterer's coordinate system origin point o_j.

The interaction can be further decomposed into interaction orders, k, with each interaction order representing the response of a scatterer to the previous excitations. The first interaction order is due to the original incident wave field and it represents the response of each scatterer, $\{_j\mathbf{W}^1\}$, isolated as a single scatterer as shown in figure 6.3 subproblem (b). The scattered wave field, $\{_s^{sc}\mathbf{W}^1\}$, of each scatterer is calculated to be used as a Pseudo incident wave field. The second interaction order response, $\{_j\mathbf{W}^2\}$, is due to the calculated scattering as a Pseudo incident wave field, $\{_s^{sc}\mathbf{W}^1\}$, of all the other scatterers on the considered scatterer as shown in figure 6.3 subproblem (c). The procedure is repeated, with the kth interaction order response, $\{_j\mathbf{W}^k\}$, is calculated from the previously calculated scatter, $\{_s^{sc}\mathbf{W}^{k-1}\}$, of all the other scatterers as shown in figure 6.3 subproblem (d). The interaction order can be represented mathematically as

$$\{_j\mathbf{W}^1\} = \{_j^{in}\mathbf{W}\}, \ k=1 \tag{5.13}$$

$$\{_j\mathbf{W}^k\} = \sum_{\substack{s=1 \\ s \neq j}}^{N} \{_s^{sc}\mathbf{W}^{k-1}\}, \ k \geq 2 \tag{5.14}$$

and the total incident wave field on the jth scatterer inside the host medium and on its interface

$$\sum_{k=1}^{\infty} \{_j\mathbf{W}^k\} = \{_j^{in}\mathbf{W}\} + \sum_{k=2}^{\infty} \sum_{\substack{s=1 \\ s \neq j}}^{N} \{_s^{sc}\mathbf{W}^{k-1}\}. \tag{5.15}$$
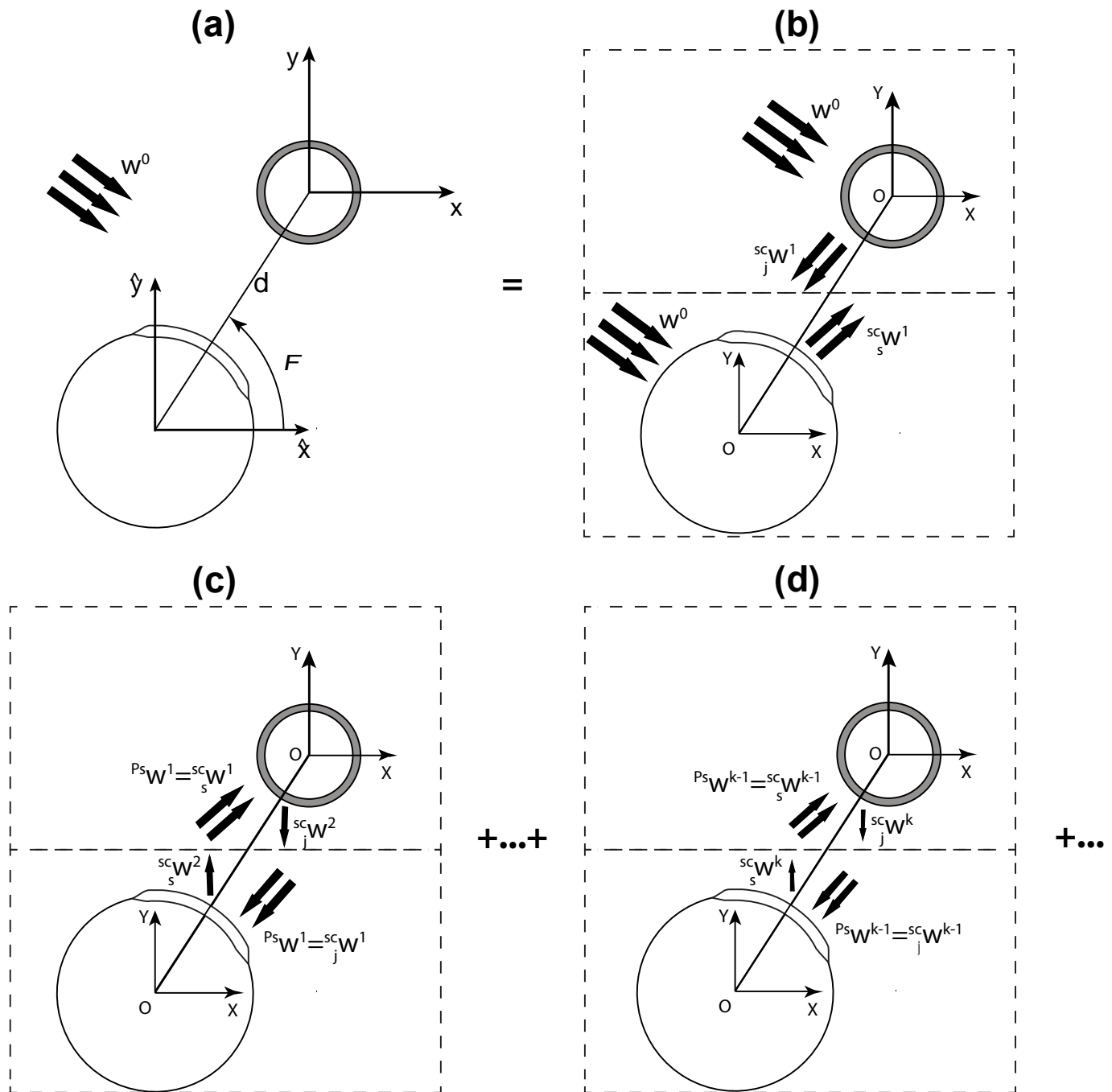
Figure 5.2: Higher interaction orders of Pseudo Incident Wave.

5.3.1 Multiple wave interactions inside the host medium

The Pseudo incident wave field inside the host medium, equation (5.15) with respect to the local coordinates of the jth scatterer can be written in terms of the admissible field given by equations (5.7)-(5.9) inside the host medium as

$$\sum_{k=2}^{\infty} \{_{j}^{Ps}\mathbf{W}^{k-1}\} = \sum_{k=2}^{\infty} \sum_{\substack{s=1 \\ s \neq j}}^{N} \xi_j \left(\sum_{m=-\infty}^{\infty} [\hat{\mathbf{H}}_m^q] e^{im\hat{\theta}} \right) \{_{s}^{sc}\mathbf{A}_m^{k-1}\} \tag{5.16}$$

where ξ_j is a transformation operator which transforms the scattering coefficients matrix $[\hat{\mathbf{H}}_m^q]$ from its local coordinate to the jth coordinates and $\{_{s}^{sc}\mathbf{A}_m^{k-1}\} = \{ \ _s^{o}A_n^{c,k} \ \ _s^{o}A_n^{s,k} \ \ _s^{o}A_n^{e,k} \ \}^T$ satisfying the radiation condition for each scatterer in its local coordinate system. The matrix is given in the appendix. The transformation operator decomposes the wave function in one polar $(\hat{r}, \hat{\theta})$ coordinate to another (r, θ) (shown in figure 5.1)(Lee and Karl, 1992; Martin, 2006) based on Graf's addition theorem (Abramowitz and Stegun, 1965; Watson, 1995)

$$H_m^{(1)}(k_w \hat{r}) e^{im\hat{\theta}} = \sum_{n=-\infty}^{\infty} \begin{cases} J_n(k_w r) H_{m-n}^{(1)}(k_w d) e^{i(m-n)\Phi} e^{in\theta}, & r < d \\ H_n^{(1)}(k_w r) J_{m-n}(k_w d) e^{i(m-n)\Phi} e^{in\theta}, & r > d \end{cases} \tag{5.17}$$

$H^{(1)}(.)$, $J(.)$ are Hankel first kind and Bessel first kind functions respectively, k_w is a generic scaling wave-number. On applying Graf's addition theorem, equation (5.17), equation (5.16) can be written as

$$[_{s,j}\hat{\mathbf{H}}_m^q] e^{im\hat{\theta}} = \sum_{n=-\infty}^{\infty} [\mathbf{J}_n^q][_{s,j}\mathbf{S}_{m-n}] e^{i(m-n)\Phi_s^j} e^{in\theta} \tag{5.18}$$

where

$$[\mathbf{J}_n^q] = \begin{bmatrix} k_L J_n'(k_L r) & \frac{in}{r} J_n(k_s r) & 0 \\ \frac{in}{r} J_n(k_L r) & -k_s J_n'(k_s r) & 0 \\ [\mathbf{J}_n]_{3,1} & [\mathbf{J}_n]_{3,2} & 0 \\ [\mathbf{J}_n]_{4,1} & [\mathbf{J}_n]_{4,2} & 0 \\ 0 & 0 & \tilde{J}_n(r) \\ 0 & 0 & \tilde{J}_n'(r) \end{bmatrix}, \tag{5.19}$$

$$[\mathbf{J}_n]_{3,1} = J'_n(k_L r) k_L \frac{\lambda}{r} + J''_n(k_L r) k_L^2 (\lambda + 2\mu) - J_n(k_L r) n^2 \frac{\lambda}{r^2}, \quad [\mathbf{J}_n]_{3,2} = \left(\frac{J_n(k_s r)}{r} - J'_n(k_s r) k_s \right) \frac{2\mu i n}{r},$$

$$[\mathbf{J}_n]_{4,1} = \frac{2\mu i n}{r} \left(J'_n(k_L r) k_L - \frac{J_n(k_L r)}{r} \right), \quad [\mathbf{J}_n]_{4,2} = \mu \left(-J''_n(k_s r) k_s^2 - J(k_s r) \frac{n^2}{r^2} + J'_n(k_s r) \frac{k_s}{r} \right),$$

$$[_{s,j}\mathbf{S}_{m-n}] = \begin{bmatrix} H_{m-n}(k_L d) & 0 & 0 \\ 0 & H_{m-n}(k_s d) & 0 \\ 0 & 0 & H_{m-n}(k_e d) \end{bmatrix}, \tag{5.20}$$

$[_{s,j}\mathbf{S}_{m-n}]$ is the separation matrix representing the separation distance between the two coordinates. The nth Pseudo incident wave is

$$\{_j^{Ps}\mathbf{W}^{k-1}\} = \sum_{\substack{s=1 \\ s \neq j}}^{N} \sum_{m=-\infty}^{\infty} \sum_{n=-\infty}^{\infty} [\mathbf{J}_n^q][_{s,j}\mathbf{S}_{m-n}]_s^{sc}\mathbf{A}_m^{k-1} e^{i(m-n)\Phi_s^j} e^{in\theta}. \tag{5.21}$$

Although this analysis uses Graf's theorem for $r < d$ the method is not limited and other forms of (equations (5.17)) Graf theorem's can be directly applied. Since this is a steady state all scattering orders have already excited all scatterers.

5.3.2 Multiple wave interactions inside the anisotropic and imperfect layers of the fiber

The piezoelectric layer is transversely anisotropic in the cross section since it is poled in the radial direction and the piezoelectric is coupled. To overcome these difficulties a piezoelectric layer model is adopted (Abdel-Gawad and Wang, 2013; Abdel-Gawad and Wang, 2018). The model couples all circumferential orders around imperfect layers using an adapted global transfer matrix for each scatterer.

The jth scatterer's inner central layer satisfies equations (5.7)-(5.9) since it is an isotropic elastic layer and the wave field on the jth scatterer interface with the host medium can be written as

$$\{_j\mathbf{W}^k\} = \sum_{n=-\infty}^{\infty} [_j\mathbf{G}_{n,m}] \{_j^T\mathbf{A}_n^k\} e^{in\theta} \tag{5.22}$$
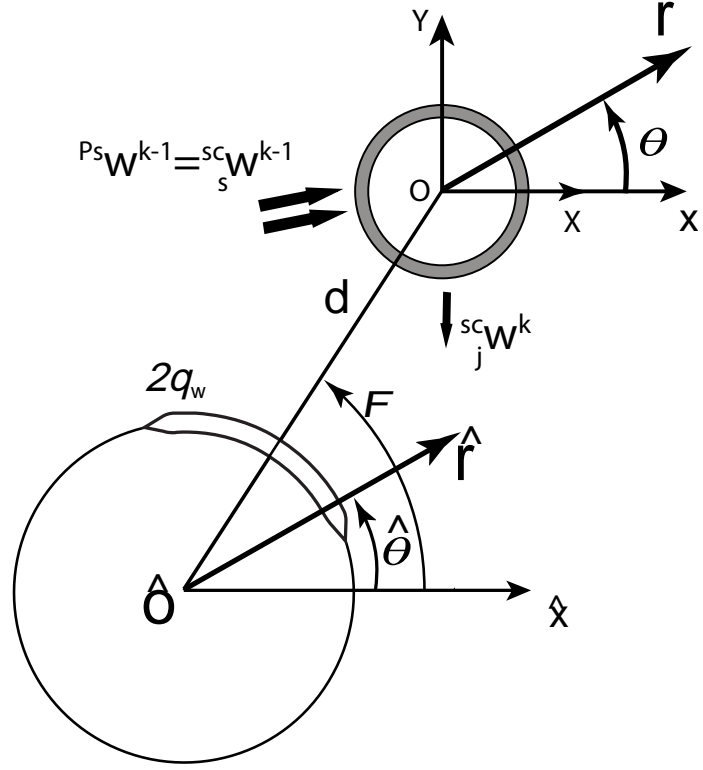
Figure 5.3: Interaction between two piezoelectric multilayered fibers.

where $[_j\mathbf{G}_{n,m}]$ is the jth scatterer consolidated transfer matrix (Abdel-Gawad and Wang, 2018) representing its scattering and the consolidated transmission properties given by

$$
[_j\mathbf{G}_n] =
\begin{bmatrix}
-[\mathbf{H}_n^{(q-)}]_{1,1} & -[\mathbf{H}_n^{(q-)}]_{1,3} & -[\mathbf{H}_n^{(q-)}]_{1,5} & [\mathbf{T}_{s+}^{(q-)}]_{1,2} & [\mathbf{T}_{s+}^{(q-)}]_{1,4} & [\mathbf{T}_{s+}^{(q-)}]_{1,6} \\
-[\mathbf{H}_n^{(q-)}]_{2,1} & -[\mathbf{H}_n^{(q-)}]_{1,3} & -[\mathbf{H}_n^{(q-)}]_{1,5} & [\mathbf{T}_{s+}^{(q-)}]_{2,2} & [\mathbf{T}_{s+}^{(q-)}]_{2,4} & [\mathbf{T}_{s+}^{(q-)}]_{2,6} \\
-[\mathbf{H}_n^{(q-)}]_{3,1} & -[\mathbf{H}_n^{(q-)}]_{1,3} & -[\mathbf{H}_n^{(q-)}]_{1,5} & [\mathbf{T}_{s+}^{(q-)}]_{2,2} & [\mathbf{T}_{s+}^{(q-)}]_{3,4} & [\mathbf{T}_{s+}^{(q-)}]_{3,6} \\
-[\mathbf{H}_n^{(q-)}]_{4,1} & -[\mathbf{H}_n^{(q-)}]_{1,3} & -[\mathbf{H}_n^{(q-)}]_{1,5} & [\mathbf{T}_{s+}^{(q-)}]_{2,2} & [\mathbf{T}_{s+}^{(q-)}]_{4,4} & [\mathbf{T}_{s+}^{(q-)}]_{4,6} \\
-[\mathbf{H}_n^{(q-)}]_{5,1} & -[\mathbf{H}_n^{(q-)}]_{5,3} & -[\mathbf{H}_n^{(q-)}]_{5,5} & [\mathbf{T}_{s+}^{(q-)}]_{2,2} & [\mathbf{T}_{s+}^{(q-)}]_{5,4} & [\mathbf{T}_{s+}^{(q-)}]_{5,6} \\
-[\mathbf{H}_n^{(q-)}]_{6,1} & -[\mathbf{H}_n^{(q-)}]_{6,3} & -[\mathbf{H}_n^{(q-)}]_{6,5} & [\mathbf{T}_{s+}^{(q-)}]_{2,2} & [\mathbf{T}_{s+}^{(q-)}]_{6,4} & [\mathbf{T}_{s+}^{(q-)}]_{6,6}
\end{bmatrix},
$$

$$
\underbrace{\hspace{4cm}}_{\text{Host medium scattering}} \quad \underbrace{\hspace{4cm}}_{\text{Consolidated transmission}}
$$

(5.23)

where $\{_j^T\mathbf{A}_n^k\}$ is a vector combining the scattered unknowns as well as the transmitted

112

unknown coefficients given by

$$\{{}_j^T\mathbf{A}_n^k\} = \left\{ \begin{array}{cc} \{{}_j^{sc}\mathbf{A}_n^k\} & \{{}_j^{tr}\mathbf{A}_n^k\} \end{array} \right\}^T \tag{5.24}$$

and $\{{}_j^{tr}\mathbf{A}_n^k\} = \{ \begin{array}{ccc} {}_j^iA_n^{c,k} & {}_j^iA_n^{s,k} & {}_j^iA_n^{e,k} \end{array} \}^T$ of the jth scatterer and the superscript $(q-)$ indicates evaluation at that interface. The consolidated transmission coefficients contain properties of the scatterer interior.

The solution is determined by the recursive application of boundary conditions on each scatterer by substituting equations (5.22) and (5.21) into equations (5.13), (5.14) and (5.15),

$$\sum_{n=-\infty}^{\infty} [{}_j\mathbf{G}_n] \{{}_j^T\mathbf{A}_n^k\} e^{in\theta} = \{{}_j^{in}\mathbf{W}\} + \{{}_j^{Ps}\mathbf{W}^{k-1}\}, \tag{5.25}$$

for each scatterer for each interaction and the total solution will be the sum

$$\sum_{k=1}^{\infty} \sum_{n=-\infty}^{\infty} [{}_j\mathbf{G}_n] \{{}_j^T\mathbf{A}_n^k\} e^{in\theta} = \{{}_j^{in}\mathbf{W}\} + \sum_{k=2}^{\infty} \{{}_j^{Ps}\mathbf{W}^{k-1}\}. \tag{5.26}$$

The use of complex exponential orthogonality $e^{in\theta}$ or collocation is possible. The proposed approach allows the scatterers to have any interior structure such as multi-layered fibers since it provides higher orders of wave fields exterior to the scatterer.

5.4 Results and discussion

In this section, the results of multiple multilayered piezoelectric fibers interactions embedded in a media with or without imperfections, represented in figure 5.1, is considered. The attention will be focused on (i) the validation of the developed interaction approach and (ii) the usage of this interaction model for evaluating the stress distribution in multi-layered media under different loading and geometric conditions. A few numerical examples to show the accuracy of the model rather than a full comprehensive

parametric study since the considered problem has many parameters. To implement the boundary conditions, the incident wave must be expressed with the respect to each scatterer's coordinate system while maintaining its relative phase, the incident wave on scatterer s with its coordinates attached to its center located at (x_s, y_s) with respect to the jth scatterer coordinate system

$$\varphi^0 = I e^{ik_L r \cos(\theta - \theta_0)}, \tag{5.27}$$

where the phase factor I is being

$$I = e^{ik_L \left(x_s \cos\theta_0 + y_s \sin\theta_0\right)}.$$

5.4.1 Limiting cases

In the limiting cases of the multilayered fibers are voids or rigidities, the problem were solved in the generalized plane stress. The problem is same as plane strain except for replacing λ by $\lambda' = 2\lambda\mu/(\mu + 2\lambda)$ in plane stress. The normalized stress σ/σ_0 is dependent upon the dimensionless wave number $k_L R$ and Poisson's ratio. For the case of voids, Poisson's ratio is chosen to be 0.35 and the dimensionless wave number is chosen at 0.2. For the rigidities case, Poisson's ratio is chosen to be 0.25 and the dimensionless wave number is chosen at 0.1. The results for the voids and rigidities at the third order interaction order under $k_L R = .2$ show an excellent agreement with the corresponding results obtained by Cheng (1969) and Cheng (1972) respectively as shown in figure 5.4 and 5.5. The number of interaction orders considered in the limiting cases were three orders and it was sufficient as shown with the excellent agreement in the examples.

5.4.2 Multilayered fibers

In the following discussion, the piezoelectric layer material is P(VDF-TrFE) and the host medium material is Polycarbonate as shown in table 6.1 with two embedded types

of damages a void and a crack. Figures 5.6 shows the normalized voltage on the piezo-electric layer interface ($\phi_0 = \dfrac{h_{33}}{c_{33}} h\sigma_0$ is the normalization voltage around the interface) at a relative frequency of $kR = 1$ for a circular void with radius R placed at an angle $\Phi = 10°$ various distances d_{12} from the center (0,0) of the piezoelectric layer, results show excellent agreement with the finite element as a further verification. The radius of the piezoelectric layer is the same as the radius of the void R and k is the host medium wave number. The same excellent agreement is shown in figures 5.7 and 5.8 for normalized radial and circumferential stresses at the piezoelectric interface with the host medium.

Another type of damage was also verified against finite element, a curved crack, results show an excellent agreement at $d_{12} = 5.5R$ however this is not the case for a very closely placed crack as shown in figures 5.9 to 5.11. Figures 5.9 to 5.11 show normalized voltage, radial stress and circumferential stress on the interface between a piezoelectric layer and the host medium with an embedded crack at $kR = 1$. The curved crack parameters are R which is the radius of the crack with its center varies at distances d_{12} from the center of the piezoelectric layer, angled at $\Phi = 10°$ and starts at an angle of 170° and ends with 190°.

A perfectly bonded one piezoelectric layered fiber sensor with radius r_s was placed at a distance $d_s = 30r_d$ from two horizontally spaced damages with radii r_d such that $r_s = .1r_d$ and the separation distance between the centers of the two damages d_d changes as shown in figure 5.12. The piezoelectric fiber is placed far from the damages to ensure the sensed volts are not interacting with the damaged scatterers and the generated signal by the piezoelectric fiber actuators is an incident P-wave. The results in figures 5.13-5.16 show that the amplitudes of the normalized volts sensed are very sensitive to the angular position of the piezoelectric fiber represented by the incident wave angles θ_0, loading frequency, and to the distance between the scatterers. The simulations were conducted with nine interactions orders ensuring convergence and that the interaction

Material	Elastic Constants $\times 10^{10}$(N/m^2)					Density 10^3 (kg/m^3)	Piezoelectric $\times 10^0$(C/m^2)				Permittivity $\times 10^{-9}$(C/Vm)	
	c_{11}	c_{33}	c_{12}	c_{13}	c_{55}	ρ	e_{31}	e_{32}	e_{33}	e_{24}	ϵ_{33}	ϵ_{11}
isotropic	$\lambda+2\mu$	λ	λ	μ								
Polycarbonate	.554	.554	.298	.298	.128	1.18	-	-	-	-	.03	.03
P(VDF-TrFE)	.47	.45	.257	.213	.12	1.3	.045	.037	-.18	-.1	.1	.01

Table 5.1: Materials used in this study.

scattered signal has died with the interaction order at which the signal died. The angles of the piezoelectric fiber are taken to simulate a signal actuated and sensed by an array of piezoelectric fibers surrounding two damages. Results also show that in most cases a third order interaction is sufficient even when the scatterers shade each other with the exception of very close proximity damages since interaction increases when scatterers are in a close proximity to each other. The recommended relative frequency for a strong detectable signal usually starts at $kr_d > 1$ and for piezoelectric fiber angled at $\theta_0 = -90$ or $\theta_0 = 0$ is about $kr_d \simeq 1.5$.

5.5 Conclusions

A new general approach is provided to the dynamic interaction of multilayered piezo-electric fiber and an imperfect bonded multilayered fiber under a plane wave. The analysis is based upon the use of eigen function expansion. The approach works when the damages are in a close proximity to each other and/or to sensors as well as for the case of far distanced damages. The validity and versatility of the present solution have been demonstrated in a unified manner by application to some specific examples. The examples discussed two types of damages however the proposed approach is general and can be easily extended to other types of damages. Numerical results of the voltage output for different configurations and frequencies are determined and analyzed. The configuration, the location of piezoelectric fibers, the location of damages, size of the damages and the loading frequencies show complicated effects on the sensed output

voltage. The sensed output voltage, yet complicated but, is very sensitive to damage characteristics. The sensed voltage on the piezoelectric layer due to a void is not as high as that of a crack which makes the identification of a void more difficult. It is also sufficient to consider the second order interaction specially if the damage is not very close to all the sensors.
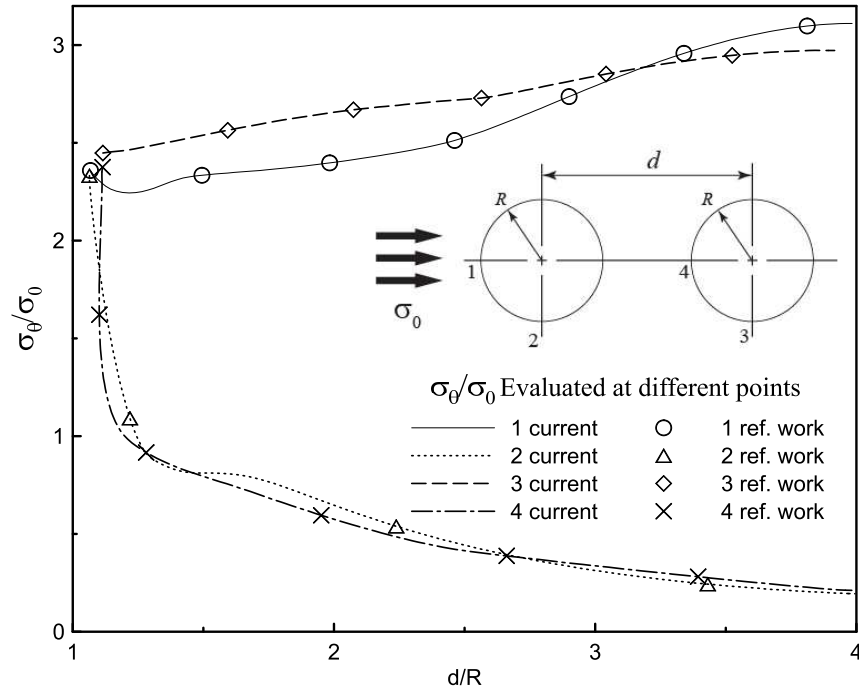
Figure 5.4: Normalized circumferential stress at different points under kR=.2 for current study versus Cheng (1972) work for interacting voids.
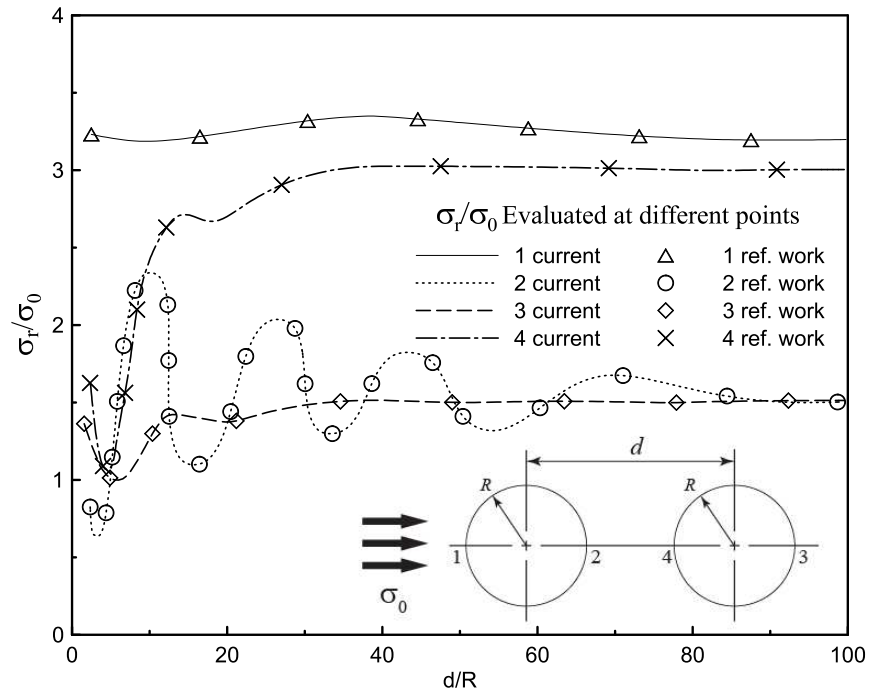
Figure 5.5: Normalized radial stress at different points under kR=.2 for current study versus Cheng (1969) work for rigidities.
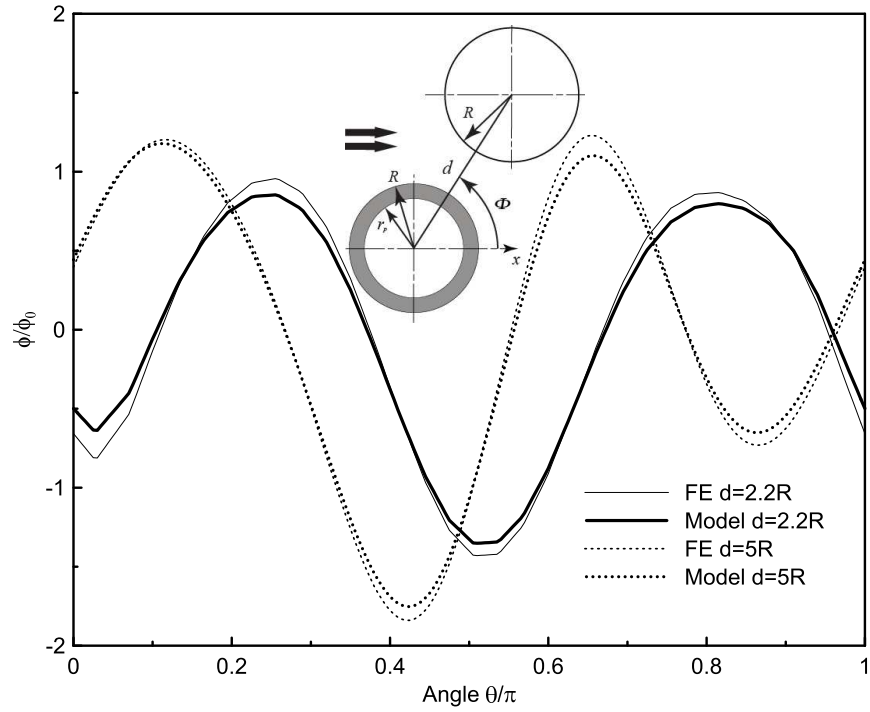
Figure 5.6: Piezoelectric voltage at the interface of a piezoelectric fiber with a host medium with an embedded void at different distances.
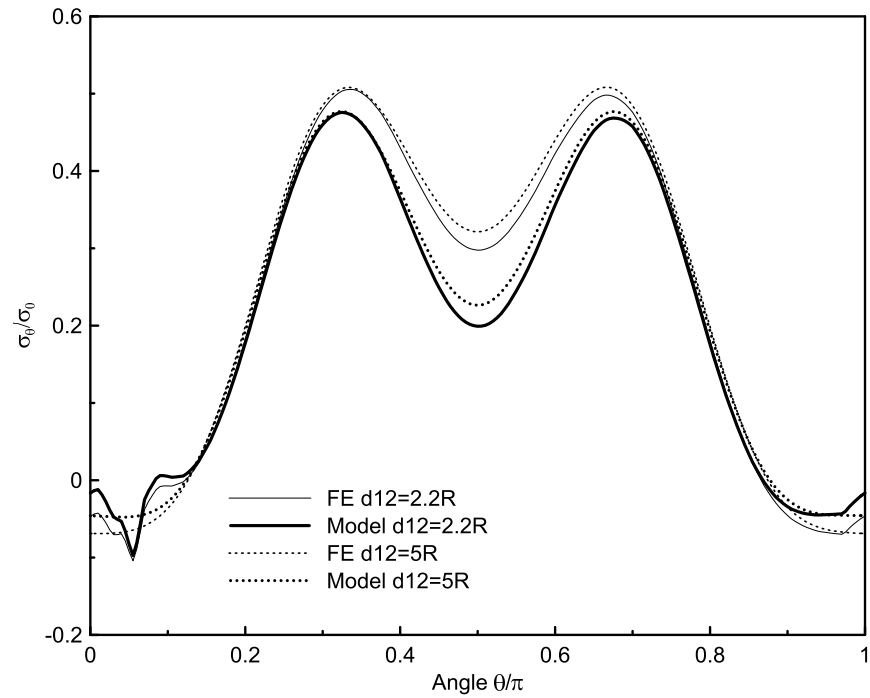
Figure 5.7: Normalized radial stress at the interface of a piezoelectric fiber with a host medium with an embedded void at different distances.
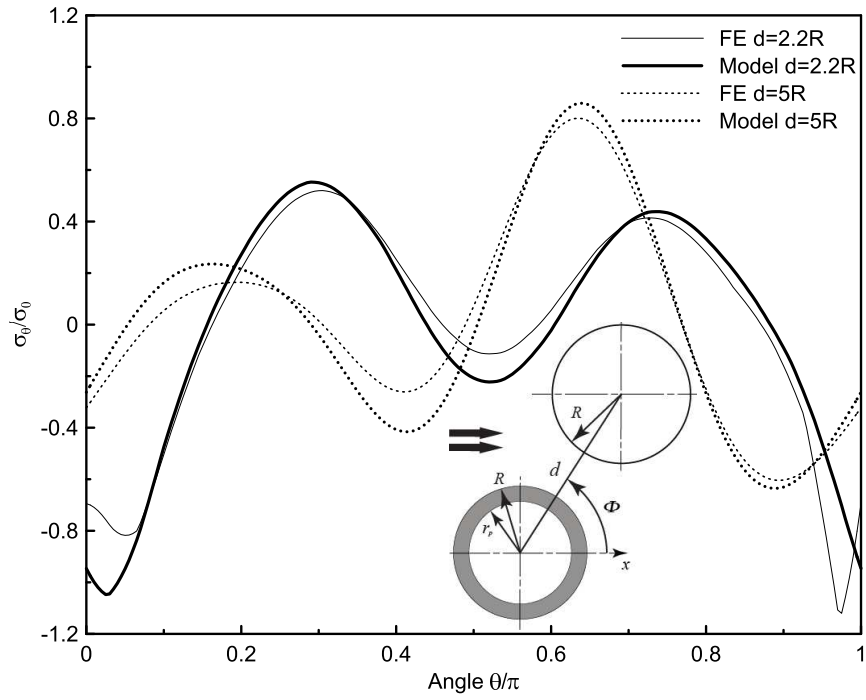
Figure 5.8: Normalized circumferential stress at the interface of a piezoelectric fiber with a host medium containing an embedded void at different distances.
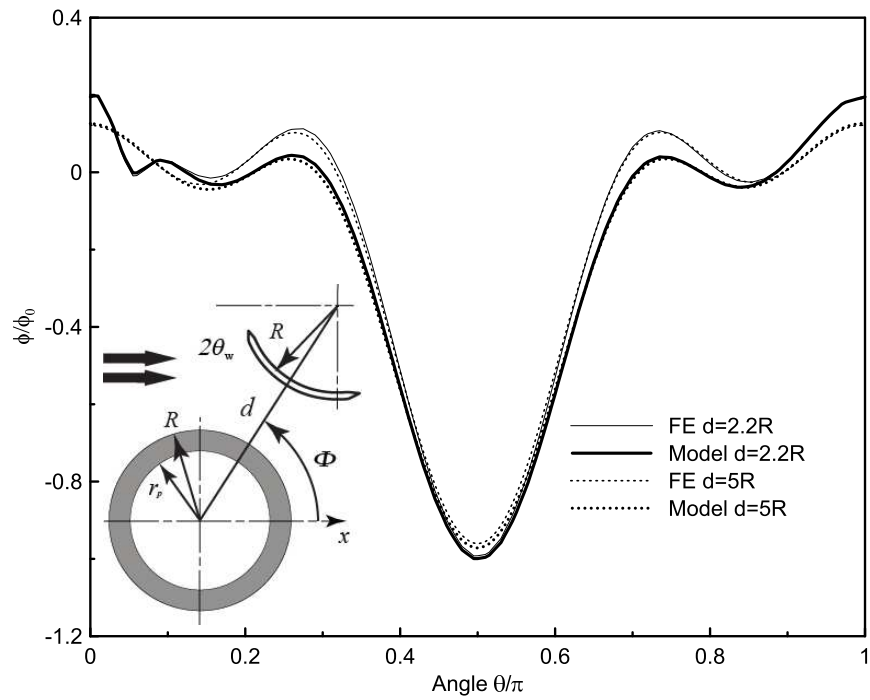
Figure 5.9: Normalized voltage at the interface of a piezoelectric fiber with a host medium containing a crack at different distances.
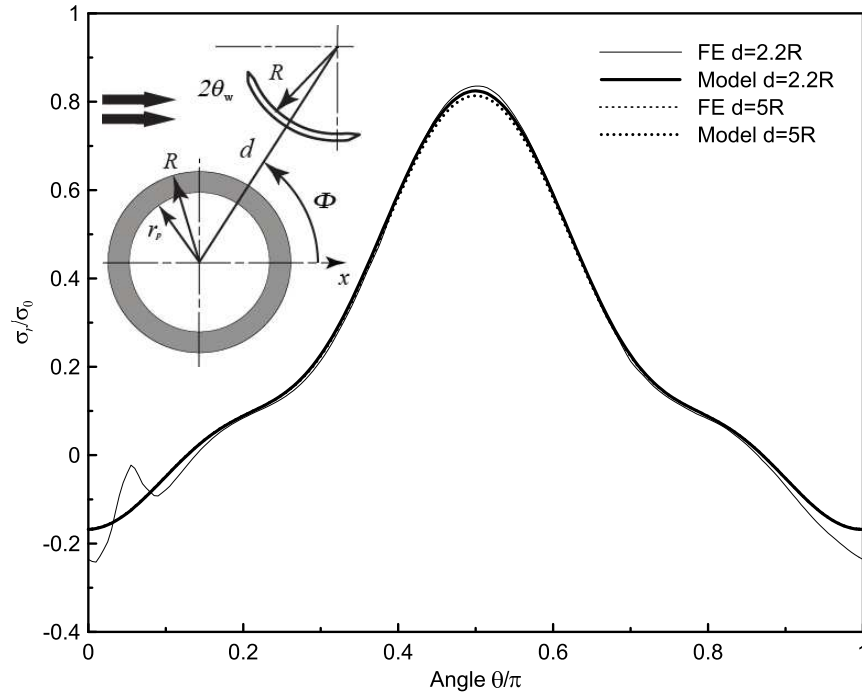
Figure 5.10: Normalized radial stress at the interface of a piezoelectric fiber with a host medium containing an embedded crack at different distances.
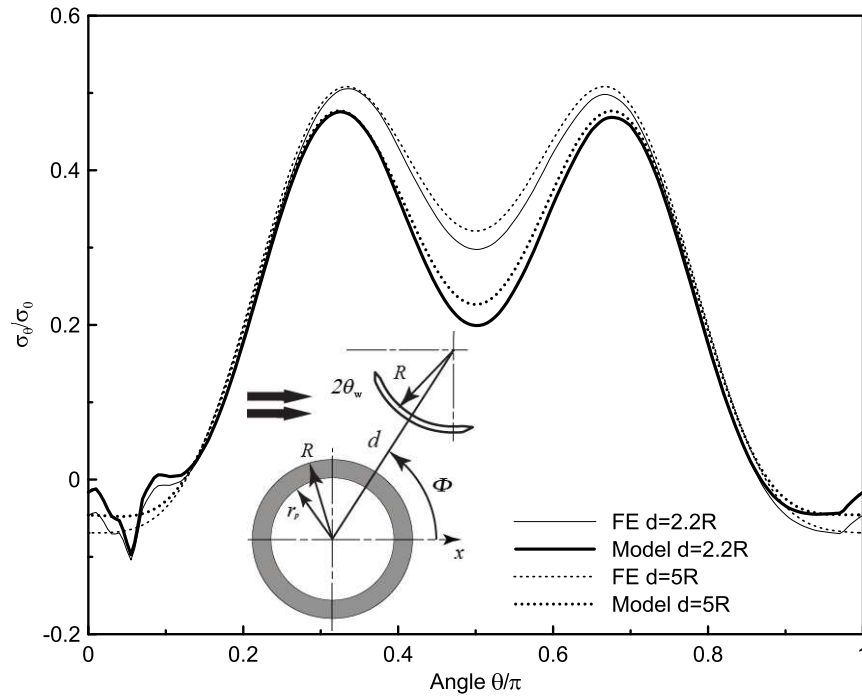
Figure 5.11: Normalized circumferential stress at the interface of a piezoelectric fiber with a host medium containing an embedded crack at different distances.
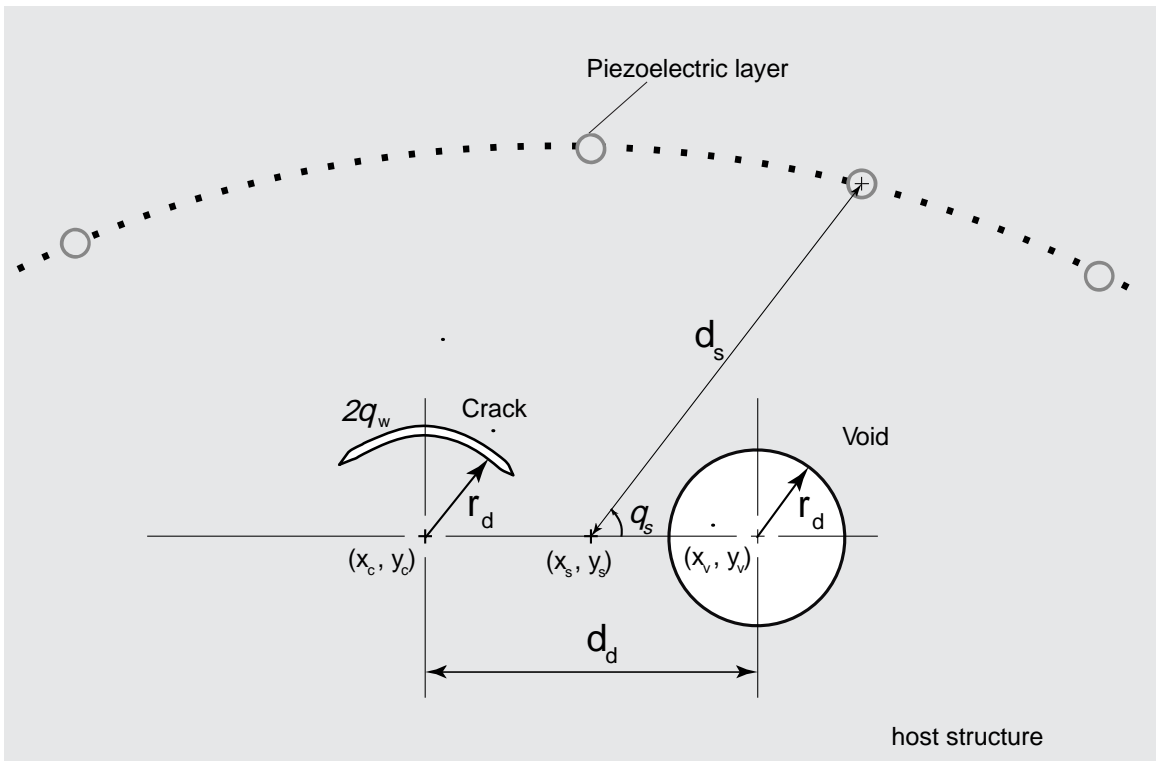
Figure 5.12: An array of piezoelectric fibers and two damages.
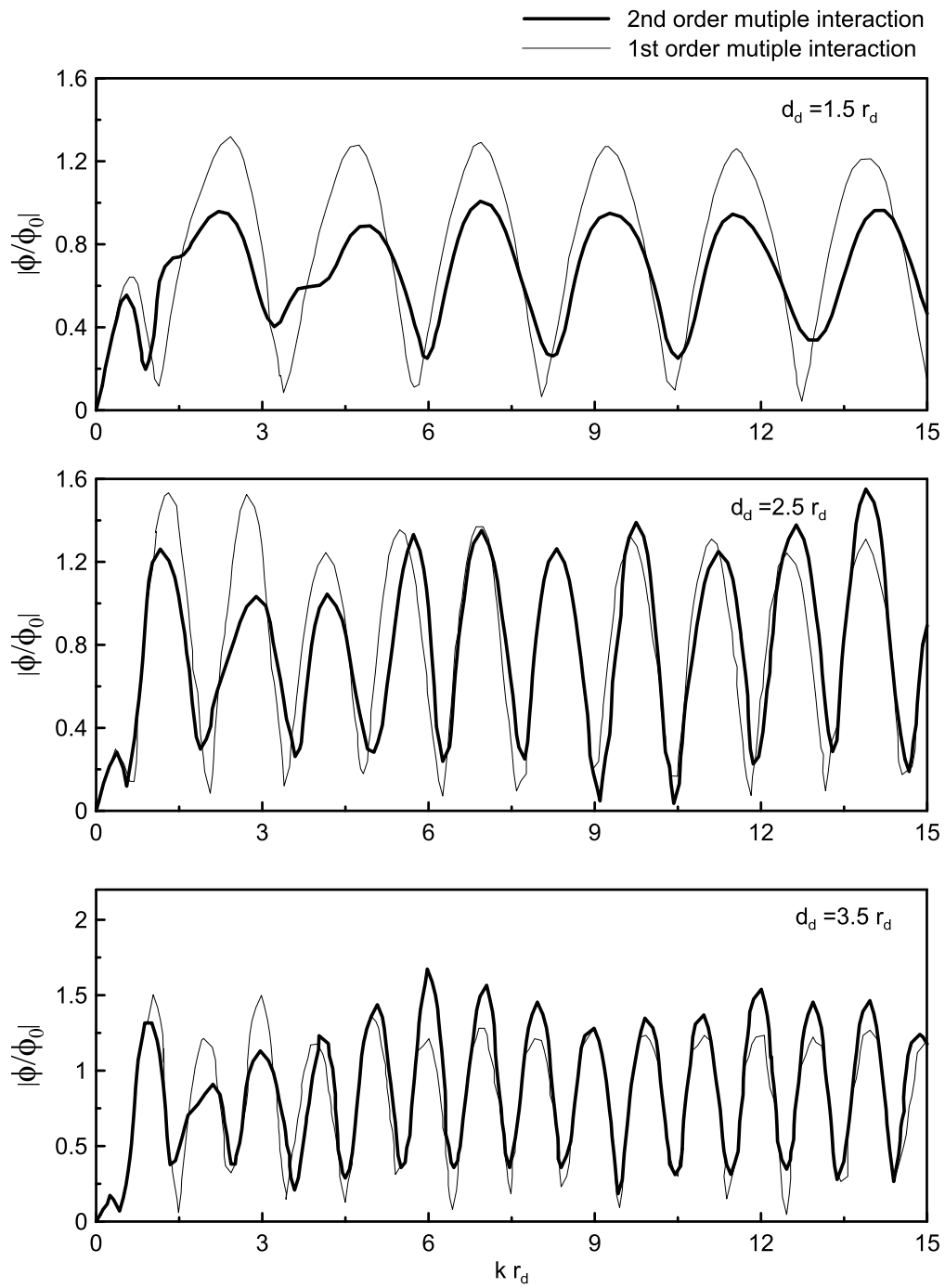
Figure 5.13: Normalized voltage of a piezoelectric fiber sensor angled at $\theta_0 = 30$ from differently spaced damages.

123
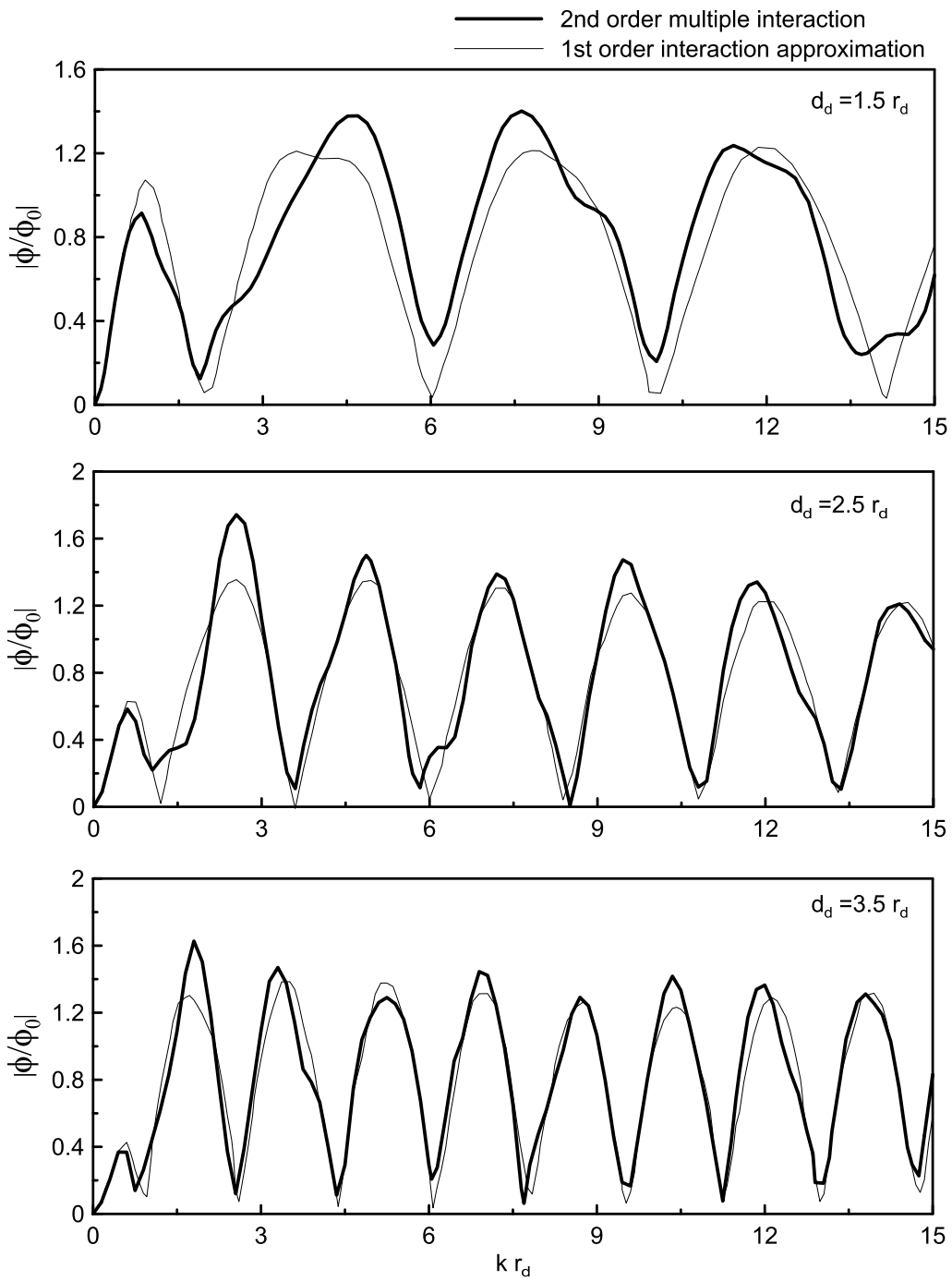
Figure 5.14: Normalized voltage of a piezoelectric fiber sensor angled at $\theta_0 = 60$ from differently spaced damages.

124
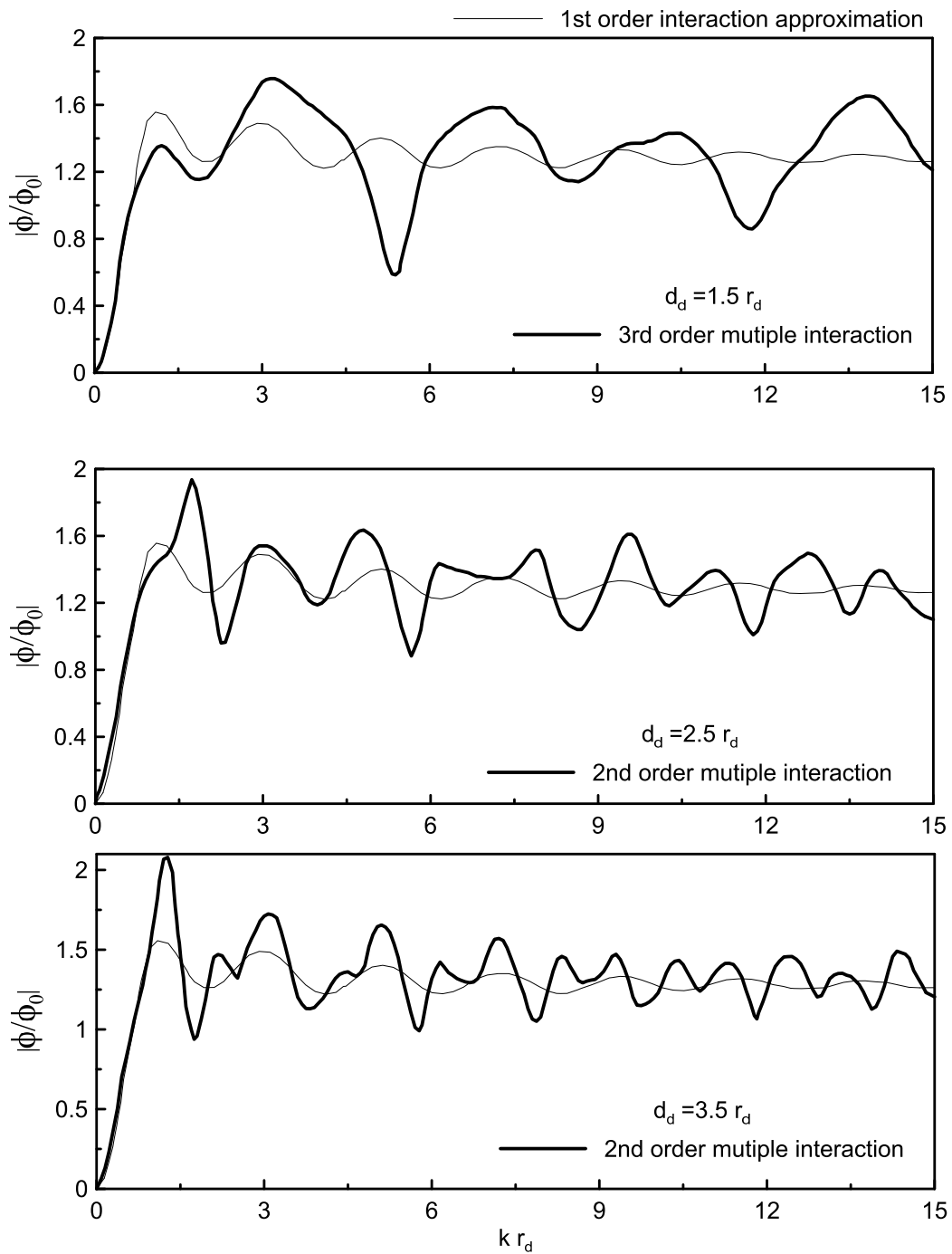
Figure 5.15: Normalized voltage of a piezoelectric fiber sensor angled at $\theta_0 = 90$ from differently spaced damages.
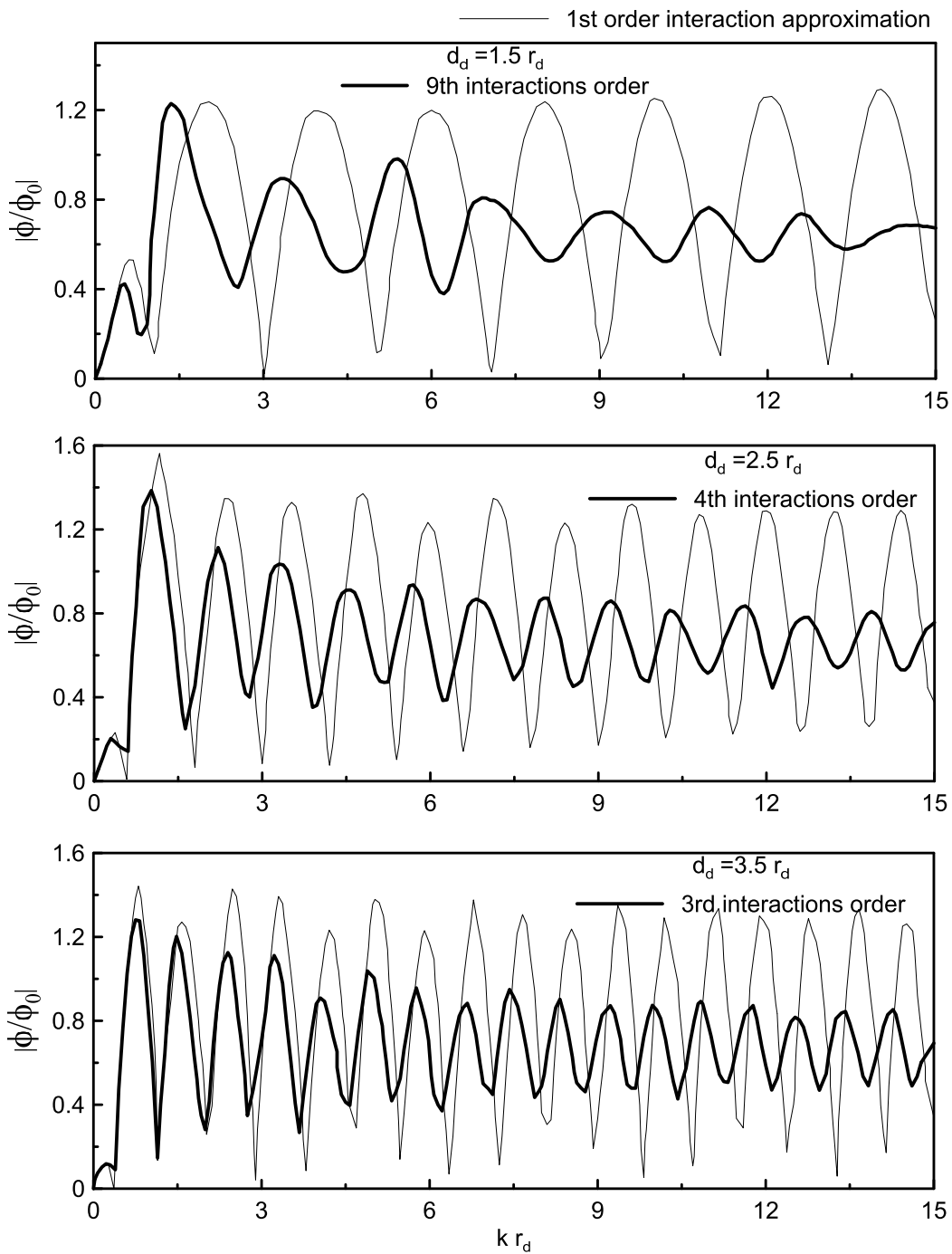
Figure 5.16: Normalized voltage of a piezoelectric fiber sensor angled at $\theta_0 = 0$ from differently spaced damages.

126

Chapter 6

Simulation for damages identification using an array of multilayered piezoelectric fibers

6.1 Introduction

Structural health monitoring and structural damage identification has attracted significant attention due to its importance in predicting and preventing catastrophic failures specially in critical structures (Das, Saha, and Patro, 2016; Doebling, Farrar, Prime, et al., 1998; Fan and Qiao, 2011; Lee and Dhital, 2013; Sohn et al., 2004; Su, Ye, and Lu, 2006). Elastic waves have been successfully used in damage identification and nondestructive evaluation of structures (Achenbach, 2000; Drinkwater and Wilcox, 2006; Giurgiutiu and Cuc, 2005; Schmerr, 2013). Various damage identification techniques were developed, with two main mechanical approaches that have relatively large damage coverage: one is based on vibration (Das, Saha, and Patro, 2016; Doebling, Farrar, Prime, et al., 1998; Fan and Qiao, 2011) and the other is based on elastic wave (Fritzen, Schulte, and Jung, 2011; Kessler, Spearing, and Soutis, 2002; Ostachowicz and Kudela, 2011; Raghavan and Cesnik, 2007). Vibration based approaches are relatively insensitive to local small damage and its vibration signals are hypersensitive to the surrounding environment and therefore, it lacks reliability and accuracy in estimating

small damages (Su, Ye, and Lu, 2006; Zhu, Huang, and Yuan, 2013). In a typical elastic based damage identification process (Huang, Song, and Wang, 2010; Wang and Huang, 2004b), actuators generate a diagnostic elastic wave in the structure. When damages are encountered, the wave is reflected and the corresponding response of the structure is measured using a system of sensors. The analysis is conducted on the measurements or recorded signals to identify the damage and the problem is formulated as an inverse problem or a system identification (Sirca Jr and Adeli, 2012). Different analysis methods have been developed to identify damage in structures from discrete measurement locations. A typical method of analysis is to directly compare the characteristic parameters of the measured signals with those of a damage free structure as a reference baseline to identify changes and therefore, potential damages (Achenbach, 2000; Giurgiutiu, 2000). Other methods of analysis which are not based on pre-known reference measurements of damage free structure have been reported (Anton, Inman, and Park, 2009; Sohn et al., 2007; Sohn et al., 2004).

Structural damage identification problem is an inverse problems, in which the measurements of the structure such as sensor readings are available, whereas the damage size, location and/or the structure physical properties are unknown. Inverse problems are difficult to solve, mainly because they behave nonlinearly and are often characterized by ill-posedness (Colton and Kress, 2012; Liu and Han, 2003). The solution of the inverse problem, based on optimization schemes, consists of an iterative process of solving the direct problem with the objective of minimizing the error between the recorded measurements on sensors and the predicted quantities of the direct problem. The iteration process is used to identify the damage parameters and/or updating the candidate model physical properties of the direct problem according to the optimization algorithm. The iterative process continues on minimizing the objective error such that the algorithm converges to the true or the best damage parameters.

The objective of this study is to identify multiple damages in a structure from

their developed voltage on an array of multilayered piezoelectric fiber sensors due to the electro-mechanical interaction between the array and the unknown damage. The recorded voltage measurements on the array of the multilayered piezoelectric fiber sensor in response to the unknown damage parameters will be simulated using a finite element model while the iterative calculations are conducted using a multiple interaction model as the direct problem (previous chapters). Two types of damages, voids and cracks, are discussed and presented in the numerical solution to illustrate the effectiveness of the proposed scheme in identifying multiple damages under sensors reading noise and with damages having irregular shapes. The embedded damage parameters including shape and location will then be estimated through minimizing the difference of the known voltage output and that determined in the developed interacting sensor/damage solution.

6.2   Problem Formulation

The problem investigated is to identify the unknown damage characteristics through the known voltage signals from an array of embedded multilayered piezoelectric fiber sensors when the structure is subjected to a time-harmonic incident wave. The array of multilayered piezoelectric fibers is long and embedded in an infinite elastic isotropic host medium in which the damages are to be identified, as shown in figure 6.1. There are two types of damage idealization models 1) circular voids and 2) curved cracks as shown in figure 6.2 to allow for the best fitting to an actual irregularly shaped void and crack. The parameters of a typical circular void are its radius r_v and the location of its center (x_v, y_v) while the parameters of a typical curved crack are its radius r_c, location of its center (x_c, y_c), starting θ_1 and ending θ_2 angles. The piezoelectric layer in any of the multilayered piezoelectric fiber array is radially polarized and therefore it is anisotropic in the transverse direction. The damaged host structure contains irregularly shaped

voids and/or cracks embedded in an isotropic infinite medium which corresponds to the case that damages are far from the boundaries. These damages are to be identified to the best fit circular void and/or cracks.

The damage identification problem is formulated as an inverse problem in which the sensor voltage readings are known while the damages locations and sizes are unknown. The solution of the inverse problem consists of the repeated solutions of the direct problem while changing damage parameters according to both an intelligent predesigned genetic and a non-linear gradient optimizer algorithm. A two-stage optimization framework is developed by combining the strengths of a newly developed predesigned intelligent genetic and a nonlinear gradient optimization strategies. The newly developed genetic algorithm as well as the Broyden–Fletcher–Goldfarb– Shanno (BFGS) algorithm are used to minimize the error between the experimental voltage readings on sensors and the calculated voltage from the direct problem solution.

Inverse problems can be solved by first guessing the missing information, solving the forward problem, and then repeatedly updating the guess in the forward model until the simulated system response best fits the measurements recorded by the sensors. In the following sub-sections, the formulation of the direct and of the inverse problems are discussed.

6.2.1   The direct problem

The direct problem is to simulate the voltage output along the piezoelectric layer in response to damages embedded under time-harmonic loading. The solution of a field variable $\hat{\mathbf{W}}$ (displacement, and stress) can be expressed in terms of the loading frequency ω as

$$\hat{\mathbf{W}} = \mathbf{W}e^{-i\omega t} \tag{6.1}$$

where $i = \sqrt{-1}$, t and ω are being the imaginary number, time and circular frequency, respectively. For convenience, the time factor $e^{-i\omega t}$ will be suppressed and only the
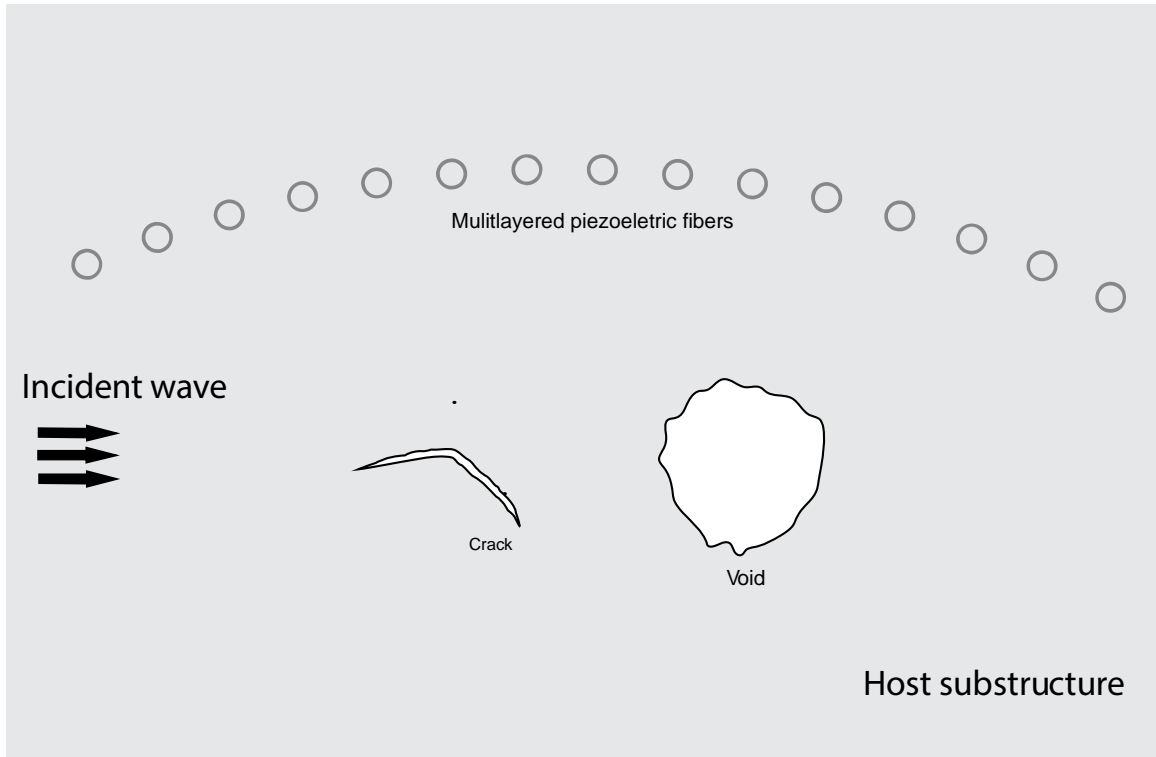
Figure 6.1: An array of multilayered piezoelectric fiber sensors and irregular shaped void and crack.

magnitudes **W** will be considered in the following discussion.

6.2.1.1 Interaction between damages and sensors

The multilayered piezoelectric fibers and/or multilayered fiber with or without imperfection will be collectively referred to as scatterers. In multiple scatterers embedded in a host medium subject to a time-harmonic wave field, the multiple scatterer problem can be decomposed into simpler subproblems involving one of the scatterers as shown in figure 6.3. These subproblems will be further decomposed to study further interactions then all will be summed up to provide the superimposed solution of the original problem. Considering one of the scatterers, scatterer j as the nominal scatterer, this scatterer is subject to a Pseudo incident wave field which consists of the original incident wave field inside the host medium and all the unknown scattering from all of the other scatterers,

Figure 6.2: An array of multilayered piezoelectric fiber sensors and best identified circular void and crack.

$$\{_j\mathbf{W}\} = \{_j^{in}\mathbf{W}\} + \sum_{\substack{s=1 \\ s \neq j}}^{N} \{_s^{sc}\mathbf{W}\} \text{ at } S_j \tag{6.2}$$

where the effects of this Pseudo incident inside the jth scatterer

$$\{_j\mathbf{W}\} = \{_j^{tr}\mathbf{W}\} - \{_j^{sc}\mathbf{W}\} \text{ at } S_j, \tag{6.3}$$

$$\{\mathbf{W}\} = \begin{bmatrix} u_r & u_\theta & \sigma_r & \sigma_{r\theta} & \phi & D_r \end{bmatrix}^T, \tag{6.4}$$

$\{_j^{in}\mathbf{W}\}$ represents the original incident wave field originating from infinity, $\{_j^{sc}\mathbf{W}\}$ represents the scatter wave field radiating from scatterer s towards scatterer j, $\{_j^{tr}\mathbf{W}\}$ represents the transmitted wave field inside the scatterer and the left hand subscript representing scatterer number starting with 1. For each scatterer the exterior host medium incident wave as well as all the scatter from all the other scatterers form the Pseudo incident waves with respect to the scatterer's coordinate system origin point o_j. The interaction can be further decomposed into interaction orders, k, with each

132

interaction order representing the response of a scatterer to the previous excitations. The first interaction order is due to the original incident wave field and it represents the response of each scatterer, $\{_j\mathbf{W}^1\}$, isolated as a single scatterer as shown in figure 6.3 subproblem (b). The scattered wave field, $\{_s^{sc}\mathbf{W}^1\}$, of each scatterer is calculated to be used as a Pseudo incident wave field. The second interaction order response, $\{_j\mathbf{W}^2\}$, is due to the calculated scatter as a Pseudo incident wave field, $\{_s^{sc}\mathbf{W}^1\}$, of all the other scatterers on the considered scatterer as shown in figure 6.3 subproblem (c). The procedure is repeated, with the kth interaction order response, $\{_j\mathbf{W}^k\}$, is calculated from the previously calculated scatter, $\{_s^{sc}\mathbf{W}^{k-1}\}$, of all the other scatterers as shown in figure 6.3 subproblem (d). The interaction order can be represented mathematically as

$$\{_j\mathbf{W}^1\} = \{_j^{in}\mathbf{W}\}, \; k=1 \tag{6.5}$$

$$\{_j\mathbf{W}^k\} = \sum_{\substack{s=1 \\ s \neq j}}^{N} \{_s^{sc}\mathbf{W}^{k-1}\}, \; k \geq 2 \tag{6.6}$$

and the total incident wave field on the jth scatterer interface with the host medium

$$\sum_{k=1}^{\infty} \{_j\mathbf{W}^k\} = \{_j^{in}\mathbf{W}\} + \sum_{k=2}^{\infty} \sum_{\substack{s=1 \\ s \neq j}}^{N} \{_s^{sc}\mathbf{W}^{k-1}\}. \tag{6.7}$$

The calculated ϕ for the assumed damage is then used as the calculated theoretical voltage of the piezoelectric fiber sensor.

6.2.2   The inverse problem

The relation between damage characteristics and the voltage output has been obtained by solving the direct problem. This relation between voltage readings on sensors and damage parameters can be integrated into an optimization algorithm to predict the damage parameters from known experimental voltage readings on sensors. There are two types of damages discussed circular voids and curved cracks to allow for the best fitting to irregularly shaped voids and cracks. The parameters of a typical circular
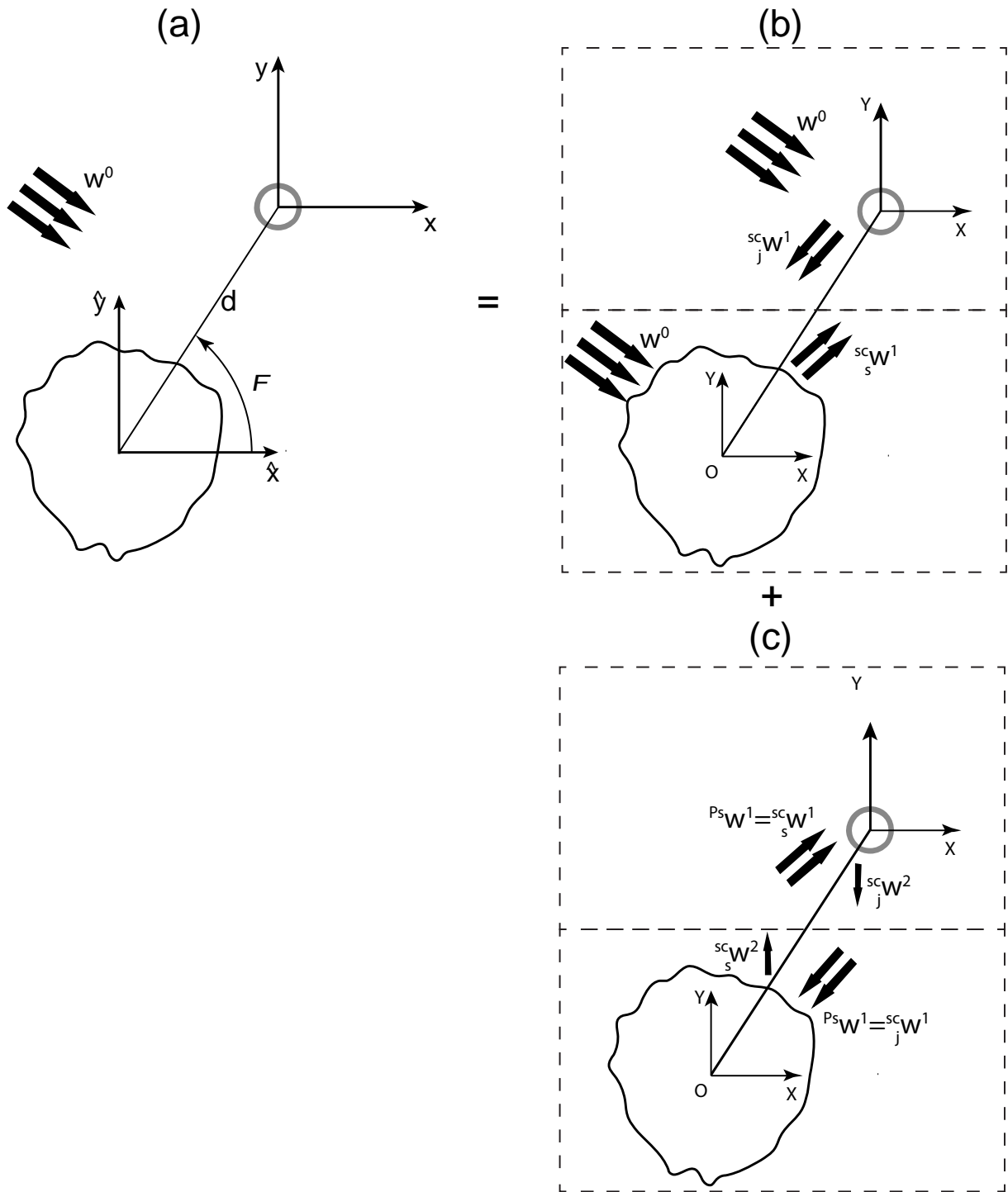
Figure 6.3: Higher interaction orders of Pseudo Incident Wave

void are its radius r_v and the location of its center (x_v, y_v) while the parameters of a typical curved crack are its radius r_c, location of its center (x_c, y_c), starting θ_1 and ending θ_2 angles. An error function $j(\mathbf{p})$ in damage parameters $\mathbf{p}$ is defined as the Euclidean distance or the least squares difference between experimental voltage reading $\phi^e(k_f R)$ and calculated $\phi^c(\mathbf{p}, k_f R)$ at different relative frequencies and R is initial guess radius. The inverse problem is then stated as determining the damage parameters $\mathbf{p} = \{p_1,\ p_2,\ ...,\ p_i,\ ...p_n\}$ which minimize the objective error function,

$$j(\mathbf{p}) = \sqrt{\sum_{f=1}^{N_k} \frac{(\phi^c(\mathbf{p}, k_f R) - \phi^e(k_f R))(\phi^c(\mathbf{p}, k_f R) - \phi^e(k_f R))^T}{\phi^e(k_f R)(\phi^e(k_f R))^T}} \qquad (6.8)$$

where T is the transpose and N_k is the total number of relative frequencies used to record voltages on sensors.

The objective function is general and can be reduced to the simple limiting case of a single frequency which corresponds to acquiring sensor readings due to only one incident wave. The general objective function permits the identification of damages when the number of damage parameters exceeds the number of sensor readings at a single frequency. The experiment can be run at multiple incident wave frequencies to generate more sensor voltage readings and it can be also used to enhance the identification.

6.2.2.1 Intelligently predesigned genetic algorithm

In global optimization, the search for a candidate solution parameters $\mathbf{p}$ (search space) to minimize the error fitness function is not limited as in local space. The genetic alogrithm is proposed to ensure the solution is not trapped in a local minimum which would prevent converging to the right solution. The genetic algorithm also does not require a proper guess of the initial parameters or the exact number of damages. Another advantage is that, it permits constraining the optimization search space for examples within limited search space or preventing damages from overlapping. Although the genetic algorithm can be used exclusively to find the solution however it is very slow

compared to local gradient-based optimization algorithms.

Instead of working with a single set of candidate solution parameters $\mathbf{p}$ in each iteration, the genetic algorithm creates a number of candidate solution parameters $\mathbf{p}^1$, $\mathbf{p}^2$,..., $\mathbf{p}^M$ (collectively known as a population) in each iteration thus parallel computing can be used. The first generation, initial population, consists of chromosomes which are a number of sets of all parameters. A vector of chromosomes $\mathbf{p} = \{p_1, p_2, ..., p_i, ...p_n\}$ with p_i as the genes which correspond to the damage parameter. The complete collection of genetic material (all chromosomes taken together) is called the genome. An evaluation of the error function for each chromosome, if a chromosome provides a value that satisfies the convergence criteria of the error function then the algorithm is terminated otherwise different operators (selection, reproduction, mutation, and crossover) are applied to update the population. The selection operator chooses those chromosomes in the population that will be allowed to reproduce as parents holding those selected chromosomes. The parents holding the fittest parent's chromosomes are selected to produce children by ranking the chromosomes based on their corresponding error function evaluations. The production operator reproduces new generations of populations by mutation and crossover of the selected parents from the previous generation. The best parents' chromosomes for example parent 1 holding $\mathbf{p}^1 = \{p_1^1, p_2^1, ...p_i^1, ...p_n^1\}$ with the best among current population and parent 2 holding $\mathbf{p}^2 = \{p_1^2, p_2^2, ...p_i^2, ...p_n^2\}$ with the second best will be allowed to produce children. The mutation operator adds changes to the parents to create mutated children. Mutation is predesigned intelligently in new generations based on nonlinear gradient operators for example, the kth parent will be used to create a child using an iteration of Broyden-Fletcher-Goldfarb-Shanno

$$\mathbf{p}^{'k} = \mathbf{p}^k - \alpha_k \left(\mathbf{H}^{(k)}\right)^{-1} \mathbf{g}^{(k)} \tag{6.9}$$

where the superscript ' is for a child, α_k is the step size, $\mathbf{H}^{(k)}$ is the Hessian matrix and $\mathbf{g}^{(k)}$ is the gradient (discussed in subsec. (6.2.2.2)). Unlike classical genetic algorithms which rely on evolutionary operators based on randomness, the newly developed algo-

rithm relies on intelligently predesigned operators. The intelligent predesigned nature of this algorithm mutates intelligently from parents based on a calculation of the gradient. The crossover operator exchanges subparts of two or more chromosomes of the selected parents to create crossover children for example, $\mathbf{p}'^1 = \{p_1^1,\ p_2^1,\ ...p_i^1,\ ...p_n^2\}$ is a possible crossover child with all genes from parent 1 and only the last gene from parent 2. The new generation of the current population is formed from all the children of the previous generation.

The intelligently predesigned genetic algorithm is dependent upon several control parameters, the initial population size, the selection criteria of the parents holding the fittest chromosome, the mutation, and crossover techniques. These control parameters should be tuned in order to achieve good performance. Each specific application may require different control parameters values for best performance (Grefenstette, 1986; Rabinovich, Givoli, and Vigdergauz, 2007; Schaefer, 2007). In the present study the following parameters combined with some general guidelines:

- A large initial population increases the probability of finding the global minimum, and the faster the convergence, however, more evaluations of the error function are required. Calculations of the direct model are the most computationally intensive operation in the optimization process. The initial population size in this study is set to 80. The diversity in location genes is ensured by setting the initial range of the population which ensures that the algorithm will not get stuck in local minimum (Anderson-Cook, 2005; Winston, 1984).

- Simple selection criteria by ranking the best parents' chromosomes according to their corresponding evaluations of the error function.

- A high crossover is recommended. A simple crossover by swapping the 5 best parents genes to produce children.

- A small mutation is recommended not only because it is computationally inten-

sive but also so the global optimization process does not get trapped in a local minimum. In each generation, only 10 children are mutated from the 10 best selected parents.

The constraints imposed on this problem are the upper, lower bounds and simple relations to prevent overlapping of damages. The algorithm will start with a number of damages (holes or cracks) more than the expected number of damages once convergence is attained, the right number will be determined.

6.2.2.2 Broyden-Fletcher-Goldfarb-Shanno (BFGS) algorithm

In the local optimization, the gradient-based Newton method through the Broyden-Fletcher-Goldfarb-Shanno (BFGS) algorithm will be used because of its great performance in solving unconstrained nonlinear local optimization problems. The results of global optimization will be used as an initial guess in the local optimization. The objective function is approximated with a quadratic function. The quadratic approximation to $j\left(\mathbf{p}\right)$ can be obtained by the second order Taylor expansion around the kth iterative parameter vector, $\mathbf{p}^{(k)}$, as

$$j\left(\mathbf{p}\right) = j\left(\mathbf{p}^{(k)} + \Delta\mathbf{p}\right) \approx j\left(\mathbf{p}^{(k)}\right) + \left(\mathbf{g}^{(k)}\right)^T \Delta\mathbf{p} + \frac{1}{2}\left(\Delta\mathbf{p}\right)^T \left(\mathbf{H}\right)^{-1}\Delta\mathbf{p} \quad (6.10)$$

where $\Delta\mathbf{p} = \mathbf{p} - \mathbf{p}^{(k)}$ and $\mathbf{g}^{(k)} = \nabla j\left(\mathbf{p}^{(k)}\right)$ is the gradient of the objective function with respect to its parameters $\mathbf{p}$

$$\mathbf{g}^{(k)} = \nabla j\left(\mathbf{p}^{(k)}\right) = \left[\begin{array}{ccccccc} \dfrac{\partial j\left(\mathbf{p}^{(k)}\right)}{\partial p_1} & \dfrac{\partial j\left(\mathbf{p}^{(k)}\right)}{\partial p_2} & \cdots & \dfrac{\partial j\left(\mathbf{p}^{(k)}\right)}{\partial p_i} & \cdots & \dfrac{\partial j\left(\mathbf{p}^{(k)}\right)}{\partial p_M} \end{array}\right]^T.$$
$$(6.11)$$

The gradient of this approximation with respect to $\Delta\mathbf{p}$ is

$$\nabla j\left(\mathbf{p}^{(k)} + \Delta\mathbf{p}\right) \approx \nabla j\left(\mathbf{p}^{(k)}\right) + \mathbf{H}\Delta\mathbf{p} \quad (6.12)$$

and setting this gradient to zero (which is the objective of optimization) provides the Newton step

$$\Delta\mathbf{p} \approx -\left(\mathbf{H}^{(k)}\right)^{-1}\mathbf{g}^{(k)}. \tag{6.13}$$

Newton's method requires computing the inverse of the Hessian matrix $(\mathbf{H})^{-1}$ in every iteration, therefore, it is not efficient. Consequently, quasi-Newton's methods are adopted, and the inverse Hessian matrix is approximated. The approximate Hessian $\mathbf{H}$ is chosen to satisfy

$$\nabla j\left(\mathbf{p}^{(k)} + \Delta\mathbf{p}\right) = \nabla j\left(\mathbf{p}^{(k)}\right) + \mathbf{H}\Delta\mathbf{p}, \tag{6.14}$$

which is called the secant equation (Taylor series of the gradient). The various quasi-Newton methods differ in their solution to the secant equation. Most methods (with some exceptions, such as Broyden's method) seek a symmetric solution $(\mathbf{H} = \mathbf{H}^T)$. The iterative procedure of calculating the parameters is repeatedly calculated as

$$\mathbf{p}^{(k+1)} = \mathbf{p}^{(k)} - \left(\mathbf{H}^{(k)}\right)^{-1}\mathbf{g}^{(k)} \tag{6.15}$$

which will head in the descent direction of the objective function when the Hessian matrix is positive definite. Since the positive definite of the Hessian matrix cannot be guaranteed for the current problem and in order to ensure the descent property of the Newton's method, Equation (6.15) is modified to

$$\mathbf{p}^{(k+1)} = \mathbf{p}^{(k)} - \alpha_k \left(\mathbf{H}^{(k)}\right)^{-1}\mathbf{g}^{(k)} \tag{6.16}$$

where α_k is the step size in the search direction $-\left(\mathbf{H}^{(k)}\right)^{-1}\mathbf{g}^{(k)}$. In the Broyden-Fletcher-Goldfarb-Shanno (BFGS) algorithm, the Hessian matrix is updated using the following formula,

$$
\begin{aligned}
\mathbf{H}^{(k+1)} = \mathbf{H}^{(k)} &+ \left[\frac{1 + \left(\Delta\mathbf{g}^k\right)^T \mathbf{H}^{(k)}\Delta\mathbf{g}^{(k)}}{\left(\Delta\mathbf{g}^k\right)^T \Delta\mathbf{g}^{(k)}}\right] \frac{\Delta\mathbf{p}^{(k)}\left(\Delta\mathbf{p}^k\right)^T}{\left(\Delta\mathbf{p}^k\right)^T \Delta\mathbf{p}^{(k)}} \\
&- \frac{\Delta\mathbf{p}^{(k)}\left(\Delta\mathbf{g}^k\right)^T \mathbf{H}^{(k)} + \mathbf{H}^{(k)}\Delta\mathbf{g}^{(k)}\left(\Delta\mathbf{p}^k\right)^T}{\left(\Delta\mathbf{g}^k\right)^T \Delta\mathbf{p}^{(k)}}
\end{aligned} \tag{6.17}
$$

where $\Delta\mathbf{p}^{(k)} = -\alpha_k \left(\mathbf{H}^{(k)}\right)^{-1}\cdot\mathbf{g}^{(k)}$, $\Delta\mathbf{g}^{(k)} = \mathbf{g}^{(k+1)} - \mathbf{g}^{(k)}$ and $\mathbf{g}^{(k)}$ is approximated using the central finite difference

$$\mathbf{g}^{(k)} \approx \frac{j\left(p_1,\ p_2,\ ...,\ p_i + \delta p_i,\ ...p_n\right) - j\left(p_1,\ p_2,\ ...,\ p_i - \delta p_i,\ ...p_n\right)}{\delta p_i} \qquad (6.18)$$

where δp_i is an infinitesimal perturbation taken as $\delta p_i = .001 p_i$. The initial Hessian matrix $\mathbf{H}^{(0)}$ can be set to any symmetric positive definite matrix, in this study, it is set to be the identity matrix $\mathbf{H}^{(0)} = \mathbf{I}$.

6.2.2.3   Multiple damages identification

A two-stage optimization is necessary for multiple damages quantitative identification specially for arbitrarily and irregular shaped multiple damages. A local optimization usually fails to solve complex multiple damages even with a very efficient search operator such as BFGS unless a good initial guess is provided to the solver. In practice, it is difficult to set a good initial guess for the multiple damages' parameters. Therefore, the global optimization using a powerful algorithm is more practical and a realistic requirement to provide a good admissible initial guess for BFGS.

A flow chart for the damage identification process is shown in figure 6.4 with the dotted rectangles representing the two optimization stages. The inputs are the experimentally recorded voltage data, structural constants, multilayered piezoelectric sensor array, and loading data are stored to be shared for the whole program. The objective function is calculated using equation (6.8) which calculates the least squares difference between experimental recorded data and the calculated data by iteratively solving the direct problem. After updating the damage parameters through the process, the estimated damage parameters approach the actual damage parameters with tolerance if convergence is achieved.

Criteria to switch the global optimization using the intelligently predesigned genetic algorithm to the local optimization using BFGS algorithm are:

- The objective function converges to less than or equal to ε_{global} which is taken in this study as a relation with respect to the relative frequency or the ratio of

$$\varepsilon_{global} = \frac{R}{z\lambda_f} = \frac{k_f R}{2\pi z}$$ where z is a suitable number larger than 10.

- The objective function does not improve any further in two consecutive generations.

For the case of unknown type or number of damages a judgment has to be done on the type and size of the damages to determine whether or not to be considered or eliminated. It can be expected that if the damage is a crack while simulations are conducted using a circular void, the objective function will not improve in two consecutive generations and the reached optimal damage parameters would produce values far from the recorded volts on the sensor array. The mathematical model to be used as a measurement tool has to be calibrated by comparing the actual recorded voltage of a known damage parameters specially of known crack tips locations. The calibration reduces any mismatch in readings and calculations.

6.3 Results and discussion

In this section, the numerical results of, multiple damages identification using the proposed optimization algorithm are presented. The examples are structured in an increasing order of difficulty considering number of damages, type of damages, number of parameters, and shape irregularity. The purpose of the following examples is to evaluate the performance of the proposed optimization algorithm in comparison to standard genetic algorithm and apply the proposed direct model in structural health monitoring. Materials used in this study are shown in table (6.1) with their material constants. The experiments were conducted at a dimensionless loading frequency of $kR = 1.5$ with k being the shear wave number of the outer medium $k_T = \omega/c_T$ and R being the outer radius enclosing the damage.

Although the intelligently predesigned genetic algorithm uses an intelligently predesigned mutation, it is still a stochastic algorithm which uses randomness from its ini-
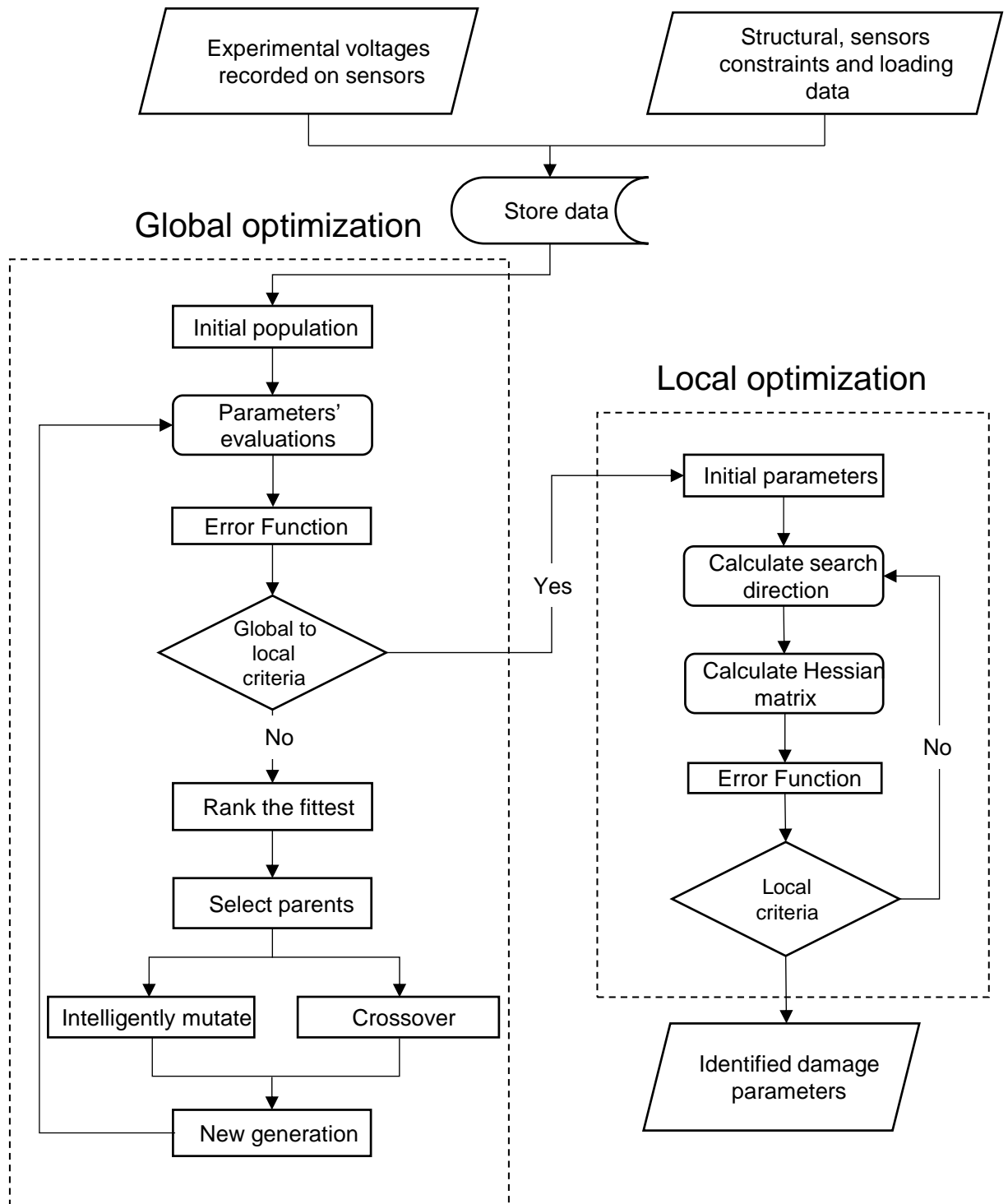
Figure 6.4: A flow chart for damage identification using intelligent predesigned genetic and gradient optimization algorithm

Material	Elastic Constants $\times 10^{10} (\text{N/m}^2)$					Density 10^3 (kg/m^3)	Piezoelectric $\times 10^0 (\text{C/m}^2)$				Permittivity $\times 10^{-9} (\text{C/Vm})$	
	c_{11}	c_{33}	c_{12}	c_{13}	c_{55}	ρ	e_{31}	e_{32}	e_{33}	e_{24}	ϵ_{33}	ϵ_{11}
isotropic	$\lambda + 2\mu$	λ	λ	μ								
PolyCarbonate	.554	.554	.298	.298	.128	1.18	-	-	-	-	.03	.03
P(VDF-TrFE)	.47	.45	.257	.213	.12	1.3	.045	.037	-.18	-.1	.1	.01

Table 6.1: Materials used in this study

tial solution to its different operators (selection, reproduction, mutation, and crossover). Stochastic algorithms might produce a slightly different solution on each independent run. Several independent runs were conducted to avoid solution uncertainty and to represent good results with the best minimum objective function value is reported.

Numerical experiments are conducted using finite element (see appendix A) to obtain observed voltage readings on an array of sensors as shown in shown in figure 6.1 to represent a real in site situation with noises. The noise levels are the highest for the irregular shapes and noise levels are calculated by comparison to simulation results using the proposed model as described in the direct problem with higher interactions orders of pseudo incident wave (Hi-PsIW). The root mean square error ($RMSE$) is used to quantify the noise levels. The root mean square is calculated for each sensor, s, by calculating the residual errors between measured voltage using finite element FE and the corresponding calculated voltage for the same point on the piezoelectric interface with the host medium

$$RMSE_s = \sqrt{\frac{\sum_{\theta=1}^{N} (\phi^{FE}_{\theta} - \phi^{Hi}_{\theta})^2}{N}} \tag{6.19}$$

where N is the total number of points along the interface. The noise level is increased by controlling the irregularity in the shapes to produce errors added to measured voltages. The errors can be randomly added to the sensors as

$$\phi^{Hi}_s = \phi^{FE}_s + p\,(RMSE_s)\,g \tag{6.20}$$

where ϕ^{Hi}_s is the equipotential voltage from higher order interaction model for sensor

143

s, ϕ_s^{FE} is the equipotential voltage from finite element calculation for sensor s, and g is the Gaussian white noise variable $p\%$ the noise level. However, it is more realistic to obtain noise from the controlled numerical experiment by adding irregularity in the damage shape.

The standard genetic algorithm, a classic rank based genetic algorithm adopted by MATLAB toolbox, is used for comparison purposes with the developed intelligent pre-designed genetic algorithm as the global optimizer. The same optimization parameters, operators and settings are used, which are the defaults, for both the standard genetic algorithm by MATLAB toolbox as those for the intelligent predesigned genetic algorithm with the exceptions of randomness in operators. In the intelligent predesigned genetic, randomness is minimized and intelligent crossover, selection, and mutation operators are used as described earlier. Global optimizer algorithms use default settings and create a partial initial population to ensure the same initial guess for comparisons (Anderson-Cook, 2005; Schaefer, 2007).

6.3.1 Single damage

Two examples for the two types of damages are considered as a single damage. These are a circular void and an arc crack.

6.3.1.1 Damage as a circular void

The optimization constraints for circular void example limit the void parameters such that $-12 < x_v < 12$, $-12 < y_v < 12$ and $0 < r_v < 6$. Table (6.2) provides a comparison of three optimization algorithms after 1200 iterations for a circular void of radius 3mm. It can be seen that intelligently predesigned algorithm combined with BFGS provides best results and converges faster. Figure 6.5 shows the convergence of the error function versus the iteration number for different optimization algorithms using slightly different circular void of radius 2.7mm and located at $x_v = 1$, $y_v = 1$. It

Damage parameters	Actual values	Initial guess	Standard GA	Standard GA+BFGS	Intel. Pre. GA+BFGS
r_ν	3	6	3.1696	3.0275	3.0009
x_ν	0	-10	-0.0339	-0.0087	-0.0012
y_ν	0	-10	0.0768	0.0109	0.0014
Error function			3.280E-04	1.350E-08	1.075E-09

Table 6.2: A comparison of different optimization algorithms for a circular void identification.
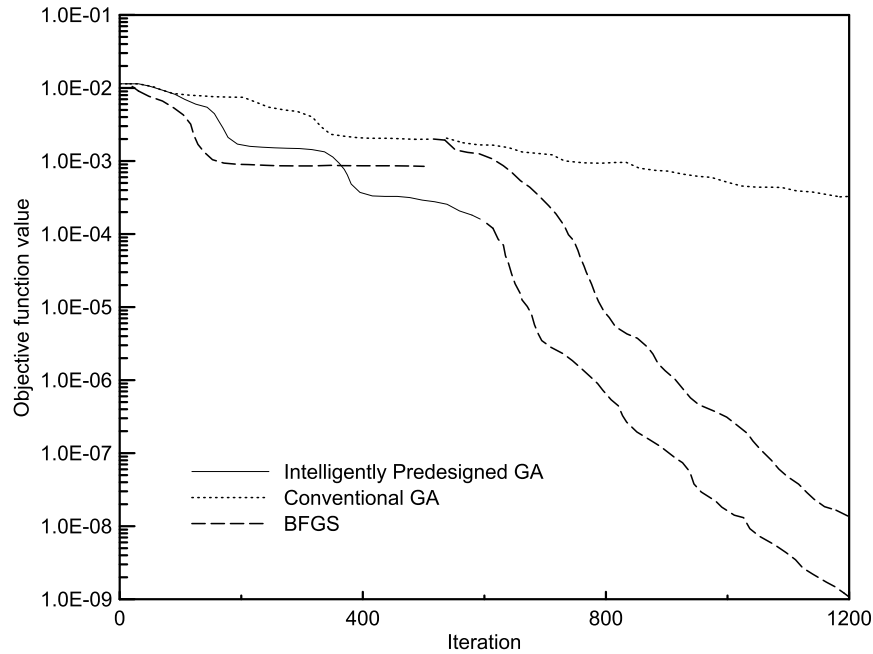
Figure 6.5: Error function versus iteration number of direct solver for the identification of a circular void.

can be seen if the initial guess was far from the actual parameters BFGS fails and gets trapped in a local minimum. The use of the standard genetic algorithm is very slow and might not converge after many iterations. The combination of genetic algorithm with BFGS provides a better solution however the combination with intelligently predesigned genetic with BFGS provides best results faster.
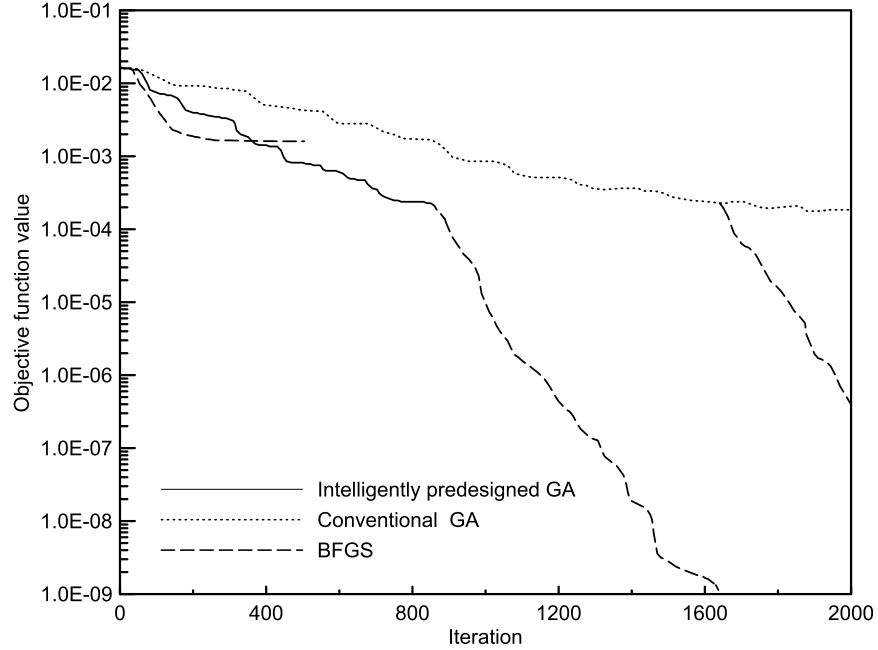
Figure 6.6: Error function versus iteration number of direct solver for the identification of a crack.

6.3.1.2 Damage as an arc crack

In this example, the damage is chosen as an arc crack with the parameters of the arc crack are $x_c = 1$, $y_c = 1$, $\theta_1 = 70°$, $\theta_2 = 110°$ and $r_c = 3$. The optimization constraints for a circular arc crack are to limit the crack parameters such that $-12 < x_c < 12$, $-12 < y_c < 12$ and $0 < r_c < 6$ without constraints on θ_1 or θ_2. Figure 6.6 shows the convergence comparison of different optimization algorithms for evaluations of the error function versus iteration number of the iterated direct problem with results showing the superiority of using a combination of intelligent predesigned and BFGS. The identified crack parameters predicted by using the intelligently predesigned genetic and BFGS algorithms are given in table 6.3. Results show that identifying a crack with 5 parameters requires more iterations than identifying a circular void; however, the identification at the same objective function value is more accurate.

Damage parameters	Actual values	Initial guess	Intelligently Predesigned GA+BFGS
r_c	3	6	2.9998
x_c	1	-10	-0.0001
y_c	1	-10	0.0002
θ_1	70	0	69.9897
θ_2	110	30	110.0012
Error function			1.136E-09

Table 6.3: Identified crack parameters.

6.3.2 Multiple damages

Multiple damages are considered as both a crack and a circular void with damage parameters set as $x_c = -4.5$, $y_c = 0.7$, $\theta_1 = 70°$, $\theta_2 = 110°$, $r_c = 3$ for the crack while $x_v = 6.5$, $y_v = 1$ and $r_v = 3$. The optimization constraints for multiple damage would limit the damage parameters such that $-12 < x_c < 12$, $-12 < y_c < 12$, $-12 < x_v < 12$, $-12 < y_v < 12$, $0 < r_v < 5$ and $0 < r_c < 5$ without constraints on θ_1 or θ_2. In addition to those optimization constraints, the separation distance d between the two damages had to be constraint as well $d > 10$ so damages will not intersect during iterations of the direct problem. Figure 6.7 shows the convergence comparison of different optimization algorithms for evaluations of the error function versus iteration number of the iterated direct problem.

The noise generated by using the finite element to conduct the numerical experiments and collect observations was less than 1%. An irregularity in the crack as well as the circular void shape is introduced to increase the noise levels by drawing a random irregular shape for both the crack and the void (as shown in figure 6.1) then the corresponding voltages polluted with noise are collected which is equivalent to adding noise to the individual sensors using Gaussian white noise. Different levels of noise were introduced and the proposed algorithm successfully identified the embedded damages to their best crack and circular void even for high noise levels as illustrated in table .
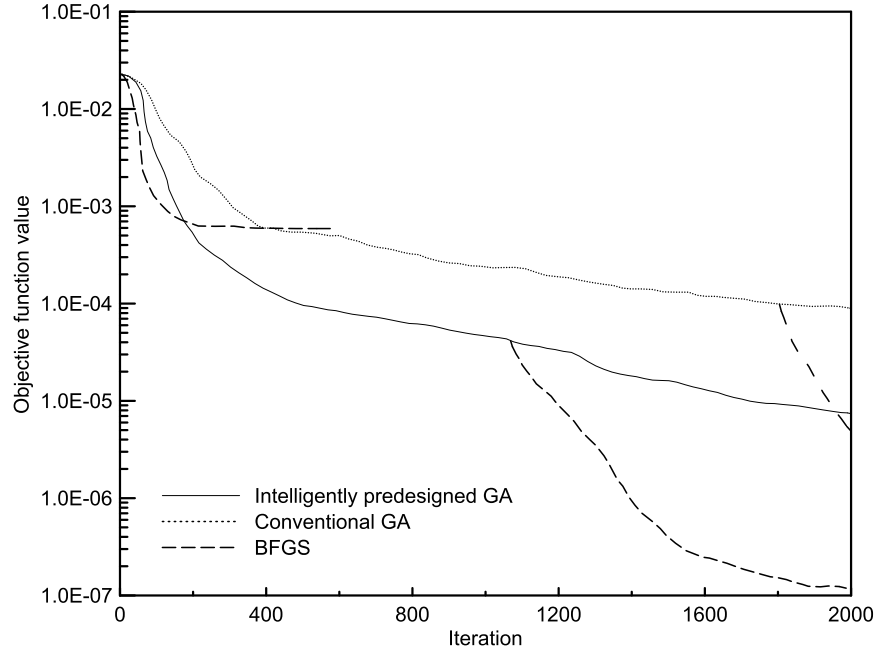
Figure 6.7: Error function versus iteration number of direct solver for the identification of multiple damage.

Damage parameters	Actual values	Initial guess	Intelligently Predesigned GA+BFGS
r_c	3	5	3.0137
x_c	-4.5	5	-4.4941
y_c	0.7	-10	0.6982
θ_1	70	0	70.0108
θ_2	110	30	110.0136
r_ν	3	5	3.0936
x_ν	6.5	-10	6.4132
y_ν	1	-5	0.9768
Error function			1.1890E-07

Table 6.4: Identification of a crack and a circular void parameters.

Noise level	Void			Crack				
	r_c	x_c	y_c	θ_1	θ_2	r_ν	x_ν	y_ν
$\sim 10\%$	3.098	-4.482	.738	70.022	110.032	3.156	6.398	1.117
$\sim 15\%$	2.892	-4.563	.652	70.045	110.090	3.281	6.315	1.212
Best fit values	3	-4.5	0.7	70	110	3	6.5	1

Table 6.5: Identification of noise polluted irregular shaped crack and void parameter.

6.4   Conclusions

This study presents a novel two-stage optimization method based on previously developed models of multilayered piezoelectric fibers and wave interactions with multiple embedded damages in the structures. The proposed method can be applied to quantify any number and any type of damages of arbitrarily shaped voids and/or cracks from the voltage signals recorded on the piezoelectric fiber sensors. The multiple damages identification method is provided to quantitatively identify irregular voids and cracks using two-stage optimization algorithms. Although two types of damages were discussed, the method can be easily extended to other types of damages by replacing the embedded damage scattering model. The identification for damages produced the size and location of the damage where cracks to be identified, it produced crack location, size and radius of curvature while for voids produced the size or radius of the circular void and location. A new intelligently predesigned genetic algorithm using predesigned mutation based on gradient calculation instead of the random mutation used in classical algorithms. The identification process is based on recorded voltages by an array of multilayered piezoelectric sensors. The voltage outputs on the sensor array due to damages are solved using the higher interaction pseudo incident wave as the direct problem while the inverse problem identified damages by using the two-stages optimization process. Numerical examples are presented, which show rapid convergence and effectiveness of the newly developed multiple damage identification method.

Chapter 7

Contributions and future work

An extensive study of multilayered piezoelectric fiber was presented. Multilayered piezoelectric fibers serve as active elements embedded in smart structures and can serve in structural health monitoring. Multilayered piezoelectric fibers can be used at high frequencies for better identification precision while other sensors. A comprehensive theoretical investigation have been conducted to study the dynamic behavior of radially polarized multilayered piezoelectric fibers, multiple fiber-damage wave interactions and the application of an array of multilayered piezoelectric fibers to identify multiple damages. A summary of the main contributions, conclusions and future work of this research is given in this chapter.

7.1   Main contributions

Four major issues essential to the application of multilayered piezoelectric fibers in the general design of smart structures and the applications of smart structural health monitoring. These issues are:

(1) how to model the dynamic electromechanical behavior of piezoelectric fibers,

(2) how to analyze the performance of multilayered piezoelectric fibers embedded as sensors and/or actuators,

(3) what is the wave field after multiple wave interactions between multiple multilayered piezoelectric fibers and damages,

(4) where are damages and what is their size and how to numerically conduct sim-

ulations to identify them using an array of multilayered piezoelectric fibers.

These four major issues required the development of new models, techniques, and algorithms. Therefore, the main contributions of the thesis can be summarized in the following subsections.

7.1.1   A new dynamic electromechanical model for piezoelectric fibers

A new dynamic electromechanical model for piezoelectric fibers was developed (Abdel-Gawad and Wang, 2013). The developed model contains the effect of the circumferential stresses and unlike traditional linear spring, it satisfies the equations of motion. The model has been verified at low and high relative frequencies. It could be used at significantly large piezoelectric layer thickness of up to 30% of the typical radius. The model includes the electric and piezoelectric coupling effects.

7.1.2   A new analysis for the performance of multilayered piezoelectric fibers as sensors and/or actuators

The performance of multilayered piezoelectric fibers as sensors and/or actuators was analyzed using a newly adapted matrix representation which can be thought of as a hybrid synthesize of the transfer and direct global matrices combined together. The significance of this representation is manifested by its ability to represent multiple layers including imperfectly bonded layers and thus can solve problems of multilayered piezoelectric fibers as sensors and/or actuators. A new imperfect interphase layer was developed and was used to study the extreme case of an arc crack interfacing the piezoelectric layer and the embedding medium. The effects of the geometry of the interface crack, elastic material properties and the frequency of the applied loads upon the resulting dynamic stresses are examined.

7.1.3 A new numerically efficient wave interactions method for multilayered piezoelectric fibers and damages

A new computationally efficient method, the Higher Interaction orders Pseudo Incident Wave (Hi-PsIW) method, is developed to determine the electro mechanical field in multiple piezoelectric layers in the presence of multiple multilayered fibers and damages. Numerical results of the dynamic stress field and the voltage output for different configurations and frequencies are determined and analyzed. The method relies on well established analytic methods as well as the high efficiency of numerically stable methods. The method is general and can be readily used by designers to evaluate stresses in smart structures or applied in damage identification algorithms to evaluate efficiently the voltages on many sensors in structural health monitoring.

7.1.4 A new simulation algorithm for multiple damage identification

A new algorithm for multiple damage identification is developed to quantitatively identify the position and the size parameter of embedded damages in structures using the recorded voltage on an array of multilayered piezoelectric fiber sensor. The calculated voltage recorded on different piezoelectric sensors in response to the existence of multiple damages with prior knowledge of the structure constants and loading data are integrated into a two stage optimization process to estimate multiple damage parameters. The first stage is based on a newly developed algorithm based on genetic algorithm eliminating the need for a good initial guess. The newly developed genetic algorithm is based on an intelligently predesigned unlike classical genetics which is based on randomness. Numerical examples show that this technique can potentially quantitatively identify damages effectively.

7.2 Recommendation for future studies

During the course of these studies, the following has been identified as potential subjects worthy of further studies:

Other types of damages   The current thesis discussed empty space damages mainly voids and cracks, it can be extended with great ease and without any additional modeling to include fluid filled and/or inclusions. Chapters 4 have briefly discussed fluids and acoustics as limiting cases. Further analysis and studies on acoustic waves could be extended based on the current models.

The current research studied the two most frequently encountered geometries of damages mainly circular voids and curved cracks. Almost all irregular shapes and cracks can be fitted to these two types of damages however other shapes can be added like elliptic voids. The current study permits additional damages to be added with just knowledge of their scattering behavior and models to be able to identify them. In that regard, the spectral extended finite element can be used and combined with the current analytic models since finite element can model complicated geometries with ease. Some preliminary studies have been conducted into extending the current analytic model and combining them with finite element; however, existing conventional finite element methods are not sufficient and can not model the wide different scales of the problem. Instead new hybrid finite element would need to be developed which combines some features of Trefftz element, singular enriched finite element (extended finite element), and spectral finite element with the developed analytic models in this research.

Pattern recognition   Damage type recognition is an active research area in itself, damages are recognized from their pattern and response. The current research did not cover that field of research area however possible research extension can be conducted based on current models using learning neural networks and artificial intelligence.

On site experimental and field work   The current thesis is mainly focused on theoretical and numerical aspects, which help in understanding the dynamic behavior of multilayered piezoelectric fibers and their application in smart structural health monitoring. Numerical experiments were conducted and all studies have been validated as well as verified versus both others limiting cases and finite element, also the current thesis has proposed methods to reduce measurement errors due to theoretical assumptions in spite all of that a need to apply these studies on real actual site structures. The experimental work should include actual multilayered piezoelectric embedded in a damaged structure, a waveform generator to generate high frequency excitation signals, a power amplifier to amplify the excitation signal, and possibly drive the piezoelectric fibers as actuators. The array of piezoelectric sensors will collect the waves and convert them into electrical signals as recorded input signals to quantitatively identify the embedded damages by using the proposed technique.

Parametric damage studies   Effect of sensor location, number of sensors, number of damages, number of damage parameters, and location of damages are all important in the identification process. Preliminary results show that accuracy of identification is affected by all those parameter specially if damages are in near proximity to each other and number of sensors are small. A parametric study is needed to cover these aspects.

Singular imperfect layer boundary condition   The current imperfect layer does not consider the local singular behavior. It is possible to enrich the current layer model with the singular behavior of crack tips.

References

1. Abdel-Gawad, S. and Wang, X. (2013). "An improved model of thin cylindrical piezoelectric layers between isotropic elastic media". *International journal of solids and structures* 50.24, pp. 4118–4132.

2. Abdel-Gawad, S. and Wang, X. (2018). "The dynamic electromechanical behavior of a multilayered piezoelectric fiber". *Journal of mechanics of materials and structures*, to be submitted.

3. Aboudi, J. (1987). "Damage in composites–modeling of imperfect bonding". *Composites science and technology* 28.2, pp. 103–128.

4. Abouraddy, A. et al. (2007). "Towards multimaterial multifunctional fibres that see, hear, sense and communicate". *Nature materials* 6.5, pp. 336–347.

5. Abramowitz, M. and Stegun, I. (1965). *Handbook of mathematical functions with formulas, graphs, and mathematical tables*. Handbook of Mathematical Functions with Formulas, Graphs, and Mathematical Tables. Available online. U.S. Govt. Print. Off.

6. Achenbach, J. D. (1972). *Wave propagation in elastic solids*. Vol. 39. North Holland.

7. Achenbach, J. (2000). "Quantitative nondestructive evaluation". *International journal of solids and structures* 37.1, pp. 13–27.

8. Advanpix, L. C. (2018). *Multiprecision computing toolbox user's manual*. Advanpix, LLC.

9. Allik, H. and Hughes, T. J. (1970). "Finite element method for piezoelectric vibration". *International journal for numerical methods in engineering* 2.2, pp. 151–157.

10. Altay, G. and Dokmeci, M. C. (2007). "Variational principles for piezoelectric, thermopiezoelectric, and hygrothermopiezoelectric continua revisited". *Mechanics of advanced materials and structures* 14.7, pp. 549–562.

11. Anderson-Cook, C. M. (2005). *Practical genetic algorithms*.

12. ANSYS-manuals, I. (2012-2018). *Documentations, help and manual: release 12-18*. ANSYS, Inc.

13. Anton, S. R., Inman, D. J., and Park, G. (2009). "Reference-free damage detection using instantaneous baseline measurements". *Aiaa journal* 47.8, pp. 1952–1964.

14. Asbeck, A. T. et al. (2014). "Stronger, smarter, softer: next-generation wearable robots". *Ieee robotics & automation magazine* 21.4, pp. 22–33.

15. Auld, B. (1990). *Acoustic fields and waves in solids*. Acoustic Fields and Waves in Solids v. 2. Krieger Publishing Company. ISBN: 9780898747836.

16. Bai, H., Taciroglu, E., Dong, S., and Shah, A. (2004). "Elastodynamic green's functions for a laminated piezoelectric cylinder". *International journal of solids and structures* 41.22, pp. 6335–6350.

17. Baker, A. A., Rose, L. F., and Jones, R. (2003). *Advances in the bonded composite repair of metallic aircraft structure*. Elsevier.

18. Ballandras, S., Laude, V., Clatot, S., and Wilm, M. (2005). "A time domain approach for the analysis of periodic structures using finite element analysis". *Ultrasonics symposium, 2005 ieee*. Vol. 1. IEEE, pp. 337–340.

19. Ballandras, S. et al. (2003). "A novel surface wave transducer based on periodically poled piezoelectric domain". *Frequency control symposium and pda exhibition jointly with the 17th european frequency and time forum, 2003. proceedings of the 2003 ieee international*. IEEE, pp. 893–896.

20. Barbarino, S. et al. (2011). "A review of morphing aircraft". *Journal of intelligent material systems and structures* 22.9, pp. 823–877.

21. Benavides, D., Segura, S., and Ruiz-Cortés, A. (2010). "Automated analysis of feature models 20 years later: a literature review". *Information systems* 35.6, pp. 615–636.

22. Benito, J., Urena, F., and Gavete, L. (2007). "Solving parabolic and hyperbolic equations by the generalized finite difference method". *Journal of computational and applied mathematics* 209.2, pp. 208–233.

23. Bent, A. A. and Hagood, N. W. (1997). "Piezoelectric fiber composites with interdigitated electrodes". *Journal of intelligent material systems and structures* 8.11, pp. 903–919.

24. Bent, A. A., Hagood, N. W., and Rodgers, J. P. (1995). "Anisotropic actuation with piezoelectric fiber composites". *Journal of intelligent material systems and structures* 6.3, pp. 338–349.

25. Bent, A. A. and Pizzochero, A. E. (2000). "Recent advances in active fiber composites for structural control". *Spie's 7th annual international symposium on smart structures and materials*. International Society for Optics and Photonics, pp. 244–254.

26. Berenger, J.-P. (1994). "A perfectly matched layer for the absorption of electromagnetic waves". *Journal of computational physics* 114.2, pp. 185–200.

27. Beskos, D. and Narayanan, G. (1983). "Dynamic response of frameworks by numerical laplace transform". *Computer methods in applied mechanics and engineering* 37.3, pp. 289–307.

28. Bian, Y., Liu, R., and Hui, S. (2016). "Fabrication of a polyvinylidene difluoride fiber with a metal core and its application as directional air flow sensor". *Functional materials letters* 9.01, p. 1650001.

29. Bian, Z., Chen, W., and Lu, C. (2008). "Wave propagation in two-layered infinite composite piezoelectric hollow cylinder with imperfect interfaces". *Piezoelectric-*

157

ity, acoustic waves, and device applications, 2008. spawda 2008. symposium on. IEEE, pp. 315–319.

30. Biwa, S., Yamamoto, S., Kobayashi, F., and Ohno, N. (2004). "Computational multiple scattering analysis for shear wave propagation in unidirectional composites". *International journal of solids and structures* 41.2, pp. 435–457.

31. Bogan, S. and Hinders, M. (1994). *Interface effects in elastic wave scattering.* Vol. 19. Springer.

32. Boller, C. (2001). "Ways and options for aircraft structural health management". *Smart materials and structures* 10.3, p. 432.

33. Bose, S. and Mal, A. (1973). "Longitudinal shear waves in a fiber-reinforced composite". *International journal of solids and structures* 9.9, pp. 1075–1085.

34. Bose, S. and Mal, A. (1974). "Elastic waves in a fiber-reinforced composite". *Journal of the mechanics and physics of solids* 22.3, pp. 217–229.

35. Bostrom, A. (2003). "Review of hypersingular integral equation method for crack scattering and application to modeling of ultrasonic nondestructive evaluation". *Appl mech rev* 56.4.

36. Bouchon, M. (2003). "A review of the discrete wavenumber method". *Pure and applied geophysics* 160.3-4, pp. 445–465.

37. Brei, D. and Cannon, B. J. (2004). "Piezoceramic hollow fiber active composites". *Composites science and technology* 64.2, pp. 245–261.

38. Bystricky, P. (2012). "Smart structures". *Wiley encyclopedia of composites.*

39. Cai, L.-W. (1998). "Full-scale simulation of multiple scattering of elastic waves in fiber reinforced composites". PhD thesis. Massachusetts Institute of Technology.

40. Cai, L.-W. (2004). "Scattering of antiplane shear waves by layered circular elastic cylinder". *The journal of the acoustical society of america* 115.2, pp. 515–522.

41. Cai, L.-W. and Williams Jr, J. H. (1999). "Full-scale simulations of elastic wave scattering in fiber-reinforced composites". *Ultrasonics* 37.7, pp. 463–482.

42. Cai, L.-W. and Williams, J. H. (1999). "Large-scale multiple scattering problems". *Ultrasonics* 37.7, pp. 453–462.

43. Cakoni, F. and Colton, D. (2005). *Qualitative methods in inverse scattering theory: an introduction.* Springer Science & Business Media.

44. Casadei, F. et al. (2012). "Piezoelectric resonator arrays for tunable acoustic waveguides and metamaterials". *Journal of applied physics* 112.6, p. 064902.

45. Cerveny, V. (2005). *Seismic ray theory.* Cambridge university press.

46. Chadwick, P. (1999). *Continuum mechanics: concise theory and problems.* Vol. 39. Dover.

47. Chan, Y.-S., Fannjiang, A. C., and Paulino, G. H. (2003). "Integral equations with hypersingular kernels—-theory and applications to fracture mechanics". *International journal of engineering science* 41.7, pp. 683–720.

48. Chandrasekharaiah, D. S. and Debnath, L. (1994). *Continuum mechanics: concise theory and problems.* Vol. 39. Academic Press.

49. Chang, F.-K. (2013). *Structural health monitoring 2013: a roadmap to intelligent structures: proceedings of the ninth international workshop on structural health monitoring, september 10–12, 2013.* DEStech Publications, Inc.

50. Chen, W., Wang, Y., Cai, J., and Ye, G. (2004). "Three-dimensional analysis of cross-ply laminated cylindrical panels with weak interfaces". *International journal of solids and structures* 41.9, pp. 2429–2446.

51. Cheng, S. (1969). "Multiple scattering of elastic waves by parallel cylinders". *Journal of applied mechanics* 36.3, pp. 523–527.

52. Cheng, S. (1972). "Dynamic stresses in a plate with circular holes". *Journal of applied mechanics* 39.1, pp. 129–132.

53. Chocat, N. et al. (2011). "Piezoelectric multimaterial fibers". *Mrs proceedings.* Vol. 1312. 1. Cambridge Univ Press.

54. Chocat, N. et al. (2012). "Piezoelectric fibers for conformal acoustics". *Advanced materials* 24.39, pp. 5327–5332.

55. Chopra, I. (2002). "Review of state of art of smart structures and integrated systems". *Aiaa journal* 40.11, pp. 2145–2187.

56. Chu, Y. and Rokhlin, S. (1995). "Determination of fiber-matrix interphase moduli from experimental moduli of composites with multi-layered fibers". *Mechanics of materials* 21.3, pp. 191–215.

57. Colton, D. and Kress, R. (2012). *Inverse acoustic and electromagnetic scattering theory*. Vol. 93. Springer Science & Business Media.

58. Crawley, E. F. (1994). "Intelligent structures for aerospace-a technology overview and assessment". *Aiaa journal* 32.8, pp. 1689–1699.

59. Cummer, S. A. and Schurig, D. (2007). "One path to acoustic cloaking". *New journal of physics* 9.3, p. 45.

60. Curie, J. and Curie, P. (1880a). "Piezo effect in quartz and some other materials-french to english". *Cr acad. sci. paris* 91.91,383, p. 1880.

61. Curie, J. and Curie, P. (1880b). "Piezoelectric and allied phenomena in rochelle salt-french to english". *Comput rend acad sci paris* 91.9, pp. 294–297.

62. Curie, J. and Curie, P. (1881). "Contractions et dilatations produites par des tensions 'electriques dans les cristaux h'emiedres a faces inclin'ees". *Comptes-rendus de l'academie des sciences* 93, pp. 1137–1140.

63. Das, S., Saha, P., and Patro, S. (2016). "Vibration-based damage detection techniques used for health monitoring of structures: a review". *Journal of civil structural health monitoring* 6.3, pp. 477–507.

64. De Basabe, J. D. and Sen, M. K. (2007). "Grid dispersion and stability criteria of some common finite-element methods for acoustic and elastic wave equations". *Geophysics* 72.6, T81–T95.

65. De Rosa, I., Santulli, C., and Sarasini, F. (2009). "Acoustic emission for monitoring the mechanical behaviour of natural fibre composites: a literature review". *Composites part a: applied science and manufacturing* 40.9, pp. 1456–1469.

66. Delsanto, P., Iordache, D., Iordache, C., and Ruffino, E. (1997). "Analysis of stability and convergence in fd simulations of the 1-d ultrasonic wave propagation". *Mathematical and computer modelling* 25.6, pp. 19–29.

67. Delsanto, P., Schechter, R., and Mignogna, R. (1997). "Connection machine simulation of ultrasonic wave propagation in materials iii: the three-dimensional case". *Wave motion* 26.4, pp. 329–339.

68. Delsanto, P., Whitcombe, T., Chaskelis, H., and Mignogna, R. (1992). "Connection machine simulation of ultrasonic wave propagation in materials. i: the one-dimensional case". *Wave motion* 16.1, pp. 65–80.

69. Delsanto, P. et al. (1994). "Connection machine simulation of ultrasonic wave propagation in materials. ii: the two-dimensional case". *Wave motion* 20.4, pp. 295–314.

70. Diamanti, K. and Soutis, C. (2010). "Structural health monitoring techniques for aircraft composite structures". *Progress in aerospace sciences* 46.8, pp. 342–352.

71. Dimitriadis, E., Fuller, C., and Rogers, C. (1991). "Piezoelectric actuators for distributed vibration excitation of thin plates". *Journal of vibration and acoustics* 113.1, pp. 100–107.

72. Doddsa, J., Meyersb, F., and Loh, K. (2012). "Enhancing the piezoelectric performance of pvdf-trfe thin films using zinc oxide nanoparticles". *Proc. of spie vol.* Vol. 8345, pp. 834515–1.

73. Doebling, S. W., Farrar, C. R., Prime, M. B., et al. (1998). "A summary review of vibration-based damage identification methods". *Shock and vibration digest* 30.2, pp. 91–105.

74. Drinkwater, B. W. and Wilcox, P. D. (2006). "Ultrasonic arrays for non-destructive evaluation: a review". *Ndt & e international* 39.7, pp. 525–541.

75. Dunkin, J. W. (1965). "Computation of modal solutions in layered, elastic media at high frequencies". *Bulletin of the seismological society of america* 55.2, pp. 335–358.

76. Ebenezer, D. and Joseph, L. (2001). "Frequency-dependent open-circuit acoustic sensitivity of fluid-filled, coated, radially polarized piezoelectric ceramic cylindrical shells of arbitrary thickness and infinite length". *Ieee transactions on ultrasonics, ferroelectrics, and frequency control* 48.4, pp. 914–921.

77. Egusa, S. et al. (2010). "Multimaterial piezoelectric fibres". *Nature materials* 9.8, pp. 643–648.

78. Ekevid, T. and Wiberg, N.-E. (2002). "Wave propagation related to high-speed train: a scaled boundary fe-approach for unbounded domains". *Computer methods in applied mechanics and engineering* 191.36, pp. 3947–3964.

79. Erdogan, F. and Gupta, G. D. (1972). "On the numerical solution of singular integral equations(singular integral equations numerical solution from gauss-chebyshev formulas for mixed boundary value problems)". *Quarterly of applied mathematics* 29, pp. 525–534.

80. Eringen, A. C. (1980). "Mechanics of continua". *Huntington, ny, robert e. krieger publishing co., 1980. 606 p.*

81. Eringen, A. C. and Maugin, G. A. (2012). *Electrodynamics of continua i: foundations and solid media.* Springer Science & Business Media.

82. Estrada, R. and Kanwal, R. P. (2012). *Singular integral equations.* Springer Science & Business Media.

83. Fan, W. and Qiao, P. (2011). "Vibration-based damage identification methods: a review and comparative study". *Structural health monitoring* 10.1, pp. 83–111.

84. Farrar, C. R., Doebling, S. W., and Nix, D. A. (2001). "Vibration–based structural damage identification". *Philosophical transactions of the royal society of london. series a: mathematical, physical and engineering sciences* 359.1778, pp. 131–149.

85. Ferreira, A. D. B., Nóvoa, P. R., and Marques, A. T. (2016). "Multifunctional material systems: a state-of-the-art review". *Composite structures.*

86. Fousse, L. et al. (2007). "Mpfr: a multiple-precision binary floating-point library with correct rounding". *Acm transactions on mathematical software (toms)* 33.2, p. 13.

87. Fritzen, C., Schulte, R., and Jung, H. (2011). "A modelling approach for virtual development of wave based shm systems". *Journal of physics: conference series.* Vol. 305. IOP Publishing, p. 012071.

88. Fu, Y. Q. et al. (2017). "Advances in piezoelectric thin films for acoustic biosensors, acoustofluidics and lab-on-chip applications". *Progress in materials science* 89, pp. 31–91.

89. Gavete, L., Gavete, M., and Benito, J. (2003). "Improvements of generalized finite difference method and comparison with other meshless method". *Applied mathematical modelling* 27.10, pp. 831–847.

90. George, J., Ebenezer, D., and Bhattacharyya, S. (2010). "Receiving sensitivity and transmitting voltage response of a fluid loaded spherical piezoelectric transducer with an elastic coating". *The journal of the acoustical society of america* 128.4, pp. 1712–1720.

91. Gibson, R. (2010). "A review of recent research on mechanics of multifunctional composite materials and structures". *Composite structures* 92.12, pp. 2793–2810.

92. Giurgiutiu, V. (2007). *Structural health monitoring: with piezoelectric wafer active sensors.* Structures and Fracture ebook Collection Series. Elsevier Science. ISBN: 9780080556796.

93. Giurgiutiu, V. (2000). "Review of smart-materials actuation solutions for aeroelastic and vibration control". *Journal of intelligent material systems and structures* 11.7, pp. 525–544.

94. Giurgiutiu, V. and Cuc, A. (2005). "Embedded non-destructive evaluation for structural health monitoring, damage detection, and failure prevention". *Shock and vibration digest* 37.2, p. 83.

95. Giurgiutiu, V. and Santoni-Bottai, G. (2011). "Structural health monitoring of composite structures with piezoelectric-wafer active sensors". *Aiaa journal* 49.3, pp. 565–581.

96. Giurgiutiu, V., Zagrai, A., and Bao, J. (2004). "Damage identification in aging aircraft structures with piezoelectric wafer active sensors". *Journal of intelligent material systems and structures* 15.9-10, pp. 673–687.

97. Givoli, D. (1991). "Non-reflecting boundary conditions". *Journal of computational physics* 94.1, pp. 1–29.

98. Givoli, D. (2004). "High-order local non-reflecting boundary conditions: a review". *Wave motion* 39.4, pp. 319–326.

99. Givoli, D. and Keller, J. B. (1990). "Non-reflecting boundary conditions for elastic waves". *Wave motion* 12.3, pp. 261–279.

100. Gopalakrishnan, S. and Mitra, M. (2010). *Wavelet methods for dynamical problems: with application to metallic, composite, and nano-composite structures.* CRC.

101. Gopalakrishnan, S., Chakraborty, A., and Mahapatra, D. R. (2007). *Spectral finite element method: wave propagation, diagnostics and control in anisotropic and inhomogeneous structures.* Springer Science & Business Media.

102. Gowthaman, S. et al. (2016). "A review on energy harvesting using 3d printed fabrics for wearable electronics". *Journal of the institution of engineers (india): series c*, pp. 1–13.

103. GRAFF, K. F. (2012). "A history of ultrasonics". *Physical acoustics v15: principles and methods* 15.

104. Grefenstette, J. J. (1986). "Optimization of control parameters for genetic algorithms". *Ieee transactions on systems, man, and cybernetics* 16.1, pp. 122–128.

105. Grisso, B. L. (2004). "Considerations of the impedance method, wave propagation, and wireless systems for structural health monitoring". PhD thesis. Virginia Polytechnic Institute and State University.

106. Gruber, F. K., Marengo, E. A., and Devaney, A. J. (2004). "Time-reversal imaging with multiple signal classification considering multiple scattering between the targets". *The journal of the acoustical society of america* 115.6, pp. 3042–3047.

107. Gsell, D. and Dual, J. (2004). "Non-destructive evaluation of elastic material properties in anisotropic circular cylindrical structures". *Ultrasonics* 43.2, pp. 123–132.

108. Gurtin, M. E. (1973). "The linear theory of elasticity". *Linear theories of elasticity and thermoelasticity.* Springer, pp. 1–295.

109. Gustavo Mendez, C. et al. (2017). "Computational material design for acoustic cloaking". *International journal for numerical methods in engineering* 112.10, pp. 1353–1380.

110. Haberman, M. R. and Norris, A. N. (2016). "Introduction to the special issue on acoustic metamaterials". *The journal of the acoustical society of america* 139.6, pp. 3239–3239.

111. Hadimani, R. et al. (2013). "Continuous production of piezoelectric pvdf fibre for e-textile applications". *Smart materials and structures* 22.7, p. 075017.

112. Hagood, N. W. and Flotow, A. von (1991). "Damping of structural vibrations with piezoelectric materials and passive electrical networks". *Journal of sound and vibration* 146.2, pp. 243–268.

113. Hajati, A. et al. (2012). "Three-dimensional micro electromechanical system piezo-electric ultrasound transducer". *Applied physics letters* 101.25, p. 253101.

114. Harker, A. (1984). "Numerical modelling of the scattering of elastic waves in plates". *Journal of nondestructive evaluation* 4.2, pp. 89–106.

115. Hasheminejad, S. and Alaei-Varnosfaderani, M. (2012). "Vibroacoustic response and active control of a fluid-filled functionally graded piezoelectric material composite cylinder". *Journal of intelligent material systems and structures* 23.7, pp. 775–790.

116. Haskell, N. A. (1953). "The dispersion of surface waves on multilayered media". *Bulletin of the seismological society of america* 43.1, pp. 17–34.

117. Hastings, F. D., Schneider, J. B., and Broschat, S. L. (1996). "Application of the perfectly matched layer (pml) absorbing boundary condition to elastic wave propagation". *The journal of the acoustical society of america* 100.5, pp. 3061–3069.

118. Hayashi, T., Song, W.-J., and Rose, J. L. (2003). "Guided wave dispersion curves for a bar with an arbitrary cross-section, a rod and rail example". *Ultrasonics* 41.3, pp. 175–183.

119. Hiptmair, R., Moiola, A., and Perugia, I. (2015). "A survey of trefftz methods for the helmholtz equation". *Arxiv preprint arxiv:1506.04521.*

120. Honarvar, F. and Sinclair, A. (1996). "Acoustic wave scattering from transversely isotropic cylinders". *The journal of the acoustical society of america* 100, p. 57.

121. Honein, B., Braga, A., Barbone, P., and Herrmann, G. (1991). "Wave propagation in piezoelectric layered media with some applications". *Journal of intelligent material systems and structures* 2.4, pp. 542–557.

122. Hoseini, M. R., Zuo, M. J., and Wang, X. (2013). "Using ultrasonic pulse-echo b-scan signals for estimation of time of flight". *Measurement* 46.9, pp. 3593–3599.

123. Hossack, J. A. and Hayward, G. (1991). "Finite-element analysis of 1-3 composite transducers". *Ultrasonics, ferroelectrics and frequency control, ieee transactions on* 38.6, pp. 618–629.

124. Huang, G., Song, F., and Wang, X. (2010). "Quantitative modeling of coupled piezo-elastodynamic behavior of piezoelectric actuators bonded to an elastic medium for structural health monitoring: a review". *Sensors* 10.4, pp. 3681–3702.

125. Huang, W., Wang, Y., and Rokhlin, S. (1996). "Oblique scattering of an elastic wave from a multilayered cylinder in a solid. transfer matrix approach". *The journal of the acoustical society of america* 99, p. 2742.

126. Huang, W., Rokhlin, S., and Wang, Y. (1995). "Effect of fiber-matrix interphase on wave propagation along, and scattering from, multilayered fibres in composites. transfer matrix approach". *Ultrasonics* 33.5, pp. 365–375.

127. Ihn, J.-B. and Chang, F.-K. (2004). "Detection and monitoring of hidden fatigue crack growth using a built-in piezoelectric sensor/actuator network: i. diagnostics". *Smart materials and structures* 13.3, p. 609.

128. Ihn, J.-B. and Chang, F.-K. (2008). "Pitch-catch active sensing methods in structural health monitoring for aircraft structures". *Structural health monitoring* 7.1, pp. 5–19.

129. Jung, J. and Taciroglu, E. (2016). "A divide-alternate-and-conquer approach for localization and shape identification of multiple scatterers in heterogeneous media using dynamic xfem". *Inverse problems and imaging* 10.1, pp. 165–193.

130. Karal Jr, F. C. and Keller, J. B. (1959). "Elastic wave propagation in homogeneous and inhomogeneous media". *The journal of the acoustical society of america* 31.6, pp. 694–705.

131. Kawamura, S., Ito, S., Yoshida, T., and Minamoto, H. (2011). "Isolation effect of a dynamic damper and a trench on ground vibration caused by a construction machine". *Applied acoustics* 72.4, pp. 151–156.

132. Kennett, B. and Kerry, N. (1979). "Seismic waves in a stratified half space". *Geophysical journal international* 57.3, pp. 557–583.

133. Kessler, D. and Kosloff, D. (1991). "Elastic wave propagation using cylindrical coordinates". *Geophysics* 56.12, pp. 2080–2089.

134. Kessler, S. S., Spearing, S. M., and Soutis, C. (2002). "Damage detection in composite materials using lamb wave methods". *Smart materials and structures* 11.2, p. 269.

135. Kessler, S. S. (2002). "Piezoelectric-based in-situ damage detection of composite materials for structural health monitoring systems". PhD thesis. Massachusetts Institute of Technology.

136. Kim, J. O. and Lee, J. G. (2007). "Dynamic characteristics of piezoelectric cylindrical transducers with radial polarization". *Journal of sound and vibration* 300.1, pp. 241–249.

137. Knopoff, L. (1964). "A matrix method for elastic wave problems". *Bulletin of the seismological society of america* 54.1, pp. 431–438.

138. Konka, H., Wahab, M., and Lian, K. (2011). "Detection and damage monitoring in composite structures using piezoelectrics". *Mechanics of time-dependent materials and processes in conventional and multifunctional materials, volume 3*. Springer, pp. 171–184.

139. Kraut, E. A. (1975). "Review of theories of scattering of elastic waves by cracks".

140. Kreja, I. (2011). "A literature review on computational models for laminated composite and sandwich panels". *Central european journal of engineering*, pp. 1–22.

141. Krenk, S. (1975). "On the use of the interpolation polynomial for solutions of singular integral equations". *Quarterly of applied mathematics* 32.4, pp. 479–484.

142. Kuang, Z.-B. (2014). *Theory of electroelasticity*. Springer.

143. Kushch, V., Shmegera, S., Brøndsted, P., and Mishnaevsky Jr, L. (2011). "Numerical simulation of progressive debonding in fiber reinforced composite under transverse loading". *International journal of engineering science* 49.1, pp. 17–29.

144. Lagasse, P. (1973). "Finite element analysis of piezoelectric elastic waveguides". *Sonics and ultrasonics, ieee transactions on* 20.4, pp. 354–359.

145. Lan, M. and Wei, P. J. (2013). "The propagation of in-plane waves in multi-layered elastic/piezoelectric composite structures with imperfect interface". *Advanced materials research*. Vol. 750. Trans Tech Publ, pp. 95–98.

146. Larbi, W. and Deü, J. (2011). "A 3d state-space solution for free-vibration analysis of a radially polarized laminated piezoelectric cylinder filled with fluid". *Journal of sound and vibration* 330.2, pp. 162–181.

147. Lee, B. and Staszewski, W. (2003a). "Modelling of lamb waves for damage detection in metallic structures: part i. wave propagation". *Smart materials and structures* 12.5, p. 804.

148. Lee, B. and Staszewski, W. (2003b). "Modelling of lamb waves for damage detection in metallic structures: part ii. wave interactions with damage". *Smart materials and structures* 12.5, p. 815.

149. Lee, C. and Tarbutton, J. A. (2014). "Electric poling-assisted additive manufacturing process for pvdf polymer-based piezoelectric device applications". *Smart materials and structures* 23.9, p. 095044.

150. Lee, C. M. (2006). "Guided elastic waves in structures with an arbitrary cross-section". PhD thesis. The Pennsylvania State University.

151. Lee, J.-R. and Dhital, D. (2013). "Review of flaws and damages in space launch vehicle: structures". *Journal of intelligent material systems and structures* 24.1, pp. 4–20.

152. Lee, U., Kim, J., Leung, A., et al. (2000). "The spectral element method in structural dynamics". *Shock and vibration digest* 32.6, pp. 451–465.

153. Lee, V. W. and Cao, H. (1989). "Diffraction of sv waves by circular canyons of various depths". *Journal of engineering mechanics* 115.9, pp. 2035–2056.

154. Lee, V. and Karl, J. (1992). "Diffraction of sv waves by underground, circular, cylindrical cavities". *Soil dynamics and earthquake engineering* 11.8, pp. 445–456.

155. Lee, W.-M. and Chen, J.-T. (2010). "Scattering of flexural wave in a thin plate with multiple circular inclusions by using the null-field integral equation approach". *Journal of sound and vibration* 329.8, pp. 1042–1061.

156. Lerch, R. (1990). "Simulation of piezoelectric devices by two-and three-dimensional finite elements". *Ultrasonics, ferroelectrics and frequency control, ieee transactions on* 37.3, pp. 233–247.

157. Li, M., Yuan, J., Guan, D., and Chen, W. (2011). "Application of piezoelectric fiber composite actuator to aircraft wing for aerodynamic performance improvement". *Science china technological sciences* 54.2, pp. 395–402.

158. Librescu, L. and Schmidt, R. (2001). "A general linear theory of laminated composite shells featuring interlaminar bonding imperfections". *International journal of solids and structures* 38.19, pp. 3355–3375.

159. Lin, X.-j., Zhou, K.-c., Zhang, X.-y., and Zhang, D. (2013). "Development, modeling and application of piezoelectric fiber composites". *Transactions of nonferrous metals society of china* 23.1, pp. 98–107.

160. Lin, Y. and Sodano, H. (2008). "Concept and model of a piezoelectric structural fiber for multifunctional composites". *Composites science and technology* 68.7, pp. 1911–1918.

161. Lin, Y. and Sodano, H. A. (2013). "Active fiber composites: modeling, fabrication, and characterization". *Smart composites: mechanics and design*, p. 99.

162. Linton, C. and Evans, D. (1990). "The interaction of waves with arrays of vertical circular cylinders". *Journal of fluid mechanics* 215, pp. 549–569.

163. Lippmann, M. (1881). "On the principle of the conservation of electricity-french to english".

164. Liu, G. and Jerry, S. Q. (2003). "A non-reflecting boundary for analyzing wave propagation using the finite element method". *Finite elements in analysis and design* 39.5-6, pp. 403–417.

165. Liu, G.-R. and Han, X. (2003). *Computational inverse techniques in nondestructive evaluation*. CRC press.

166. Liu, W. and Kriz, R. D. (1998). "Multiple wave scattering in fiber-reinforced composites: micromechanical viewpoint". *Wave motion* 27.3, pp. 223–244.

167. Livani, M., Khaji, N., and Zakian, P. (2018). "Identification of multiple flaws in 2d structures using dynamic extended spectral finite element method with a universally enhanced meta-heuristic optimizer". *Structural and multidisciplinary optimization* 57.2, pp. 605–623.

168. Lonkar, K. and Chang, F.-K. (2014). "Modeling of piezo-induced ultrasonic wave propagation in composite structures using layered solid spectral element". *Structural health monitoring* 13.1, pp. 50–67.

169. Love, A. E. H. (2013). *A treatise on the mathematical theory of elasticity*. Cambridge university press.

170. Lowe, M. J. (1995). "Matrix techniques for modeling ultrasonic waves in multi-layered media". *Ultrasonics, ferroelectrics and frequency control, ieee transactions on* 42.4, pp. 525–542.

171. Lü, C., Yang, J., Wang, J., and Chen, W. (2009). "Power transmission through a hollow cylinder by acoustic waves and piezoelectric transducers with radial polarization". *Journal of sound and vibration* 325.4, pp. 989–999.

172. Lu, X., Qu, H., and Skorobogatiy, M. (2017). "Piezoelectric microstructured fibers via drawing of multimaterial preforms". *Scientific reports* 7.1, p. 2907.

173. Lynch, J. P. and Loh, K. J. (2006). "A summary review of wireless sensors and sensor networks for structural health monitoring". *Shock and vibration digest* 38.2, pp. 91–130.

174. Malvern, L. (1969). *Introduction to the mechanics of a continuous medium*. Prentice-Hall series in engineering of the physical sciences. Prentice-Hall.

175. Manbachi, A. and Cobbold, R. S. (2011). "Development and application of piezoelectric materials for ultrasound generation and detection". *Ultrasound* 19.4, pp. 187–196.

176. Manolis, G. D. and Beskos, D. E. (1988). *Boundary element methods in elastodynamics*. Unwin Hyman London.

177. Marengo, E. A., Gruber, F. K., and Simonetti, F. (2007). "Time-reversal music imaging of extended targets". *Ieee transactions on image processing* 16.8, pp. 1967–1984.

178. Martin, P. A. (2006). *Multiple scattering: interaction of time-harmonic waves with n obstacles*. 107. Cambridge University Press.

179. Matt, H., Bartoli, I., and Scalea, F. L. di (2005). "Ultrasonic guided wave monitoring of composite wing skin-to-spar bonded joints in aerospace structures". *The journal of the acoustical society of america* 118.4, pp. 2240–2252.

180. Maugin, G. A. (2013). *Continuum mechanics of electromagnetic solids*. Vol. 33. Elsevier.

181. McKeighen, R. (2001). "Finite element simulation and modeling of 2-d arrays for 3-d ultrasonic imaging." *Ieee transactions on ultrasonics, ferroelectrics, and frequency control* 48.5, pp. 1395–1405.

182. Meguid, S. and Wang, X. (1995). "On the dynamic interaction between a microdefect and a main crack". *Proceedings of the royal society of london. series a: mathematical and physical sciences* 448.1934, p. 449.

183. Meguid, S. and Wang, X. (2000). "An elastodynamic analysis of interacting inhomogeneities in advanced composites". *Mechanics of materials* 32.12, pp. 797–805.

184. Meguid, S. A. and Wang, X. (2013). "Elasto-dynamic behaviour of interacting inhomogeneities and cracks". *Icf13*.

185. Melenk, J. M. and Babuška, I. (1996). "The partition of unity finite element method: basic theory and applications". *Computer methods in applied mechanics and engineering* 139.1-4, pp. 289–314.

186. Mills, D. M. and Smith, S. W. (2002). "Multi-layered pzt/polymer composites to increase signal-to-noise ratio and resolution for medical ultrasound transducers. ii. thick film technology". *Ultrasonics, ferroelectrics and frequency control, ieee transactions on* 49.7, pp. 1005–1014.

187. Mitra, M. and Gopalakrishnan, S. (2016). "Guided wave based structural health monitoring: a review". *Smart materials and structures* 25.5, p. 053001.

188. Moes, N., Dolbow, J., and Belytschko, T. (1999). "A finite element method for crack growth without remeshing". *International journal for numerical methods in engineering* 46.1, pp. 131–150.

189. Morse, P. and Feshbach, H. (1953). *Methods of theoretical physics*. International series in pure and applied physics v. 2. McGraw-Hill.

190. Mow, C. and Pao, Y. (1971). *The diffraction of elastic waves and dynamic stress concentrations*. Rand Corporation.

191. Mu, J. and Rose, J. L. (2008). "Guided wave propagation and mode differentiation in hollow cylinders with viscoelastic coatings". *The journal of the acoustical society of america* 124, p. 866.

192. Mukdadi, O. M. and Datta, S. K. (2003). "Transient ultrasonic guided waves in layered plates with rectangular cross section". *Journal of applied physics* 93.11, pp. 9360–9370.

193. Mukdadi, O. M. et al. (2002). "Elastic guided waves in a layered plate with rectangular cross section". *The journal of the acoustical society of america* 112.5, pp. 1766–1779.

194. Mykhaskiv, V. (2005). "Transient response of a plane rigid inclusion to an incident wave in an elastic solid". *Wave motion* 41.2, pp. 133–144.

195. Nakatani, K. et al. (2007). "An experimental study on the identification of delamination in a composite material by the passive electric potential ct method". *Measurement science and technology* 18, p. 49.

196. Nayfeh, A. (1995). *Wave propagation in layered anisotropic media: with applications to composites.* Vol. 39. North Holland.

197. Nayfeh, A., Abdelrahman, W., and Nagy, P. (2000). "Analyses of axisymmetric waves in layered piezoelectric rods and their composites". *The journal of the acoustical society of america* 108, p. 1496.

198. Nayfeh, A. and Nagy, P. (1996). "General study of axisymmetric waves in layered anisotropic fibers and their composites". *Journal of the acoustical society of america* 99.2, pp. 931–941.

199. Nelson, R., Dong, S., and Kalra, R. (1971). "Vibrations and waves in laminated orthotropic circular cylinders". *Journal of sound and vibration* 18.3, pp. 429–444.

200. Nemat-Nasser, S. and Srivastava, A. (2011). "Overall dynamic constitutive relations of layered elastic composites". *Journal of the mechanics and physics of solids* 59.10, pp. 1953–1965.

201. Nilsson, E. et al. (2013). "Poling and characterization of piezoelectric polymer fibers for use in textile sensors". *Sensors and actuators a: physical* 201, pp. 477–486.

202. Norris, A. and Shuvalov, A. (2010). "Wave impedance matrices for cylindrically anisotropic radially inhomogeneous elastic solids". *The quarterly journal of mechanics and applied mathematics* 63.4, pp. 401–435.

203. Norris, A. and Shuvalov, A. (2012). "Elastodynamics of radially inhomogeneous spherically anisotropic elastic materials in the stroh formalism". *Proceedings of the royal society a: mathematical, physical and engineering science* 468.2138, pp. 467–484.

204. Norris, A. N. and Conoir, J.-M. (2011). "Multiple scattering by cylinders immersed in fluid: high order approximations for the effective wavenumbers". *The journal of the acoustical society of america* 129.1, pp. 104–113.

205. Oden, J. T. and Reddy, J. N. (2012). *Variational methods in theoretical mechanics*. Springer Science & Business Media.

206. Opsal, J. L. and Visscher, W. M. (1985). "Theory of elastic wave scattering: applications of the method of optimal truncation". *Journal of applied physics* 58.3, pp. 1102–1115.

207. Ostachowicz, W. and Kudela, P. (2011). "Elastic waves for damage detection in structures". *New trends in vibration based structural health monitoring*. Springer, pp. 247–302.

208. Pao, Y.-H. (1978). "Electromagnetic forces in deformable continua". *In: mechanics today. volume 4.(a78-35706 14-70) new york, pergamon press, inc., 1978, p. 209-305. nsf-supported research.* Vol. 4, pp. 209–305.

209. Pao, Y. (1983). "Elastic waves in solids". *Journal of applied mechanics* 50, p. 1152.

210. Patera, A. T. (1984). "A spectral element method for fluid dynamics: laminar flow in a channel expansion". *Journal of computational physics* 54.3, pp. 468–488.

211. Pauley, K. and Dong, S. (1976). "Analysis of plane waves in laminated piezoelectric plates". *Wave electronics* 1, pp. 265–285.

212. Pettit, J., Walker, A., Cawley, P., and Lowe, M. (2014). "A stiffness reduction method for efficient absorption of waves at boundaries for use in commercial finite element codes". *Ultrasonics* 54.7, pp. 1868–1879.

213. Predoi, M. V., Castaings, M., Hosten, B., and Bacon, C. (2007). "Wave propagation along transversely periodic structures". *The journal of the acoustical society of america* 121.4, pp. 1935–1944.

214. Qian, Z., Jin, F., Kishimoto, K., and Lu, T. (2008). "Scattering of elastic p-waves by a transversely isotropic piezoelectric cylinder embedded in a polymer matrix". *Smart materials and structures* 17, p. 045019.

215. Rabinovich, D., Givoli, D., and Vigdergauz, S. (2007). "Xfem-based crack detection scheme using a genetic algorithm". *International journal for numerical methods in engineering* 71.9, pp. 1051–1080.

216. Raghavan, A. and Cesnik, C. (2007). "Review of guided-wave structural health monitoring". *Shock and vibration digest* 39.2, pp. 91–116.

217. Raghavan, A. and Cesnik, C. E. (2005). "Piezoelectric-actuator excited-wave field solutions for guided-wave structural health monitoring". *Smart structures and materials.* International Society for Optics and Photonics, pp. 313–323.

218. Raghavan, A., Cesnik, C. E., et al. (2007). "3-d elasticity-based modeling of anisotropic piezocomposite transducers for guided wave structural health monitoring". *Transactions-american society of mechanical engineers journal of vibration and acoustics* 129.6, p. 739.

219. Rajabi, M. and Hasheminejad, S. (2009). "Acoustic resonance scattering from a multilayered cylindrical shell with imperfect bonding". *Ultrasonics* 49.8, pp. 682–695.

220. Rajabi, M. and Mojahed, A. (2018). "Active acoustic cloaking spherical shells". *Acta acustica united with acustica* 104.1, pp. 5–12.

221. Rajagopal, P. et al. (2012). "On the use of absorbing layers to simulate the propagation of elastic waves in unbounded isotropic media using commercially available finite element packages". *Ndt & e international* 51, pp. 30–40.

222. Ramadan, K. S., Sameoto, D., and Evoy, S. (2014). "A review of piezoelectric polymers as functional materials for electromechanical transducers". *Smart materials and structures* 23.3, p. 033001.

223. Ramesh, R. and Ebenezer, D. (2005). "Analysis of axially polarized piezoelectric ceramic rings". *Ferroelectrics* 323.1, pp. 17–23.

224. Rathod, V., Mahapatra, D. R., Jain, A., and Gayathri, A. (2010). "Characterization of a large-area pvdf thin film for electro-mechanical and ultrasonic sensing applications". *Sensors and actuators a: physical* 163.1, pp. 164–171.

225. Ray, L. R., Koh, B.-H., and Tian, L. (2000). "Damage detection and vibration control in smart plates: towards multifunctional smart structures". *Journal of intelligent material systems and structures* 11.9, pp. 725–739.

226. Ricks, D. and Schmidt, H. (1994). "A numerically stable global matrix method for cylindrically layered shells excited by ring forces". *The journal of the acoustical society of america* 95, p. 3339.

227. Rizzi, S. and Doyle, J. (1992). "A spectral element approach to wave motion in layered solids". *Journal of vibration and acoustics* 114.4, pp. 569–577.

228. Rizzo, F., Shippy, D., and Rezayat, M. (1985). "A boundary integral equation method for radiation and scattering of elastic waves in three dimensions". *International journal for numerical methods in engineering* 21.1, pp. 115–129.

229. Rokhlin, S. and Huang, W. (1992). "Ultrasonic wave interaction with a thin anisotropic layer between two anisotropic solids: exact and asymptotic-boundary-condition methods". *The journal of the acoustical society of america* 92, p. 1729.

230. Rokhlin, S. and Huang, W. (1993). "Ultrasonic wave interaction with a thin anisotropic layer between two anisotropic solids. ii. second-order asymptotic boundary conditions". *The journal of the acoustical society of america* 94, p. 3405.

231. Rose, J. L. (2002). "A baseline and vision of ultrasonic guided wave inspection potential". *Journal of pressure vessel technology* 124.3, pp. 273–282.

232. Ross, R. (2016). "Integrated vehicle health management in aerospace structures". *Structural health monitoring (shm) in aerospace structures*. Elsevier, pp. 3–31.

233. Ruffino, E. and Delsanto, P. (1999). "Problems of accuracy and reliability in 2-d lisa simulations". *Computers & mathematics with applications* 38.5, pp. 89–97.

234. Saini, R. K., Bajpai, J., and Bajpai, A. (2013). "Advances in smart wearable systems". *Responsive materials and methods: state-of-the-art stimuli-responsive materials and their applications*, p. 169.

235. Sancar, S. and Pao, Y.-H. (1981). "Spectral analysis of elastic pulses backscattered from two cylindrical cavities in a solid. part i". *The journal of the acoustical society of america* 69.6, pp. 1591–1596.

236. Sancar, S. and Sachse, W. (1981). "Spectral analysis of elastic pulses backscattered from two cylindrical cavities in a solid. part ii". *The journal of the acoustical society of america* 69.6, pp. 1597–1609.

237. Satyanarayan, L., Mohan, K., Krishnamurthy, C., and Balasubramaniam, K. (2008). "Finite difference time domain simulation of ultrasonic phased array sector scan for imaging cracks in large pipes, elbows, and tee sections". *Research in nondestructive evaluation* 19.2, pp. 61–86.

238. Satyanarayan, L., Sridhar, C., Krishnamurthy, C., and Balasubramaniam, K. (2007). "Simulation of ultrasonic phased array technique for imaging and sizing of defects using longitudinal waves". *International journal of pressure vessels and piping* 84.12, pp. 716–729.

239. Scandrett, C. and Achenbach, J. (1987). "Time-domain finite difference calculations for interaction of an ultrasonic wave with a surface-breaking crack". *Wave motion* 9.2, pp. 171–190.

240. Schaefer, R. (2007). *Foundations of global genetic optimization*. Studies in Computational Intelligence. Springer Berlin Heidelberg. ISBN: 9783540731924.

241. Schmerr Jr, L. W. (2014). *Fundamentals of ultrasonic phased arrays*. Vol. 215. Springer.

242. Schmerr, L. (2013). *Fundamentals of ultrasonic nondestructive evaluation: a modeling approach*. Springer US. ISBN: 9781489901422.

243. Schmerr, L. W. (2016). "An ultrasonic system". *Fundamentals of ultrasonic nondestructive evaluation*. Springer, pp. 1–13.

244. Schmerr, L. and Song, J.-S. (2007). *Ultrasonic nondestructive evaluation systems*. Springer.

245. Schmidt, D., Hillger, W., Szewieczek, A., and Sinapius, M. (2013). "Structural health monitoring based on guided waves". *Adaptive, tolerant and efficient composite structures*. Springer, pp. 449–462.

246. Schulz, M. J., Sundaresan, M. J., Ghoshal, A., and Pai, P. F. (2000). "Active fiber composites for structural health monitoring". *Spie's 7th annual international symposium on smart structures and materials*. International Society for Optics and Photonics, pp. 13–24.

247. Sedighi, M. and Shakeri, M. (2009). "A three-dimensional elasticity solution of functionally graded piezoelectric cylindrical panels". *Smart materials and structures* 18, p. 055015.

248. Shen, Y. and Cesnik, C. E. (2017). "Modeling of nonlinear interactions between guided waves and fatigue cracks using local interaction simulation approach". *Ultrasonics* 74, pp. 106–123.

249. Siao, J.-T., Dong, S., and Song, J. (1994). "Frequency spectra of laminated piezoelectric cylinders". *Journal of vibration and acoustics* 116.3, pp. 364–370.

250. Sinclair, C. E. (2009). "Elastic wave modelling in anisotropic media using the spectral-element method". PhD thesis. The University of Adelaide.

251. Sirca Jr, G. and Adeli, H. (2012). "System identification in structural engineering". *Scientia iranica* 19.6, pp. 1355–1364.

252. Sodagar, S. and Honarvar, F. (2010). "Improvements to the mathematical model of acoustic wave scattering from transversely isotropic cylinders". *Scientia iranica transaction b: mechanical engineering* 17.3, pp. 157–166.

253. Sodano, H. A., Inman, D. J., and Park, G. (2004). "A review of power harvesting from vibration using piezoelectric materials". *Shock and vibration digest* 36.3, pp. 197–206.

254. Sohn, H., Park, H. W., Law, K. H., and Farrar, C. R. (2007). "Combination of a time reversal process and a consecutiv outlier analysis for baseline-free damage diagnosis". *Journal of intelligent material systems and structures* 18.4, pp. 335–346.

255. Sohn, H. et al. (2004). *A review of structural health monitoring literature*. Los Alamos National Laboratory Los Alamos,, New Mexico.

256. Sprague, M. and Geers, T. (2008). "Legendre spectral finite elements for structural dynamics analysis". *Communications in numerical methods in engineering* 24.12, pp. 1953–1965.

257. Sridharan, C., Muralidharan, A., Balasubramaniam, K., and Krishnamurthy, C. (2006). "A simulation study on the impact echo array technique for concrete structure ndt". *Nondestructive testing and evaluation* 21.3-4, pp. 123–140.

258. Standard, A. (1987). "Standard 176-1987". *Ieee standard on piezoelectricity.*

259. Staszewski, W., Boller, C., and Tomlinson, G. R. (2004). *Health monitoring of aerospace structures: smart sensor technologies and signal processing*. Wiley. com.

260. Stepinski, T., Uhl, T., and Staszewski, W. (2013). *Advanced structural damage detection: from theory to engineering applications*. Wiley. ISBN: 9781118536117.

261. Stolyarov, A. M. et al. (2013). "Multimaterial functional fibers". *Optical fiber communication conference*. Optical Society of America.

262. Su, Z. and Ye, L. (2009). *Identification of damage using lamb waves: from fundamentals to applications*. Lecture Notes in Applied and Computational Mechanics. Springer London. ISBN: 9781848827844.

263. Su, Z., Ye, L., and Lu, Y. (2006). "Guided lamb waves for identification of damage in composite structures: a review". *Journal of sound and vibration* 295.3, pp. 753–780.

264. Sumiya, T., Biwa, S., and Haïat, G. (2013). "Computational multiple scattering analysis of elastic waves in unidirectional composites". *Wave motion* 50.2, pp. 253–270.

265. Sun, C. and Vaidya, R. (1996). "Prediction of composite properties from a representative volume element". *Composites science and technology* 56.2, pp. 171–179.

266. Sun, H., Waisman, H., and Betti, R. (2013). "Nondestructive identification of multiple flaws using xfem and a topologically adapting artificial bee colony algorithm". *International journal for numerical methods in engineering* 95.10, pp. 871–900.

267. Sun, H., Waisman, H., and Betti, R. (2014a). "A multiscale flaw detection algorithm based on xfem". *International journal for numerical methods in engineering* 100.7, pp. 477–503.

268. Sun, H., Waisman, H., and Betti, R. (2014b). "A two-scale algorithm for detection of multiple flaws in structures modeled with xfem". *Proc. of spie vol.* Vol. 9063, pp. 906322–1.

269. Sun, H., Waisman, H., and Betti, R. (2016). "A sweeping window method for detection of flaws using an explicit dynamic xfem and absorbing boundary layers". *International journal for numerical methods in engineering* 105.13, pp. 1014–1040.

270. Taciroglu, E., Liu, C., Dong, S., and Chun, C. (2004). "Analysis of laminated piezoelectric circular cylinders under axisymmetric mechanical and electrical loads with a semi-analytic finite element method". *International journal of solids and structures* 41.18, pp. 5185–5208.

271. Tao, G., Abouraddy, A. F., Stolyarov, A. M., and Fink, Y. (2015). "Multimaterial fibers". *Lab-on-fiber technology*. Springer, pp. 1–26.

272. Tao, G., Stolyarov, A. M., and Abouraddy, A. F. (2012). "Multimaterial fibers". *International journal of applied glass science* 3.4, pp. 349–368.

273. Thompson, R. B. (1983). "Quantitative ultrasonic nondestructive evaluation methods". *Journal of applied mechanics* 50.4b, pp. 1191–1201.

274. Thompson, R. B. and Thompson, D. O. (1985). "Ultrasonics in nondestructive evaluation". *Proceedings of the ieee* 73.12, pp. 1716–1755.

275. Thompson, R. and Wadley, H. (1989). "The use of elastic wave-material structure interaction theories in nde modeling". *Critical reviews in solid state and material sciences* 16.1, pp. 37–89.

276. Thomson, W. (1950). "Transmission of elastic waves through a stratified solid medium". *Journal of applied physics* 21.2. Introduced Transfer matrix, pp. 89–93.

277. Towfighi, S. and Ehsani, M. (2002). "Elastic wave propagation in circumferential direction in anisotropic cylindrical curved plates". *Journal of applied mechanics* 69, p. 283.

278. Trefethen, L. N. (2000). *Spectral methods in matlab*. Vol. 10. Siam.

279. Twersky, V. (1952). "Multiple scattering of radiation by an arbitrary configuration of parallel cylinders". *The journal of the acoustical society of america* 24.1, pp. 42–46.

280. Tzou, H.-S. (2012). *Piezoelectric shells: distributed sensing and control of continua*. Vol. 19. Springer Science & Business Media.

281. Uchino, K. (1996). *Piezoelectric actuators and ultrasonic motors*. Vol. 1. Springer Science & Business Media.

282. Ursu, I., Enciu, D., and Toader, A. (2017). "Towards structural health monitoring of space vehicles". *Aircraft engineering and aerospace technology* 89.6, pp. 920–927.

283. Varadan, V. V. (1978). "Scattering matrix for elastic waves. ii. application to elliptic cylinders". *The journal of the acoustical society of america* 63, p. 1014.

284. Varadan, V. V. and Varadan, V. K. (1979). "Scattering matrix for elastic waves. iii. application to spheroids". *The journal of the acoustical society of america* 65, p. 896.

285. Varadan, V. K., Varadan, V. V., and Pao, Y.-H. (1978). "Multiple scattering of elastic waves by cylinders of arbitrary cross section. i. sh waves". *The journal of the acoustical society of america* 63, p. 1310.

286. Varatharajulu, V. and Pao, Y.-H. (1976). "Scattering matrix for elastic waves. i. theory". *The journal of the acoustical society of america* 60, p. 556.

287. Visscher, W. M. (1981). "Calculation of the scattering of elastic waves from a penny-shaped crack by the method of optimal truncation". *Wave motion* 3.1, pp. 49–69.

288. Wang, C. H., Rose, J. T., and Chang, F.-K. (2004). "A synthetic time-reversal imaging method for structural health monitoring". *Smart materials and structures* 13.2, p. 415.

289. Wang, J., Duan, H., Zhang, Z., and Huang, Z. (2005). "An anti-interpenetration model and connections between interphase and interface models in particle-reinforced composites". *International journal of mechanical sciences* 47.4, pp. 701–718.

290. Wang, K., Wang, B., and Kitamura, T. (2016). "A review on the application of modified continuum models in modeling and simulation of nanostructures". *Acta mechanica sinica* 32.1, pp. 83–100.

291. Wang, L. and Rokhlin, S. I. (2004). "Modeling of wave propagation in layered piezoelectric media by a recursive asymptotic method". *Ultrasonics, ferroelectrics and frequency control, ieee transactions on* 51.9, pp. 1060–1071.

292. Wang, S. et al. (2017). "Flexible piezoelectric fibers for acoustic sensing and positioning". *Advanced electronic materials* 3.3.

293. Wang, X. and Zhong, Z. (2003). "Three-dimensional solution of smart laminated anisotropic circular cylindrical shells with imperfect bonding". *International journal of solids and structures* 40.22, pp. 5901–5921.

294. Wang, X., Pan, E., and Roy, A. (2007). "Scattering of antiplane shear wave by a piezoelectric circular cylinder with an imperfect interface". *Acta mechanica* 193.3-4, pp. 177–195.

295. Wang, X. and Huang, G. (2002). "Wave propagation induced by multiple piezoelectric actuators in electromechanical structures". *Journal of pressure vessel technology* 124.3, pp. 311–318.

296. Wang, X. and Huang, G. (2003). "On the elastic wave propagation induced by a network of piezoelectric actuators". *Acta mechanica* 160.1-2, pp. 1–18.

297. Wang, X. and Huang, G. (2004a). "Study of elastic wave propagation induced by piezoelectric actuators for crack identification". *International journal of fracture* 126.3, pp. 287–306.

298. Wang, X. and Huang, G. (2008). "On the dynamic behavior of piezoelectric sensors and actuators embedded in elastic media". *Acta mechanica* 197.1, pp. 1–17.

299. Wang, X. and Meguid, S. (1997). "Diffraction of sh-wave by interacting matrix crack and an inhomogeneity". *Journal of applied mechanics* 64.3, pp. 568–575.

300. Wang, X. and Meguid, S. (1999). "Dynamic interaction between a matrix crack and a circular inhomogeneity with a distinct interphase". *International journal of solids and structures* 36.4, pp. 517–531.

301. Wang, X. D. and Huang, G. (2004b). "Identification of embedded cracks using back-propagating elastic waves". *Inverse problems* 20.5, p. 1393.

302. Wang, X., Abdel-Gawad, S., Huangchao, Y., and Wang, C. (2015). "On the pseudo-incident wave technique for interacting inhomogeneities in electromechanical problems". *6th international conference on computational methods for coupled problems in science and engineering*. Venice, Italy, pp. 440–451.

303. Waterman, P. (1969). "New formulation of acoustic scattering". *The journal of the acoustical society of america* 45.6, pp. 1417–1429.

304. Waterman, P. (1976). "Matrix theory of elastic wave scattering". *The journal of the acoustical society of america* 60.3, pp. 567–580.

305. Waterman, P. (2009). "T-matrix methods in acoustic scattering". *The journal of the acoustical society of america* 125.1, pp. 42–51.

306. Watson, G. (1995). *A treatise on the theory of bessel functions*. Cambridge Mathematical Library. Cambridge University Press. ISBN: 9780521483919.

307. Wilkie, W. K. et al. (2000). "Low-cost piezocomposite actuator for structural control applications". *Spie's 7th annual international symposium on smart structures and materials*. International Society for Optics and Photonics, pp. 323–334.

308. Willberg, C., Duczek, S., Vivar-Perez, J. M., and Ahmad, Z. (2015). "Simulation methods for guided wave-based structural health monitoring: a review". *Applied mechanics reviews* 67.1, p. 010803.

309. Williams, R. B., Grimsley, B. W., Inman, D. J., and Wilkie, W. K. (2002a). "Manufacturing and mechanics-based characterization of macro fiber composite actuators". *Asme 2002 international mechanical engineering congress and exposition*. American Society of Mechanical Engineers, pp. 79–89.

310. Williams, R., Park, G., Inman, D., and Wilkie, W. (2002b). "An overview of composite actuators with piezoceramic fibers". *Proc. 20th international modal analysis conference.*

311. Wilm, M., Ballandras, S., and Laude, V. (2004). "Non periodic acoustic devices radiating in semi-infinite solids simulated by a combination of finite element analysis and a boundary element method". *Ultrasonics symposium, 2004 ieee.* Vol. 3. IEEE, pp. 1620–1623.

312. Wilm, M. et al. (2005). "Three-dimensional modelling of micromachined-ultrasonic-transducer arrays operating in water". *Ultrasonics* 43.6, pp. 457–465.

313. Winston, P. (1984). *Artificial intelligence.* Addison-Wesley series in computer science. Addison-Wesley. ISBN: 9780201082593.

314. Wolf, J. and Song, C. (1996). *Finite-element modelling of unbounded media.* Wiley.

315. Wu, C., Chiu, K., Wang, Y., et al. (2008). "A review on the three-dimensional analytical approaches of multilayered and functionally graded piezoelectric plates and shells". *Cmc: computers, materials, & continua* 8.2, pp. 93–132.

316. Wu, T.-T. and Gong, J.-H. (1993). "Application of transient elastic waves to the nondestructive evaluation of plate structure with cavity or inclusion". *The journal of the acoustical society of america* 94.3, pp. 1453–1460.

317. Yang, J. (2006). *An introduction to the theory of piezoelectricity.* Advances in Mechanics and Mathematics. Springer US. ISBN: 9780387235462.

318. Yang, R.-B. and Mal, A. K. (1994). "Multiple scattering of elastic waves in a fiber-reinforced composite". *Journal of the mechanics and physics of solids* 42.12, pp. 1945–1968.

319. Yang, R.-B. and Mal, A. K. (1996). "Elastic waves in a composite containing inhomogeneous fibers". *International journal of engineering science* 34.1, pp. 67–79.

320. Yang, Y., Cascante, G., and Anna Polak, M. (2009). "Depth detection of surface-breaking cracks in concrete plates using fundamental lamb modes". *Ndt & e international* 42.6, pp. 501–512.

321. Yin, X., Morris, S. A., and O'Brien Jr, W. D. (2003). "Ultrasonic pulse-echo subwavelength defect detection mechanism: experiment and simulation". *Journal of nondestructive evaluation* 22.3, pp. 103–115.

322. Zagrai, A. et al. (2010). "Piezoelectric wafer active sensor structural health monitoring of space structures". *Journal of intelligent material systems and structures* 21.9, pp. 921–940.

323. Zhang, J., Li, T., Ye, W., and Zhu, X. (2010). "Acoustic radiation of damped cylindrical shell with arbitrary thickness in the fluid field". *Journal of marine science and application* 9.4, pp. 431–438.

324. Zhao, X. et al. (2007). "Active health monitoring of an aircraft wing with embedded piezoelectric sensor-actuator network: i. defect detection, localization and growth monitoring". *Smart materials and structures* 16.4, p. 1208.

325. Zhong, Z. and Meguid, S. (1997). "Interfacial debonding of a circular inhomogeneity in piezoelectric materials". *International journal of solids and structures* 34.16, pp. 1965–1984.

326. Zhou, C., Su, Z., and Cheng, L. (2011). "Probability-based diagnostic imaging using hybrid features extracted from ultrasonic lamb wave signals". *Smart materials and structures* 20.12, p. 125005.

327. Zhou, P., Wu, C., and Ma, G. (2006). "Contact resistance prediction and structure optimization of bipolar plates". *Journal of power sources* 159.2, pp. 1115–1122.

328. Zhu, R., Huang, G., and Yuan, F. (2013). "Fast damage imaging using the time-reversal technique in the frequency–wavenumber domain". *Smart materials and structures* 22.7, p. 075028.

329. Zou, N. and Nehorai, A. (2009). "Circular acoustic vector-sensor array for mode beamforming". *Signal processing, ieee transactions on* 57.8, pp. 3041–3052.

Appendices

Appendices for chapter 2

Appendix A

The coupled mathematical theory of elastodynamics and electrostatic of a piezoelectric solid continuum is formulated in terms of body force $\mathbf{b}$, surface force (traction) $\mathbf{t}$, stress tensor $\boldsymbol{\sigma}$, electric displacement vector $\mathbf{D}$, strain tensor $\boldsymbol{\varepsilon}$, electric field $\mathbf{E}$, displacement vector $\mathbf{u}$ and electric potential of a piezoelectric body ϕ. The theory uses piezoelectric materials as the solid continuum constitutive coupling the elastic behavior of a material to its behavior as a dielectric through the piezoelectric effects (Eringen, 1980; Pao, 1978). The theory assumes that the piezoelectric solid continuum is subject to small deviations i.e. the material remains elastic and dielectric during deviations with linear deformations within the elastic material zone. Piezoelectric materials are anisotropic elastic coupled with dielectric properties which are generally characterized by 21 independent stiffness coefficients $\mathbf{C}$ and piezoelectric coupling coefficients $\mathbf{e}$. In addition to the displacement, $\mathbf{u}(\mathbf{x}, t)$, the velocity and acceleration of a particle in the body are of interest. The mass density ρ becomes an important parameter in measuring the inertia. The general governing equations are a set of equations describing the physics, the geometry, the constitutive, the boundary conditions and the initial conditions defined for a body of volume V and enclosed by a surface S (Gurtin, 1973; Kuang, 2014).

Physical Equations:

The linear momentum equations per unit volume describing the motion of and the electric charge equation of a continuum solid:

$$\nabla \cdot \boldsymbol{\sigma} = -\mathbf{b} + \rho \ddot{\mathbf{u}} \qquad \mathbf{x} \text{ in } V \qquad\qquad (2.\text{A}.1)$$

where ∇ is the delta operator, $\boldsymbol{\sigma}$ is the second order stress tensor, $\mathbf{b}$ is the body force vector, ρ is the mass density and $\ddot{\mathbf{u}}$ is the acceleration vector.

$$\nabla \cdot \mathbf{D} = \rho_f \qquad \mathbf{x} \text{ in } V \tag{2.A.2}$$

where $\mathbf{D}$ is electrical displacement vector which is equivalent to electric flux density measured in Coulombs as a charge unit per square meter and ρ_f free charge density $\rho_f = 0$. Equations (2.A.1) and (2.A.2) are alternatively called after their developers as Cauchy's linear momentum also according to Malvern (1969) Cauchy's first law of motion [1] and Gauss's law (the first equation of Maxwell's four equations of classical electrodynamics).

Geometric Equations:

$$\boldsymbol{\varepsilon} = \frac{1}{2} \left[\nabla \mathbf{u} + (\nabla \mathbf{u})^{\mathrm{T}} \right] \qquad \mathbf{x} \text{ in } V \tag{2.A.3}$$

where $\boldsymbol{\varepsilon}$ is the second order strain tensor and $\mathbf{u}$ is the displacement vector.

$$\mathbf{E} = - \nabla \phi \tag{2.A.4}$$

where $\mathbf{E}$ is the electric field vector measured in volts per meter, ϕ is the electric potential typically measured in volts (a scalar quantity).

Constitutive Equations:

$$\begin{bmatrix} \boldsymbol{\sigma} \\ \mathbf{D} \end{bmatrix} = \begin{bmatrix} \mathbf{C} & -\mathbf{e}^T \\ \mathbf{e} & \boldsymbol{\epsilon}^s \end{bmatrix} \begin{bmatrix} \boldsymbol{\varepsilon} \\ \mathbf{E} \end{bmatrix} \qquad \mathbf{x} \text{ in } V \tag{2.A.5}$$

where $\mathbf{C}$ is a fourth order tensor of the elastic constitutive coefficients, $\boldsymbol{\epsilon}^s$ is a second order tensor of the dielectric or permittivity coefficients, $\mathbf{e}$ is a third order tensor of the piezoelectric stress effect or piezoelectric coupling, and the superscript s means measured at constant strain (which will be suppressed from here-after). Using equation (2.A.5), the stress can be written as

$$\boldsymbol{\sigma} = \frac{1}{2} \mathbf{C} : \left[\nabla \mathbf{u} + (\nabla \mathbf{u})^{\mathrm{T}} \right] - \mathbf{e}^T \mathbf{E} \tag{2.A.6}$$

---

[1] Cauchy's first law of motion uses the principle of conservation of linear momentum while Cauchy's second law of motion uses the principle of conservation of angular momentum.

with the colon in equation (2.A.6) representing the double dot product (Kuang, 2014; Sinclair, 2009) between the forth order tensor and second order tensor which produce a second order stress tensor,

$$\boldsymbol{\sigma} = \mathbf{C} : \boldsymbol{\varepsilon} = C_{ijkl}\varepsilon_{kl}\mathbf{e}_i\mathbf{e}_j \tag{2.A.7}$$

where $\mathbf{e}_i$ and $\mathbf{e}_j$ are unit vectors in the i and j direction respectively. Equation (2.A.6) is the direct piezoelectric effect where an applied mechanical stress, $\boldsymbol{\sigma}$, produces an electric field polarization, $\mathbf{E}$, which is directly proportional in amplitude to the stress.

Boundary Conditions:

$$\mathbf{u}(\mathbf{x}, t) = \bar{\mathbf{u}} \qquad \mathbf{x} \text{ on } S_1$$
$$\mathbf{n} \cdot \boldsymbol{\sigma}(\mathbf{x}, t) = \bar{\mathbf{t}} \qquad \mathbf{x} \text{ on } S_2 \tag{2.A.8}$$

$$\phi(\mathbf{x}, t) = \bar{\phi} \qquad \mathbf{x} \text{ on } S_3$$
$$\mathbf{n} \cdot \mathbf{D}(\mathbf{x}, t) = \bar{d} \qquad \mathbf{x} \text{ on } S_4 \tag{2.A.9}$$

Initial Conditions:

$$\mathbf{u}(\mathbf{x}, t = 0) = \mathbf{u}_0$$
$$\dot{\mathbf{u}}(\mathbf{x}, t = 0) = \mathbf{v}_0 \qquad \mathbf{x} \text{ in } V \tag{2.A.10}$$

where $\bar{\mathbf{u}}$, $\bar{\mathbf{t}}$, $\bar{\phi}$, $\bar{d}$, $\mathbf{u}_0$, and $\mathbf{v}_0$ are prescribed quantities.

Isotropic elastic materials can be specialized from anisotropic material by characterizing them with any two elastic moduli (two material constants) such as Young's modulus, shear modulus, Poisson's ratio, and Lame's constants. Any homogeneous isotropic linear elastic materials can be uniquely determined by Lame constants λ, μ as

$$\mathbf{C} = \lambda\mathbf{I}^4 + 2\mu\mathbf{II} \tag{2.A.11}$$

where

$$\mathbf{I}^4 = \delta_{ij}\delta_{kl}\mathbf{e}_i\mathbf{e}_j\mathbf{e}_k\mathbf{e}_l$$

is the fourth-order identity tensor and

$$\mathbf{II} = \frac{1}{2}\left(\delta_{ik}\delta_{jl}\mathbf{e}_i\mathbf{e}_k\mathbf{e}_j\mathbf{e}_l + \delta_{il}\delta_{jk}\mathbf{e}_i\mathbf{e}_l\mathbf{e}_j\mathbf{e}_k\right)$$

is the symmetric part of the fourth-rank identity tensor.

Combining equations (2.A.1) and (2.A.6) with the symmetry in $C_{ijkl} = C_{ijlk}$ for an elastic non piezoelectric (ignoring piezoelectric coupling) results in

$$\boldsymbol{\nabla} \cdot \mathbf{C} : [\boldsymbol{\nabla}\mathbf{u}] + \mathbf{b} = \rho\ddot{\mathbf{u}} \qquad (2.A.12)$$

by using tensor properties, and the fact that $\mathbf{C}$ is a constant tensor,

$$\mathbf{C} : \boldsymbol{\nabla}^2\mathbf{u} + \mathbf{b} = \rho\ddot{\mathbf{u}} \qquad (2.A.13)$$

Equation (2.A.6) can be specialized for an isotropic elastic material (for non piezoelectric-ignoring piezoelectric coefficients) as

$$\boldsymbol{\sigma} = \lambda \left(\boldsymbol{\nabla} \cdot \mathbf{u}\right) \mathbf{I} + 2\mu \left[\boldsymbol{\nabla}\mathbf{u} + \left(\boldsymbol{\nabla}\mathbf{u}\right)^{\mathrm{T}}\right] \qquad (2.A.14)$$

where $\mathbf{I} = \delta_{ij}\mathbf{e}_i\mathbf{e}_j$ is the second-order identity tensor, λ and μ are Lame elastic moduli constants. Equations (2.A.1), and (2.A.14) can be combined into one vector equation for $\mathbf{u}\left(\mathbf{x}, t\right)$ resulting in Navier-Cauchy equation of motion,

$$\left(\lambda + 2\mu\right) \boldsymbol{\nabla}\boldsymbol{\nabla} \cdot \mathbf{u} + \mu\boldsymbol{\nabla}^2\mathbf{u} + \mathbf{b} = \rho\ddot{\mathbf{u}} \qquad (2.A.15)$$

for an isotropic homogeneous material. The same equation can be derived from equation (2.A.13) by specializing the anisotropic material to an isotropic material. Equations (2.A.12-2.A.15) form a set of coupled differential equations to be solved analytically or numerically.

Appendix B

Consider first the simple case of steady state waves in which the time dependence is harmonic; that is,

$$\mathbf{u}\left(\mathbf{x}, t\right) = Ue^{-i\omega t}, \qquad (2.B.1)$$

and the media is an isotropic homogeneous free of sources $\mathbf{b}$ in V and $\bar{\mathbf{t}}$ and $\bar{\mathbf{u}}$ on S vanish. The initial conditions are omitted and $\ddot{\mathbf{u}} = -\omega^2\mathbf{u}$. Free steady-state waves in an infinite medium, a half space medium, a plate, a circular cylinder, and a sphere have

all been investigated (Pao, 1983) by decomposing the displacement $\mathbf{u}$ into (Achenbach, 1972; Pao, 1983)

$$\mathbf{u} = \boldsymbol{\nabla}\varphi + \boldsymbol{\nabla}\times\boldsymbol{\psi} \tag{2.B.2}$$

where φ is a scalar potential displacement associated with P-waves and $\boldsymbol{\psi}$ is a potential displacement vector associated with S-waves. The two displacement potentials satisfy Helmholtz equation

$$\left(\boldsymbol{\nabla}^2 + k_L^2\right)\varphi = 0, \quad \left(\boldsymbol{\nabla}^2 + k_T^2\right)\psi = 0 \tag{2.B.3}$$

k_L and k_T are wave numbers given by

$$k_L = \frac{\omega}{c_L}, \quad k_T = \frac{\omega}{c_T} \tag{2.B.4}$$

where c_L and c_T are the longitudinal and transverse wave speeds of the elastic medium,

$$c_L = \sqrt{\frac{\lambda + 2\mu}{\rho}}, \quad c_T = \sqrt{\frac{\mu}{\rho}} \ . \tag{2.B.5}$$

Using separation of variables, φ and ψ can be written as the multiplication of functions in a coordinate system. For a cylindrical coordinate system $(r,\ \theta,\ z)$, the multiplied functions take the form of

$$f(r,\theta,z) = R(r)\Theta(\theta)Z(z)e^{-i\omega t} \tag{2.B.6}$$

with Bessel as the solution to the differential of the radial function and complex exponential as the solution of the other functions.

Consider second the complicated case of an anisotropic media under a simple steady state waves are represented by

$$\mathbf{u} = \mathbf{u}^A e^{\mathbf{k}\cdot\mathbf{r}-\omega t} \tag{2.B.7}$$

where $\mathbf{u}^A$ is the displacement amplitude vector, wave-number vector $\mathbf{k} = k\mathbf{n}$, $\mathbf{n}$ is the wave propagation direction, and $\mathbf{r}$ is the chosen coordinate. The displacement amplitude vector can be written as $\mathbf{u}^A = A\hat{\mathbf{u}}$ (Rokhlin and Huang, 1992).

A harmonic response is assumed, that is $\mathbf{u} = \mathbf{u}^A e^{i(k\boldsymbol{n}\cdot\boldsymbol{r}-\omega t)}$, with the kinematics for harmonic displacement $\mathbf{u} = \mathbf{u}^A e^{i(k\mathbf{n}\cdot\mathbf{r}-\omega t)} = \mathbf{u}^A e^{ik(\mathbf{n}\cdot\mathbf{r}-ct)}$

$$\dot{\mathbf{u}} = -i\omega\mathbf{u},$$

$$\ddot{\mathbf{u}} = -\omega^2\mathbf{u}.$$

This leads to an eigen value problem with its characteristic equation is called Christoffel equation (Nayfeh, 1995) as

$$\left(\mathbf{\Lambda} - c^2\mathbf{I}\right)\hat{\mathbf{u}} = \mathbf{0} \tag{2.B.8}$$

where $\mathbf{\Lambda} = C_{ijkl}n_j n_l \mathbf{e}_j \mathbf{e}_l$ is a second order tensor (3×3 real symmetric matrix, the eigen values are real and the associated eigen vectors are orthogonal with the dependency on propagation direction n_j, n_l which is problematic in anisotropic materials) and $\mathbf{e}_j$ is the unit vector in j direction (Nayfeh, 1995, p34). The eigen values $c = \dfrac{\omega}{k}$ are the phase velocities $\mathbf{v} = c\mathbf{n}$ and its eigen vectors directions $\hat{\mathbf{u}}$ called polarizations directions (polarization here is the direction of displacement vector).

At the interface of two perfectly bonded layers in contact, the boundary conditions (2.A.8) and (2.A.9) are replaced by the continuity condition,

$$\mathbf{u}_i = \mathbf{u}_{i+1} \text{ and } \mathbf{n} \cdot \boldsymbol{\sigma}_i = \mathbf{n} \cdot \boldsymbol{\sigma}_{i+1} \text{ in } S_i \tag{2.B.9}$$

$$\phi_{0i} = \phi_{0i+1} \text{ and } \mathbf{n} \cdot \mathbf{D}_i = \mathbf{n} \cdot \mathbf{D}_{i+1} \text{ in } S_i \tag{2.B.10}$$

Appendix C

In FE rather than using the equations of motion (equations (2.A.1) and (2.A.2)) and the associated boundary conditions (equations (2.A.8) and (2.A.9)) directly which are called the strong form, an integrated form is used by dotting the physical governing equations (2.A.1) and (2.A.2) with an arbitrary test vector then integrating by parts over the model volume, and imposing the free boundary conditions (equations (2.A.8) and (2.A.9)). The resulting form is called the weak form and its matrix form is

$$\mathbf{M}\ddot{\mathbf{u}}_i + \mathbf{C}\dot{\mathbf{u}} + \mathbf{K}_{uu}\mathbf{u} + \mathbf{K}_{u\phi}\{\phi_i\} = \mathbf{f} \tag{2.C.1}$$

$$\mathbf{K}_{u\phi}^T \mathbf{u} + \mathbf{K}_{\phi\phi} \{\phi_i\} = \mathbf{q} \tag{2.C.2}$$

where $\mathbf{M}$, $\mathbf{C}$, $\mathbf{K}_{uu}$, $\mathbf{K}_{u\phi}$, $\mathbf{K}_{\phi\phi}$, $\mathbf{f}$, and $\mathbf{q}$ are the mass, damping, stiffness, piezoelectric coupling stiffness, dielectric and charge vector stiffness respectively, the superscript T represents transpose (Allik and Hughes, 1970; Lonkar and Chang, 2014).

Appendices for chapter 3

The general elastic solution of an isotropic layer can be obtained using displacement potentials. The results are presented in this section. The displacements can be expressed in terms of the displacement potentials as:

$$u_r = \varphi_{,r} + \frac{1}{r}\psi_{,\theta}, \ u_\theta = \frac{1}{r}\varphi_{,\theta} - \psi_{,r}.$$

The stress components are

$$\sigma_r = \lambda\nabla^2\varphi + 2\mu\left[\varphi_{,r^2} + \left(\frac{1}{r}\psi_{,\theta}\right)_{,r}\right]$$

$$\sigma_\theta = \lambda\nabla^2\varphi + 2\mu\left[\frac{1}{r}\left(\varphi_{,r} + \frac{1}{r}\varphi_{,\theta^2}\right) + \frac{1}{r}\left(\frac{1}{r}\psi_{,\theta} - \psi_{,r\theta}\right)\right]$$

$$\sigma_{r\theta} = \mu\left[2\left(\frac{1}{r}\varphi_{,r\theta} - \frac{1}{r^2}\varphi_{,\theta}\right) + \left(\frac{1}{r^2}\psi_{,\theta^2} - r\left(\frac{1}{r}\psi_{,r}\right)_{,r}\right)\right].$$

Using the general solution of the displacement potentials given by equations (3.13) and (3.14). The displacement and stress fields can be obtained as

$$u_r = \sum_{n=0}^{\infty} k_L \left\{ J'_n(k_L r) \begin{pmatrix} A_n^{(1)} \\ A_n^{(2)} \end{pmatrix}^T + H'_n(k_L r) \begin{pmatrix} A_n^{(3)} \\ A_n^{(4)} \end{pmatrix}^T \right\} \begin{pmatrix} \cos(n\theta) \\ \sin(n\theta) \end{pmatrix}$$
$$+ \frac{n}{r} \left\{ J_n(k_s r) \begin{pmatrix} -A_n^{(5)} \\ A_n^{(6)} \end{pmatrix}^T + H_n(k_s r) \begin{pmatrix} -A_n^{(7)} \\ A_n^{(8)} \end{pmatrix}^T \right\} \begin{pmatrix} \sin(n\theta) \\ \cos(n\theta) \end{pmatrix}$$

$$u_\theta = \sum_{n=0}^{\infty} \frac{n}{r} \left\{ J_n\left(k_L r\right) \begin{pmatrix} -A_n^{(1)} \\ A_n^{(2)} \end{pmatrix}^T + H_n\left(k_L r\right) \begin{pmatrix} -A_n^{(3)} \\ A_n^{(4)} \end{pmatrix}^T \right\} \begin{pmatrix} \sin\left(n\theta\right) \\ \cos\left(n\theta\right) \end{pmatrix}$$

$$-k \left\{ J_n'\left(k_s r\right) \begin{pmatrix} A_n^{(5)} \\ A_n^{(6)} \end{pmatrix}^T + H_n'\left(k_s r\right) \begin{pmatrix} A_n^{(7)} \\ A_n^{(8)} \end{pmatrix}^T \right\} \begin{pmatrix} \cos\left(n\theta\right) \\ \sin\left(n\theta\right) \end{pmatrix}$$

$$\sigma_r = \sum_{n=0}^{\infty} \left(J_n'\left(k_L r\right) k_L \frac{\lambda}{r} + J_n''\left(k_L r\right) k_L^2\left(\lambda + 2\mu\right) - J_n\left(k_L r\right) n^2 \frac{\lambda}{r^2} \right) \begin{pmatrix} A_n^{(1)} \\ A_n^{(2)} \end{pmatrix}^T \begin{pmatrix} \cos\left(n\theta\right) \\ \sin\left(n\theta\right) \end{pmatrix}$$

$$+ \sum_{n=0}^{\infty} \left(H_n'\left(k_L r\right) k_L \frac{\lambda}{r} + H_n''\left(k_L r\right) k_L^2\left(\lambda + 2\mu\right) - H_n\left(k_L r\right) n^2 \frac{\lambda}{r^2} \right) \begin{pmatrix} A_n^{(3)} \\ A_n^{(4)} \end{pmatrix}^T \begin{pmatrix} \cos\left(n\theta\right) \\ \sin\left(n\theta\right) \end{pmatrix}$$

$$+ \sum_{n=0}^{\infty} \left(\frac{J_n\left(k_s r\right)}{r} - J_n'\left(k_s r\right) k_s \right) \frac{2\mu n}{r} \begin{pmatrix} A_n^{(5)} \\ -A_n^{(6)} \end{pmatrix}^T \begin{pmatrix} \sin\left(n\theta\right) \\ \cos\left(n\theta\right) \end{pmatrix}$$

$$+ \sum_{n=0}^{\infty} \left(\frac{H_n\left(k_s r\right)}{r} - H_n'\left(k_s r\right) k_s \right) \frac{2\mu n}{r} \begin{pmatrix} A_n^{(7)} \\ -A_n^{(8)} \end{pmatrix}^T \begin{pmatrix} \sin\left(n\theta\right) \\ \cos\left(n\theta\right) \end{pmatrix}$$

$$\sigma_{r\theta} = \mu \left\{ \sum_{n=0}^{\infty} \left(\frac{J_n\left(k_L r\right)}{r} - J_n'\left(k_L r\right) k_L \right) \frac{2n}{r} \begin{pmatrix} A_n^{(1)} \\ -A_n^{(2)} \end{pmatrix}^T \begin{pmatrix} \sin\left(n\theta\right) \\ \cos\left(n\theta\right) \end{pmatrix} \right.$$

$$+ \sum_{n=0}^{\infty} \left(\frac{H_n\left(k_L r\right)}{r} - H_n'\left(k_L r\right) k_L \right) \frac{2n}{r} \begin{pmatrix} A_n^{(3)} \\ -A_n^{(4)} \end{pmatrix}^T \begin{pmatrix} \sin\left(n\theta\right) \\ \cos\left(n\theta\right) \end{pmatrix}$$

$$+ \sum_{n=0}^{\infty} \left(-J_n''\left(k_s r\right) k_s^2 - J\left(k_s r\right) \frac{n^2}{r^2} + J_n'\left(k_s r\right) \frac{k_s}{r} \right) \begin{pmatrix} A_n^{(5)} \\ A_n^{(6)} \end{pmatrix}^T \begin{pmatrix} \cos\left(n\theta\right) \\ \sin\left(n\theta\right) \end{pmatrix}$$

$$\left. + \sum_{n=0}^{\infty} \left(-H_n''\left(k_s r\right) k_s^2 - H_n\left(k_s r\right) \frac{n^2}{r^2} + H_n'\left(k_s r\right) \frac{k_s}{r} \right) \begin{pmatrix} A_n^{(7)} \\ A_n^{(8)} \end{pmatrix}^T \begin{pmatrix} \cos\left(n\theta\right) \\ \sin\left(n\theta\right) \end{pmatrix} \right\}$$

$$\sigma_\theta = \sum_{n=0}^{\infty} \left(J_n''\left(k_L r\right) k_L^2 \lambda - J_n\left(k_L r\right)\left(\lambda + 2\mu\right)\frac{n^2}{r^2} + \frac{\left(\lambda + 2\mu\right)}{r} J_n'\left(k_L r\right) k_L \right) \begin{pmatrix} A_n^{(1)} \\ A_n^{(2)} \end{pmatrix}^T \begin{pmatrix} \cos\left(n\theta\right) \\ \sin\left(n\theta\right) \end{pmatrix}$$

$$+ \sum_{n=0}^{\infty} \left(\lambda H_n''\left(k_L r\right) k_L^2 - H_n\left(k_L r\right)\left(\lambda + 2\mu\right)\frac{n^2}{r^2} + H_n'\left(k_L r\right) k_L \frac{\left(\lambda + 2\mu\right)}{r} \right) \begin{pmatrix} A_n^{(3)} \\ A_n^{(4)} \end{pmatrix}^T \begin{pmatrix} \cos\left(n\theta\right) \\ \sin\left(n\theta\right) \end{pmatrix}$$

$$+ \sum_{n=0}^{\infty} \left(\frac{J_n\left(k_s r\right)}{r} - J_n'\left(k_s r\right) k_s \right) \frac{2\mu n}{r} \begin{pmatrix} -A_n^{(5)} \\ A_n^{(6)} \end{pmatrix}^T \begin{pmatrix} \sin\left(n\theta\right) \\ \cos\left(n\theta\right) \end{pmatrix}$$

$$+ \sum_{n=0}^{\infty} \left(\frac{H_n\left(k_s r\right)}{r} - H_n'\left(k_s r\right) k_s \right) \frac{2\mu n}{r} \begin{pmatrix} A_n^{(7)} \\ -A_n^{(8)} \end{pmatrix}^T \begin{pmatrix} \sin\left(n\theta\right) \\ \cos\left(n\theta\right) \end{pmatrix} .$$

Appendices for chapter 4

Appendix A

The stress fields in terms of displacement potentials are (Mow and Pao, 1971)

$$\sigma_r = \lambda \nabla^2 \varphi + 2\mu \left[\varphi_{,rr} + \left(\frac{1}{r} \psi_{,\theta} \right)_{,r} \right],$$ (4.A.1)

$$\sigma_\theta = \lambda \nabla^2 \varphi + 2\mu \left[\frac{1}{r} \left(\varphi_{,r} + \frac{1}{r} \varphi_{,\theta^2} \right) + \frac{1}{r} \left(\frac{1}{r} \psi_{,\theta} - \psi_{,r\theta} \right) \right],$$ (4.A.2)

$$\sigma_{r\theta} = \mu \left[2 \left(\frac{1}{r} \varphi_{,r\theta} - \frac{1}{r^2} \varphi_{,\theta} \right) + \left(\frac{1}{r^2} \psi_{,\theta\theta} - r \left(\frac{1}{r} \psi_{,r} \right)_r \right) \right].$$ (4.A.3)

Using the general solution of the displacement potentials given by equations (4.52) and (4.53). The displacement and stress fields can be obtained as

$$\varphi = \sum_{n=-\infty}^{\infty} \left(\begin{array}{cc} J_n(k_L r), & H_n^{(1)}(k_L r) \end{array} \right) \left(\begin{array}{c} A_n^{(1)} \\ A_n^{(2)} \end{array} \right) e^{in\theta}$$ (4.A.4)

$$\psi = \sum_{n=-\infty}^{\infty} \left(\begin{array}{cc} J_n(k_s r), & H_n^{(1)}(k_s r) \end{array} \right) \left(\begin{array}{c} A_n^{(3)} \\ A_n^{(4)} \end{array} \right) e^{in\theta}$$ (4.A.5)

$$u_r = \sum_{n=0}^{\infty} k_L \left(\begin{array}{c} J_n'(k_L r) \\ H_n'(k_L r) \end{array} \right)^T \left(\begin{array}{c} A_n^{(1)} \\ A_n^{(2)} \end{array} \right) e^{in\theta} + \frac{in}{r} \left(\begin{array}{c} J_n(k_s r) \\ H_n(k_s r) \end{array} \right)^T \left(\begin{array}{c} A_n^{(3)} \\ A_n^{(4)} \end{array} \right) e^{in\theta}$$

$$u_\theta = \sum_{n=0}^{\infty} \frac{in}{r} \left(\begin{array}{c} J_n(k_L r) \\ H_n(k_L r) \end{array} \right)^T \left(\begin{array}{c} A_n^{(1)} \\ A_n^{(2)} \end{array} \right) e^{in\theta} - k_s \left(\begin{array}{c} J_n'(k_s r) \\ H_n'(k_s r) \end{array} \right)^T \left(\begin{array}{c} A_n^{(3)} \\ A_n^{(4)} \end{array} \right) e^{in\theta}$$

$$\sigma_r = \sum_{n=0}^{\infty} \begin{pmatrix} (2\mu)\, k_L^2 J_n''\,(k_L r) - \lambda k_L^2 J_n\,(k_L r) \\ (2\mu)\, k_L^2 H_n''\,(k_L r) - \lambda k_L^2 H_n\,(k_L r) \end{pmatrix}^T \begin{pmatrix} A_n^{(1)} \\ A_n^{(2)} \end{pmatrix} e^{in\theta}$$

$$+ \sum_{n=0}^{\infty} \frac{2\mu i n}{r} \begin{pmatrix} J_n'\,(k_s r)\, k_s - \dfrac{1}{r} J_n\,(k_s r) \\ H_n'\,(k_s r)\, k_s - \dfrac{1}{r} H_n\,(k_s r) \end{pmatrix}^T \begin{pmatrix} A_n^{(3)} \\ A_n^{(4)} \end{pmatrix} e^{in\theta}$$

$$\sigma_\theta = \sum_{n=0}^{\infty} \begin{pmatrix} \left(-\lambda k_L^2 - 2\mu \left(\dfrac{n}{r}\right)^2\right) J_n\,(k_L r) + \dfrac{2\mu}{r} J_n'\,(k_L r)\, k_L \\ \left(-\lambda k_L^2 - 2\mu \left(\dfrac{n}{r}\right)^2\right) H_n\,(k_L r) + \dfrac{2\mu}{r} H_n'\,(k_L r)\, k_L \end{pmatrix} \begin{pmatrix} A_n^{(1)} \\ A_n^{(2)} \end{pmatrix} e^{in\theta}$$

$$+ \sum_{n=0}^{\infty} \frac{2\mu i n}{r} \begin{pmatrix} \dfrac{J_n(k_s r)}{r} - J_n'\,(k_s r)\, k_s \\ \dfrac{H_n(k_s r)}{r} - H_n'\,(k_s r)\, k_s \end{pmatrix}^T \begin{pmatrix} A_n^{(3)} \\ A_n^{(4)} \end{pmatrix} e^{in\theta}$$

$$\sigma_{r\theta} = \mu \left\{ \sum_{n=0}^{\infty} \frac{2in}{r} \begin{pmatrix} \left(k_L J_n'\,(k_L r) - \frac{1}{r} J_n\,(k_L r)\right) \\ \left(k_L H_n'\,(k_L r) - \frac{1}{r} H_n\,(k_L r)\right) \end{pmatrix}^T \begin{pmatrix} A_n^{(1)} \\ A_n^{(2)} \end{pmatrix} \right.$$

$$+ \sum_{n=0}^{\infty} \begin{pmatrix} -J\,(k_s r)\, \frac{n^2}{r^2} - J_n''\,(k_s r)\, k_s^2 + J_n'\,(k_s r)\, \frac{k_s}{r} \\ -H_n\,(k_s r)\, \frac{n^2}{r^2} - H_n''\,(k_s r)\, k_s^2 + H_n'\,(k_s r)\, \frac{k_s}{r} \end{pmatrix}^T \left. \begin{pmatrix} A_n^{(3)} \\ A_n^{(4)} \end{pmatrix} \right\} e^{in\theta}$$

Appendix B

The elements of the coefficient matrix , $\mathbf{Q}_n$, for a linear elastic isotropic layer with dielectric properties are presented here.

$$\mathbf{Q}_n = \begin{bmatrix} k_L J_n'\,(k_L r) & k_L H_n'\,(k_L r) & \frac{in}{r} J_n\,(k_s r) & \frac{in}{r} H_n\,(k_s r) & 0 & 0 \\ \frac{in}{r} J_n\,(k_L r) & \frac{in}{r} H_n\,(k_L r) & -k_s J_n'\,(k_s r) & -k_s H_n'\,(k_s r) & 0 & 0 \\ Q_{31} & Q_{32} & Q_{33} & Q_{34} & 0 & 0 \\ Q_{41} & Q_{42} & Q_{43} & Q_{44} & 0 & 0 \\ 0 & 0 & 0 & 0 & Q_{55} & Q_{56} \\ 0 & 0 & 0 & 0 & Q_{65} & Q_{66} \end{bmatrix}$$

Using the general solution of the displacement potentials given by equations (4.52) and (4.53). Standard displacement and stress field can be obtained as

$$Q_{31} = J'_n(k_L r) k_L \frac{\lambda}{r} + J''_n(k_L r) k_L^2 (\lambda + 2\mu) - J_n(k_L r) n^2 \frac{\lambda}{r^2}$$

$$Q_{32} = H'_n(k_L r) k_L \frac{\lambda}{r} + H''_n(k_L r) k_L^2 (\lambda + 2\mu) - H_n(k_L r) n^2 \frac{\lambda}{r^2}$$

$$Q_{33} = \left(\frac{J_n(k_s r)}{r} - J'_n(k_s r) k_s \right) \frac{2\mu i n}{r}$$

$$Q_{34} = \left(\frac{H_n(k_s r)}{r} - H'_n(k_s r) k_s \right) \frac{2\mu i n}{r}$$

$$Q_{41} = 2\mu \frac{in}{r} \left(J'_n(k_L r) k_L - \frac{J_n(k_L r)}{r} \right)$$

$$Q_{42} = 2\mu \frac{in}{r} \left(H'_n(k_L r) k_L - \frac{H_n(k_L r)}{r} \right)$$

$$Q_{43} = \mu \left(-J''_n(k_s r) k_s^2 - J(k_s r) \frac{n^2}{r^2} + J'_n(k_s r) \frac{k_s}{r} \right)$$

$$Q_{43} = \mu \left(-H''_n(k_s r) k_s^2 - H_n(k_s r) \frac{n^2}{r^2} + H'_n(k_s r) \frac{k_s}{r} \right)$$

$$Q_{55} = J_n(r), \ Q_{56} = H_n(r)$$

$$Q_{65} = -\epsilon J'_n(r), \ Q_{65} = -\epsilon H'_n(r)$$

General fluid coefficient matrix

$$\mathbf{Q}_n^F = \begin{bmatrix} \frac{1}{\omega \rho^{(F)} c_L^{(F)}} J_1\left(k_L^{(F)} r\right) & \frac{1}{\omega \rho^{(F)} c_L^{(F)}} H_1\left(k_L^{(F)} r\right) \\ -J_0\left(k_L^{(F)} r\right) & -H_0\left(k_L^{(F)} r\right) \end{bmatrix}$$

Piezoelectric coefficient matrix

$$\mathbf{Q}_n^{(p)} = \begin{bmatrix} J_\gamma\left(\kappa^{(p)} r\right) & H_\gamma\left(\kappa^{(p)} r\right) \\ \overline{c}_{33}^{(p)} J_{\gamma,r}\left(\kappa^{(p)} r\right) + \frac{\overline{c}_{23}^{(p)}}{r} J_\gamma\left(\kappa^{(p)} r\right) & \overline{c}_{33}^{(p)} H_{\gamma,r}\left(\kappa^{(p)} r\right) + \frac{\overline{c}_{23}^{(p)}}{r} H_\gamma\left(\kappa^{(p)} r\right) \end{bmatrix}$$

General elastic layer coefficient matrix

$$\mathbf{Q}^{(e)}(r) = \begin{bmatrix} J_\gamma\left(\kappa^{(e)} r\right) & H_\gamma\left(\kappa^{(e)} r\right) \\ \overline{c}_{33}^{(e)} J_{\gamma,r}\left(\kappa^{(e)} r\right) + \frac{\overline{c}_{23}^{(e)}}{r} J_\gamma\left(\kappa^{(e)} r\right) & \overline{c}_{33}^{(e)} H_{\gamma,r}\left(\kappa^{(e)} r\right) + \frac{\overline{c}_{23}^{(e)}}{r} H_\gamma\left(\kappa^{(e)} r\right) \end{bmatrix}$$

Proposed layer model matrices

$$\mathbf{K}^+ = \begin{bmatrix} -\frac{c_{33}}{h} - \frac{c_{23}}{2\bar{r}} & \frac{1}{2} \\ \frac{\rho h \omega^2}{2} - \frac{h c_{22}}{2\bar{r}^2} - \frac{c_{23}}{\bar{r}} & \frac{r^+}{\bar{r}} \end{bmatrix}^{-1} \tag{4.B.1}$$

$$\mathbf{K}^- = -\begin{bmatrix} \frac{c_{33}}{h} - \frac{c_{23}}{2\bar{r}} & \frac{1}{2} \\ \frac{\rho h \omega^2}{2} - \frac{h c_{22}}{2\bar{r}^2} + \frac{c_{23}}{\bar{r}} & \frac{-r^-}{\bar{r}} \end{bmatrix}^{-1} \tag{4.B.2}$$

Exact solution derivation

-Using equation (4.63) reduce problem to

$$\begin{bmatrix} A^{(1)} \\ A^{(q)} \end{bmatrix} = \begin{bmatrix} \left(\mathbf{T}_{s+}^{q-}\right)_{1,1} & -\left(\mathbf{Q}^{(q-)}\right)_{1,2} \\ \left(\mathbf{T}_{s}^{q-}\right)_{2,1} & -\left(\mathbf{Q}^{(q-)}\right)_{2,2} \end{bmatrix}^{-1} \mathbf{W}^{in} \tag{4.B.3}$$

$$\begin{bmatrix} A^{(1)} \\ A^{(q)} \end{bmatrix} = \frac{1}{|\mathbf{G}|} \begin{bmatrix} -\left(\mathbf{Q}^{(q-)}\right)_{2,2} u_r^{in} + \left(\mathbf{Q}^{(q-)}\right)_{1,2} \sigma_r^{in} \\ -\left(\mathbf{T}_{s}^{q-}\right)_{2,1} u_r^{in} + \left(\mathbf{T}_{s+}^{q-}\right)_{1,1} \sigma_r^{in} \end{bmatrix} \tag{4.B.4}$$

where

$$\mathbf{G} = \begin{bmatrix} \left(\mathbf{T}_{s+}^{q-}\right)_{1,1} & -\left(\mathbf{Q}^{(q-)}\right)_{1,2} \\ \left(\mathbf{T}_{s}^{q-}\right)_{2,1} & -\left(\mathbf{Q}^{(q-)}\right)_{2,2} \end{bmatrix} \tag{4.B.5}$$

since $p = 2$

$$\mathbf{W}^{p-} = \frac{1}{|G|} \begin{bmatrix} \left(\mathbf{Q}^{(1+)}\right)_{1,1} \left\{ -\left(\mathbf{Q}^{(q-)}\right)_{2,2} u_r^{in} + \left(\mathbf{Q}^{(q-)}\right)_{1,2} \sigma_r^{in} \right\} \\ \left(\mathbf{Q}^{(1+)}\right)_{1,2} \left\{ -\left(\mathbf{Q}^{(q-)}\right)_{2,2} u_r^{in} + \left(\mathbf{Q}^{(q-)}\right)_{1,2} \sigma_r^{in} \right\} \end{bmatrix} \tag{4.B.6}$$

- using exact analytic

$$\begin{bmatrix} A_1^{(p)} \\ A_2^{(p)} \end{bmatrix} = \left(\mathbf{Q}_n^{(p-)}\right)^{-1} \mathbf{W}^{p-} \tag{4.B.7}$$

-

$$\mathbf{T}_s^{q-} = \mathbf{M}^p \mathbf{Q}^{1+} \tag{4.B.8}$$

-where $\mathbf{M}^p$ can be for exact analytic

$$\mathbf{M}^p = \mathbf{Q}^{(p+)} \left(\mathbf{Q}^{(p-)}\right)^{-1} \tag{4.B.9}$$

201

and

$$\phi^+ = A_1^{(p)} h_{33} J_\gamma \left(\kappa^{(p)} r^+ \right) + A_2^{(p)} h_{33} H_\gamma \left(\kappa^{(p)} r^+ \right)$$

$$+ \int\limits_{r_2}^{r_3} \left(A_1^{(p)} \frac{h_{32}}{r} J_\gamma \left(\kappa^{(p)} r^+ \right) + A_2^{(p)} \frac{h_{32}}{r} H_\gamma \left(\kappa^{(p)} r^+ \right) \right) dr \qquad (4.\text{B}.10)$$

-or $\mathbf{M}^p$ can be for proposed model

$$\mathbf{M}^p = \mathbf{K}^+ \left(\mathbf{K}^- \right)^{-1} \qquad (4.\text{B}.11)$$

$$\mathbf{M}^p = \begin{bmatrix} -\frac{c_{33}}{h} - \frac{c_{23}}{2\bar{r}} & \frac{1}{2} \\ \frac{\rho\omega^2}{2} - \frac{c_{22}}{2\bar{r}^2} - \frac{c_{23}}{h\bar{r}} & \frac{r^+}{h\bar{r}} \end{bmatrix}^{-1} \left(- \begin{bmatrix} \frac{c_{33}}{h} - \frac{c_{23}}{2\bar{r}} & \frac{1}{2} \\ \frac{\rho\omega^2}{2} - \frac{c_{22}}{2\bar{r}^2} + \frac{c_{23}}{h\bar{r}} & \frac{-r^-}{h\bar{r}} \end{bmatrix} \right) \qquad (4.\text{B}.12)$$

and

$$\mathbf{W}^{p+} = \left(\mathbf{M}^p \right)^{-1} \mathbf{W}^{p-} \qquad (4.\text{B}.13)$$

or since $p = q - 1$

$$\mathbf{W}^{p+} = \left(\mathbf{M}^{q-1} \right)^{-1} \mathbf{W}^q \qquad (4.\text{B}.14)$$

$$\mathbf{W}^{p+} = \left(\mathbf{M}^{q-1} \right)^{-1} \mathbf{W}^q \qquad (4.\text{B}.15)$$

$$\phi^+ = \frac{1}{\epsilon_{33}} \left(e_{33} \left(u_r^+ - u_r^- \right) + \frac{e_{32} h}{\bar{r}} \bar{u}_r \right) \qquad (4.\text{B}.16)$$

Appendices for chapter 5

Appendix A

The following linear solver (based on Matlab, Multiprecision toolbox, and modified column scaling) has been used throughout the study as shown in flowchart A.5.

Appendix B

Bessel functions are the solutions of Bessel's differential equation which arise when solving Helmholtz equation by separation of variables in cylindrical coordinates (Watson, 1995)

$$\left(\frac{R(r)_{,rr}}{R(r)} + \frac{1}{r}\frac{R(r)_{,r}}{R(r)} + \frac{1}{r^2}\frac{\Theta(\theta)_{,\theta\theta}}{\Theta(\theta)} + \frac{Z_{,zz}}{Z} + k^2 \right) = 0 \tag{5.B.1}$$

$$R\left(r\right)_{,rr} + \frac{1}{r}R\left(r\right)_{,r} + \left(\frac{-\nu^2}{r^2} + k^2 \right)R = 0 \tag{5.B.2}$$

The radial functions, in theory, could be any two of the Bessel functions $J_\nu(kr)$, $Y_\nu(kr)$, $H_\nu^{(1)}(kr)$, and $H_\nu^{(2)}(kr)$, however, in practice, it is essential for the stability of the numerical solution to represent the potential as

$$R(r) = \left\langle J_\nu\left(kr\right)H_\nu^{(1)}\left(kr_{j+1}\right), \frac{H_\nu^{(1)}\left(kr\right)}{H_\nu^{(1)}\left(kr_j\right)} \right\rangle \tag{5.B.3}$$

where $J_n\left(.\right)$ is Bessel function of the first kind, $H_n\left(.\right)$ is Hankel function or Bessel function of the third kind and the use of the $\langle \rangle$ indicates that the full solution is a linear combination of these expressions.
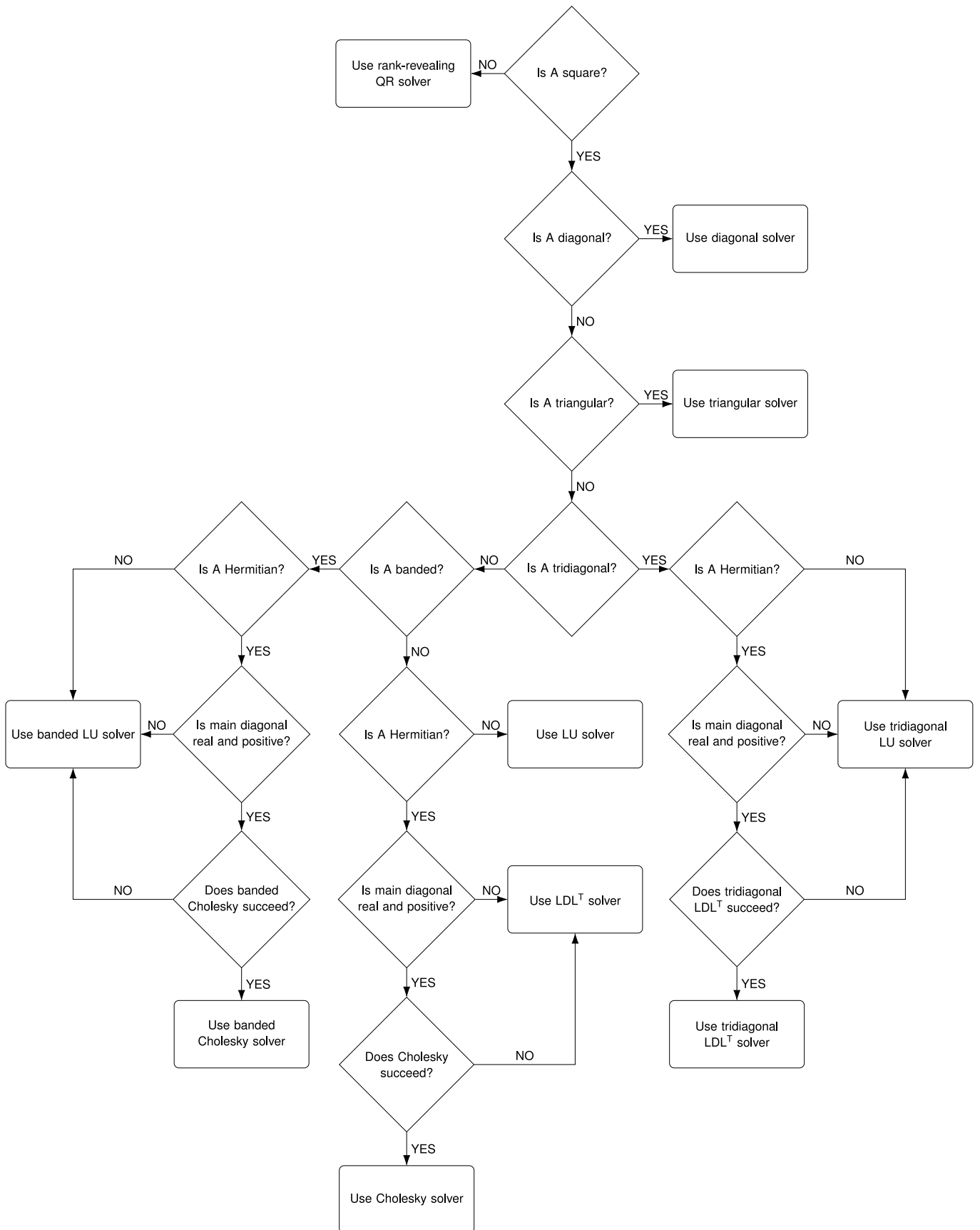
Flowchart A.5: Linear solver used

Appendices for chapter 6

Appendix A

Several techniques have been developed to treat wave propagation in an infinite media or unbounded domains since finite element methods require boundary conditions: these are non-reflecting boundary conditions (NRBC) (Givoli, 1991; Givoli, 2004; Givoli and Keller, 1990), absorbing layer methods (Berenger, 1994; Hastings, Schneider, and Broschat, 1996), and infinite element methods. Infinite elements are special elements of finite area (2D) or volume (3D) formulated to satisfy the Sommerfeld radiation condition, ensuring total radiation of waves from a source, but their performance is poor in elastodynamic problems (Liu and Jerry, 2003; Rajagopal et al., 2012). Non-Reflecting Boundary Conditions (NRBC) are similar in concept but have no area (2D) or volume (3D) and require modification of the standard solving procedure, therefore, the codes have to be specifically developed.

Absorbing layer methods consider a finite region which is typically made of the same FE elements as the rest of the model and attached to the boundaries of the domain of interest. These methods can be incorporated into commercial FE packages thereby, making use of existing elements that are already offered within the package. Two absorbing layer techniques for elastodynamic problems have been used in this study: absorbing regions/layers with gradually increased damping and perfectly matched layers.

The structural infinite element, INFIN257, is not used to model an infinite domain since the element adapts to the theory of mapped element for static analysis. The gradually increased damping layer is used for dynamic analysis. In ANSYS 16 and higher, the structural perfectly matched layer (PML) feature is used as an artificial material to simulate the unbounded medium by truncating the structural unbounded domain.

PML's are defined by using the SOLID185, SOLID186, and SOLID187 elements with KEYOPT(15) = 1. In a structural harmonic analysis, the outgoing elastic waves are absorbed by the PML without any reflections. The frequency range for PML is wide even static analysis, the domain boundary edge displacement is attenuated rapidly in the PML without affecting the values of displacement within the under study (normal) FEA domain. Modeling PML requires a closure for three-dimensional models (a cubic or spherical enclosure) with more than three layers. The PML can accommodate the symmetry of the model. The displacement values on the exterior surface of structural PML must be set to zero. The current solid structural PML feature does not support transient analysis. For dynamic analysis, the element adopts the theory of absorbing boundary (ANSYS-manuals, 2012-2018).